



DISSERTATION - RC143505

# Cyclic Behaviour of Slab-Column Connections using the Engineered Cementitious Composite

ASDAM TAMBUSAY  
3113 301 017

## SUPERVISORS:

Prof. Ir. Priyo Suprobo M.S., Ph.D.

Dr. Eng. A. Arwin Amiruddin, S.T., MT.

DOCTORAL PROGRAMME  
FIELD OF STUDY STRUCTURAL ENGINEERING  
DEPARTMENT OF CIVIL ENGINEERING  
FACULTY OF CIVIL ENGINEERING AND PLANNING  
INSTITUT TEKNOLOGI SEPULUH NOPEMBER  
SURABAYA  
2017

*This page intentionally left blank*

## **DECLARATION**

I, Asdam Tambusay, hereby declare that the following thesis has been composed by me and expressed in my own words, that the work has been carried out by myself, and that it has not been presented in any previous application for a higher degree

*This page intentionally left blank*

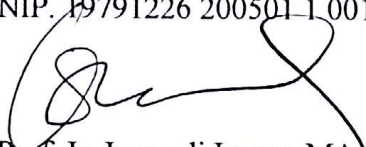
## APPROVAL SHEET

A dissertation submitted to Institut Teknologi Sepuluh Nopember for the degree  
of **DOCTOR OF PHILOSOPHY**

Asdam Tambusay  
NRP. 3113 301 017

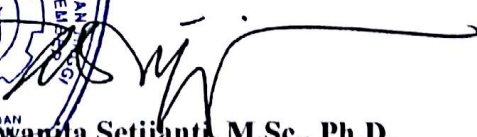
Exam Date: 25 July 2017  
Graduation Period: September 2017

Approved by:

1.   
Prof. Ir. Priyo Suprobo, MS., Ph.D. (Supervisor)  
NIP. 19590911 198403 1 001
2.   
Dr. Eng. A. Arwin Amiruddin, ST., MT. (Co-Supervisor)  
NIP. 19791226 200501 1 001
3.   
Prof. Ir. Iswandi Imran, MA.Sc., Ph.D. (Examiner 1)  
NIP. 19631206 199603 1 001
4.   
Ir. Handayanu, M.Sc., Ph.D. (Examiner 2)  
NIP. 19630728 198803 1 001
5.   
Endah Wahyuni, ST., M.Sc., Ph.D. (Examiner 3)  
NIP. 19700201 199512 2 001



Dean of Faculty of Civil Engineering and Planning

  
Ir. Purwana Setijanta, M.Sc., Ph.D.  
NIP. 19590427 198503 2 001

*This page intentionally left blank*

## Perilaku Siklik Hubungan Pelat-Kolom Menggunakan Material *Engineered Cementitious Composite*

Nama Mahasiswa : Asdam Tambusay  
NRP : 3113 301 017  
Promotor : Prof. Ir. Priyo Suprobo MS., Ph.D.  
Co-Promotor : Dr. Eng. A. Arwin Amiruddin, ST., MT.

### ABSTRAK

Penyelidikan eksperimen di laboratorium dilakukan untuk mempelajari perilaku struktur hubungan pelat-kolom akibat kondisi pembebanan yang relatif tinggi. Dalam penelitian ini, alternatif baru diusulkan untuk meningkatkan respons struktur hubungan pelat-kolom. Alternatif ini menggunakan jenis material yang berorientasi semen yakni *engineered cementitious composite* (ECC) bersama dengan penggunaan elemen drop panel pada bagian sambungan yang berfungsi sebagai penebalan lokal. Untuk menunjukkan penerapan alternatif yang diusulkan, tiga jenis benda uji diuji terhadap beban gravitasi konstan dan beban lateral siklik. Benda uji tersebut merupakan benda uji skala 1:2 yang juga merupakan representasi model interior hubungan pelat-kolom pada prototipe bangunan flat slab. Semua benda uji didesain tanpa menggunakan tulangan geser pada pelat, namun rasio tulangan lenturnya didesain cukup rendah dengan nilai berkisar 0.01. Hal ini dilakukan untuk menjamin bahwa benda uji akan berperilaku dalam kondisi *under-reinforced* sehingga mengizinkan tulangan lentur pada pelat mengalami pelepasan terlebih dahulu sebelum kegagalan beton pada benda uji. Jumlah tulangan pelat dan kolom yang digunakan pada benda uji adalah tipikal untuk setiap spesimen. Benda uji kontrol, di sini sebut sebagai benda uji pertama, di fabrikasi menggunakan beton konvensional, sedangkan benda uji kedua dan ketiga di fabrikasi dengan kombinasi material ECC dan beton konvensional. Pada benda uji kedua dan ketiga, ECC hanya dicor pada daerah penebalan lokal (drop panel). Mutu beton konvensional dan ECC pun didesain relatif sama. Semua benda uji dibebani dengan skenario beban siklik lateral yang sama. Pengecualian hanya terjadi pada penentuan nilai rasio beban gravitasi (GSR) di mana benda uji pertama, kedua dan ketiga memiliki GSR 0,08, 0,05, dan 0,25 secara berurutan. Perbedaan nilai rasio beban gravitasi dilakukan untuk mengetahui kinerja ECC dalam menahan beban gravitasi yang cukup signifikan.

Selain pengujian secara eksperimen di laboratorium, analisis nonlinear menggunakan perangkat numerik juga dilakukan dalam penelitian ini sebagai perbandingan hasil eksperimen yang telah diperoleh. Dalam hal ini, tiga jenis perangkat numerik digunakan untuk menyimulasikan perilaku hubungan pelat-kolom. Di samping verifikasi hasil eksperimen, analisis lebih lanjut juga dilakukan

untuk menjelaskan mekanisme gaya-gaya dalam yang bekerja pada benda uji hubungan pelat-kolom ketika dibebani beban gravitasi dan beban lateral siklik, sebagai contoh, distribusi tegangan utama pada pelat, atau mekanisme pembentukan sendi plastis.

Berdasarkan hasil eksperimental, hal ini jelas terbukti bahwa semua benda uji mengalami kegagalan dalam kondisi lentur. Hal ini terlihat dari sebagian besar retak yang terjadi pada daerah pelat merupakan retak yang tegak lurus dengan arah pembebanan, di mana retak ini pun merambat selebar lebar pelat. Di sisi lain, terlihat pula bahwa benda uji kedua menunjukkan kenaikan kapasitas beban lateral dua kali lipat lebih besar daripada benda uji kontrol. Di samping itu, setelah kenaikan rasio simpangan 3,5%, benda uji kedua tidak mengalami penurunan kekuatan, sedangkan benda uji kontrol menunjukkan kehilangan kekuatan lateral yang signifikan pada rasio simpangan yang sama. Berdasarkan hasil pengamatan pada benda uji ketiga, jelas terlihat bahwa respons benda uji ini hampir menyerupai benda uji kedua meskipun dibebani dengan rasio beban gravitasi menengah. Berdasarkan evaluasi kriteria ACI 374.1-05, benda uji kedua dan ketiga secara umum memenuhi persyaratan sebagai struktur tahan gempa, meskipun benda uji yang diusulkan belum layak direkomendasikan untuk diterapkan pada kategori desain seismik IV karena kekakuan awal yang tidak memadai.

Berdasarkan hasil analisis numerik, hal ini menunjukkan bahwa kurva histerisis dan *backbone* yang diperoleh pada pengujian eksperimen menunjukkan tren yang sama dengan kurva histerisis dan *backbone* analisis numerik. Hal lain juga menunjukkan bahwa nilai tegangan utama pada pelat masih lebih rendah dari kuat tekan beton, sehingga mengimplikasikan bahwa benda uji belum mengalami *crushing* pada beton. Hal ini juga dapat diasosiasikan dengan fenomena yang terjadi selama pengujian eksperimen, di mana semua benda uji tidak mengalami *crushing* bahkan sampai pada akhir pembebanan.

**Kata kunci**—hubungan pelat kolom, ECC, drop panel, beban gravitasi, beban lateral siklik.

## **Cyclic Behaviour of Slab-Column Connections using the Engineered Cementitious Composite**

Student's Name : Asdam Tambusay  
Student's ID : 3113 301 017  
Supervisor : Prof. Ir. Priyo Suprobo MS., Ph.D.  
Co-Supervisor : Dr. Eng. A. Arwin Amiruddin, ST., MT

### **ABSTRACT**

An experimental investigation has been undertaken to study the behaviour of slab-column connections subjected to high loading conditions. A novel alternative to improve the structural response of slab-column connections is proposed. The proposed alternative employs the use of a cement-based engineered cementitious composite (ECC) material along with the addition of drop panel attached to the connection. To demonstrate the applicability of this alternative, the three test specimens were tested under combined gravity and cyclic lateral loading. These specimens were half-scale representations of interior slab-column connections in a prototype flat slab building. All test specimens had no shear reinforcement provided in the slab, yet the longitudinal reinforcement ratio was designed relatively low, with the ratio approximately 0.01. This is to ensure that the specimens were in under-reinforced section thereby allowing the reinforcing bars to yield prior to specimen failure. The amount of reinforcing bars used to make the specimen was typical to each of test specimens. The control specimen, hereinafter referred to as the first specimen, was cast using conventional concrete, while other second and third specimen were cast with ECC and conventional concrete. In both latter specimens, ECC was only placed within the local thickening area. The grades of conventional concrete and ECC were also designed similarly. All specimens were subjected to similar cyclic displacement routine. The only exception lies on the application of gravity shear ratio (GSR) in which the value of GSR of first, second, and the third specimen was 0.08, 0.05, and 0.25 respectively. The influence of the different range of gravity shear ratio was examined to assess the performance of ECC resisting the intermediate gravity load.

Apart from the experimental investigation, a number of nonlinear finite element simulations have also been included in this study for comparative purposes with regard to the experimental results. As such, three different finite element software packages have been used to perform the nonlinear analysis. In addition to the experimental verification, further analysis has been carried out to lucidly explain the internal mechanisms of slab-column connections when being subjected to combined gravity and cyclic lateral loading, for instance, the principal stress distribution alongside the slab, and the governance of plastic hinge zone.

From the experimental results, it is evident that the failure of all specimens is regarded as flexure failure, showing the majority of inclined crack is perpendicular

to loading direction which also extends towards the entire width of the slab. It is also shown that the second specimen exhibits better behavioural response than control specimen whereby the lateral load capacity is nearly twice higher than the first specimen. Furthermore, upon the drift ratio of 3.5%, the second specimen does not undergo strength degradation, whereas in the control specimen the prominent loss of strength is apparent at 3.5% drift level, implying the response is on the verge of failure. With regard to the results from the third specimen, it is shown the overall behaviour resembles the response of the second specimen despite being subjected to intermediate gravity loading. In accordance with the evaluation of acceptance criteria, the second and third specimen generally comply the requirements as an earthquake proof and resistant structure. The only exception is that the proposed structure is not yet recommended to be applied in seismic design category IV due to inadequate initial stiffness provided by the structure.

In terms of numerical results, it is shown that the hysteretic and backbone curves obtained from experimental tests are in good agreement with the hysteretic and backbone curves obtained from the nonlinear finite element analysis. It is also shown that the magnitude of principal stress is still less than the compressive stress of concrete, owing to the fact that the specimens do not undergo concrete crushing. This also can be associated with the phenomenon captured in the experimental investigation where all the test specimens did not experience concrete crushing up to the final stage of loading.

**Keywords**—slab-column connection, ECC, drop panel, gravity load, cyclic load.

## ACKNOWLEDGEMENTS

This thesis represents not only my work behind the desk, but it is also a milestone in years of study at ITS and specifically within the Laboratory of Concrete and Building Materials. Despite my short of experiences throughout these years, I have learned a multitude of knowledge thereby helping me be the person who has a grounded mindset. It has also been an incredible journey for me because I have been given many opportunities beyond my expectation.

First and foremost, I wish to thank my advisor, Professor Priyo Suprobo, director of the Laboratory of Concrete and Building Materials at ITS. He has been truly supportive since the first day I began working with him. Throughout these years, he provided me with his wisdom, enthusiasm, inspiration, and invaluable advice. His profound and broad knowledge, continuous encouragement, inspiring ideas, keen instruction and supervision, and meticulous revisions massively helped me to achieve this work. I have learned a lot through my wealth of experience with him on his excellent academic, professional and personal levels. This dissertation would not be possible and fruitful without his excellent guidance and encouragement throughout the entire process of my study.

I also would like to express my sincere gratitude to my second advisor, Faimun PhD, for being such a supportive person. His understanding of structural engineering has helped me a lot to manage to complete this thesis. His suggestion, criticism and constructive comments have been invaluable in the preparation of this thesis.

My sincere gratitude also goes to my third advisor, Dr. Arwin Amiruddin, for devoting his time to my experimental program at the University of Hasanuddin. He provided me fundamental insight based on his experience working in the laboratory.

Special thanks are due to other members of the committee, Professor Iswandi Imran, Handayanu PhD, and Endah Wahyuni PhD, for their time, criticism, invaluable and qualified review, and also the suggestions of the materials of this thesis.

I wish to acknowledge the Ministry of Research, Technology, and Higher Education of the Republic of Indonesia for the financial support throughout my study under the scheme of Master-Doctor Internship Programme (PMDSU) Scholarship.

I also wish to acknowledge all the supports provided by WIKA Beton Tbk., and for putting this research as a priority, particularly during the fabrication of the specimens. My genuine thanks also go to PT. Hanil Jaya Steel for supplying the reinforcing steel.

I would like to extend my deepest appreciation and gratitude to the Laboratory of Structure and Materials at Hasanuddin University for providing technical and administrative services during my experimental investigation.

Truly grateful to my best flatmate as well as my colleague at the University, Indra Komara, who has been truly such a very encouraging friend throughout my ups and down. Big thanks also go to my academic peer, Wahyuniarsih Sutrisno. She literally reached out to me and always provided me with such up-to-date information. I could not thank her enough for her fruitful discussion and comments.

My genuine gratitude is also extended to my very kind host-supervisor, Dr. Benny Suryanto; an assistant professor at Heriot-Watt University in Edinburgh whom I have been working with. He provided me with his broad knowledge and understanding of concrete mechanics. I have found his enthusiasm and work ethic inspiring.

I also wish to thank Jonathon Luke Fox and Danah Saraireh for being such good mates when I was in the UK. They gave me the warmest welcome, and they helped me a lot throughout my programme. I was so lucky to have such opportunity to meet them in person.

I would like to express my sincere gratitude to my friendly academic peers at Master Program in the field of Structural Engineering at ITS, for creating the warmest environment throughout these years.

Last but not least, I would like to express my sincere love and deepest gratitude to my big beloved families. Their continuous supports, encouragement, and prayers greatly helped me to achieve this work. I am especially grateful for the genuine and limitless love and tremendous help from my mum and dad along with my siblings.

## TABLE OF CONTENTS

<b>THESIS COVER</b> .....	i
<b>APPROVAL SHEET</b> .....	iii
<b>ABSTRAK</b> .....	v
<b>ABSTRACT</b> .....	vii
<b>ACKNOWLEDGEMENTS</b> .....	ix
<b>TABLE OF CONTENTS</b> .....	xi
<b>LIST OF FIGURES</b> .....	xv
<b>LIST OF TABLES</b> .....	xxi
<b>LIST OF NOTATIONS</b> .....	xxiii
<b>CHAPTER 1 INTRODUCTION</b> .....	1
1.1. Background.....	1
1.2. Research Significance.....	5
1.3. Research Objectives.....	6
1.4. Scope of Research.....	7
1.5. Hypothesis Adopted.....	8
<b>CHAPTER 2 LITERATURE REVIEW</b> .....	11
2.1. Flat Slab Structural System.....	11
2.2. Mechanics of Slab-Column Connections.....	13
2.3. Failure Mode of Slab-Column Connection.....	15
2.4. General Setups of Slab-Column Connections Tested under Gravity and Lateral and Loading.....	16
2.5. Influence of Flexural Reinforcement Ratio.....	17
2.6. The Use of Drop Panel in Flat Slab Structure.....	19
2.7. Engineered Cementitious Composite (ECC).....	24
2.8. Acceptance Criteria for Earthquake Proof and Resistant Structures	29
2.9. Ductility.....	31
2.10. Previous Experimental Investigation on the Cyclic Behaviour of Slab-Column Connections (Prawatwong <i>et al.</i> 2008).....	32
2.11. Numerical Analysis of Flat Slab Structure (Genikomsou <i>et al.</i> 2014).....	34

<b>CHAPTER 3 EXPERIMENTAL PROGRAMME</b> .....	37
3.1. Analytical Design of Shear Stress in the Slab.....	37
3.2. Specimen Design.....	39
3.3. Specimen Preparation.....	43
3.3.1. Reinforcing cage and strain gauge installation.....	43
3.3.2. Casting and curing.....	45
3.4. Mix Design of Concrete and ECC.....	47
3.5. Mechanical Properties of Material.....	50
3.5.1. Properties of normal concrete.....	50
3.5.2. Properties engineered cementitious composite.....	51
3.5.3. Properties of reinforcing bar.....	54
3.6. Experimental Activities.....	56
3.6.1. Test setup.....	56
3.6.2. Pre-test activities.....	58
3.7. Loading protocol.....	59
3.8. Instrumentation.....	61
3.9. Monitoring and Data Acquisition.....	63
3.10. Evaluation of Test Results.....	64
<b>CHAPTER 4 EXPERIMENTAL RESULTS AND DISCUSSION</b> .....	67
4.1. Load-Drift Relationship and Cracking Behaviour.....	67
4.2. Analytical Evaluation Based on Design Codes.....	76
4.3. Connection Lateral Drift Capacity.....	79
4.4. Evaluation of Acceptance Criteria.....	81
4.4.1. Strength degradation.....	81
4.4.2. Concept of strong column/weak beam.....	83
4.4.3. Initial stiffness.....	85
4.4.4. Stiffness degradation.....	87
4.4.5. Energy dissipation.....	89
4.5. Slab Flexural Reinforcement Strain Readings.....	92
<b>CHAPTER 5 FINITE ELEMENT ANALYSIS</b> .....	99
5.1. Work Package 1 – ABAQUS.....	99
5.1.1. Overview.....	99

5.1.2. Element model.....	100
5.1.3. Material properties.....	100
5.1.4. Mesh and boundary conditions.....	107
5.1.5. Loading scenario.....	107
5.1.6. The solution of nonlinear problems.....	108
5.1.7. Results and discussion of ABAQUS.....	113
5.2. Work Package 2 – SAP2000.....	122
5.2.1. Overview.....	122
5.2.2. Hysteretic rules.....	124
5.2.3. Parameters controlling hysteretic response.....	126
5.2.4. Developed model of slab-column connection using SAP2000.....	126
5.2.5. Results and discussions of SAP2000.....	129
5.3. Work Package 3 – ZEUS NL.....	131
5.3.1. Overview.....	131
5.3.2. Material models.....	132
5.3.3. Element model.....	134
5.3.4. Analytical model of slab-column connection using ZEUS-NL.....	135
5.3.5. Results and discussion of ZEUS-NL.....	135
5.4. Summary of Numerical Analyses.....	137
5.5. Further Analysis of Prototype Slab-Column Connections.....	138
<b>CHAPTER 6 CONCLUSIONS AND RECOMMENDATIONS.....</b>	<b>143</b>
6.1. Conclusions.....	143
6.2. Recommendations for Future Research.....	146
<b>REFERENCES.....</b>	<b>149</b>
<b>APPENDIX A: PRELIMINARY DESIGN OF SPECIMEN S1.....</b>	<b>159</b>
<b>APPENDIX B: PRELIMINARY DESIGN OF SPECIMEN S2.....</b>	<b>165</b>
<b>APPENDIX C: PRELIMINARY DESIGN OF SPECIMEN S3.....</b>	<b>171</b>
<b>BIOGRAPHY.....</b>	<b>177</b>

*This page intentionally left blank*

## LIST OF FIGURES

<b>Figure 1.1</b>	The location of plastic hinge mechanisms in the flat slab structure as flexural moment resisting frame.....	8
<b>Figure 1.2</b>	The location of plastic hinge mechanisms in the flat slab structure as special moment resisting frame.....	9
<b>Figure 2.1</b>	Typical form of flat slab structure.....	11
<b>Figure 2.2</b>	Illustration of joint location of slab-column connections.....	12
<b>Figure 2.3</b>	Critical region around slab-column connection.....	13
<b>Figure 2.4</b>	Critical section (perimeter) of slab-column connection.....	14
<b>Figure 2.5</b>	Transfer of uniform gravity load unbalanced moment within the critical section: (a) uniform shear stress due to gravity load; (b) eccentric shear stress due to unbalanced moment; (c) total shear stress.....	14
<b>Figure 2.6</b>	Schematic model for shear and moment transfer of slab-column connection.....	15
<b>Figure 2.7</b>	Formation of flexural cracks due to lateral load.....	16
<b>Figure 2.8</b>	Drop panel members in flat slab structure.....	19
<b>Figure 2.9</b>	Four types of connections in flat slab system.....	22
<b>Figure 2.10</b>	Effective slab widths: (a) termed as strength; (b) termed as stiffness.....	23
<b>Figure 2.11</b>	Uniaxial tensile stress-strain relationship and crack widths of ECC with the additional information of typical tensile response of conventional concrete to facilitate direct comparison.....	26
<b>Figure 2.12</b>	Pre-cracked ECC plates: (a) testing procedure; (b) crack patterns of selected plates within constant moment span at failure.....	28
<b>Figure 2.13</b>	Quantities used in evaluating acceptance criteria.....	31
<b>Figure 2.14</b>	Unacceptable hysteretic behaviour.....	31
<b>Figure 3.1</b>	Prototype of proposed flat slab structure with dual system [unit in metre]: (b) 2D plan; (c) side view in longitudinal direction (x-axis); (a) 3D isometric view.....	40

<b>Figure 3.2</b>	Schematic geometry of test specimen [unit in millimetre]: (a) top view; (b) longitudinal direction (x-axis).....	41
<b>Figure 3.3</b>	Reinforcement layouts [unit in millimetre]: (a) slab top reinforcement bars; (b) slab bottom reinforcement bars; (c) longitudinal and web reinforcement of column.....	42
<b>Figure 3.4</b>	Chronological process of reinforcing cage, starting from the fabrication to the adjustment in the formwork (steel mould) along with the installation of strain gauges.....	44
<b>Figure 3.5</b>	Phase of casting the specimen with ECC.....	46
<b>Figure 3.6</b>	Packing of specimen.....	47
<b>Figure 3.7</b>	Setup of direct tensile test of ECC dog-bone shape.....	50
<b>Figure 3.8</b>	Compressive stress-strain relationship of ECC cubes.....	53
<b>Figure 3.9</b>	Tensile stress-strain relationship of ECC dog-bone shapes.....	54
<b>Figure 3.10</b>	Tensile stress-strain response of reinforcing bars.....	55
<b>Figure 3.11</b>	Test set up of slab-column connection.....	56
<b>Figure 3.12</b>	Schematic testing configurations [unit in millimetre]: (a) side view in longitudinal direction; (b) top view.....	57
<b>Figure 3.13</b>	Uplift technique for test specimen.....	59
<b>Figure 3.14</b>	Lateral displacement routine.....	61
<b>Figure 3.15</b>	Location of strain gauges and LVDTs: (a) strain gauges at top slab reinforcing bars; (b) strain gauges at bottom slab reinforcing bars; (c) strain gauges of column and LVDTs seen from longitudinal direction; (d) strain gauges of column observed from transversal direction.....	62
<b>Figure 3.16</b>	Scheme of experimental test and data acquisitions.....	63
<b>Figure 4.1</b>	Load-drift relationship of specimen S1: (a) hysteretic behaviour with additional photo of final crack pattern, (b) traditional hand-drawn crack pattern observed on the top and bottom surface of the slab.....	68
<b>Figure 4.2</b>	Load-drift relationship of specimen S2: (a) hysteretic behaviour with additional photo of final crack pattern, (b) traditional hand-	71

	drawn crack pattern observed on the top and bottom surface of the slab.....	
<b>Figure 4.3</b>	Load-drift relationship of specimen S3: (a) hysteretic behaviour with additional photo of final crack pattern, (b) traditional hand-drawn crack pattern observed on the top and bottom surface of the slab.....	74
<b>Figure 4.4</b>	Comparison of backbone (envelope) curves of all specimens in each cycle of the loading sequence.....	75
<b>Figure 4.5</b>	Drift capacity versus gravity shear ratio of slab-column connections using drop panel with continued slab reinforcements.....	80
<b>Figure 4.6</b>	Illustrated graph for defining the strength degradation for all specimens: (a) specimen S1, (b) specimen S2, (c) specimen S3..	82
<b>Figure 4.7</b>	Illustrated graph for describing the stiffness degradation for all specimens: (a) specimen S1, (b) specimen S2, (c) specimen S3..	88
<b>Figure 4.8</b>	Illustrated graph of the parallelogram of ideal energy dissipation for all specimens: (a) specimen S1, (b) specimen S2, (c) specimen S3.....	91
<b>Figure 4.9</b>	1 Longitudinal strain profiles of specimen S1 measured in the slab reinforcing bars: (a) top reinforcing bars, (b) bottom reinforcing bars.....	93
<b>Figure 4.10</b>	Longitudinal strain profiles of specimen S2 measured in the slab reinforcing bars: (a) top reinforcing bars, (b) bottom reinforcing bars.....	95
<b>Figure 4.11</b>	Longitudinal strain profiles of specimen S3 measured in the slab reinforcing bars: (a) top reinforcing bars, (b) bottom reinforcing bars.....	97
<b>Figure 5.1</b>	Element types of FE model: (a) C3D8R linear brick element for concrete; (b) T3D2 truss element for reinforcement bars.....	99
<b>Figure 5.2</b>	Parameters of concrete damage plasticity model: (a) compressive response of concrete and ECC; (b) tensile response	102

	of concrete; (c) typical damage evolution of concrete and ECC; (d) tensile response of ECC.....	
<b>Figure 5.3</b>	Assumed average stress-strain relationship of reinforcements embedded in concrete.....	105
<b>Figure 5.4</b>	Finite element mesh and boundary conditions (unit is in millimetre).....	106
<b>Figure 5.5</b>	Loading etiquette in numerical simulation using displacement control method.....	107
<b>Figure 5.6</b>	First equilibrium iteration in an increment.....	109
<b>Figure 5.7</b>	Second equilibrium iteration in an increment.....	112
<b>Figure 5.8</b>	Predicted load-drift relationship of specimen S1: (a) hysteretic loop and (b) backbone curves.....	113
<b>Figure 5.9</b>	Predicted load-drift relationship of specimen S2: (a) hysteretic loop and (b) backbone curves.....	113
<b>Figure 5.10</b>	Predicted load-drift relationship of specimen S3: (a) hysteretic loop and (b) backbone curves.....	113
<b>Figure 5.11</b>	Principal stress distribution of specimen S1: (a) stress at the slab top surface in the positive loading, (b) stress at the slab bottom surface in the positive loading, (c) stress at the slab top surface in the negative loading, and (d) stress at the slab bottom surface in the negative loading.....	116
<b>Figure 5.12</b>	Principal stress distribution of specimen S2: (a) stress at the slab top surface in the positive loading, (b) stress at the slab bottom surface in the positive loading, (c) stress at the slab top surface in the negative loading, and (d) stress at the slab bottom surface in the negative loading.....	116
<b>Figure 5.13</b>	Principal stress distribution of specimen S3: (a) stress at the slab top surface in the positive loading, (b) stress at the slab bottom surface in the positive loading, (c) stress at the slab top surface in the negative loading, and (d) stress at the slab bottom surface in the negative loading.....	117

<b>Figure 5.14</b>	Diagonal compression struts: (a) specimen S1, (b) specimen S2, and (c) specimen S3.....	118
<b>Figure 5.15</b>	Location of plastic hinge zone in the slab-column connection....	119
<b>Figure 5.16</b>	Longitudinal strain plots of specimen S1.....	120
<b>Figure 5.17</b>	Longitudinal strain plots of specimen S2.....	121
<b>Figure 5.18</b>	Hysteretic characteristic of a typical reinforced member and the idealisation.....	122
<b>Figure 5.19</b>	Basic parameters for pivot hysteretic mode.....	123
<b>Figure 5.20</b>	Pivot point designations.....	125
<b>Figure 5.21</b>	Contours for (a) $\alpha$ parameter and (b) $\beta$ parameter.....	126
<b>Figure 5.22</b>	Developed model of slab-column connection in SAP2000.....	127
<b>Figure 5.23</b>	Input parameters of pivot hysteretic model.....	128
<b>Figure 5.24</b>	Computed hysteretic loop from SAP2000 with the superimposed hysteretic loop from experiments: (a) specimen S1, (b) specimen S2, and (c) specimen S3.....	130
<b>Figure 5.25</b>	Decomposition of a rectangular reinforced concrete section.....	131
<b>Figure 5.26</b>	Material models for ZEUS-NL analysis: (a) compressive response of concrete, (b) tensile response of steel, (c) tensile response for ECC, and (d) compressive response for ECC.....	133
<b>Figure 5.27</b>	2D analytical model of slab-column connection in ZEUS-NL....	134
<b>Figure 5.28</b>	Computed hysteretic loop from ZEUS-NL with the overlaid hysteretic loop from experiments: (a) specimen S1, (b) specimen S2, (c) and specimen S3.....	137
<b>Figure 5.29</b>	Schematic comparisons among finite element packages.....	138
<b>Figure 5.30</b>	Computed hysteretic loop of prototype slab-column specimens: (a) specimen S1, (b) specimen S2, and (c) specimen S3.....	141

*This page intentionally left blank*

## LIST OF TABLES

<b>Table 2.1</b>	The proposition of the slab effective width.....	22
<b>Table 2.2</b>	Mechanical properties of synthetic fibres.....	25
<b>Table 2.3</b>	Mechanical properties of PVA fibres.....	25
<b>Table 2.4</b>	Previous studies of various R/ECC structural elements.....	27
<b>Table 3.1</b>	Detail of mix proportion of conventional concrete.....	48
<b>Table 3.2</b>	Specification of PVA fibres (Nycon USA).....	49
<b>Table 3.3</b>	Detail of mix proportion of engineered cementitious composite.....	49
<b>Table 3.4</b>	Chemical properties of coal fly ash (ASTM C618).....	52
<b>Table 3.5</b>	Chemical compound contained in fly ash.....	52
<b>Table 3.6</b>	Tensile properties of reinforcements.....	55
<b>Table 3.7</b>	Target of drift ratio at each cycle.....	60
<b>Table 4.1</b>	Specimen test data summary.....	67
<b>Table 4.2</b>	Analytical evaluation on the transfer mechanism of shear and moment flexure based on design specifications.....	77
<b>Table 4.3</b>	Feasibility of strength degradation to each of test specimens...	83
<b>Table 4.4</b>	Evaluation of strong column/weak beam to each of test specimens.....	85
<b>Table 4.5</b>	Ratio of lateral resistance and nominal strength for the evaluation of initial stiffness for all test specimens.....	86
<b>Table 4.6</b>	Adequacy of stiffness degradation of all test specimens.....	89
<b>Table 4.7</b>	Ratio of actual and ideal energy dissipation of all test specimens.....	92
<b>Table 5.1</b>	Summary of scale factors for reinforced concrete true model...	139
<b>Table 5.2</b>	Ratio of maximum load capacity of prototype over half-scale model of slab-column connections.....	139

*This page intentionally left blank*

## LIST OF NOTATIONS

<b>CHAPTER 2</b>			
$V_g$	= Uniform shear force due to gravity load		$\epsilon_u$ = Strain at ultimate load
$M_u$	= Unbalanced moment		$\epsilon_y$ = Strain at yield load
$\gamma_f$	= Fraction of unbalanced moment transferred by flexure		$\mu_o$ = Rotation ductility
$\gamma_v$	= Fraction of unbalanced moment transferred by shear		$\theta_u$ = Rotation at ultimate load
$h$	= Slab thickness		$\theta_y$ = Rotation at yield load
$\rho_b$	= Reinforcement ratio in balance condition		$\mu_s$ = Displacement ductility
$\rho$	= Reinforcement ratio		$\Delta_u$ = Displacement at ultimate load
$\alpha$	= Effective width beam coefficient		$\Delta_y$ = Displacement at yield load
$\alpha_r$	= Modified factor on the $c_2/c_1$		$f_{pu}$ = Maximum breaking load
$\alpha_s$	= The effective beam width coefficients on the $l_1/l_2$ and $c_1/l_2$		$f'_c$ = Compressive strength of concrete
$l_2'$	= Equivalent effective width		<b>CHAPTER 3</b>
$l_2$	= Slab width		$M_u$ = The portion of unbalanced moment transferred by flexure
$\mu$	= The effect of the Poisson's ratio		$M_{exp}$ = Unbalanced moment obtained from experimental test
$c$	= Column width		$F_{exp}$ = Lateral load obtained from experimental test
$b$	= The effective slab width		$H_{col}$ = Total height of the column
$F_{exp}$	= Lateral load at yield point		$\gamma_f$ = The fraction of moment transferred by flexure
$F_{max}$	= Lateral load at peak point		$b_1$ = Width of critical section in the direction of loading
$\lambda$	= Overstrength factor for the test column		$b_2$ = Width of critical section measured perpendicular to $b_1$
$\mu_c$	= Curvature ductility		$v_u$ = Total shear stress
$\varphi_u$	= Curvature at ultimate load		$V_g$ = Shear force in the critical section caused by gravity load
$\varphi_y$	= Curvature at yield load		$A_c$ = Area of critical section calculated by $b_o \times d$
$\mu_e$	= Strain ductility		

$M_u$	=	The unbalanced moment represented as eccentric shear stress
$\gamma_v$	=	Fraction of unbalanced moment transferred by shear
$c$	=	Extreme fibre distance
$J_c$	=	Section property analogous to the polar moment of inertia of the critical section
$l_1$	=	Critical length parallel to loading direction
$l_2$	=	Critical length perpendicular to loading direction
$d$	=	Effective slab thickness
$b_o$	=	Critical perimeter
$b_o'$	=	Critical lines
$v_n$	=	Nominal shear stress
$v_c$	=	Shear stress provided by concrete
$v_s$	=	Shear stress provided by stirrup(s)
$v_f$	=	Shear stress provided by fibres
$\beta_c$	=	Ratio of long section to short section
$\alpha_s$	=	Constant coefficient, 40 for interior column and 30 for exterior column
$f'_c$	=	Concrete compressive strength
$f_t$	=	Designed tensile yield strength
$b_0$	=	Peripheral length to critical section
$\gamma_b$	=	Reduction factor
$f_y$	=	Yield strength of steel
$f_u$	=	Ultimate strength of steel

$\varepsilon_y$  = Strain corresponding to yield point

$\varepsilon_u$  = Strain corresponding to ultimate point

$DR$  = Drift ratio

#### CHAPTER 4

$V_g$  = Shear force in the critical section caused by gravity load

$A_c$  = Area of critical section calculated by  $b_o \times d$

$v_n$  = Nominal shear stress

$M_u$  = Unbalanced moment

$V_{u,p}$  = Predicted direct shear force

$V_u$  = Direct shear stress

$\gamma_v$  = Fraction of unbalanced moment transferred by shear

$v_u$  = Total shear stress

$v_c$  = Shear stress provided by concrete

$v_f$  = Shear stress provided by fibres

$\gamma_f$  = Fraction of unbalanced moment transferred by flexure

$c_2$  = Column width perpendicular to loading direction

$h$  = Slab thickness

$M_f$  = Flexural moment capacity

$b_o$  = Critical perimeter of slab

$d$  = Effective width of slab measured from the tensile (top) reinforcing bar to the compression surface (bottom) of the slab

$f'_c$  = Concrete compressive strength



$\sigma_{c0}$	=	Uniaxial compressive strength	$R_a$	=	Force residual for the iteration
$\varepsilon$	=	Flow potential eccentricity	$P$	=	External forces
$K$	=	Deviatoric invariant ratio	$\Delta u_a$	=	Total incremental displacement
$\Psi$	=	Dilation angle	$K_a$	=	New tangent stiffness for the structure
$\nu$	=	Viscosity parameter	$a$	=	Designated equilibrium point
$d_c$	=	Compression damage	$b$	=	New equilibrium point
$d_t$	=	Tension damage	$c_b$	=	New displacement correction for the structure
$\sigma_{true}$	=	True uniaxial tensile stress of steel	$u_b$	=	New updated displacement configuration
$\varepsilon_{true}$	=	True strain of steel	$\Delta u_b$	=	New total incremental displacement
$\varepsilon_{nom}$	=	Nominal strain of steel	$\Delta T$	=	Initial time increment
$\varepsilon_{pl}$	=	Plastic strain of steel	$T_{tot}$	=	Total step time
$\Delta P$	=	Small load increment	$\alpha$	=	Pivot parameter for hysteretic model
$K_0$	=	Structure's tangent stiffness	$\beta$	=	Pivot parameter for hysteretic model
$u_0$	=	Initial displacement configuration	$\eta$	=	Pivot parameter for hysteretic model
$c_a$	=	Displacement correction for the structure	$P$	=	Pivot point ranging from P <sub>1</sub> to P <sub>4</sub>
$u_a$	=	Updated displacement configuration			
$I_a$	=	Internal forces			

# CHAPTER 1

## INTRODUCTION

### 1.1. Background

Many laboratory and analytical studies have been carried out over the past decades to improve the response of reinforced concrete structures under seismic loading. Regarding the prior studies, the majority has been done primarily on relatively new type reinforced concrete members, with the design not only consider on improving the structural performance but also how to construct the more economical system in the long run. It is worth mentioning that earthquake action is a displacement oriented in nature whereby the forces acting on the structure are controlled by strength and stiffness. In such situation, if the strength and stiffness of service condition are insufficient, the structure will be prone to govern excessive deformation which will also be followed by a major crack propagation.

To date the development of reinforced concrete structure has drawn upon many alternatives to build in the cost-effective system. One of such is flat slab system which offers modest design, flexibility in architecture, more spacious room area due to the absence of beam members, and fast construction time (Erberik and Elnashai, 2004). In addition, flat slab structural system also has high occupancy rate and allows to add a number of floors in the highly restricted area (Robertson *et al.*, 2002). Since this class of structure has gained popularity among engineers, flat slab structure has been established in various types (*e.g.* simple flat plate, flat slab with drop panels, flat slab with column heads, etc.). Regardless of above advantages, the seismic behaviour of flat slab structure, however, still becomes a profound consideration. If the design of structure is not considered properly, the flat slab structure is more prone to encounter progressive collapse when subjected to high unbalanced moments and uniform shear forces. In such situation, the prominence of local failure in some structural members will propagate vastly towards other members thereby leading to catastrophe. Although it is considered as a low probability phenomenon, the adverse effect of the damage can cause accidents and great loss (Qian and Li, 2013)

In general, there are two types of failures that must be accounted for in the design of flat slabs (viz, flexure and shear). Flexural failure is characterised by an inclined crack perpendicular to loading direction which extends towards the entire width of the slab, whereas slab failing in shear exhibits an inclined crack of 20-45 degrees to the horizontal that surrounds the perimeter of the column, creating a failure surface that resembles a truncated pyramid. This failure is commonly referred to as punching shear as the column appears to punch through the slab. Punching shear failure is typically brittle and results in a nearly complete loss of shear capacity, leading to progressive collapse to an entire floor, either with little or without any warning.

The collapse of flat slab building, in reality, is perhaps the best example to date to demonstrate the importance of preventing progressive failure. Several cases of flat slab structure which were indicated by the brittle punching shear failure occurred at L'Ambiance Plaza in Connecticut 1987 (Heger 1991), Commonwealth Avenue in Massachusetts 1971, Skyline Plaza in Virgin Island 1973, and Harbour Cay Condominium Building in Florida in 1981 (King and Dalatte, 2004). Other similar reported cases also took place in Mexico 1985, where 91 buildings collapsed severely due to the seismic events, and also 40 buildings were heavily damaged (Megally and Ghali, 2000).

Upon the past incidents, a deep consideration to limit the number of parameters in design has been taken into account. Design specification such as ACI 318-14 has determined the required limitations to design and calculate the punching shear capacity in the critical section of the slab-column connection. In addition to ACI 318-14, ASCE/SEI 7-10 has also limited the use of flat slab structure into specific requirements. In moderate or high seismic regions, the addition of more rigid members such as shear walls or external moment resisting beams is inevitable in order to provide sufficient lateral load resistance. Although flat slab frames are not designed to contribute the major lateral resistance, they still must demonstrate sufficient strength, stiffness, and ductility to support gravity loads while undergoing lateral displacements during the seismic event. With regard to its structural response, seismic-induced lateral displacement mostly generates unbalanced moment at slab-column connections. This unbalanced moment delivers shear stress

concentration in the critical region of the slab. Due to gravity load, uniform shear stress also forms and sums up the stress from unbalanced moment thereby causing the slab to undergo high shear stress. If the shear capacity is inadequate, the brittle punching failure may occur (Dovich and Wight, 2005).

To deal with the fragility of the flat slab, there has been extensive research carried out to provide in-depth insights into the full behaviour of slab-column connection. For example, the utilisation of web reinforcements in the slab along the critical perimeter. Robertson *et al.* (2002) studied the response of slab-column connections subjected to lateral cyclic loading with the use of three distinct shear reinforcements: closed stirrups, one-leg stirrups, and shear studs. It was shown that web reinforcements could improve the lateral drift capacity up to 8.0% prior to punching failure. During the observation, it was evident that the failure was in the flexural mode, causing the stirrups did not achieve the ultimate capacity. Gunadi *et al.* (2012) investigated the similar experiment by proposing the modification of shear stud configuration in the form of stud rails. The results highlighted the initial flexural cracks led to decrease in initial stiffness. However, it could effectively show the improvement in energy dissipation.

Another alternative was also considered by employing drop panel as local thickening (ACI 352.1R-89). Drop panel works effectively to reduce the negative moment in the slab-column joint and also increases the stiffness which can reduce the excessive lateral deformation. In addition to that, drop panel is used to improve the shear capacity of the structural member significantly even though it still generates brittle failure (Megally and Ghali, 2000). An experimental study conducted by Prawatwong *et al.* (2008) has confirmed the influence of drop panel in the behavioural response of the slab-column connections. In their experiments, interior slab-column connections with and without drop panel members were constructed. The study also included the utilisation of post-tensioned system to enable the sufficient response to resist the cyclic lateral loading. It was shown that punching shear was not yet to occur in the specimen with drop panel up to 4.0% drift cycle but rather experienced at the drift ratio of 6.0%. On the contrary, the specimen without drop panel exhibited punching shear failure at 2.0% drift level.

In addition to the above alternatives, the use of fibre-reinforced concrete was also proposed to study the behaviour of slab-column connections. McHarg *et al.* (2002) investigated the usage of steel fibres combined with high longitudinal reinforcement ratio adjacent to the column. This research was focused on the performance of the slab-column connection subjected to gravity loading. Steel fibres with the volume fraction of 0.5% were given in distance of 500 mm from column face, or it was equal to 3.3 times of the slab thickness. The results exposed the improvement in terms of strength over the punching shear. The increase of ductility was also evident and furthermore, crack widths were relatively small during service condition. While there seems to be a number of methods for improving the way in which the structure behaves, the results have not been able to trigger the changes in any design code. Therefore, further relevant studies are necessary in order to fully compromise the fragility of flat slab structure as well as to exploit the predominance in other types of materials.

The present study is focused on the improvement of slab-column connection behaviour under gravity and cyclic lateral load. Drop panel is proposed herein as it gives a promising response in terms of providing sufficient lateral stiffness. The main novelty of this research lies in the use of cement-based fibrous material, termed as engineered cementitious composite (ECC). This type of material is preferred due to its capability of avoiding brittle damage as well as offering the good performance. Since the complex response of slab-column connection occurs within the critical perimeter, the ECC material is only considered to be cast within the local thickening, or in this case at the drop panel element.

This study is among the first to use ECC material for investigating the behaviour of structural connections. The underlying reason for selecting the ECC material is highly driven by its ability to exhibit high tensile ductility in the form of pseudo-strain hardening response (Sahmaran and Li, 2008). In addition to that, it is also known that polyvinyl alcohol (PVA) fibres offer the important role of increasing the behavioural response in order to withstand shear and flexural stresses (Li, 2002). In general, the tensile stress-strain response of ECC material generates strain hardening behaviour with strain approximately ranging between 3-5% prior to fibres rupture, while in the opposite, regular concrete exhibits brittle response

with tensile strain normally up to 0.01% (Tambusay *et al.*, 2017). It should also be noted that the tensile response of ECC material can possibly go beyond that, depending on the fibres positions inside the matrix and proper mixing procedure. Aside from this, ECC material also demonstrates multiple yet closely-spaced micro cracks with cracks width under 100  $\mu\text{m}$  prior to fibres rupture.

Another aspect which strengthens this hypothesis in relation to the material selection is basically based on the experimental results brought by Fukuyama *et al.* (2000). The experiment was concerned about the response of beam-column joint with or without the use of ECC material as the specimens were subjected to lateral cyclic loading. The results indicated the increase of energy dissipation as well as the damage tolerance at the end of the loading course. Additionally, brittle failure was prevented, leading to the more ductile structure. It was also observed that bond splitting phenomenon did not occur in the specimen with ECC material. Based on above justifications, the use of ECC material in slab-column connection can potentially be applied to upgrade the structural the structural response. To demonstrate the applicability of ECC, the present work focuses on the test of slab-column connections under gravity and cyclic lateral load. The results from this study are expected to contribute to creating the sustainable civilisation in the future.

## **1.2. Research Significance**

It is inevitable that the fragility of the flat slab has led to structural collapses in the past seismic events. Although there seems to be a number of studies concerning to this issue, the results still have not been able to trigger the modifications in any design code. Facts on the ground also show that the current flat slab structure still has poor initial stiffness and significant stiffness degradation. In addition to that, brittle punching shear failure occurred in the connections also indicates a relatively small lateral drift capacity and low energy dissipation. Considering all the above, the main significance of this study lies on the utilisation of engineered cementitious composite material that could be further used as a potential alternative to improve the behaviour of the flat slab as an earthquake proof and resistant building structure. As a stepping stone toward achieving this goal, this

study is expected to result in the better behavioural response at the connections of flat slab system.

### **1.3. Research Objectives**

The aim of this study is to analyse the behaviour of slab-column connection due to combined constant gravity and reversed lateral load. Since a new type of cement-based material, otherwise termed as ECC, is proposed, it is anticipated to exploit the potency of ECC to result in the more ductile response with less damage. Aside from using conventional web reinforcement in the slab, this study adopts an additional member of what is called as drop panel. Slab flexural reinforcements, either longitudinal or transversal steel, are designed with low ratio and are positioned continuously to the column. The following specific objectives of this study are:

1. To investigate the hysteretic response of slab-column connections through an experimental program and finite element analysis.
2. To provide insights into the progression of cracks during the course of loading.
3. To obtain the relation of drift capacity due to the influence of gravity shear ratio on the slab.
4. To evaluate the acceptance criteria of the slab-column connections based on ACI 374.1-05 as an earthquake proof and resistant structure with particular focusing on the initial stiffness, stiffness degradation, strong column/weak beam, strength degradation, and energy dissipation.
5. To facilitate direct information regarding the flexural strain gauge readings from the slab reinforcing steel throughout the loading process.
6. To perform the nonlinear finite element analysis as a means to verify the experimental results.
7. To provide a better picture regarding the distribution of principal stress alongside the slab and diagonal compression strut at the joint with the value of stress is in correspondence with the peak load.

8. To evaluate the performance of slab-column connections in dissipating the earthquake energy through the visual observation from the length of plastic hinge zone.

#### **1.4. Scope of Research**

The present work involves experimental investigation and numerical analysis to study the behaviour of slab-column connections using ECC material and drop panel member. By considering the probability of work in the laboratory as well as making this research more focused, a number of limitations are given as follows:

1. Specimens are half-scale representation of interior slab-column connections taken as subassembly system in a prototype of flat slab structure using the dual system.
2. Specimens are tested under constant gravity load and uniaxial cyclic lateral load in the form of displacement controlled. The loading protocol is in accordance with ACI 374.2R-13. The biaxial load is not considered in the loading protocol.
3. Test specimens are subjected to cyclic lateral load starting from the linear elastic to nonlinear response with minimum expected drift ratio of 3.5%.
4. The gravity load is applied using prestressing technique, whereas the cyclic lateral load is applied to the specimens using automated cyclic hydraulic actuator with the displacement being increased not less than one and one-quarter times, and not more than one and one-half times of the previous displacement. The load is recorded using a load cell mounted on the hydraulic actuator, while the horizontal displacement at column tip is recorded using 200-mm linear variable displacement transducer and is positioned alongside the stroke of the actuator. All the data are collected automatically by the data acquisition system.
5. Strains of slab reinforcements are recorded by strain gauges throughout the course of testing with the data being transmitted using the data logger.
6. During testing, the crack pattern is observed on the top and bottom surface of the slab using traditional, hand-drawn technique.

7. 3D nonlinear finite element analysis using ABAQUS is performed by assuming the interaction between concrete and reinforcing steel to be perfectly bonded in order to avoid challenging computation time during the iteration process caused by nodal slip due to bond losses.
8. In finite element analysis, the relationship of stress-strain of ECC under compression is assumed to fit the constitutive modelling of conventional concrete.

### 1.5. Hypothesis Adopted

The work described in this thesis examines the study on the behaviour of slab-column connection tested under gravity and cyclic lateral load. This research has been directed towards the development of engineered cementitious composite material as a replacement of conventional concrete as well as the utilisation of drop panel member to improve the behaviour of above structure. This present work is based on the assumption that in a typical design of flat slab frames, the slab-column connections are considered to carry gravity load, and they are not intended to

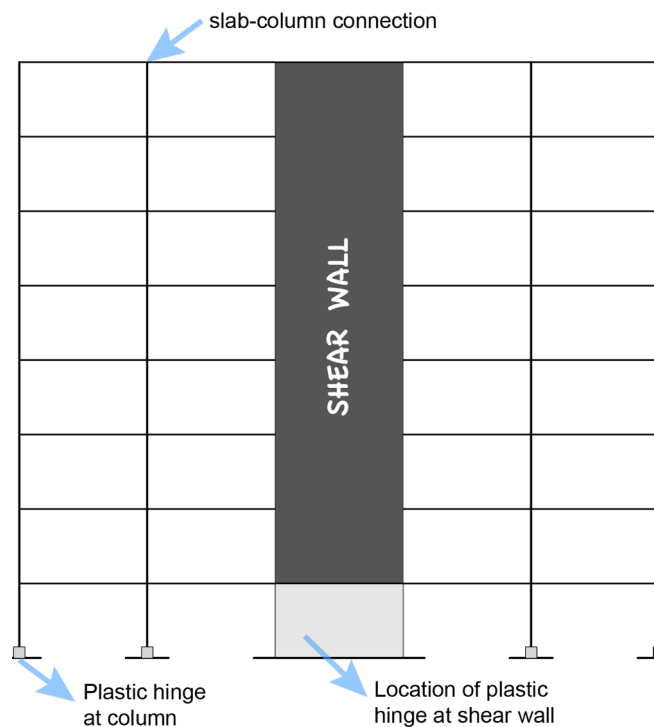


**Figure 1.1** The location of plastic hinge mechanisms in the flat slab structure as flexural moment resisting frame.

contribute to lateral resistance. In such situation, the plastic hinge mechanisms are anticipated to merely occur in rigid members such as shear walls (see **Figure 1.1**).

In general, when considering the design of reinforced concrete structure as a dual system, the proportion of stiffness in elastic condition during the earthquake can be determined in such a way, for example, 85% of earthquake forces are transferred to the shear wall, while the remaining forces are transferred to frames. Additionally, in terms of strength, frames should at least be able to carry not less than 25% of earthquake forces (SNI 1726:2012; ASCE/SEI 7-10). This is to ensure that while shear wall has already failed, frames still have reserved capacity to withstand the earthquake forces. In other words, this is also called as second defence mechanism where plastic hinge mechanisms are expected to occur within the frames thereby allowing the structure to withstand inelastic deformation due to the earthquake.

Although the failure pattern seems to be tangible, however, it is of importance to note that earthquake is regarded as unforeseen loading conditions, meaning the magnitude of seismic forces are unpredictable and they could have been higher than

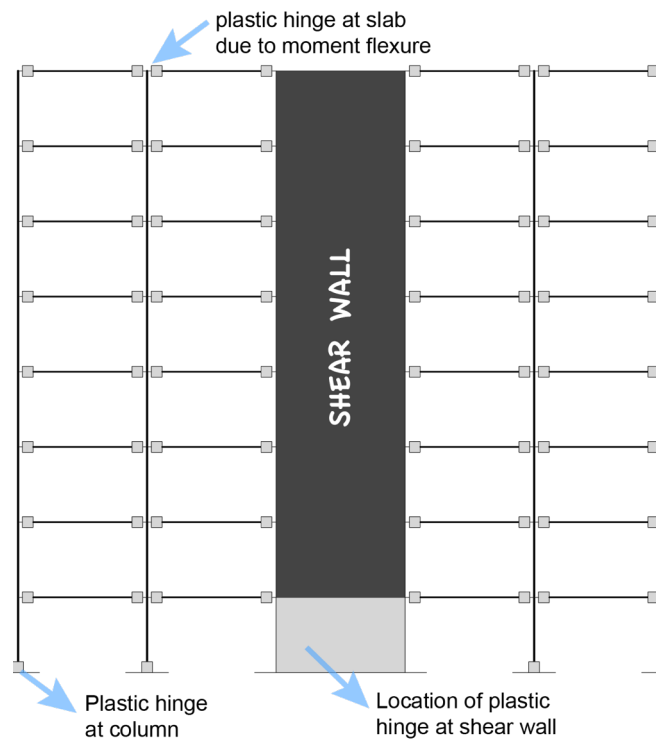


**Figure 1.2** The location of plastic hinge mechanisms in the flat slab structure as special moment resisting frame.

that of expected in the calculation. Given this fact, if the slab-column connections are not adequately designed to carry such immense forces, the punching shear stress, indicated as brittle nature of concrete, may be the case which may also trigger the likelihood of flat slab structure to govern the progressive collapse. When considering the use of engineered cementitious composite material incorporated by addition of drop panel member, it is anticipated that the behavioural response of slab-column connection can be improved thereby permitting the possibility of the slab-column frames to withstand earthquake forces. In such condition, the plastic hinge mechanisms of the slab-column connections occur due to moment flexure (see **Figure 1.2**). As a stepping stone toward achieving this goal, this study may offer the probability of flat slab structure to be classified as earthquake proof and resistant building.

## CHAPTER 2

### LITERATURE REVIEW

#### 2.1. Flat Slab Structural System

Flat slab system shown in **Figure 2.1** is a form of floor system in a reinforced concrete building that offers prospective benefits over the conventional reinforced moment-resisting frames (Erberik and Elnashai, 2004). The dominant dissimilarity between the flat slab and other types of building lies in its type which only consists of a monolithic structural component in the form of the slab, column, and slab-column connection as its primary members.

As the structure does not employ any beam member, the fast construction time and more economical rate become the major points for offering the good alternative. However, regarding the structural response along the joints, a more complex behaviour is essentially inevitable. It is indicated by the punching shear phenomenon, causing the shear stress dominated the internal mechanism at the joint location following the prominent drop in strength. In addition, the uniform shear stress due to gravity load is one of the factors that may trigger the punching shear failure in the connection (Bompa, 2011).

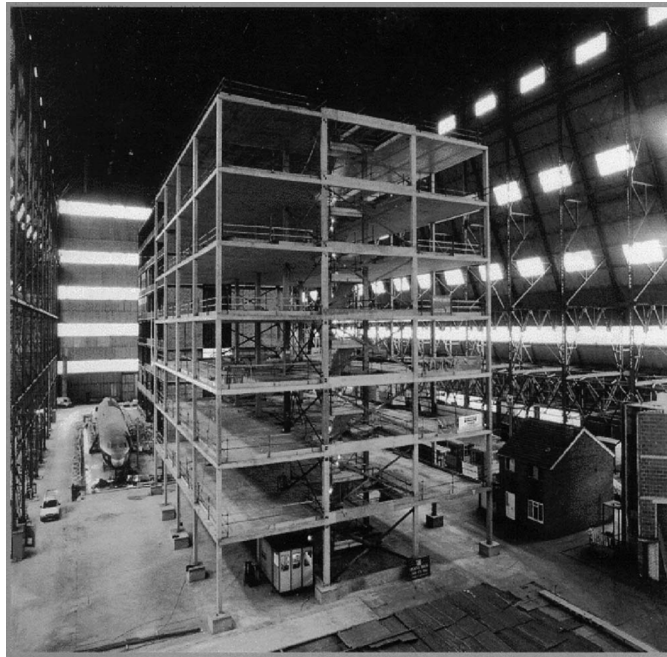


**Figure 2.1** Typical form of flat slab structure (El-Dardiry *et al.*, 2002).

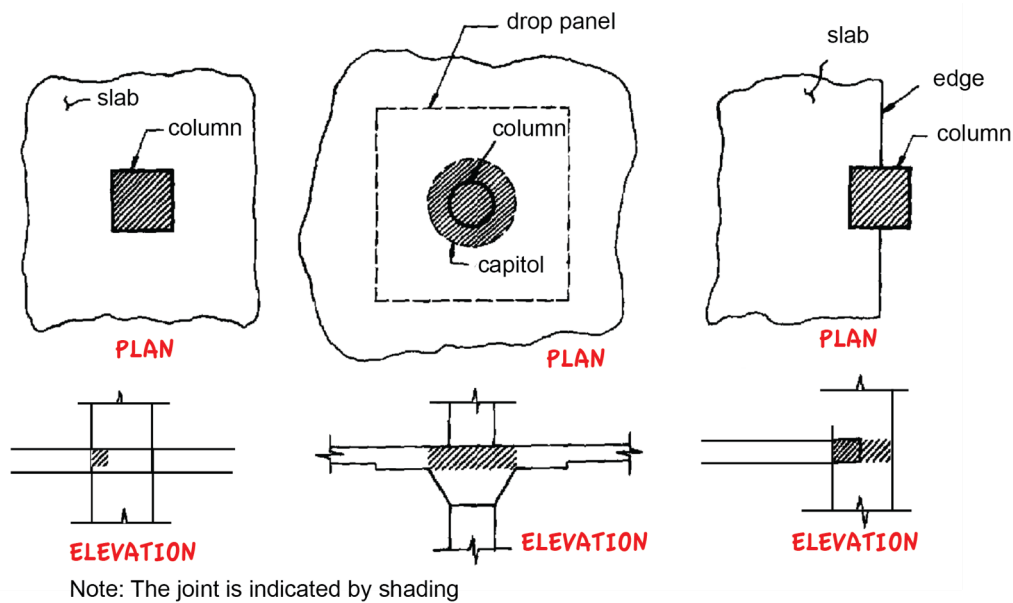


**Figure 2.2** Illustration of joint location of slab-column connections (ACI 318).

Flat slab structure is known as a two-way slab system according to SNI 2847:2013 and ACI 318-14. In the majority of building construction, flat slab structure has a few variations including the flat plate with or without web reinforcements, flat slab with drop panel or shear capital, and so on. Early design specifications adopted by the American Concrete Institute was based on a report by the Joint Committee of 1924. It was discussed to give the recommendation with regard to the shear stress calculation and the allowable shear stress.

Based on the previous studies, the fragility of flat slab system is caused by the combination of gravity and lateral loads. When flat slab structure is subjected to lateral loading, the unbalanced moment will deliver the significant stresses in the critical area of the connections and also the uniform shear forces from gravity loads will sum up the local shear stresses (Gunadi et al., 2012). At this point, it is evidently true that gravity loading can decrease drift capacity of slab-column connections (Megally and Ghali, 2000) as well as decrease the initial stiffness (Robertson *et al.*, 2000), ductility (Pan and Moehle, 1992), and load-carrying capacity (Robertson and Durrani, 1992). Since the general behavioural response shows the tendency of weaknesses, design codes like SNI 2847:2013 and ACI 318-14 categorise flat slab system into the intermediate moment-resisting frame. When

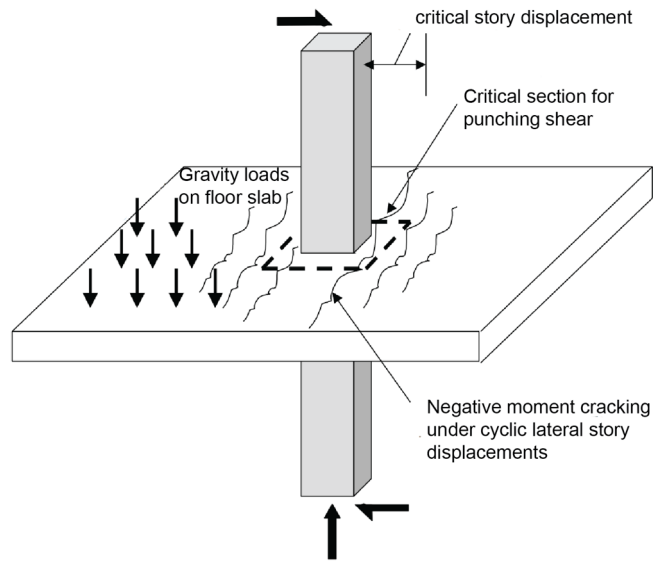


**Figure 2.3** Critical region around slab-column connection (Jirsa, 2009).

it is built in the low or intermediate seismic regions, the single system is allowed. On the other hand, when it is designed in the high seismic regions, the use of a dual system with the contribution of shear walls is necessarily important. In reference to previous statements, it is also clear that design specification does not allow to design the flat slab structure in the level of special moment resisting frame whether using single or dual system (ASCE/SEI 7-10). This can obviously cause the non-efficiency in terms of advancing the sustainable construction related to high-rise building constructions.

## 2.2. Mechanics of Slab-Column Connection

The slab-column connection shown in **Figure 2.2** is defined as a joint which is located in the part of the column within the depth of the slab including drop panel and having plan dimensions equal to those of the column at the intersection between the column and the bottom surface of the slab or drop panel (ACI 352.1R-89). In flat slab structure, punching shear failure is most likely to occur around the slab adjacent to the column face. This phenomenon inclines to take place because structural members do not have sufficient strength when the columns give dominant punching action. Furthermore, the region of slab-column connection presented in

**Figure 2.3** is described of having the tendency of punching shear behaviour. Lateral deformation occurred during the course of loading can result in moment and shear at the joint while additionally, gravity load can also contribute to give significant uniform stress at the similar location (Jirsa, 2009).

ACI 318-14 also outlines that load transfer transpired along the connection of the critical perimeter involves shear forces  $V_g$  and unbalanced moments  $M_u$ . The shear forces at the slab-column connections are affected by the transfer of shear stresses uniformly in the area of the critical section near to column face as illustrated in **Figure 2.4**. Furthermore, unbalanced moments are triggered due to the influence of lateral load, resulting in two mechanisms (ACI 318-14). In this case, a fraction of the unbalanced moment given by  $\gamma_f M_u$  must be considered to be transferred by flexure within an effective slab width between lines that are one and one-half slab or drop panel thickness ( $1.5h$ ) outside opposite faces of the column (ACI 318-14). On the other hand, a fraction of unbalanced moment known by  $\gamma_v M_u$  must be

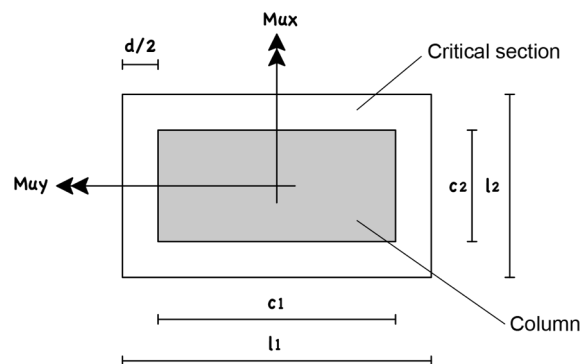


**Figure 2.4** Critical section (perimeter) of slab-column connection.

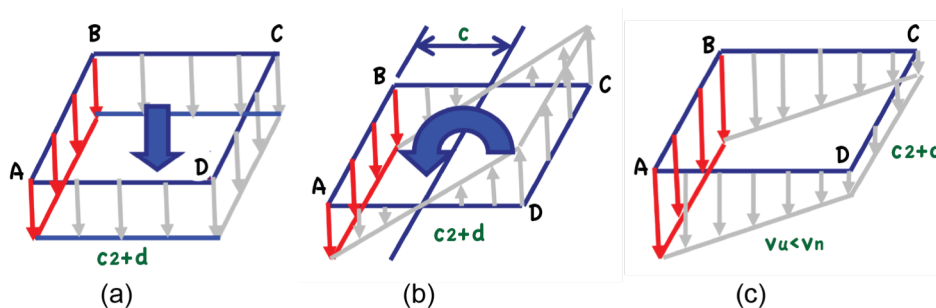


**Figure 2.5** Transfer of uniform gravity load unbalanced moment within the critical section: (a) uniform shear stress due to gravity load; (b) eccentric shear stress due to unbalanced moment; (c) total shear stress (ACI 318).

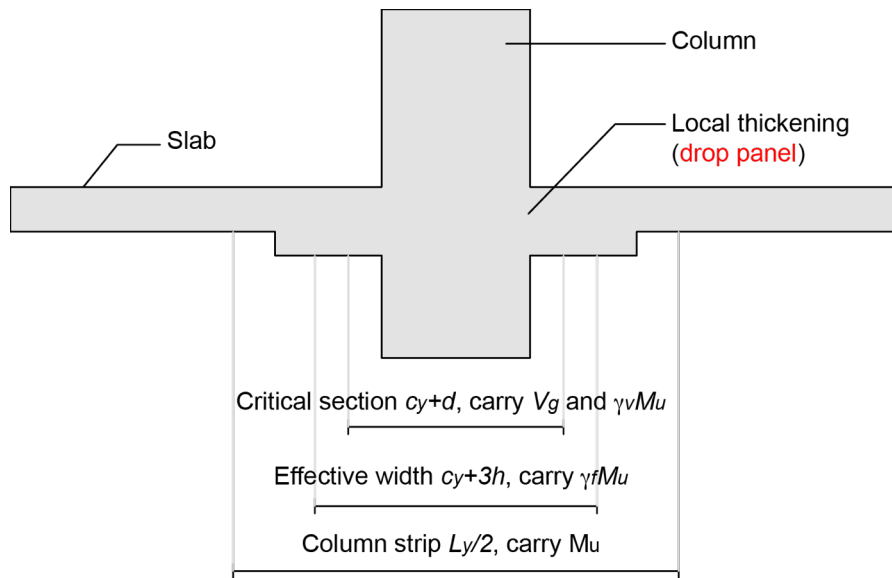


**Figure 2.6** Schematic model for shear and moment transfer of slab-column connection.

transferred by shear at the critical section of the slab-column connection. **Figure 2.5** describes the transfer mechanisms of uniform shear stresses caused by gravity loading and unbalanced moments at the critical perimeter. It is indicated that the combined shear stresses are obtained from the linear summation between these two factors. In the overall situation, transfer scheme of moment and shear in slab and column during the loading course is illustrated in **Figure 2.6**.

### 2.3. Failure Mode of Slab-Column Connection

Failure in flat slab structure is caused by the complex behaviour as a result of the unbalanced moment and shear transfer mechanism in the connections due to combined gravity and lateral loads (Shah, 2005). During the seismic event, the unbalanced moment can result in significant eccentric shear stress in the slab area (Megally and Ghali, 2000). Presented in **Figure 2.7** is the illustration of connection response due to lateral loading applied in the column tip. It is shown that during the loading sequence in the positive direction, flexural cracks start to appear in the area of negative moment indicated by the condition when the top fibre of stress diagram in a reinforced concrete is being pulled. At the same time, other cracks also start to

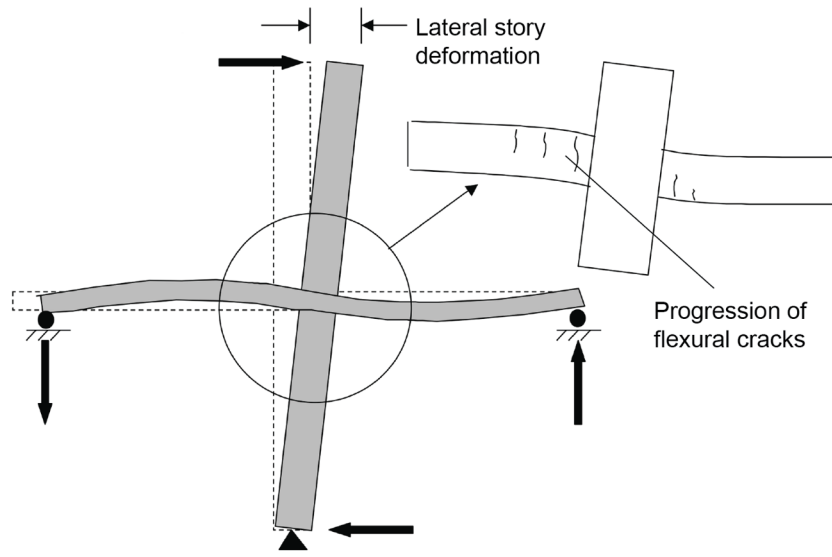


**Figure 2.7** Formation of flexural cracks due to lateral load (Jirsa, 2009).

develop at the bottom of the slab in positive moment across the loading point. As the loading is reversely alternated, the cracks appear in the same condition (Jirsa, 2009). At this point, the number of cracks and positive moment capacity in the opposite direction exhibit depending on the ratio of bottom longitudinal reinforcements. As having such compound behavioural response, it may lead to the vulnerability on resisting a number of applied loads causing the severe damage, termed as progressive collapse (Tegos and Tsonos, 1996).

#### **2.4. General Setups of Slab-Column Connections Tested under Gravity and Lateral Loading**

There has been extensive research carried out to give a better understanding in regard to the behaviour of slab-column connections under combined gravity and reversed cyclic lateral load. A variety of testing configurations has also been commissioned by different researchers. For convenience, most tests have usually been done by implementing the subassembly techniques referred to the prototype of the building. In addition to that, a reasonable assumption for determining boundary conditions of the tested specimens has also been considered. For slab supports, simple supports along the slab edges are mounted to simulate a point of

contra-flexure at mid-span in the slab. Also, simple support pinned connection at the base ends is also used to generate an inflection point in the column at mid height.

While there seems to be convenient to proceed this method, however, a major challenge in these test lies on how to apply and sustain a constant gravity loading throughout the test. Several approaches have been proposed to overcome this challenge. One of such is by hanging the portable concrete blocks to provide the constant superimposed dead load. However, this method limited the researchers to testing under very low or high gravity shear ratio. Another test variable that has ranged widely is the influence of flexural reinforcement ratio. Some researchers tend to use the overly amount of flexural reinforcements with the ratio over 1% to force the punching shear failure. This is associated with the over-reinforced section whereby concrete would crush prior to the yielding of flexural reinforcements. Further explanations regarding the effect of flexural reinforcement ratio are discussed in the following section.

## **2.5. Influence of Flexural Reinforcement Ratio**

Flexural reinforcements on the slab are necessarily used in the column strip to withstand the gravity load acting on the structural member. Although they are designed to sustain the flexural moment, the increase in ratio can obviously affect the punching shear capacity of the connection and the lateral stiffness significantly (Tian *et al.* 2008). As stated in SNI 2847:2013, slab effective width is a part of column strip that is also designed to carry the unbalanced moment flexure. In other words, the flexural reinforcements within the effective width of the slab are designed to strongly carry the fraction of the flexural moment with strength shall not be less than half of the reinforcements in the column strip or it can be given as  $0.375\rho_b$ .

A few of studies have been carried out related to the effect of flexural reinforcement ratio in the slab. Tian *et al.* (2008) were among the first to demonstrate the significant role on the influence of flexural reinforcement ratio in relation to the behaviour of slab-column connections. This study focused on the effect of flexural reinforcement ratios of 0.5% and 1.0% within the effective width of the slab. The columns of all specimens were heavily reinforced so that they

remained elastic under lateral loading. An experimental investigation was done with five large-scale specimens. The specimens were loaded with respect to gravity and lateral load. The results highlighted that punching failure of connections with low reinforcement ratio was not induced by reaching the critical shear stress under gravity and lateral load. The typical failure was more interpreted as shear deformation-driven shear failure occurred when the inclined cracks were exhausted which could be attributed to the concrete splitting across a plane. In contrast, as the reinforcement ratio increased, connection punching capacity and lateral stiffness increased significantly. At 1.25% drift level, punching shear failure was introduced without affecting the capacity to carry the constant gravity load. However, it might not be the case since ratio was limited up to 1.0%.

In the article written by Muttoni (2008), Kinnunen and Nylander (1960) studied the influence of varying ratios of slab flexural reinforcement in slab-column connections with regard to their punching shear capacity. The results highlighted these following dictations:

- (i) For low reinforcement ratio ( $\rho = 0.5\%$ ), it was shown that structure behaved in the more ductile manner where all the flexural reinforcement bars had yielded. In this particular case, it was confirmed that the strength of slab was limited by flexural capacity and punching shear occurred in a certain condition where large inelastic deformation occurred.
- (ii) For intermediate reinforcement ratio ( $\rho = 1.0\%$ ), some of the flexural reinforcement bars had yielded in the region nearby the column. However, punching shear was stricken before all the reinforcement bars yielded, owing to the fact that the strength in the slab was smaller than its flexural capacity.
- (iii) High reinforcement ratio ( $\rho = 2.1\%$ ), it was evident that punching shear occurred in a condition where all flexural reinforcement bars were yet to yield. Moreover, the response was indicated by a very brittle behaviour. From this inclination, it was confirmed that the strength of the slab was way too small compared to its flexural capacity.

From these relevant research, it can be concluded that the increase in flexural reinforcement ratio can somehow increase the punching shear capacity but by putting to the high amount of ratio can also cause the over-reinforced behaviour

which can associate by the crushing of concrete prior to the yield of reinforcement bars.

## 2.6. The Use of Drop Panel in Flat Slab Structure

In general, drop panel is used to reduce the negative moment in the joint over the slab as well as increase the stiffness to lessen the lateral deformation caused by the applied loading (ACI 318-14). Drop panel is also used to thicken the slab in the joint towards the slab effective width in order to give sufficient shear strength for avoiding the early punching shear failure (Sathawane and Deothale, 2012). Since conventional flat slab structure is not designed to have web reinforcements in the slab, drop panel used to be the only option of providing the better behavioural response by putting more thickness in the joint. There has been a few research focusing on the behaviour of flat slab structure by using the drop panel as local thickening member of the joint. These studies designed drop panel elements based on the recommendation given by ACI specification. To give a better picture of drop panel, **Figure 2.8** illustrates how drop panels are applied to the flat slab structure.

ACI 318-14 outlines the limitation in design whereby drop panel is used to reduce the amount of negative moment over the column of a flat slab, the size of drop panel shall be in accordance with the following:

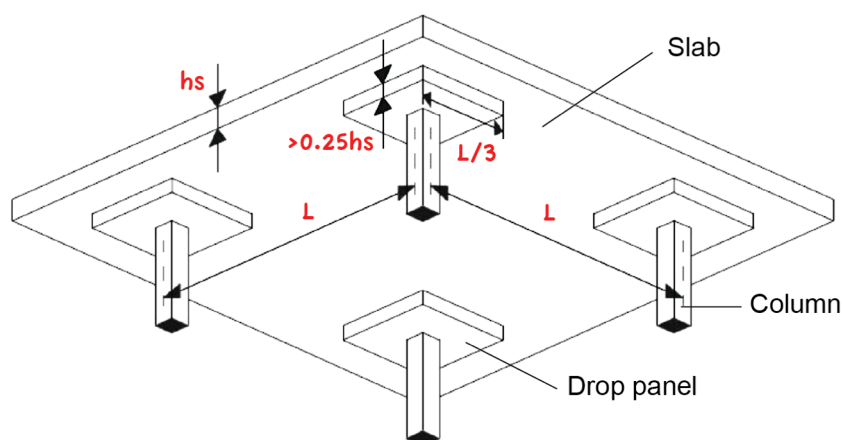


**Figure 2.8** Drop panel members in flat slab structure (ACI 318).

- (i) Drop panel shall extend in each direction from centreline of support a distance not less than one-sixth the span length measured from centre-to-centre of supports in that direction.
- (ii) Projection of drop panel below the slab shall be at least one-quarter the slab thickness beyond the drop.
- (iii) In computing required slab reinforcement, the thickness of drop panel below the slab shall not be assumed greater than one-quarter the distance from the edge of drop panel to edge of the column.

Given that ACI 318-14 also mentions the modification of slab in thickness of the critical section must consider the assessment of shear strength.

Designing drop panel can be done using *direct design method* arranged by ACI 318-14 or SNI 2847:2013. However, it is important to note that there are several limitations has been outlined as follows:

- (i) There shall be a minimum of three continuous spans in each direction.
- (ii) Panels shall be rectangular, with a ratio of longer to shorter span centre-to-centre of supports within a panel not greater than 2.
- (iii) Successive span lengths centre-to-centre of supports in each direction shall not differ by more than one-third the longer span.
- (iv) Offset of columns by a maximum of 10% of the span (in direction of offset) from either axis between centrelines of successive columns shall be permitted.
- (v) All loads shall be due to gravity only and uniformly distributed over an entire panel. The live load shall not exceed two times dead load.

Designing of flat slab structure can also be done by adopting the effective beam width method. This method has been extensively used to predict the lateral drift and amount of unbalanced moments in slab due to lateral load. Numerous research showed that modification on drop panel dimension in the interior and exterior can provide the increase in response significantly. Choi *et al.* (2001) were among the first to study the coefficient of effective width for a larger span of slab-column connections which was calculated using finite element programme tool. This relevant study used the following fundamental assumptions to reckon the effective width coefficient:

- (i) The inflection lines are assumed to occur along slab mid-span perpendicular to the bending direction.
- (ii) The slab-column interface is infinitely stiff in bending, such that an applied moment at the column-slab junction will result in a rigid body rotation of the interface, termed as stiffening effect.
- (iii) In regard to the deformation of the slab under latera loads, the boundary conditions are assumed as sway conditions such that boundaries perpendicular to loading direction are restrained against displacement and the other boundaries defect freely with zero rotation about axes along the boundaries.
- (iv) Material nonlinearity such as the effect of the slab creep, cracking, and reinforcement ratio of the slab is not considered.
- (v) The gravity loads including the self-weight are not taken into account, and the basic Poisson's ratio is assumed to be zero.

In this particular study, Choi *et al.* (2001) simulated four types of slab-column connection model as seen in **Figure 2.9**. These types of model consisted of interior connections, edge connections with bending perpendicular to the edge, edge connections with bending parallel to the edge, and corner connections which were abbreviated as INT, PER, PAR, and COR, respectively. The results proposed the effective width coefficient consisting of considered parameters viz.  $l_1/l_2$ ,  $c_2/c_1$ , and  $c_1/l_2$  which are given in **Equation (2.1)**.

$$\alpha = \frac{l_2'}{l_2} = \frac{1}{1-\nu^2} \alpha_r \alpha_s \quad (2.1)$$

where:

$l_2'$  and  $l_2$  = equivalent effective width, slab width

$1 / 1 - \mu^2$  = the effect of the Poisson's ratio

$\alpha_r$  = modified factor on the  $c_2/c_1$

$\alpha_s$  = the effective beam width coefficients on the  $l_1/l_2$  and  $c_1/l_2$ .

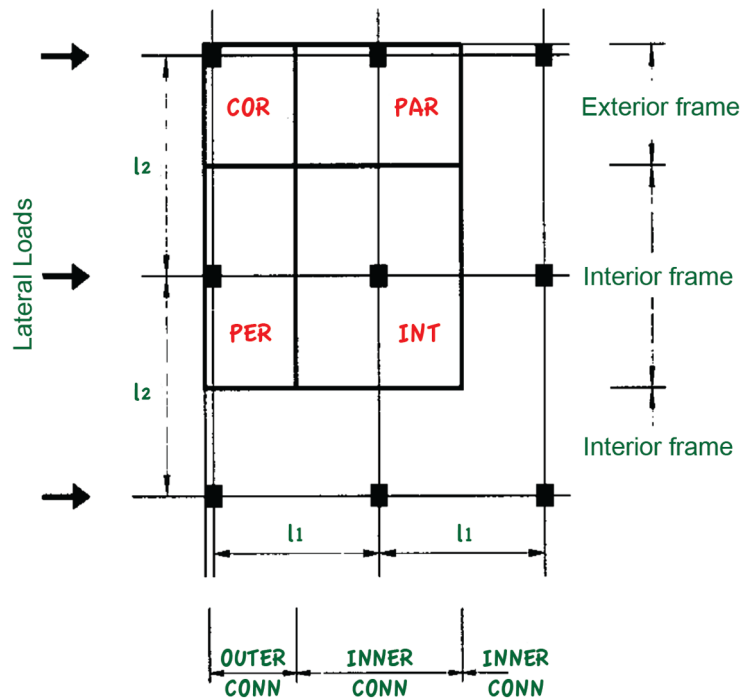


**Figure 2.9** Four types of connections in flat slab system (Choi *et al.*, 2001).

**Table 2.1** The effective width of slab (Dovich and Wight, 2005).

Effective width	Drop panel element		Slab mid-span
	Exterior connection	Interior connection	
Strength	$c_1 + c_2$	$l_2/3$	$l_2/2$
Initial stiffness	$c_1 + c_2$	$l_2/3$	$l_2/3$

Dovich and Wight (2005) also studied the influence of effective widths of drop panel on the flat slab structure due to lateral load, presenting the analysis of two-dimensional nonlinear frames. In their study, the parameters in the model were based on the experimental data obtained from two-floor and two-span of flat slab structure. Furthermore, the approach of effective widths is categorised into two different types described and summarised in **Figure 2.10** and **Table 2.1**, respectively. The results indicated that effective slab widths for initial stiffness in interior connections gave flexural stiffness way better than that of effective slab widths for strength. In contrast, the effective slab widths for strength generated low

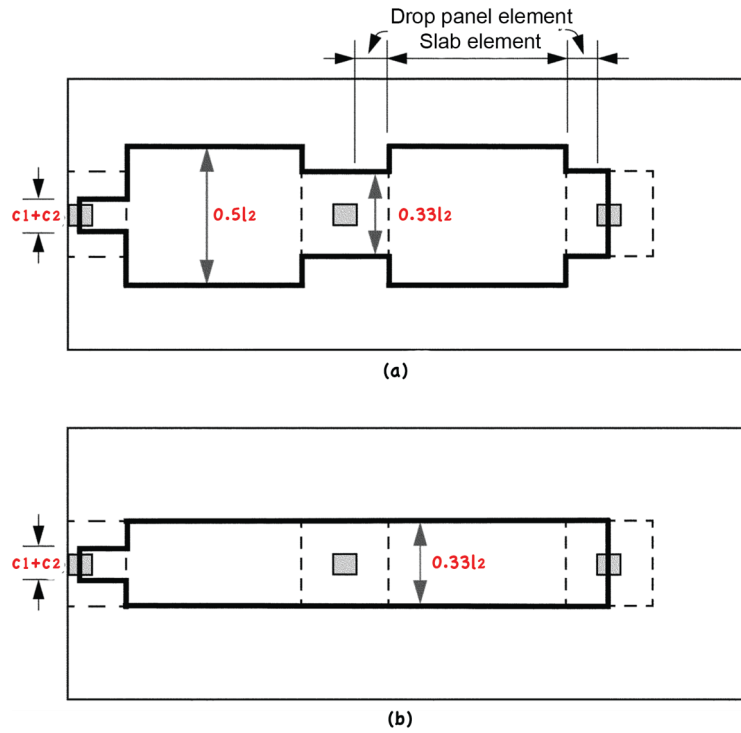


**Figure 2.10** Effective slab widths: (a) termed as strength; (b) termed as stiffness (Dovich and Wight, 2005).

stiffness in the exterior connections due to significant flexural cracks occurred in the structure.

Tavio and Hemawan (2009) also did the similar study where the research was focused on determining the proper equations of effective slab widths by comparing the results from previous studies. The proposed equations to calculate the effective slab widths are given in **Equations (2.2)**.

(i) For exterior connections

$$b = \frac{l_1}{10} + \frac{l_2}{6} + \frac{c_1}{3} \quad (2.2a)$$

(ii) For interior connections

$$b = \frac{l_1}{20} + \frac{l_2}{6} + \frac{c_1}{4} \quad (2.2b)$$

The results showed by the proposed equations of effective slab widths both in interior and exterior connections were considered to be accurate on predicting the moment distribution.

## **2.7. Engineered Cementitious Composite (ECC)**

It is of common that concrete is a brittle material with a relatively high compressive strength and a low tensile strength. In a typical design of reinforced concrete structure, steel reinforcement must be provided at locations which are subjected to tensile stresses. This is to ensure that the structural element would exhibit adequate cracking control which is essential for providing the required strength and durability. For the member subjected to moment and dominant shear, premature shear failure may occur in structural members containing little or no shear reinforcement such as in thick sections and wide beams (Collins *et al.*, 1997, Sherwood *et al.*, 2006, and Collins *et al.*, 1999), or in ordinary beams weakened by tensile forces (Bhide *et al.*, 1989). Failure can also occur in heavily reinforced element under unforeseen loading conditions such as an earthquake (Ghee *et al.*, 1989, Maekawa and An, 2000).

To date, extensive research has now been carried out to develop a new type of material that could improve the response of reinforced structures. As such, a collaborative effort between the US and Japanese researchers since 1996 has focused on the development of ductile material element for a various structural application which is based on a new materials technology. The emphasis was primarily made on the use of unique cement-based material to alleviate the brittle nature of concrete and hence increase the strength and damage tolerance. As a result, the work has created a new materials technology so-called engineered cementitious composite (ECC) which is microstructurally designed using micromechanical principles. ECC, in essence, is a class of high-performance fibre reinforced cementitious composite characterised by a large tensile capacity, with the ratio of ultimate tensile strain to cracking strain of 200 or more (Suryanto *et al.*, 2012). The high ductility is normally achieved through pseudo-strain hardening behaviour with increasing in tensile stress. The strain capacity is relatively in excess

**Table 2.1** Mechanical properties of synthetic fibres (Soe *et al.*, 2013).

Type of fibre	Tensile strength (MPa)	Young's modulus (GPa)	Fibre elongation (%)	Density
PVA	880 - 1600	25 - 40	6 - 10	1.30
PP	600	5	25	0.91
Nylon	750 - 900	3.4 - 4.9	13 - 25	1.10
PE	250 - 700	1.4 - 2.2	10 - 15	0.95

**Table 2.2** Mechanical properties of PVA fibres (Soe *et al.*, 2013).

Specification	Fibre code	Diameter (mm)	Tensile strength (MPa)	Young's modulus (GPa)	Elongation (%)
Standard	RM182	0.014	1600	37	7
	RF400	0.2	1000	30	7
	RF1000	0.31	1000	29	7
	RF4000	0.67	900	30	7
Ductile	REC7	0.027	1600	37	6
	REC15	0.04	1600	37	6
	REC100	0.1	1100	30	10

of 3% prior to fibres rupturing (Kakuma *et al.*, 2010). Furthermore, ECC is also referred to as bendable concrete as it provides the ability to withstand high flexural and shear stresses (Li, 2002). From a structural point of view, the ultra-ductile behaviour of ECC, combined with its flexible processing requirements, isotropic properties, and moderate fibre content make it especially suitable for critical elements in seismic applications where high performance such as energy dissipation, steel or concrete deformation compatibility, and spall resistance are required.

ECC is typically made by finest material components such as cement, fly ash, silica sand with the average grain of approximately 100 to 200  $\mu\text{m}$  and moderate fibre content (typically 2% calculated by the volume fraction of the specimen). In addition, high range water reducer (HRWR) is also used to reduce the amount of water while maintaining the level of viscosity and workability. The mixing process of ECC does not relatively differ with the conventional concrete (Li, 1998).

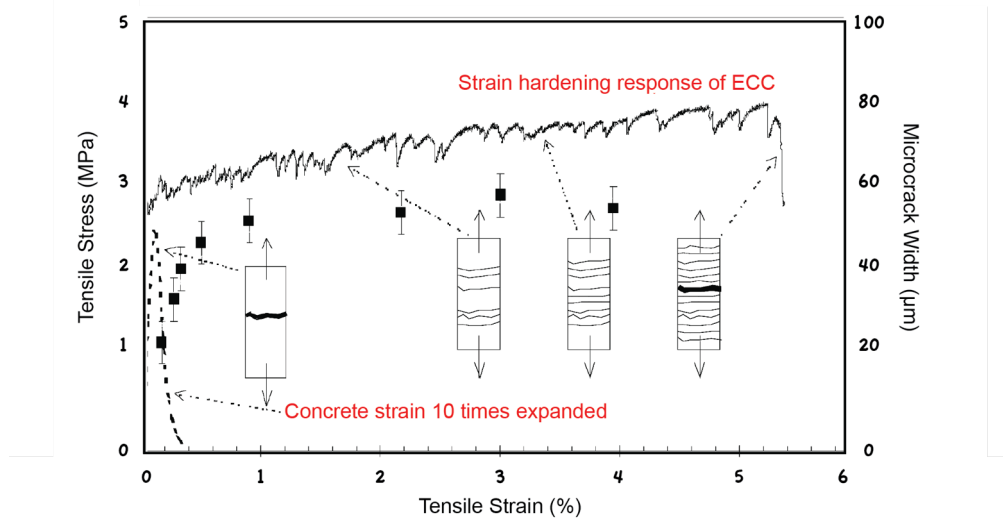


**Figure 2.11** Uniaxial tensile stress-strain relationship and crack widths of ECC with the additional information of a typical tensile response of conventional concrete to facilitate direct comparison (Li, 2006).

With regard to the material improvement, fibres have been used to increase the toughness of quasi-brittle cement based material (Roth, 2008). As the ability to produce high tensile ductility, ECC is originally designed to have strain-hardening behaviour using micromechanical concept; thus the excessive tensile strain capacity can be achieved more than 2% through multiple cracking (Li and Wu, 1992). PVA fibres have been used as they offer low modulus in contrast to steel fibres nor carbon fibres which have high modulus. The underlying reason is that high modulus basically can increase the strength and toughness of the material; however, it is also assessed to exhibit more brittle behaviour causing the improper enhancement of strain hardening and ductility. On the contrary, low modulus can postulate better ductility and also can diminish the number of cracks (Soe *et al.*, 2013). **Table 2.2** summarises the mechanical properties of relevant fibres made from synthetic material for cementitious composite. It is shown that PVA fibres offer highest strength and modulus yet lower than steel fibres in general. **Table 2.3** also presents the material properties with regard to various types of PVA fibres, as well as their distinctive specification.

**Figure 2.11** provides a better picture in the comparison between ECC material and standard regular concrete regarding the tensile response. It is shown,

**Table 2.4** Previous studies of various R/ECC structural elements.

Types of structural element	Type of loading and reinforcement	Reference
Flexural elements	Reversed cyclic	Fischer and Li, 2002
	Monotonic (GFRP)	Li and Wang, 2002
	Reversed cyclic (CFRP)	Fischer and Li, 2003a
	Fatigue	Kim <i>et al.</i> , 2004
Shear beam elements	Reversed cyclic	Kanda <i>et al.</i> , 1998
	Reversed cyclic	Fukuyama <i>et al.</i> , 2000
	Monotonic	Shimizu <i>et al.</i> , 2006
Beam-column connections	Monotonic	Kabele and Kanakubo, 2007
	Reversed cyclic	Parra-Montesinos and Wight, 2000
Wall elements	Reversed cyclic	Parra-Montesinos and Wight, 2000
	Repeated shear	Kanda <i>et al.</i> , 1998
	Reversed cyclic	Kesner and Billington, 2005
Column element	Reversed cyclic	Fukuyama <i>et al.</i> , 2006
	Reversed cyclic	Fukuyama <i>et al.</i> , 2000
Frame	Reversed cyclic (steel and CFRP)	Fischer and Li, 2003b
Steel/ECC interactions	Monotonic flexure (plate/ECC)	Walter <i>et al.</i> , 2004
	Monotonic shear (stud/ECC)	Qian and Li, 2006
	Monotonic tension (anchor/ECC)	Leung <i>et al.</i> , 2006; Qian, 2007

in fact, the stress-strain relationship curve of ECC material gives a much better response as it exhibits pseudo-strain hardening behaviour with strains up to 5% and multiple micro cracks with width under 100  $\mu\text{m}$ . While in contrast, conventional concrete only generates very low tensile strains nearly 0.01%. In other words, ECC provides high curvature diagram during the increase in load capacity and still behaves in a ductile manner after reaching its yielding point (Li, 2006). In recent years, there has been much emphasis placed on introducing the application of ECC material in structural components. This can be seen in work involving flexural elements, structural joints, walls frames structure and so on. Researcher such as Li (2007) summarises the previous work by other researchers to arise the gap among these studies (see **Table 2.4**). Fukuyama *et al.* (2000) demonstrated the increasing effect on the performance of beam members strengthened with PVA-ECC material due to cyclic lateral load. The results showed that the utilisation of PVA-ECC

material indicated ductile behaviour. Additionally, PVA fibres were functioned as reinforcements for not only shear and bond splitting but also confinement of concrete expansion during the post-yielding response to post-peak response. It was also noted that maximum shear crack widths up to 5% rad in deflection angle of PVA-ECC beams were less than 0.3 mm, indicating the maximum limit value for durability. Through this test, it can be clarified that PVA-ECC has much feasibility to upgrade the structural performance and damage tolerance of structural elements.

With regard to the seismic response of the structure, a study conducted by Li *et al.* (2014) has focused on the pinching effect and energy dissipation of reinforced engineered cementitious composite shear walls. It is shown that the shear wall made from reinforced ECC are enabled to enhance the ductility in tensile principal stress direction, leading to the marginal increase in pinching effect than that of reinforced concrete shear wall. The slight increase is generally caused by a small measure of tensile strength provided by ECC, albeit it has high ductility in tension. In addition to pinching effect, the dissipated energy of ECC shear wall is increased with the value of more than thrice than that of the concrete shear wall.

Further study regarding the shear-critical ECC members with anisotropic stress and strain fields was done by Suryanto *et al.* (2010). Eight ECC plates were tested under four-point bending, including the first two plates as control specimens (Plates S1 and S2, 250×400×20 mm) and six main plates taken as (Plate S3 to S8,

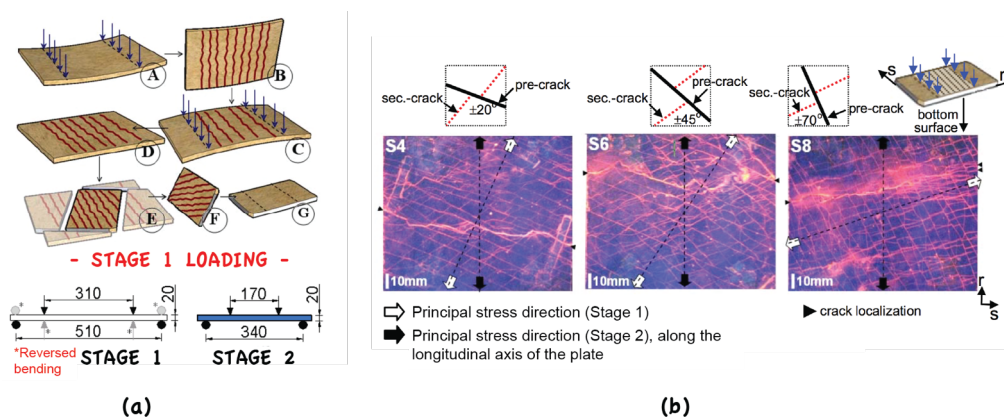


**Figure 2.12** Pre-cracked ECC plates: (a) testing procedure; (b) crack patterns of selected plates within constant moment span at failure (Suryanto *et al.*, 2010).

420×550×20 mm). The control specimens were loaded to failure while the remaining main specimens were pre-loaded until the tensile strain at the bottom of the plates within the constant moment span reached either 40 or 70% of ultimate tensile strain (see Step A in **Figure 2.12(a)**). To remove the residual mid-span displacement, Step B was introduced whereby the main plates were rotated upside down and pre-loaded (Step C). Following this, the main plates were cut in a certain orientation into the size of control specimens (Step E).

Since the pre-cracks were at a certain angle to the plate width (viz. 0°, 20°, 45°, and 70°), it was possible to induce the tensile and shear stresses along the pre-cracks interface. Shown in **Figure (b)**, the results highlighted the crack pattern of Plates S4, S6, and S8 after failure and within the constant moment span. It was proven that the newly formed cracks were nearly orthogonal, suggesting the significant anisotropy exhibited due to less stress transfer along the pre-cracks. From this study, it can also be confirmed that the reduction in strength tends to increase with increasing pre-crack orientation and then begins to decrease when the orientation of the pre-crack approaches 90 degrees.

Based on the previous work, it is anticipated that the use of ECC can, therefore, increase the behaviour of structural elements, even when pre-cracking is induced the strength reduction is not highly notable. Although a number of studies seems to be tangible, however, it is evident from **Table 2.4** that either experimental or numerical analysis of ECC slab-column connections has not been done yet. Given that the work presented would provide improved insights with regard to the structural response of R/ECC slab-column connections tested under combined gravity and cyclic lateral load.

## **2.8. Acceptance Criteria for Earthquake Proof and Resistant Structures**

The reinforced concrete structural element which is designed to withstand the seismic loading must behave in inelastic condition without experiencing the significant decrease in regard to the strength. Given that ACI 318-14 has specified the minimum requirements permitted to carry out the design (see ACI 318-14 Chapter 21). However, for a new type of proposed structural system which is yet to be mentioned in the regulation of an earthquake-resistant structure, the

demonstration involving experimental evidence and analysis must be examined to provide the information that the proposed system has strength and toughness equal to or exceeding those provided by a comparable monolithic reinforced concrete structure. ACI 374.1-05 states the toughness as the ability of the entire lateral-force resisting system to maintain structural integrity and continue to carry the required gravity load at the maximum lateral displacement anticipated for seismic events.

To deal with this acceptance criteria, ACI 374.1-05 specifies the minimum conditions that has not been fully met the requirements from ACI 318-14 whereby these following conditions must be achieved through experimental tests as a validation of the strong column/weak beam structure prior to being constructed in the high seismic regions or designed to have high performance during the seismic event.

a) *Initial stiffness*

To provide adequate initial stiffness, the nominal strength must be developed before the drift ratio exceeds an initial drift ratio consistent with the allowable story drift specified in IBC 2000. In other words, the lateral resistance must be equal to or greater than nominal strength  $F_{exp}$  before its drift ratio exceeds the drift ratio specified in Table 1617.3, IBC 2000.

b) *Stiffness degradation*

Stiffness degradation is defined as secant stiffness whereby at the end of third cycle of loading associated with drift ratio of 0.35, with value from a drift ratio of -0.0035 to a drift ratio of +0.0035 shall have been not less than 0.05 times the stiffness for the initial drift ratio calculated in linear elastic condition (see **Figure 2.13**).

c) *Strength degradation*

As seen in **Figure 2.14**, peak force for a given loading direction at the third cycle at the end of loading shall have been not less than  $0.75F_{max}$  for the same loading direction.

d) *Strong column/weak beam*

The maximum lateral resistance  $F_{max}$  recorded in the test shall not exceed  $\lambda F_{exp}$  where  $\lambda$  is the specified over-strength factor for the test column taken as 1.2.

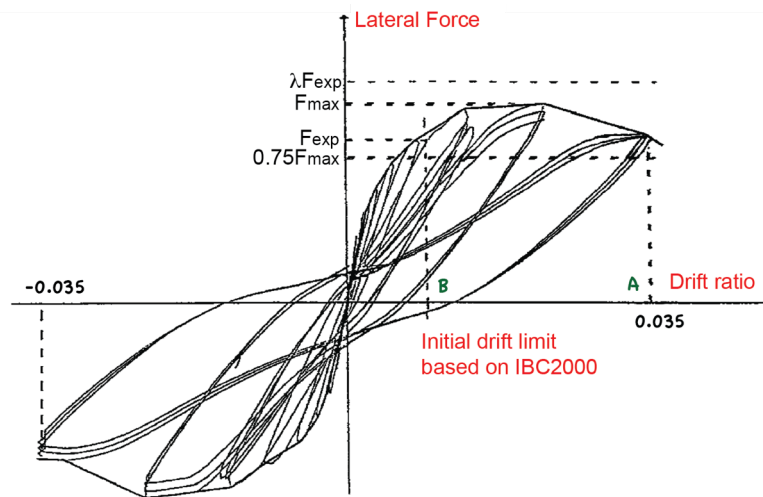


**Figure 2.13** Quantities used in evaluating acceptance criteria (ACI 374).

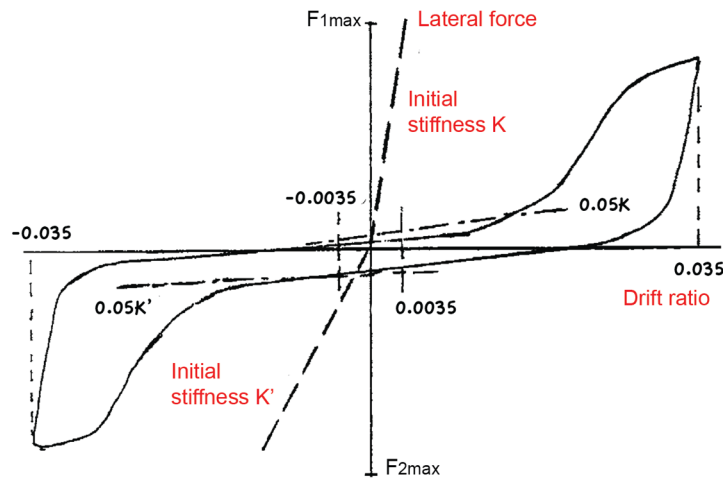


**Figure 2.14** Unacceptable hysteretic behaviour (ACI 374).

e) *Energy dissipation*

The relative energy dissipation ratio shall have been not less than 1/8 calculated based on the third cycle at the end of loading history.

**2.9. Ductility**

Ductility is expressed as the ability of structural members to deform in nonlinear condition without losing the toughness significantly (Rashid and Mansur, 2005). In other words, ductility  $\mu$  is defined as the ratio of maximum deformation

$\mu_u$  over the deformation at yielding point  $\mu_y$  (see **Equation 2.3**) In terms of definitions, ductility is classified in various type such as:

$$\mu = \frac{\Delta_u}{\Delta_y} \quad (2.3)$$

a) *Curvature ductility*

Curvature ductility is defined as the ratio of curvature angle at maximum level to yielded curvature angle (see **Equation 2.4**).

$$\mu_\varphi = \frac{\varphi_u}{\varphi_y} \quad (2.4)$$

b) *Strain ductility*

As expressed in **Equation 2.5**, strain ductility is outlined as the ratio of maximum strain occurred during the course of loading over the strain at the first yielding condition.

$$\mu_\varepsilon = \frac{\varepsilon_u}{\varepsilon_y} \quad (2.5)$$

c) *Rotational ductility*

Rotational ductility, given in **Equation 2.6**, is expressed as the ratio between maximum rotational plastic hinge and yield hinge.

$$\mu_\theta = \frac{\theta_u}{\theta_y} \quad (2.6)$$

d) *Displacement ductility*

Displacement or drift ductility is defined as the ratio of maximum drift in the inelastic condition compared to drift in the yield regime (see **Equation 2.7**).

$$\mu_\Delta = \frac{\Delta_u}{\Delta_y} \quad (2.7)$$

## 2.10. Previous Experimental Investigation on the Cyclic Behaviour of Slab-Column Connections (Prawatwong *et al.*, 2008)

One of few experimental investigations on the effect of drop panel in interior slab-column connections was done by Prawatwong *et al.* (2008). The study also included the use and the non-use of drop panel specimen to provide direct

comparisons in terms of behavioural response. To exhibit a better response, the post-tensioned system was used. Two specimens were tested under cyclic lateral load with constant gravity shear ratio. The cyclic lateral load was applied by adopting the displacement controlled method to govern the better descending part of the hysteretic loop known as the load-drift response. The specimens were loaded to failure indicated by the majority of cracks alongside the critical perimeter of the specimens. Details of information in regard to this work are outlined as follows:

a) *Detail of specimens*

Specimens used in this study consisted of two interior slab-column connection models. Specimens were subassembly model of slab-column connections taking from the prototype of common flat slab system. The first specimen was the model of slab-column connection with drop panel, while the second specimen did not use drop panel. Specimens were constructed in one-third scale with the employment of post-tensioned system, involving grade 270 of the seven-wire strand with nominal diameter of 12.7 mm. Eight tendons were installed in the same direction of lateral load. Six tendons were placed with space between one to another was 350 mm, while the other two were installed with a distance of 290 mm (refer to the article for clarification). Prior to applying the gravity load, each tendon was stressed using a hydraulic jack to dictate the uniform normal stress. The amount of jacking force in each tendon was ~147 kN which corresponded to  $0.8f_{pu}$ .

b) *Material properties*

Concrete compressive strength  $f'_c$  of the first and second specimen was 41 and 46 MPa, respectively. The yield strength of reinforcement bar  $f_y$  with respect to the first and second specimen was 503 and 324 MPa, while the ultimate tensile strength was 503 and 491 MPa. As aforesaid, both of specimens were also strengthened with post-tensioned system grade of 270 with the yield stress and ultimate stress of first and second specimens were 1780 and 1902 MPa and 1763 and 1947 MPa.

c) *Gravity shear ratio*

The amount of gravity load was based on the calculation of gravity shear ratio with the value of 0.28 and 0.13 for the first and second specimen in respective

order. In the real testing, this gravity loading was given using packs of sand bags.

*d) Lateral cyclic load*

The lateral cyclic load represented from earthquake loading was given by the hydraulic actuator which was placed in the column tip horizontally. The lateral cyclic load was provided in the form of displacement controlled starting from elastic drift level up to drift ratio of 6%. The increment of the desired displacement was done in slow phases referring to the procedure explained in ACI 374.2R-13.

*e) Set up of tested specimens*

The boundary condition at the column base was represented by pinned support mounted in the pitch of strong floor. The position of the hydraulic actuator was set thoroughly in the top of the column horizontally. For edge-slab supports, pin-ended bars were used to allow the slab to move horizontally in the same direction with the lateral load.

*f) Scope of analysis*

The analysis in regard to the results of testing was based on the comparison of the behavioural response of specimens. The results include these following parameters: hysteretic curve and the effect of gravity shear ratio to drift capacity.

Through these tests, it was shown that specimen without drop panel exhibited punching shear failure at drift level of 2%. The result also indicated that gravity shear ratio gave significant effect on the drift capacity. Specimen with drop panel, on the other hand, showed an improvement regarding the drift capacity. It was observed that the second specimen was able to deform up to drift ratio of 6% with peak load at 4% drift level.

## **2.11. Numerical Analysis of Flat Slab Structure (Genikomsou *et al.*, 2014)**

As having difficulties and time consuming, numerical analysis is the only option to provide in-depth insight regarding the comprehensive behaviour of structural elements. Using this approach, it was possible to simulate the slab-column connection models under various loading formations. One of such was done

by Genikomsou *et al.*, (2014) by using ABAQUS software programme. The analysis was carried out to understand the phenomena of punching shear occurred in the critical area of slab-column connections. Specimen models were built in the form of three-dimensional shape adopting linear brick elements. The concrete element was a deformed solid element known as C3D8R with three degrees of freedom. For reinforcement bars, a discrete element of T3D2 was used as it can generate the tension and compression behaviour.

Nonlinear material property of concrete was damage plasticity as it can be used to simulate static, cyclic, or fatigue response. In addition to that, damage plasticity was assessed to have the ability for modelling the quasi-brittle material. It is of interest to note that damage plasticity model adopted stiffness degradation was used to account the descending part in nonlinear regime from load-deformation or stress-strain relationship.

*This page intentionally left blank*

## CHAPTER 3

### EXPERIMENTAL PROGRAMME

The purpose of this chapter is to address in details about the experimental programme related to the present work. This chapter comprises the analytical calculation of shear stress in the slab-column connections of flat slab, design of test specimens, and experimental activities (preparation and testing programme). In addition, the results from the compressive and tensile tests of concrete, engineered cementitious composite material, and reinforcing steel are also included herein.

#### 3.1. Analytical Design of Shear Stress in the Slab

Preliminary design of the test specimens concerning the slab member was calculated based on *direct design method* as specified in ACI 318-14 and SNI 2847:2013. These calculations cover the design of specimen geometry, a number of required reinforcements in both members (slab and column), determination of internal forces and control of shear stress due to combined gravity and lateral load. According to ACI 421.1R-99, transfer of moment acting on slab-column connections in the form of flexure can be calculated based on **Equations (3.1)**.

$$M_u = \gamma_f \times M_{exp} \text{ where } \gamma_f = 1 / \left( 1 + \frac{2}{3} \sqrt{\frac{b_1}{b_2}} \right) \quad (3.1)$$

where:

- $M_u$  : the portion of unbalanced moment transferred by flexure, N-mm
- $M_{exp}$  : unbalanced moment obtained from experimental test ( $F_{exp} \times H_{col}$ ), N-mm
- $F_{exp}$  : lateral load obtained from experimental test, N
- $H_{col}$  : total height of the column, mm
- $\gamma_f$  : the fraction of moment transferred by flexure
- $b_1$  : width of critical section in the direction of loading, mm
- $b_2$  : width of critical section measured perpendicular to  $b_1$ , mm

Per ACI 421.1R-99, the portion of unbalanced moment transferred in the form eccentric shear stress in the critical section is given by  $\gamma_v M_u$ . The factor of  $\gamma_v = 1 - \gamma_f$  is a fraction of the unbalanced moment in the form of shear stress. The calculation of total shear stress acting on the structure due to uniform shear stress and unbalanced moment is expressed in **Equation (3.2)**.

$$v_u = \frac{V_g}{A_c} + \frac{\gamma_v M_u c}{J_c} \text{ where } M_u = M_{\text{exp}} \text{ and } J_x = d \left( \frac{l_2^3}{6} + \frac{l_1 l_2^2}{2} \right) + \frac{l_2 d^3}{6} \quad (3.2)$$

where:

- $V_g$  : shear force in the critical section caused by gravity load, N
- $M_u$  : the unbalanced moment represented as eccentric shear stress, N-mm
- $A_c$  : area of critical section calculated by  $b_o' \times d$ , mm<sup>2</sup>
- $b_o$  : critical perimeter obtained from  $2 \times (l_1 + l_2)$ , mm (for two-way slab)
- $b_o'$  : critical lines perpendicular to loading direction obtained from  $2 \times l_1$  (for one-way slab)
- $l_1; l_2$  :  $c_1 + d; c_2 + d$  where  $c_1, c_2$  is the column width and  $d$  is slab effective thickness, mm
- $c$  : extreme fibre distance, mm
- $J_c$  : section property analogous to the polar moment of inertia of the critical section, mm<sup>4</sup>

$$v_n = v_c + v_s + v_f \quad (3.3)$$

Once the accumulative shear stress has been calculated; subsequently, the nominal shear stress must be taken into account to control the value of total shear stress as specified in ACI 318-14. Given that, **Equation (3.3)** provides the calculation to control the total shear stress over the nominal shear stress. ACI 318-14 also outlines in detail that nominal shear strength of concrete  $v_c$  (US. Customary) is classified according to the part of what is being reviewed.

- (i)  $v_c = \left(2 + \frac{4}{\beta_c}\right) \sqrt{f'_c}$ , where  $\beta_c$  is the ratio of long section to short section measured from the column or the area where the loading is applied.
- (ii)  $v_c = \left(\frac{\alpha_s d}{b_0} + 2\right) \sqrt{f'_c}$ , where  $\alpha_s$  is 40 for interior column, 30 for exterior column, and 20 for corner column
- (iii)  $v_c = 4\sqrt{f'_c}$

It is a necessity to realise that the present study does not involve the contribution of any shear reinforcement over the slab, hence the second variable  $v_s$  from **Equation (3.3)** is intentionally neglected. However, for the test specimen which engages the utilisation of high tensile fibrous material, the inclusion of fibres is utterly considerable. Since it has not been stated in any ACI design codes, the equation from JSCE specification focusing on HPFRCC material is deliberately preferred [see **Equation (3.4)**].

$$v_f = f_t + b_0 \times d / \gamma_b \quad (3.4)$$

where  $v_f$  is designed punching shear capacity exerted by fibres,  $f_t$  is designed tensile yield strength of HPFRCC obtained from the uniaxial tensile test,  $b_0$  is the peripheral length of the critical section,  $d$  is the effective height of the slab, and  $\gamma_b$  is reduction factor. Since **Equation (3.4)** states the result of punching shear strength in force unit [N], the shear stress due to fibres influences can closely be interpreted closely similar to the value of tensile shear stress [MPa] over the reduction factor.

### 3.2. Specimen Design

Three half-scale slab-column connections with identical geometry were tested under combined gravity and lateral displacements. The specimen design was based on the experimental investigation by Gunadi *et al.* (2012). However, due to the difference related to strengthened technique, original specimen configuration

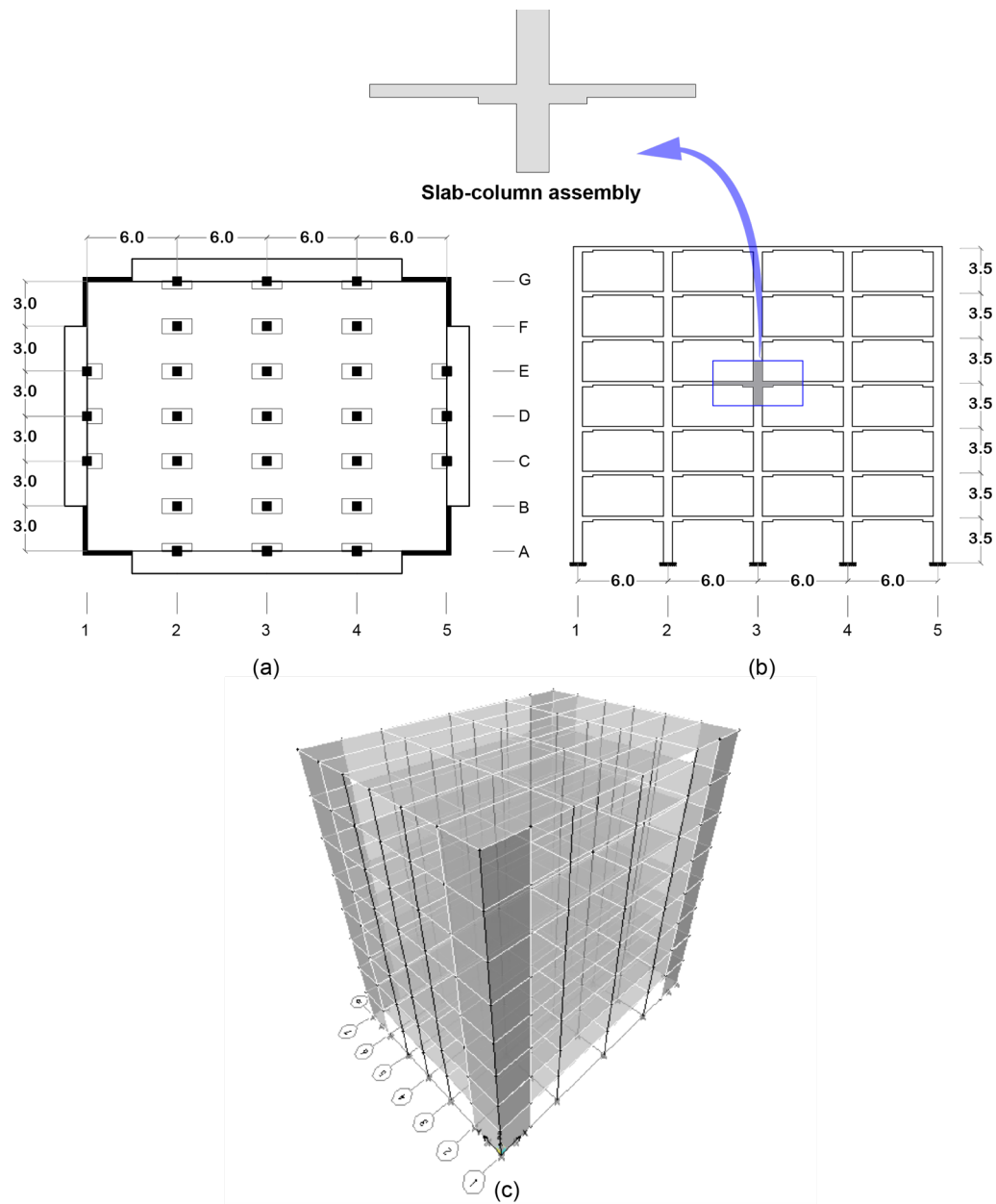


**Figure 3.1** Prototype of proposed flat slab structure with dual system [unit in metre]: (b) 2D plan; (c) side view in longitudinal direction (x-axis); (a) 3D isometric view.

was modified using drop panel to fit with the present model. The preliminary design of test specimen can be seen in Appendices. As presented in **Figure 3.1**, the specimen was a type of subassembly model which was originally adopted from a multi-story prototype dual system flat slab structure consisted of slabs, columns, drop panel, and structural (shear) walls. The longitudinal and transversal span from support to support was 6.0 m and 3.0 m respectively, with a typical floor height of

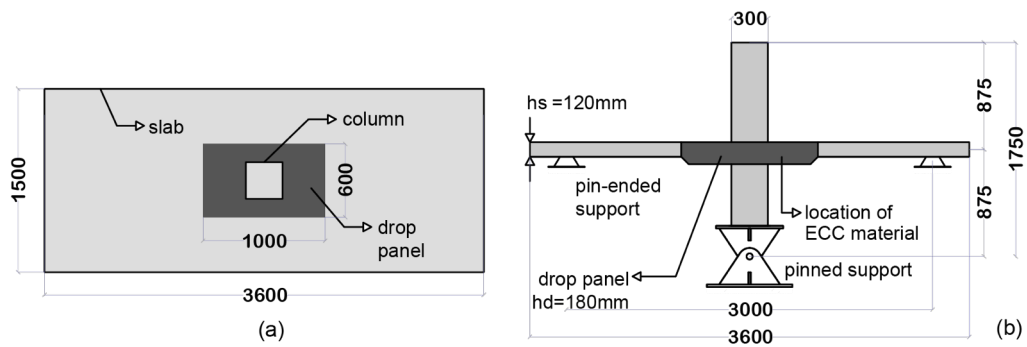


**Figure 3.2** Schematic geometry of test specimen [unit in millimetre]: (a) top view; (b) longitudinal direction (x-axis).

3.5 m and the slab thickness of 0.24 m (see **Figure 3.1(a)** and **Figure 3.1(b)**). Since the structural geometry was a half-scale model, then the typical geometry of the test slab-column assembly specimen was 3.0 m in the longitudinal span, and 1.5 m in the transversal span with the height of the column is 1.75 m. The slab thickness was 0.12 m outside the local thickening region while the total thickness of drop panel element was 0.18 m (see **Figure 3.2(a)** and **Figure 3.2(b)**). The determination of drop panel thickness was in accordance with ACI 318-14 as stated in Chapter 2).

The flexural reinforcement in the slab was designed to carry gravity loads and was also expected to alleviate the extreme shear effect caused by lateral loading. For design purposes, the compressive strength  $f'_c$  of concrete and ECC were assumed to achieve a grade of 50 MPa and M45, respectively. The yield strength  $f_y$  of the reinforcing bars were varied where  $f_y$  of flexural reinforcement in the slab was 325 MPa,  $f_y$  of longitudinal reinforcement bar of the column was 390 MPa, and the stirrup yield strength was 327 MPa. As shown in **Figure 3.3(a)**, the slab top longitudinal reinforcement layouts were set to be dense in the region adjacent to column face, referred to critical section area, with space of 50 mm up to the perimeter of local thickening member while outside this region the space was altered to 120 mm, resulting in the reinforcement ratio of 1.0% within the column strip. On the other hand, described in **Figure 3.3(b)**, the bottom slab longitudinal reinforcement layouts were customised to be a bit spacious with distance of 120 mm at the local thickening and continue to be more spacious outside the local thickening member (space between two reinforcements was 200 mm), ensuing

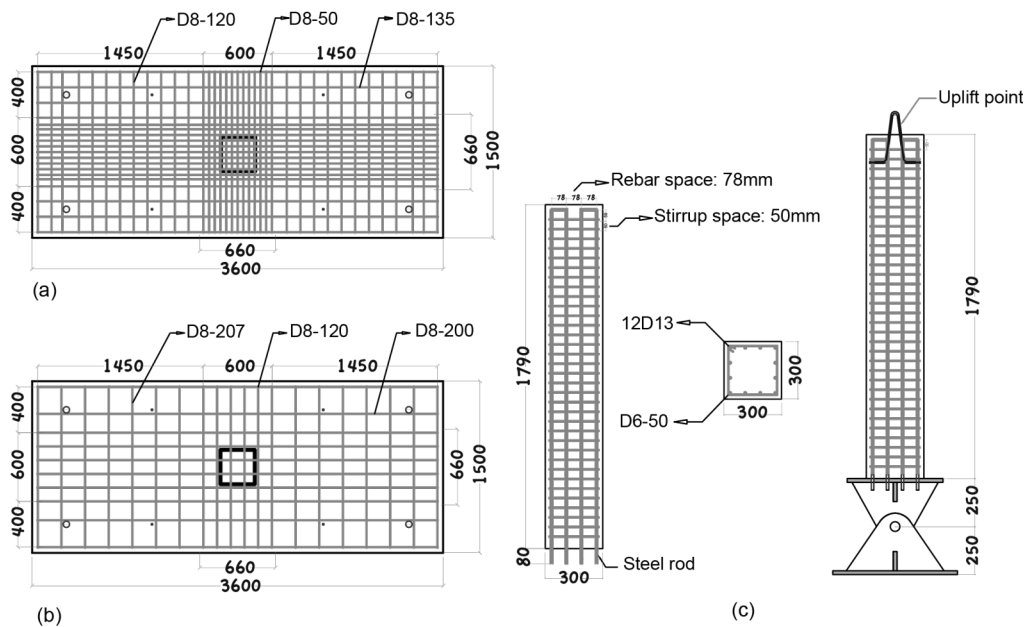


**Figure 3.3** Reinforcement layouts [unit in millimetre]: (a) slab top reinforcement bars; (b) slab bottom reinforcement bars; (c) longitudinal and web reinforcement of column.

0.6% of tensile reinforcement ratio within the column strip section. Per Section 13 of ACI 318-14, the slabs were intentionally provided with continuous reinforcing bars in both directions to pass through the column reinforcement cage. It is a must to consider since these bars, referred to integrity steel, were intended to transfer the gravity loads to the column during the course of loading, especially after punching occurs at the connection to evade the severe failure. Furthermore, as can be seen in **Figure 3.3(c)**, it is also noted that the stirrups were designed to be highly condensed as they were originally envisioned to generate high over-strength factor of the column. At some point, it was also designed to resist all anticipated bending moments. Longitudinal reinforcements in the column were designed to penetrate the concrete cover at the column base as the purpose to attach the specimen to the pinned support in later setup. However, since it seemed unmanageable to attach these longitudinal bars onto the support using nuts, the bottom part of these longitudinal bars were cut with the length of 250 mm measured from the column base, and subsequently were replaced using steel rods. It was done by merging the two different fabricated materials using welding technique.

Each test specimen was basically identical in geometry and reinforcement layouts. It was only varied in the utilisation of matrix material namely conventional concrete and ECC. Detail of the test specimens is listed as follows:

- (i) Specimen S1, hereinafter referred to as control specimen of the slab-column subassembly, is fabricated by using normal concrete and is subjected to low gravity shear ratio (GSR) with the value of 0.08 corresponding to inner critical section nearby column face (see **Appendix A**).
- (ii) Specimen S2, normally similar to specimen S1, is fabricated using ECC and conventional concrete (for more details see **Figure 3.2(b)**) and is tested under the same loading condition as the control specimen. Due to the inclusion of ECC material, however, the value of GSR is drastically reduced by 0.05 which is corresponded with outer critical section (see **Appendix B**).
- (iii) Specimen S3 is similar to specimen S2 with the only exception is that it is subjected to intermediate gravity shear ratio of 0.25 and is occurred at outer critical section nearby drop panel face (for clarity see **Appendix C**).

### **3.3. Specimen Preparation**

#### **3.3.1. Reinforcing cage and strain gauge installation**

The reinforcing bars for each specimen, consisting of 29-Nos of slab longitudinal reinforcing bars, 44-Nos of slab transversal reinforcing bars, 12-Nos of column longitudinal bars, and 35-Nos of stirrups, were supplied by PT. Hanil Jaya Steel Surabaya. Prior to making the cage, the flexural reinforcing bars were cut to the required size of the specimen. Stirrups were also prepared and bent in the desired dimension to fit the required size of the column section measured from inner wall of the steel mould. The making of reinforcing cages was done in four phases. The first step was to assemble the longitudinal and transversal reinforcing bars of the slab separately for the top and bottom reinforcements by referring to the reinforcement layouts illustrated in the previous chapter. The assembly was done using welding technique to maintain the position of each rebar. After completing this, the subsequent phase was carried out by assembling the top and bottom of the slab reinforcing bars and then the welding process was done in the same way as the first step. In the third phase, column stirrups were firstly tied using wires on the



**Figure 3.4** Chronological process of reinforcing cage, starting from the fabrication to the adjustment in the formwork (steel mould) along with the installation of strain gauges.

longitudinal bars around the top part of the column to allow the column longitudinal bars passing through the slab reinforcements. Lastly, the final phase was then continued by placing the rest of the stirrups around the slab towards to bottom part of the column.

To deal with the strain gauge installation, the corroded surface of the reinforcing bars was first removed. For threaded reinforcing bars such as used in the column, grinding technique was applied as it provides an easier process to detach the ribs. Following this, the coarse and fine sanded belts were also used in the subsequent phase to smoothen the surface. For plain steel bars, the use of the coarse and fine sanded belts was sufficient on creating the proper surface for strain gauge placement. After this step had been done, the cleaning liquid was then lubricated alongside the surface of the reinforcing bars to ensure that they are free

from any residual rust. Once all of these preparation steps were completed, the strain gauge type of FLA-2-11 was attached to the surface of the steel bars by using fast drying gauge adhesive, called as CN-Y glue. It is important to mention that one such way to avoid any slip of gauge sensor during the drying process, the cable next to the sensor must be tied up by rolling over the aluminium tape. After the attachment of gauge was done, the SB tape was then used to coat the sensor along and the cable near to the sensor and then the aluminium tape was used again to layer up the protection as well as to prevent any damage of the gauge during the concrete placement. Once all the gauges had been installed, the inspection was then proceeded using the voltmeter to measure the resistance. To provide a better picture with regard to the experimental preparation, **Figure 3.4** illustrates the whole complete process of making the reinforcing cages and installing the strain gauges.

### **3.3.2. Casting and curing**

Before starting to cast the concrete, all of the material components were prepared. The steel moulds were also lubricated with oil to ease the dismantle process. While waiting for the materials to be moved in a bucket of the mixer, reinforcement cage of the test specimen was put onto the steel mould. The strain gauge cables were protected using plastic pipes and aluminium tapes to prevent the damage during the casting. The steel rods at the column base were also covered with aluminium tapes to maintain the thread quality just in case if there is any segregation of concrete around the column base during the casting. The procedure of casting was simply straightforward since it was done at the concrete batching plant in WIKA Beton Makassar. By referring to the mixture proportion as explained in the previous section, both for normal concrete and ECC, mixing was done thoroughly. The casting procedure for each specimen was varied due to the addition of ECC material along the mould. The casting process for each specimen was done separately for a different day. For specimen S1, the casting was done in a single batch whereby fresh concrete was poured directly into the mould and internally vibrated with a poker.

Differ to the specimen S1, the specimen S2 and S3 were cast in three phases using two different matrix materials (see **Figure 3.5**). The bottom part of the

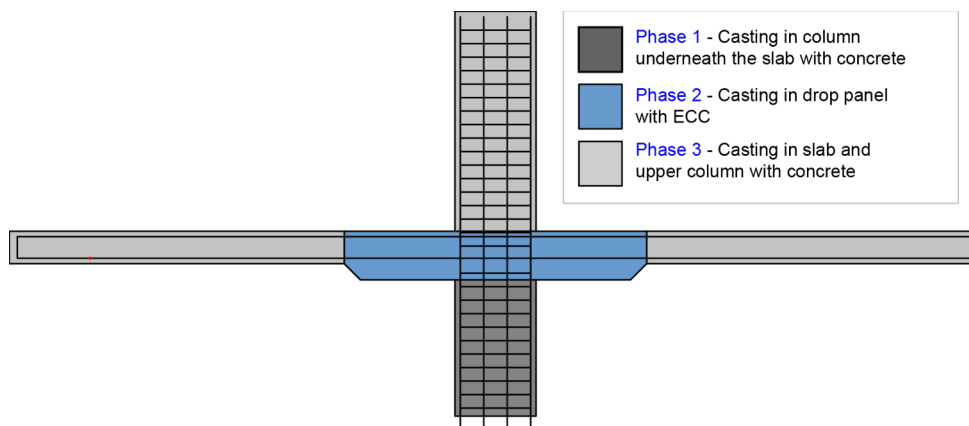


**Figure 3.5** Phase of casting the specimen with ECC.

column was firstly cast using conventional concrete up to the peripheral line between column and drop panel. While waiting for the normal concrete to set, mixing of ECC material was carried through in four batches, allowing the fibres to be well-dispersed. After the mixing sequence of ECC material was done, immediately ECC was poured into the region of the local thickening member. Subsequently, conventional concrete was then poured to the slab and upper part of the column. Besides the main specimen, three concrete cubes (150×150×150-mm) for normal concrete and (50×50×50-mm) for ECC were also used to determine the compressive strength of the relevant test specimen. Additionally, the dog-bone shape moulds were also prepared for the ECC specimens to determine the tensile response of the material.

Immediately after casting, the top surface of the slab, column, and the cubes was trowelled smooth and then covered with polythene sheeting. In the following day, they were stripped and the regularly wetted and stored in a sheltered outdoor environment, reflecting common site practice until required for testing (28 days after casting). During the course of curing, the inspection of strain gauges was done in every week using the voltmeter. It was shown that apparently there were several strain gauges broke when the specimens were being cast. Prior to moving the specimens to the laboratory, a platform for each sample, as seen in **Figure 3.6**, was constructed using wood to ease the mobilisation process. After 28 days of curing, all of the specimens were then transported using a dump truck to the laboratory.



**Figure 3.6** Packing of specimen.

### **3.4. Mix Design of Concrete and ECC**

In regular concrete, the concrete mix design consisted of coarse aggregate with a maximum size of 20 mm, fine aggregate, ordinary Portland cement (Type 1), superplasticizer, and water. The mix proportion for concrete with a grade of 50 MPa was proposed. Detail of mixture proportion is listed in **Table 3.1**. Water to cement ratio of 0.2 was used in the conventional concrete mixing to achieve 28-days average compressive strength of 50 MPa. The superplasticizer, type of TamCem 60 RA, was also used to reduce the amount of water while maintaining the level of consistency and workability. A standard mixing procedure was applied in three phases. The first step was to mix the coarse aggregate and sand. In the second step, the cement was poured with the addition of water to maintain the volume of cement. Lastly, after 2-3 minutes of mixing, the superplasticizer was given slowly, and then the mixing was continued until the homogeneity was achieved. Besides the main specimens, a standard concrete cube (150×150×150-mm) was used to determine the compressive strength of concrete, while tensile testing for conventional concrete was neglected.

For ECC, prior to conducting the experimental tests for the main specimens, the evaluation with regard to the performance of ECC material was done through material investigations. It was of any concern to ensure that the mixture proportion of ECC material, as well as the procedure of mixing sequences, were appropriate.

**Table 3.1** Detail of mix proportion of conventional concrete.

Material	Concrete C35/45
Cement (C), kg/m <sup>3</sup>	590
Coarse aggregate (CA), kg/m <sup>3</sup>	1078
Sand (S), kg/m <sup>3</sup>	633
Water (W), kg/m <sup>3</sup>	125
Superplasticiser, kg/m <sup>3</sup>	4.36

The standard of ECC material consisted of ordinary Portland cement (C), fly ash (FA), silica sand (S) with typical grain size ranged from 100 to 200  $\mu\text{m}$ , PVA fibres, and high range water reducer (HRWR). PVA fibres type of RECS15 were ordered from Nycon Corporation USA with specification listed in **Table 3.2**. The standard of mixture proportion of ECC material with a grade of C35/45 used in this study is shown in **Table 3.3**. To deal with ECC, the compressive strength was initially taken into account prior to performing the tensile tests. It is important since the grade of the material must be controlled to fit with the desired strength. In this study, the typical mix design for ECC with a grade of C35/45 was suggested. The sand to binder ratio of 0.36 was used to maintain adequate stiffness and volume stability. Additionally, water to binder ratio of 0.26 was also used to attain an excellent balance of fresh and hardened properties. Special consideration in mixing process was also taken into account since ECC is a sensitive material. Tools and materials had been ensured clean to avoid secondary chemical reaction throughout the casting process. In proper sequence, fly ash, cement, sand, and 80% of water were manually mixed in mortar mixer for approximately 1 to 2 minutes to avoid the loss of light volume in cement and fly ash. Automatic mixing with normal speed was then performed for 2 minutes, following the addition of HRWR and 20% of water. Subsequently, the mixing process was continued with normal speed for approximately 2 to 3 minutes, and then PVA fibres were added slowly. The speed was then maintained constant in the final step with duration of 4 to 5 minutes until the fibres were well-dispersed.

A standard mortar cube (50×50×50-mm) was used to cast ECC material. After curing process had been completed, the compression test was done in day-28

**Table 3.2** Specification of PVA fibres (Nycon USA).

Diameter ( $\mu\text{m}$ )	Length (mm)	Elastic modulus (GPa)	Tensile strength (MPa)	Density
38	8	40	1600	1.30

**Table 3.3** Detail of mix proportion of engineered cementitious composite.

Material	Mixture proportion
FA/C	1.2
W/B*	0.26
S/C	0.8
HRWR/C, %	0.86
Cement (C), $\text{kg}/\text{m}^3$	570
Fly Ash (FA), $\text{kg}/\text{m}^3$	684
Sand (S), $\text{kg}/\text{m}^3$	455
Water (W), $\text{kg}/\text{m}^3$	331
Fibres (PVA), $\text{kg}/\text{m}^3$	26
HRWR, $\text{kg}/\text{m}^3$	4.9

\*B: binder (cement + fly ash)

to obtain compressive strength. Subsequently, further investigation was carried out to determine the response of ECC material in tension. The uniaxial tensile test was examined to govern an understanding in terms of ECC response under tension. In general, it is well-known that the tensile test for concrete or quasi-brittle material is carried out by adopting the splitting test method. However, using this method, it is not possible to provide the stress-strain response, fracture energy, and elastic modulus of the material since it has limited source for only providing the tensile strength. Considering this fact, uniaxial direct tensile was then preferred in ECC material to give comprehensive results in terms of ECC tensile behaviour. Furthermore, the stress-strain curve obtained from this test can be used in the future to determine the constitutive model regarding the material properties of ECC in finite element modelling. In relation to this, ECC dog-bone shape specimen according to CRD-C 260-01 was used to carry out the uniaxial direct tensile test for ECC. Since it postulates weakness section in the middle part of the shape and

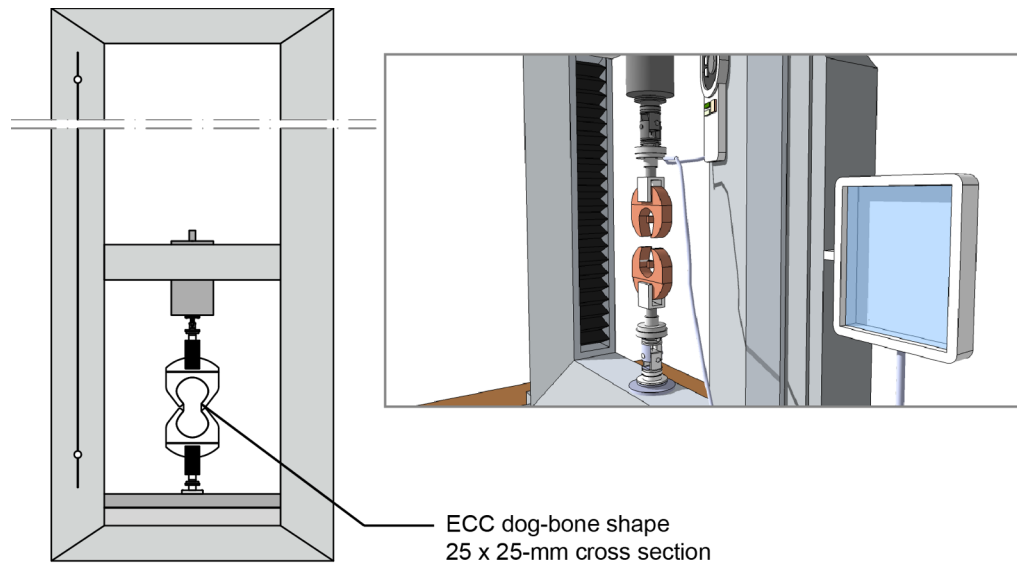


**Figure 3.7** Setup of direct tensile test of ECC dog-bone shape.

thereby resulting in horizontal cracks along the width, dog-bone shape specimen was preferable. Set up of ECC dog-bone shape is illustrated in **Figure 3.7**. After the curing process had been completed, the test was carried out using the universal testing machine. A displacement controlled method with the rate of 0.01 mm/s was adopted. Through these process, it was shown that compression and tension response were appropriately undertaken.

### **3.5. Mechanical Properties of Material**

Prior of testing the main specimens, material investigations were carried out to obtain the mechanical properties of the concrete, ECC, and reinforcing bars. Compression tests of the concrete cube were conducted in the Laboratory of WIKA Beton Makassar while compression and tensile tests for ECC samples as well as the tensile tests for reinforcing bars were carried out in the Laboratory of Material and Building Construction – Sepuluh Nopember Institute of Technology. Details of the results for each material are discussed in the following subsections.

#### **3.5.1. Properties of normal concrete**

Three concrete cubes (150×150×150-mm) for each specimen were tested in accordance with British standard using old-fashioned compression testing machine. Since this machine had no deformation control feature, it was not possible to

generate the load-deformation curve or even stress and strain curve. After obtaining the compressive strength from the cubes, the conversion to cylinder compressive strength was then taken into account, resulting in the average compressive strength of 47.7 MPa, 47.9 MPa, 46.5 MPa with respect to specimen S1, S2, and S3. Splitting test for conventional concrete was deliberately neglected since the result using theoretical approach does not vary. The tensile strength of normal concrete was determined with the value approximately 10 to 15 percent of its compressive strength according to ACI 318-14.

### **3.5.2. Properties of engineered cementitious composite**

In advance of presenting the results of mechanical properties of ECC, the analysis of fly ash from x-ray fluorescence (XRF) test is discussed herein. This is essential since the main material constituent of ECC, as cement-based, employs the utilisation of fly ash as its dominant compound to create the micromechanical model. For evaluating the quality of fly ash, whether or not it is possible to be applied in ECC, ASTM C618 has specified the minimum criteria in relation to the chemical characteristic for coal fly ash (see **Table 3.4**). For this purpose, the investigation of fly ash was carried out in the Laboratory of Central Material – State University of Malang. Only one batch of fly ash used in each of test specimens; thus, the analysis was then only performed once. Through this test, the identification of chemical elements contained in fly ash was possible to be known for determining the class of the fly ash. Mainly, only three elements are needed to be concerned in order to define the class of the fly ash whereby all of these three elements are bound by the oxide element. Shown in **Table 3.5**, it is evident that the summation value of three dependent compounds ( $\text{SiO}_2$ ,  $\text{Al}_2\text{O}_3$ , and  $\text{Fe}_2\text{O}_3$ ) has exceeded the minimum requirement as class *F* fly ash, meaning this class is highly suitable to be applied in the cement based material such as ECC. When class *F* fly ash is used as a replacement of some volume in Portland cement, it offers the advantages to increase the strength and workability, yet to decrease the water demand. However, it should be noted that the time of set may be somewhat delayed. Also, the early compressive strength (before 28 days) may be decreased slightly.

**Table 3.4** Chemical properties of coal fly ash (ASTM C618).

Chemical compound		Class		
		N	F	C
SiO <sub>2</sub> + Al <sub>2</sub> O <sub>3</sub> + Fe <sub>2</sub> O <sub>3</sub>	Min %	70	70	50
SO <sub>3</sub>	Max %	4	5	5
Moisture content	Max %	3	3	3
Loss of ignition	Max %	10	6	6

**Table 3.5** Chemical compound contained in fly ash.

Compound	Mass [%]	Compound	Mass [%]
Al <sub>2</sub> O <sub>3</sub>	14.10	MnO	0.20
SiO <sub>2</sub>	27.70	Fe <sub>2</sub> O <sub>3</sub>	37.5
SO <sub>3</sub>	1.12	NiO	0.25
P <sub>2</sub> O <sub>5</sub>	0.50	CuO	0.19
K <sub>2</sub> O	2.76	ZnO	0.09
CaO	10.67	SrO	1.32
TiO <sub>2</sub>	3.31	ZrO <sub>2</sub>	1.00
V <sub>2</sub> O <sub>3</sub>	0.18	Eu <sub>2</sub> O <sub>3</sub>	0.60
Cr <sub>2</sub> O <sub>3</sub>	0.11	ReO <sub>2</sub>	0.33

To obtain the compressive strength of ECC, three mortar cubes with the size of 50×50×50-mm were tested using modern UTM compression machine in accordance with ASTM C109. During testing, the load and deformation of cubes were monitored in the computer to generate the compressive stress-strain relationship. Through this experiment, the results showed that the averagely converted ECC compressive strength for specimen S2, and S3 was 46.4 MPa, and 51.8 MPa, respectively. **Figure 3.8** presents the average compressive stress-strain relationship of ECC with a grade of C35/45 obtained from the cubes for each specimen. Inspection of the stress-strain curve highlights that the compressive properties of ECC are not prominently distinctive from normal concrete or even for high strength concrete. However, it is evident that the post-peak behaviour of ECC under compression tends to descend more gently than normal concrete in general, accompanied by a gradual bulging of the specimen rather than explosive in crushing failure.

In regard to obtaining the tensile properties of ECC, the uniaxial direct tensile test was carried out using the dog-bone ECC shape (detail of sample is illustrated in the previous section). Highlighted in this experiment, the typical tensile behaviour of ECC dog-bone shape shows the characteristic of steady state crack width, allowing the dog-bone ECC shape to reach the tensile strain capacity in excess of 3%. In addition to that, the crack width which is governed by the micromechanics between fibre-matrix interaction within ECC also allows the suppression of crack growth with the replacement of smaller cracks form. According to **Figure 3.9**, to identify the behavioural response of ECC under tension, the curve is characterised by a number of regions under loading. The description of each region is linear elastic, strain hardening associated with plastic deformation, and tension stiffening whereby the behaviour is on the edge of its residual strength. In the linear elastic region, the dog-bone still exhibits initial response whereby the formation of cracks is yet to occur. As the displacement increases, there is a transitional region toward the strain hardening behaviour causing the progression of multiple micro cracks appeared on the weak section whereby the fibres start to bridge the cracks. The formation of this multiple micro cracks is necessary to achieve high tensile ductility. As the displacement further

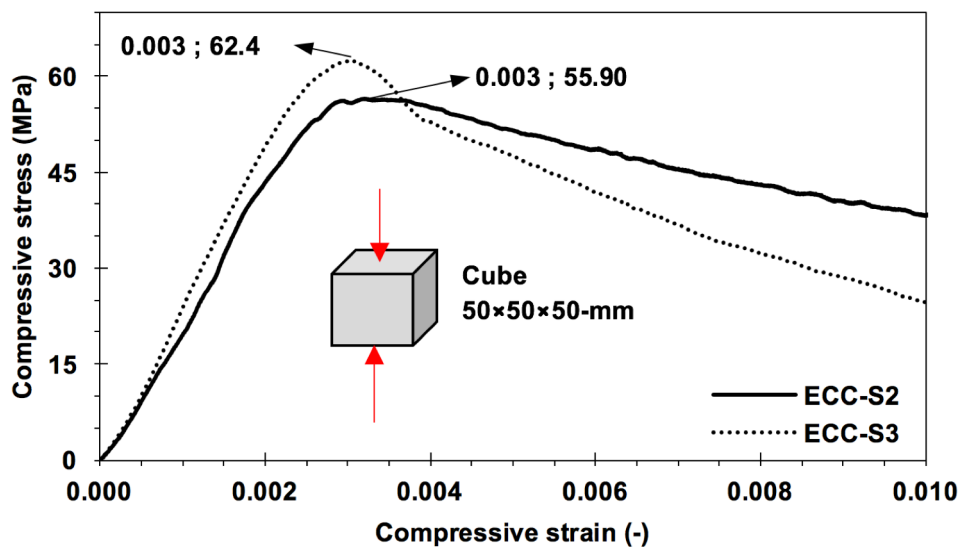


**Figure 3.8** Compressive stress-strain relationship of ECC cubes.

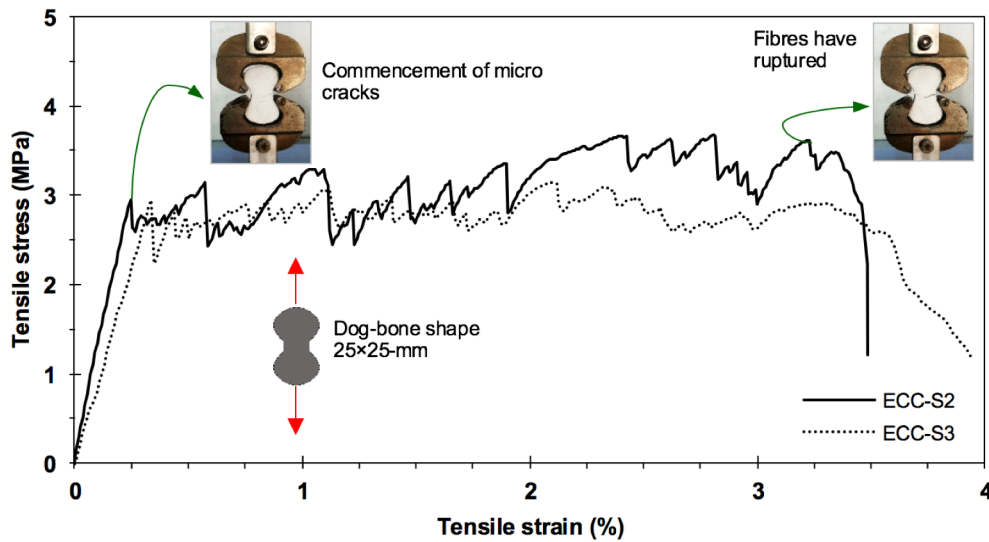


**Figure 3.9** Tensile stress-strain relationship of ECC dog-bone shapes.

increases beyond its peak load, the tension-softening response occurs followed by the condition whereby fibres have ruptured. It should be noted that after undergoing this condition, ECC is no different with normal concrete, showing the significant loss of strength. It should be noted that the high performance of ECC in tension is normally obtained by the presence of a number of fibres interacted to the matrix with well-dispersed distribution thereby governing the pseudo-strain hardening behaviour. However, opposite scenario might also be occurring when and if the homogeneity of the fibres is not achieved. On account of that, it is of importance to maintain the consistency of fibre distribution within the matrix. This can be done by avoiding the use of internal vibrator thereby preventing the fibres to lie on the bottom of the formwork.

### 3.5.3. Properties of reinforcing bar

To find out the tensile properties of the reinforcing bars, the uniaxial tensile test was carried out using the universal testing machine in accordance with ASTM A370-05. 3-Nos of 1 meter bars were prepared for each diameter to account the average properties in terms of tensile stress-strain response. During the material test, instead of using point-based strain gauge, the strains were measured automatically by the sensor provided in the machine and transferred to a computer.

Given that the results might not be as accurate as using the strain gauges, meaning it may lead to the conservative results.

Similar to other tensile tests of reinforcing steel in general, the evaluation of tensile properties in this present study is judged by the uniaxial tensile stress-strain relationship. Normally in tension, the behaviour of the reinforcing bars is characterised in two distinct responses, including linear elastic and strain hardening behaviour followed by the increase in stress up to the peak point. The linear elastic region is identified by the linear gradient starting from zero value to the certain value up to the transitional line of strain hardening (see **Figure 3.10**). On the other hand, the strain hardening response is associated with the condition whereby the stiffness has been altered due to the inelastic behaviour of the reinforcement. To provide in-detail results, the summary of the material properties of all reinforcing bars is presented in **Table 3.6**.

**Table 3.6** Tensile properties of reinforcements.

Rebar type	Bar size (mm)	Area (mm <sup>2</sup> )	Elastic region		Inelastic region	
			$f_y$ (MPa)	$\epsilon_y$ (%)	$f_u$ (MPa)	$\epsilon_u$ (%)
Threaded	12.78	128.01	394.89	0.197	499.90	13.61
Plain	7.96	49.76	324.87	0.217	480.50	11.65
Plain	5.89	27.23	327.07	0.192	480.39	10.62

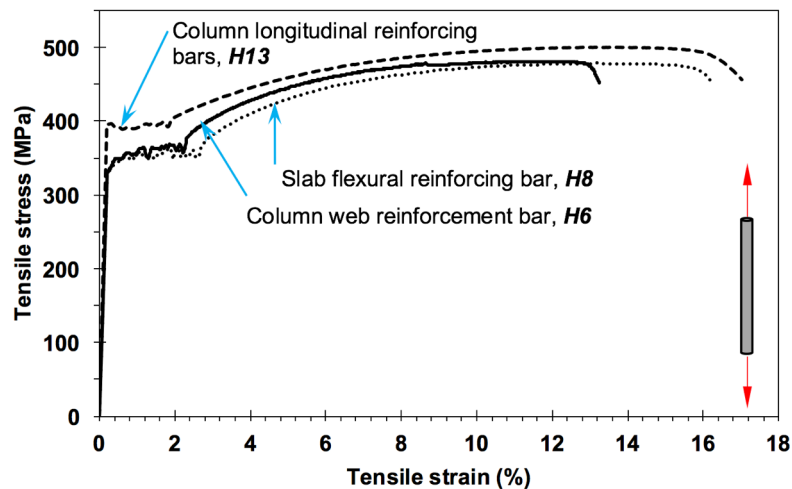


**Figure 3.10** Tensile stress-strain response of reinforcing bars.

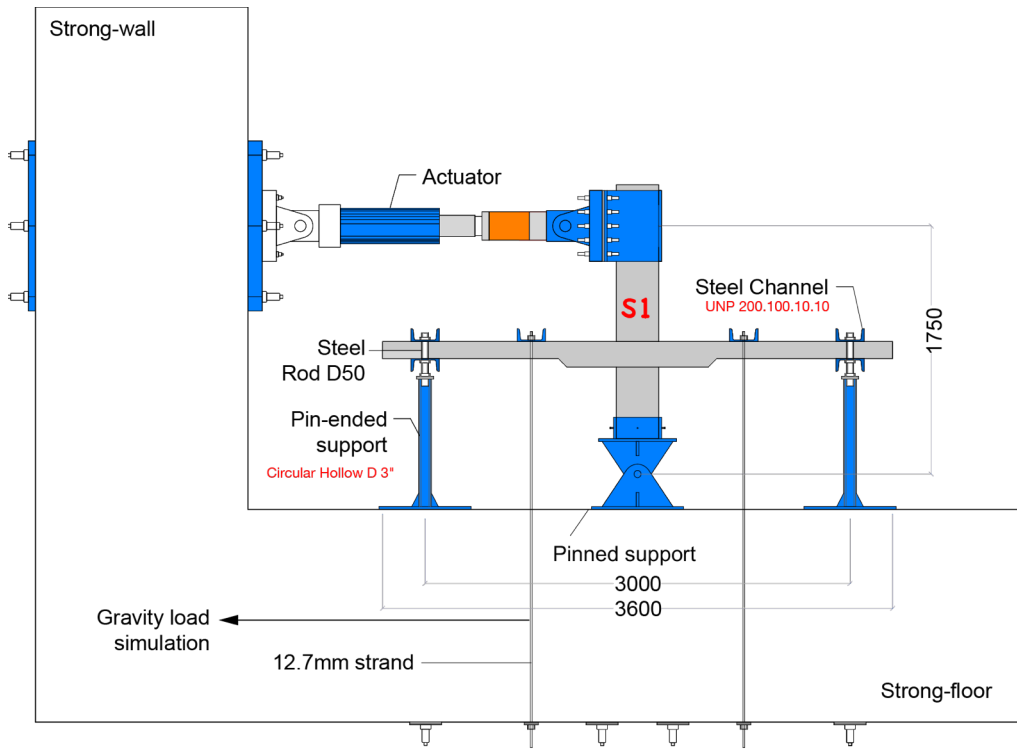


**Figure 3.11** Test set up of slab-column connection.

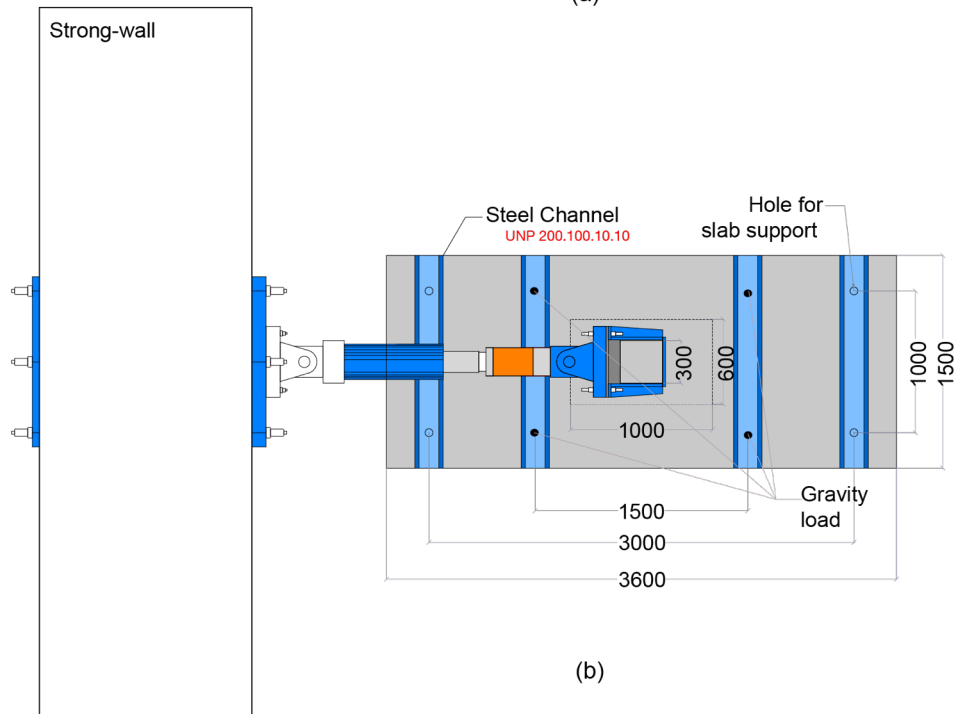
### **3.6. Experimental Activities**

#### **3.6.1. Test setup**

The experiment was carried out at the Laboratory of Structure and Material Hasanuddin University in Makassar. The laboratory is equipped with strong-floor, strong-wall, a hydraulic pump, and servo-controlled cyclic hydraulic actuator. The arrangement of slab-column connection specimen and test rig is shown in **Figure 3.11**, with the schematic of testing arrangement for slab-column connection shown in **Figure 3.12(a)**. The specimen was placed onto the supports made specifically to fit the geometry of the specimen members. Prior to moving the specimen to the location of the test, all supports were attached and positioned to strong-floor; likewise, the cyclic hydraulic actuator was also installed on the strong-wall. It is of any concern to mention that the surface of the pinned support was intentionally perforated according to the position of each longitudinal bar of the column. Given that, it was possible to restraint the column base onto the pinned support by penetrating the steel rods into the holes. After settling this, the specimen was lifted up using an overhead crane with the capacity of 100 kN and was positioned according to where the position of the supports. The column base of the specimen



(a)



(b)

**Figure 3.12** Schematic testing configurations [unit in millimetre]: (a) side view in longitudinal direction; (b) top view.

was then placed onto the pinned support allowing the steel rods to be fastened using nuts. Following this, both of slab edges were also restrained using pin-ended steel rod in each corner of the slab. To provide uniform restraint, spreader beams were placed on top and underneath the slab edges and were fastened using nuts around the corners. An underlying reason for choosing the pin-ended steel rod is that it permits the specimen to have horizontal movement while prohibiting the vertical movement. Prior to connecting the cyclic hydraulic actuator alongside the column tip, the specimen was adjusted to remain flat using the bubble level. To do this, the slab supports were accustomed in such ways until the slab level was remained flat.

A constant gravity load was simulated with four prestressing strands (Grade 270, 12.7-mm diameter, 7-wire low-relaxation) pulling down at the mid-point of the slab through the strong-floor. The spreader beams were also used and were placed on the top surface of the slab to give uniform load distributions [see **Figure 3.12(b)**]. Beneath the surface of the strong-floor, strands were stressed and fastened with bearing plates and barrel wedges to prevent the significant loss of the stress. A manual hydraulic jack was used to give the jacking force for each strand. In addition to that, the load cell was also used to monitor the amount of force given to the strand. Since only one pair available during the testing process, jacking force at each strand was given gradually, starting from 50% of the desired loading to 75% and 100%. After dealing with this, cyclic lateral loading was then proceeded by pumping the hydraulic actuator.

### **3.6.2. Pre-test activities**

Prior to moving the test specimen to the test rig, a consideration of how to lift up the specimen with proper method was taken into account. Translocation of the specimen was done with an overhead crane by considering the additional internal forces acting on the specimen due to its self-weight load. It was decided to move the specimen with lift point positioned at the top surface of the column. During the process of making the reinforcement cage, some closed-hooks 12.7-wire strands were attached within the both of slab edges as well as in the top of the column. With the main lift point assigned at the column tip, internal forces in the form of maximum negative moments occur around the slab nearby the column face.

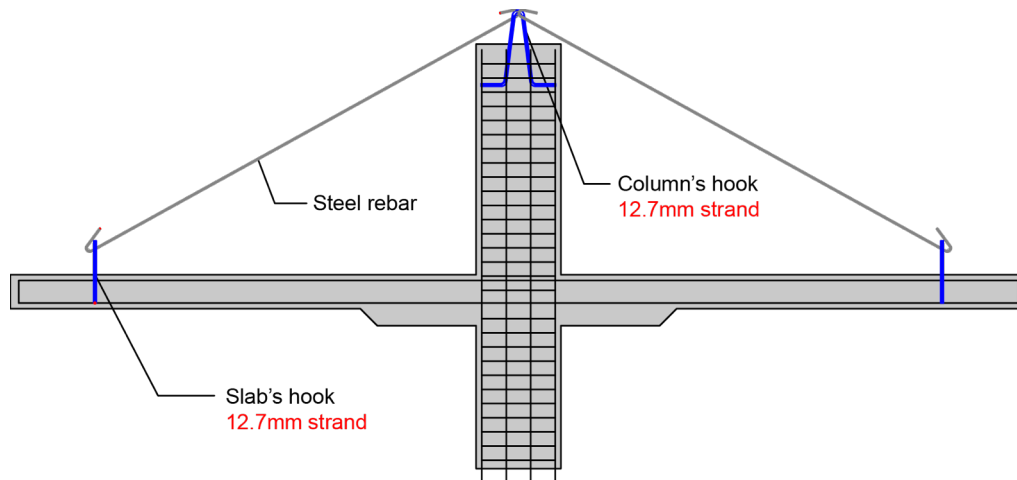


**Figure 3.13** Uplift technique for test specimen.

Following this, in order to avoid the formation of premature cracks occurred during this process, it was important to calculate the capacity of cracking moment of the slab as well as the tensile stress of the column whereby the value shall not be less than the flexural moment due to self-weight and rupture stress respectively. **Figure 3.13** provides a better understanding of how this whole process was carried out.

### 3.7. Loading Protocol

Gravity loading applied in this study was reasonably presumed to consist of slab self-weight, superimposed dead load and 30% of reduced live load as uniformly distributed loads on the slab (referred to Robertson *et al.*, 2002). Prior to deciding the magnitude of gravity loading given on the slab, it should be noted that the test specimen is a half-scale model which means the magnitude of self-weight is only half of it. At this point, the self-weight load must be multiplied twice to reckon the whole weight taken from its prototype. To deal with this, half of self-weight load must be transferred into superimposed dead load thereby resulting in the same condition with the prototype. However, apart from this consideration, the main purpose of subjecting the specimen to gravity load was how to give the right magnitude that can result in desired gravity shear ratio for specimen S1 to S3 which in this case was 0.08, 0.05, and 0.25 respectively. After the setup process was completed and before undergoing the first drift cycle, the gravity loading was applied to the slab such that a uniform shear stress ( $V_g/A_c$ ) was attained on the

critical section of the connection. The required applied gravity loading for each specimen was corresponded to the preferred gravity shear ratio as aforementioned in the previous section.

Once the gravity loading was all set, lateral displacement was then applied at the top of the column using hydraulic jack actuator with the load capacity of 1500 kN and stroke of 100 mm. For this purpose, the displacement was applied in regard to what is shown in **Figure 3.14** with the target of displacement to each loading point based on the recommendation from ACI-374.2R-13. The target of drifts for each cycle is summarised in **Table 3.7**. It is of any concern to know that the lateral drift ratio is defined as the ratio of applied lateral drift to the total height of the specimen [see **Equation (3.5)**].

$$DR = \frac{\text{Total applied displacement}}{\text{Total height of specimen}} \times 100\% \quad (3.5)$$

where the total height of the specimen was taken as 1750 mm and the applied drift ratio was based on applied displacement during the cycle of the loading.

Throughout each drift cycle, a steady, but a relatively small decrease from gravity loading was observed due to strand relaxation and specimen damage. At the

**Table 3.7** Target of drift ratio at each cycle.

Cycle	Target displacement (mm)	Target drift ratio (%)
1	3.5	0.20
2	4.375	0.25
3	6.125	0.35
4	8.75	0.50
5	13.125	0.75
6	17.5	1.00
7	24.5	1.40
8	30.625	1.75
9	38.5	2.20
10	48.125	2.75
11	61.25	3.50
12	70	4.00

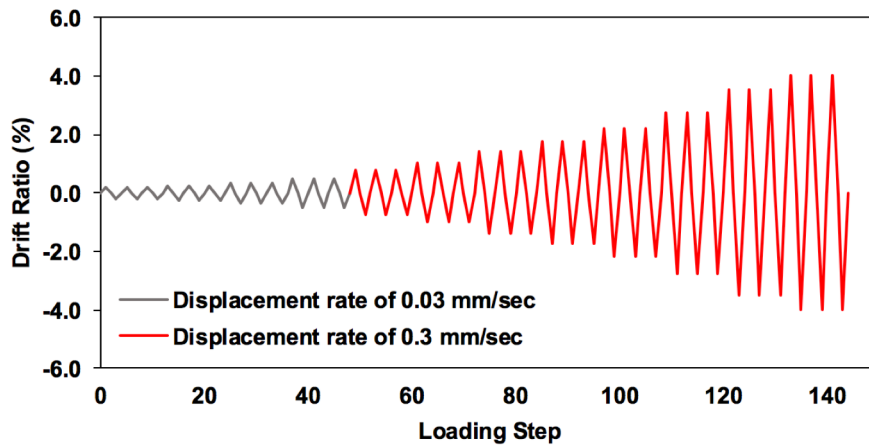


**Figure 3.14** Lateral displacement routine.

end of each drift cycle whereby the displacement was set to zero, strands were released and reloaded to forces corresponding to the target gravity shear ratio. As the displacement increased significantly (higher drift cycles), a large amount of gravity loading had reduced as the slab experienced more damage, the cycle was paused, and gravity load was then readjusted before continuing.

### 3.8. Instrumentation

In each specimen, a total of 8 and 6 strain gauges were mounted in the same direction of lateral loading on the top and bottom of slab flexural reinforcements respectively. The strain gauges were placed along the critical section to the column strip. For this purpose, these strain gauges were used to give an idea when and if the slab rebar has yielded during the increase of load levels. **Figure 3.15(a)** and **Figure 3.15(b)** show the strain gauge layouts on the top and bottom of slab reinforcements. The gauges are labelled as “T” and “B” in the first character with respect to the top and bottom location where these gauges are being attached. The number of strain gauges in the slab reinforcements are duplicated just in case if one gauge breaks during the casting process or implies bad reading in the testing. The second character indicates the side of the gauges seen from the column centre line whereby “W” and “E” stand for West and East side, respectively.

The specific location of the individual strain gauge on the slab reinforcement can be expressed by hashtag and number put in the last abbreviation (viz. TW#1, BW#1, and so on). To be more precise, hashtag and number of #1 and #2 denote

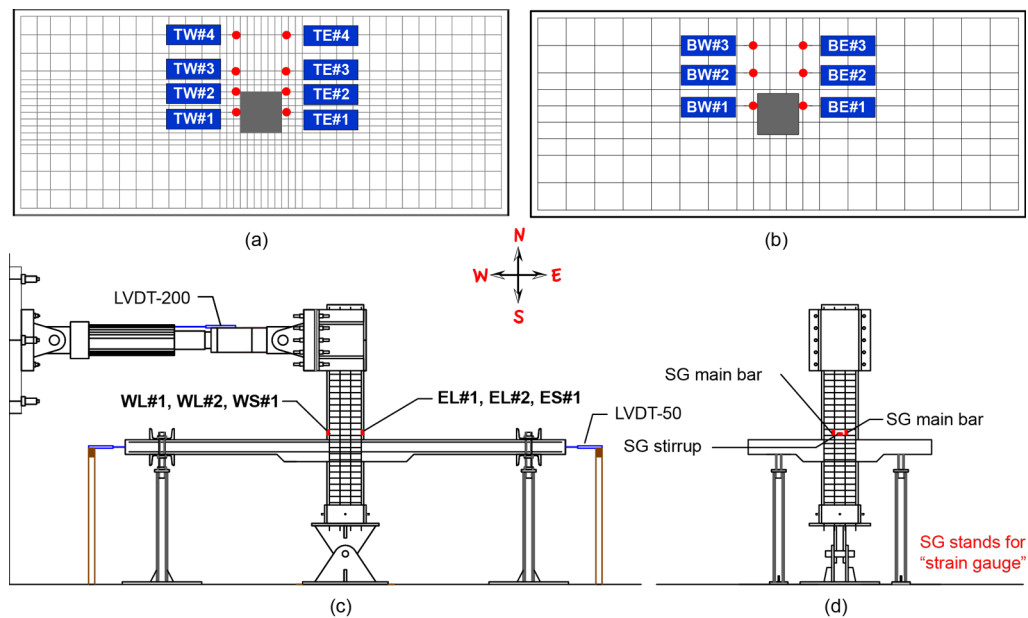


**Figure 3.15** Location of strain gauges and LVDTs: (a) strain gauges at top slab reinforcing bars; (b) strain gauges at bottom slab reinforcing bars; (c) strain gauges of column and LVDTs seen from longitudinal direction; (d) strain gauges of column observed from transversal direction.

the actual location in the critical region, while #3 and #4 refer to the position with respect to effective slab width and column strip. For column, a total of 6 strain gauges were used consisting of 4 strain gauges placed on the longitudinal reinforcing bars and other 2 strain gauges for column stirrup. These gauges were attached at the location where the negative moments occur. **Figure 3.15(c)** and **Figure 3.15(d)** provide the illustration of the gauges' actual location. For the style of abbreviation, the gauges in the column are labelled with four characters, for instance, WL#1 stands for "West Longitudinal #1", WS#1 symbolises "West Stirrup #1".

To measure the displacement occurred during the course of loading, 3 LVDTs were used in the specimen where their locations can also be seen in **Figure 3.15(c)**. Horizontal displacements of the column tip were acquired with one LVDT placed on the hydraulic actuator parallel to the location of the stroke. Two LVDTs in the both edges of the slab were also installed to give a better control of slab movement.

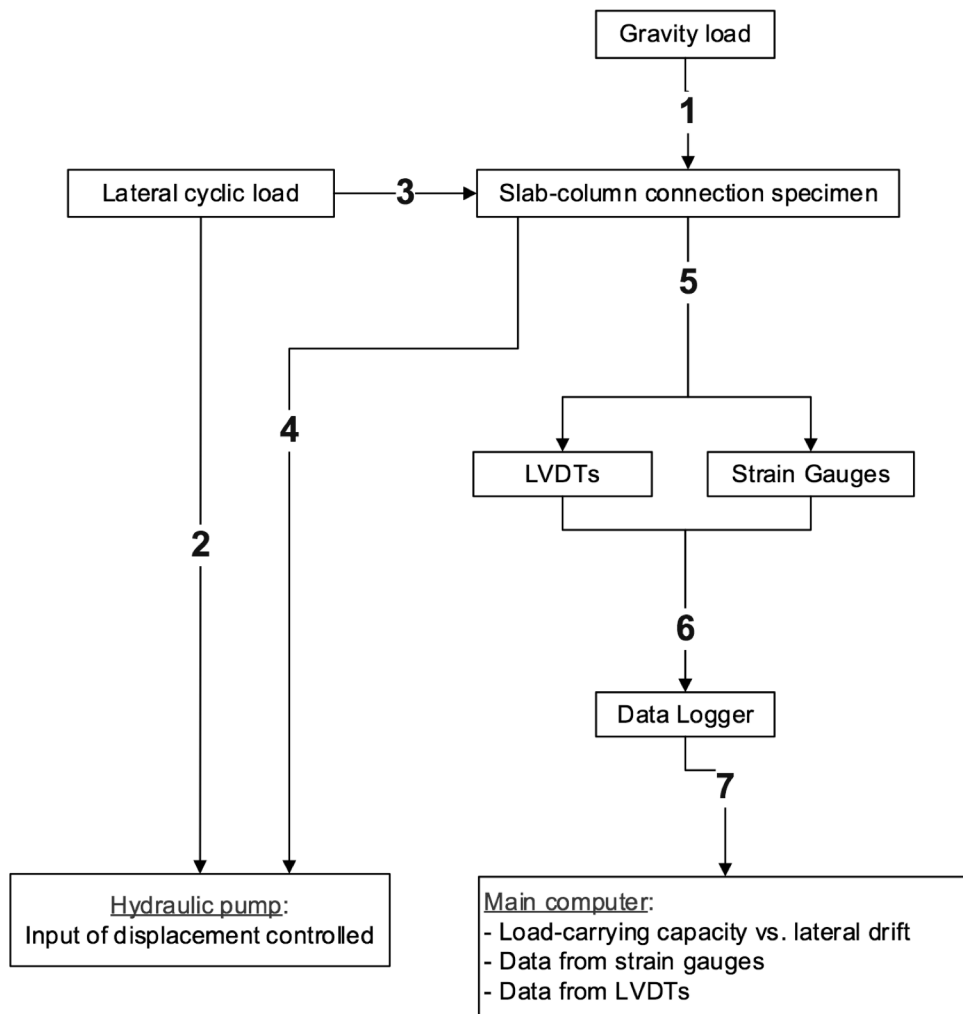


**Figure 3.16** Scheme of experimental test and data acquisitions.

### 3.9. Monitoring and Data Acquisition

Scheme of monitoring and data acquisition used in this study to provide the results from the experimental test is illustrated in **Figure 3.16**. One main computer was employed to connect the instrumentations as well as to monitor the data output during the testing. As having two connectors, the hydraulic actuator was connected to the hydraulic pump and main computer. By mean of this, one cable connected to the hydraulic pump was used to proceed the displacement controlled sequences during the testing process while another cable connected to the main computer was used to record the actual load capacity of the load cell in the hydraulic actuator. All mounted strain gauges and linear variable displacement transducer (LVDT) were

also connected to data logger while the cable from data logger was plugged in to the main computer.

### **3.10. Evaluation of Test Results**

The evaluation of the behavioural response of slab-column connection was addressed using the data from experimental tests. This was done to provide the relevant information with regard to the emphasis on this research. Additionally, the evaluation was also done to assess the acceptance criteria of the specimen in relation to the minimum requirements specified in ACI 374.1-05. Some aspects of evaluation that become the main considerations of this research are briefly discussed as follows:

*a) Crack pattern*

The evolution of cracks in the critical region of slab adjacent to the column face due to combined gravity and the lateral load is pronounced. This crack progression, known as the crack pattern, is also justified as an initial indication of the difference in response of specimen. The progression of crack up to crack tip is seen in the last cycle of loading course. This also indicates the tendency of the crack path as the load is being applied to the specimen.

*b) Strain of reinforcing bars*

Point-based strain gauges, placed on the several locations on the reinforcing bars, are used to give an idea when and if the reinforcing bars have yielded. Moreover, the relationship between load and strain is also addressed to monitor the behaviour of reinforcing bars.

*c) Load-drift relationship*

The relationship of lateral load-carrying capacity and drift ratio, termed as hysteretic curve, is presented as the main concern of this study to evaluate the behavioural response of the specimen with regard to initial stiffness, stiffness degradation, strength degradation, behaviour of strong column/weak beam, and energy dissipation as specified in ACI 374.1-05.

*d) Relationship of gravity shear ratio and drift ratio*

The response of gravity shear ratio versus drift capacity is discussed. It should be noted that it is one of the profound factors which needs to be considered

on a scale of design. Referring to the previous studies, the influence of intermediate gravity shear ratio indeed affects the performance of the slab-column connection to sustain lateral load and thereby leading to the poor capacity of drift ratio. Since the present study proposed a new type of cement based fibrous material, the need to assess this such behaviour is imperative.

*This page intentionally left blank*

## CHAPTER 4

### EXPERIMENTAL RESULTS AND DISCUSSION

Results from the experimental tests for all specimens labelled as S1, S2, and S3, are discussed in this chapter. Each section will focus on a specific response of each specimen according to what has been collected from the instrumentations. Besides that, each specimen will also be reviewed independently to provide the in-depth understandings with regard to their behaviour as well as their comparison from one to another. For the purpose of discussion, all figures and tables are initially analysed and presented toward the end of this chapter. Also, to give more clear statements, the related slab-column specimen is classified according to their labels namely specimen S1, S2, and S3 respectively.

**Table 4.1** Specimen test data summary

Test results of specimen	S1	S2	S3
Gravity shear ratio ( $V_g/A_c$ )/ $v_n$	0.08	0.05	0.25
Maximum positive horizontal load, kN	56.54	114.68	106.70
Maximum negative horizontal load, kN	-69.57	-114.30	-104.33
Positive drift at maximum horizontal load, %	2.8	4.0	3.5
Negative drift at maximum horizontal load, %	-2.8	-4.0	-3.5
Maximum drift attained before failure, %	3.5	N/A	4
Type of failure	Flexure	Flexure	Flexure

#### 4.1. Load-Drift Relationship and Cracking Behaviour

The load-drift relationship and cracking behaviour of all specimens are presented in **Figure 4.1** to **Figure 4.3** with the maximum lateral load-carrying capacity and drift level in both directions summarised in **Table 4.1**. Additional

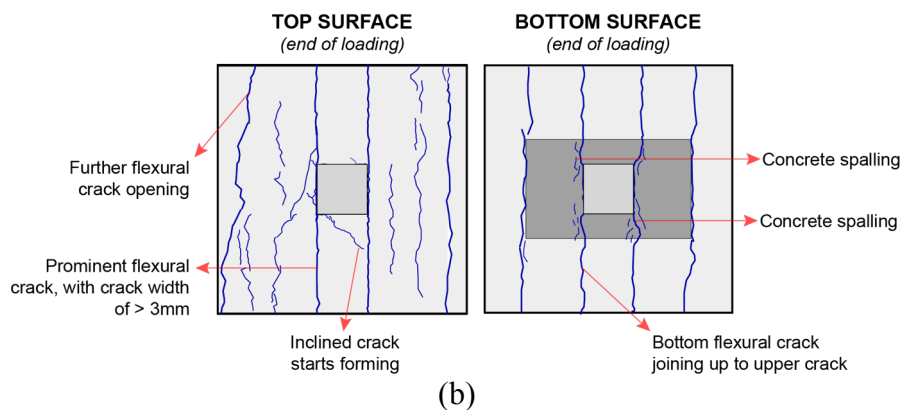
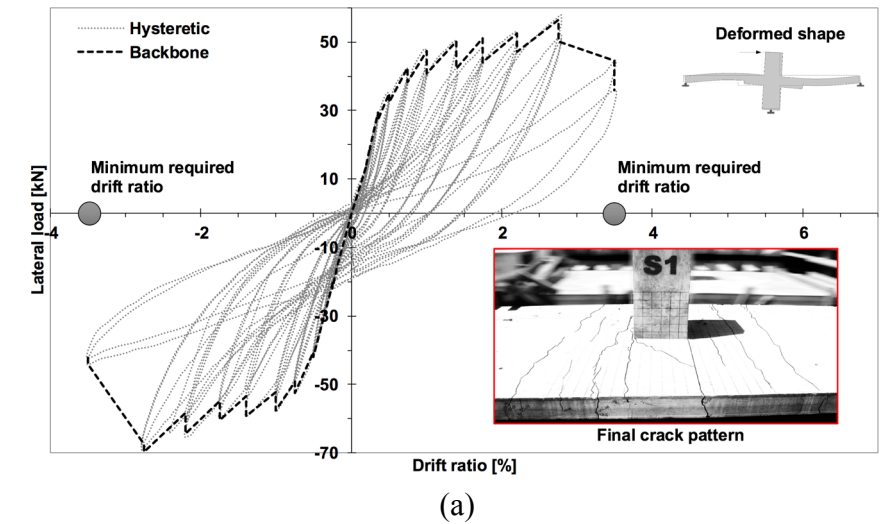


**Figure 4.1** Load-drift relationship of specimen S1: (a) hysteretic behaviour with additional photo of final crack pattern, (b) traditional hand-drawn crack pattern observed on the top and bottom surface of the slab.

information concerning the failure mechanisms of all specimens is also recapped in the same table. To make it easier when identifying the location of cracks, the principal directions of cyclic lateral load are defined by the positive and negative value of lateral load corresponding to East and West side respectively.

### Specimen S1

Shown in **Figure 4.1(a)**, the load-drift relationship, otherwise known as the hysteretic curve, generally indicates the phenomenon to what is termed as pinching effect. It is proven that there is a noticeable decrease of stiffness in each cycle from both loading-unloading and reloading condition. This occurrence can also be

identified with the tiny area inside the loop apparent in each cycle. In addition to that, it is also spotted that during the second and third cycle of the loading phase, the loss of lateral capacity is evident followed by the slight reduction in lateral stiffness. When the load level has reached the certain value, the significant drop of lateral stiffness is notable thereby causing the specimen response to deviate from linearity.

Using the backbone curve as provided in **Figure 4.1(a)**, the load-drift relationship of specimen S1 can be divided into three main stages:

- (i) an initial region where the response is linear;
- (ii) a transitional region at the load level of approximately 33.1 kN where the specimen behaves in inelastic response.
- (iii) another descending curve with the decrease of lateral load-carrying capacity at the drift ratio of 3.5%.

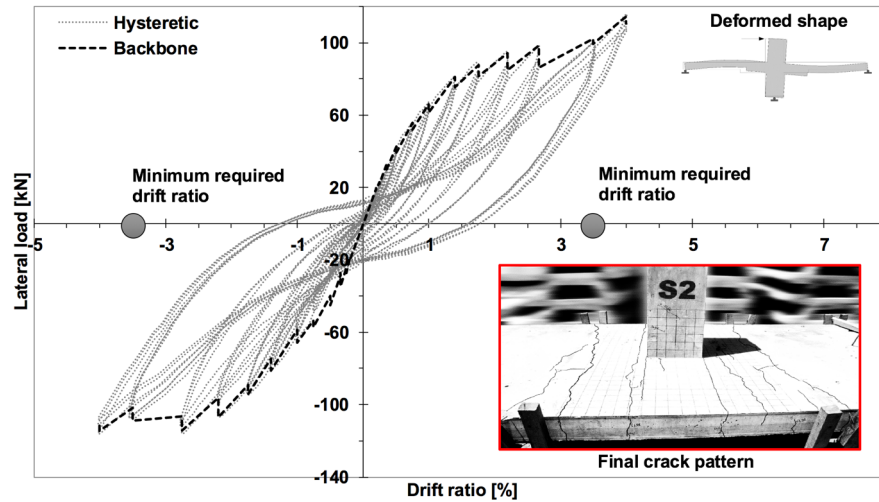
At the end of the loading phase, this specimen relatively achieves the minimum requirement of drift ratio though it seems to be evident that the strength degradation does occur in the specimen.

To provide insights into the full behaviour of the related specimen, the observation concerning the cracking behaviour is discussed herein. Before applying the cyclic lateral load, the gravity load was given by stressing four high grade wire strands from underneath the strong floor. At the end of the loading, it was observed that there was no visible crack occurred in the specimen S1, particularly on the critical section or close to the peripheral line between the column face and the slab. Once the gravity load remained constant, reversed cyclic lateral load was then given with the initial displacement rate of 0.03 mm/sec. During testing, it was spotted that the first cracks appeared at ~0.25% drift ratio. These cracks transpired on the critical perimeter around the slab-column connection, specifically on the top and bottom surface of the plate, representing the East and West side respectively. These visible crack bands are associated with flexural cracks since the path is perpendicular to the loading direction. When the loading was reversed, the new flexural cracks formed reversely on the top surface of the slab in West side and the bottom surface in East side at the same time. As the cyclic lateral load continued to increase, the new formation of flexural cracks was apparent where these cracks impeccably

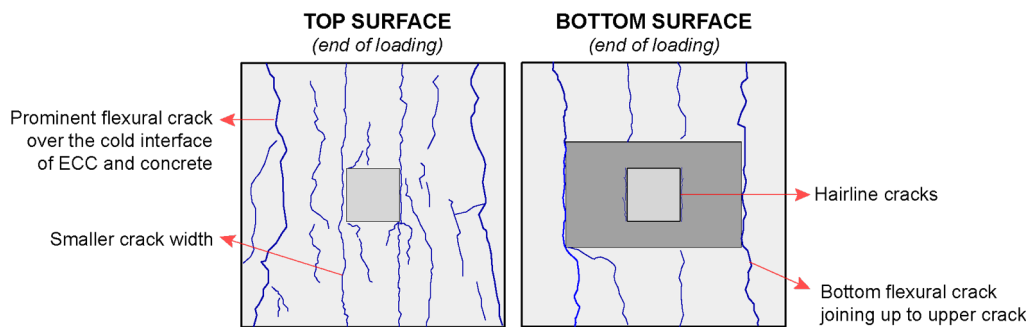
propagated beyond its critical section toward the slab edge and increased in width, causing the slab thickness to undergo the vertical cracks. In addition to that, as the load further increased beyond its yielding point, additional flexural cracks also formed outside the region of critical perimeter but still within the column strip. It was suspected that noticeable jump in the crack widths during the cracking process occurred when the longitudinal reinforcing bars had yielded already. It was also of interest to note that there was no visible sign of diagonal crack formation occurred in the commencement of nonlinear regime, ceasing the tendency of punching shear response. On top of that, when the load in excess the yield capacity (viz. 55 kN) or more like in the post-peak response with drift level of 3.5%, it was interesting to note that the load had passed the maximum capacity and dropped to 29% averagely in both directions, the latter being due to the spalling of concrete occurred on the underside surface of drop panel. At the same time, it was also sighted that other flexural cracks over the critical section displayed a more discernible increase in crack widths (see **Figure 4.1(b)**). During the observation throughout the test, it was proven that flexural cracks were formed in the critical region near the column face and drop panel. This then indicates that the specimen had the tendency to reach its flexural capacity in advance of punching shear failure.

## **Specimen S2**

The load-drift relationship of specimen S2 is similar, in many respects, to specimen S1 discussed earlier, with the exception that specimen S2 has not experienced strength degradation throughout the loading process up to 4.0% drift ratio (see **Figure 4.2(a)**). In addition to that, it is shown that the behavioural response of specimen S2 is strongly affected by the presence of ECC material, leading to significant increase in lateral load capacity nearly twice higher compared to specimen S1. It is also evident that the influence of micromechanical properties, as well as the orientation of randomly dispersed fibres, can indeed alleviate the tendency to generate major pinching effect thereby leading to more stable and higher energy dissipation. Referring to backbone curve in the same figure, it is noticed that in the commencement of lateral loading, specimen initially undergoes of what is typically presumed as linear-elastic behaviour up to load level of 58 kN



(a)



(b)

**Figure 4.2** Load-drift relationship of specimen S2: (a) hysteretic behaviour with additional photo of final crack pattern, (b) traditional hand-drawn crack pattern observed on the top and bottom surface of the slab.

which is also corresponded to 0.75% drift ratio. As the loading increases, the first linear gradient changes gradually thereby causing the change in lateral stiffness as well. This situation is related to what is typically called as nonlinear response where the specimen exhibits inelastic behaviour when reaching the post-yielding zone. Over this circumstance, the progression of structural cracks is susceptible because the reinforcing bars have yielded thereby causing the specimen to undergo the phenomenon to what is known as the tensile cracking of concrete. It is important to mention that during testing, the loading was stopped at the drift ratio of 4.0% due to the technical issue; therefore, the degradation in regard to the lateral load capacity cannot be observed.

To give in-depth discernments into the full behaviour of specimen S2 in relation to cracking behaviour, the final crack patterns from the traditional hand-drawn crack observations, also shown in **Figure 4.2(b)**, is discussed herein according to its sequential process. Prior to subjecting the specimen to the cyclic lateral load, the gravity load was firstly applied to the slab using the same method as the control specimen. At the end of the loading, it was evident that crack was not yet to occur in the specimen, particularly in the critical area around the connection. As the cyclic lateral load was then given to the specimen with the displacement rate of 0.03 mm/sec, the first visible cracks occurred in the specimen nearby connection at  $\sim 0.5\%$  drift ratio. Based on this sign, it is clearly implied that specimen S2 gives the proper response to resist the prominent cracks grow by maintaining the steady and minor progression of the crack opening in the linear region up to post-cracking zone. Nevertheless, some micro cracks might be susceptible to have been taken place during the increment of drift level up to  $\sim 0.25\%$ , but they were just not visible to be observed with naked eyes. In other words, it can also be said that specimen S2 gives the better cracking behaviour than the control specimen due to latter cracks showing up in the higher drift level than in the control specimen whereby the first discernible cracks appeared under the drift ratio of  $\sim 0.5\%$ .

As the loading progressed, the formation of closed-space orthogonal cracks began to increase, resulting in the extension of cracks tip. It was of interest to note that the flexural cracks initially developed on the top surface of the slab across the negative moment section adjacent to column face in East side. At the same time, the flexural cracks also progressed on the bottom of the slab on the opposite face associated with West side. When the lateral load was reversed, these cracks were evidently closed, and other additional yet similar cracks in the opposite direction opened, causing the flexural cracks to appear on the bottom surface of the slab in East side as well as the top surface of the slab in West side. As the lateral load further increased beyond its yielding zone, the localised crack bands, both in width and length, developed and propagated toward the edge of the slab, triggering the vertical crack formations in the slab thickness as both cracks on the top and underside face merged. It was also sighted that additional structural cracks inclined to grow in the interface between local thickening and plate. Most likely, it seemed

that cracks preferred to find the weak spot to control their progression over the specimen thereby resulting in the nearly-equal crack strips with ones showed in the critical zone around the joint. Throughout the loading process, it was visibly observed that more cracks occurred on the top surface of the slab rather than on the bottom surface. On top of that, it was also evident that the formation of new crack bands only occurred during the first cycle of loading and nurtured as the loading increased. Not only that, the formation of cracks was extensively affected by the influence of fibres-matrix interaction to bridge the cracks in advance of fibres rupturing.

### **Specimen S3**

Without repeating all the details, the response of specimen S3 is very similar, in many respects, to the other specimens discussed previously. The only exception is that this specimen tends to undergo more pinching effect and less stable response due to the influence of intermediate gravity shear ratio. Shown in **Figure 4.3(a)**, the lateral load capacity in the negative direction is somewhat lower than in the positive direction. This indication is susceptibly caused by the influence of dominant flexural moment due to gravity load. In a certain drift level when the specimen is subjected to the lateral load, the summation of gravity and lateral load can induce the significant flexural moment at one side of the slab. As the load being reversed, the flexural moment on the opposite side is reduced. This phenomenon can also be associated in regard to what is called as the effect of prominent crack evolution. This means, in general, when cracks begin to form in the positive loading direction, the negative lateral load capacity cannot be fully achieved the same as the lateral load in the positive direction because the previous cracks have resulted in the reduction of lateral stiffness. Regardless of this condition, however, the lateral load capacity of specimen S3 is still much higher than the control specimen. This condition is highly driven by the influence of ECC material to accommodate better behavioural response while maintaining constant and tight crack widths. Despite being subjected to intermediate gravity shear ratio; the specimen is still capable of reaching the minimum required drift ratio of 3.5% without experiencing the degradation in lateral load capacity.

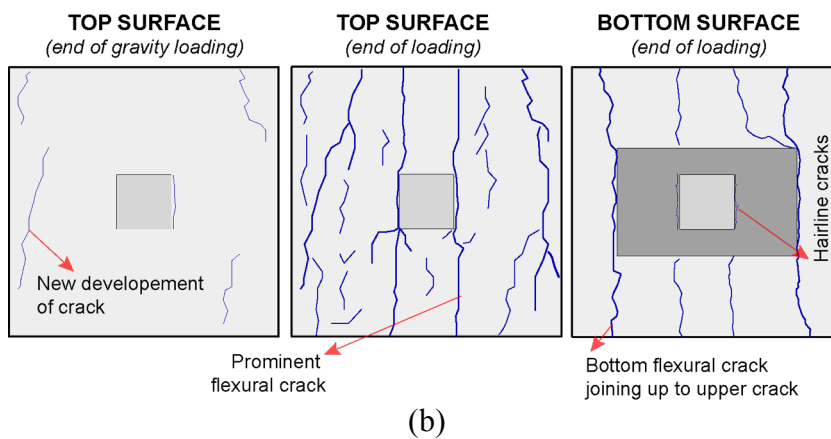
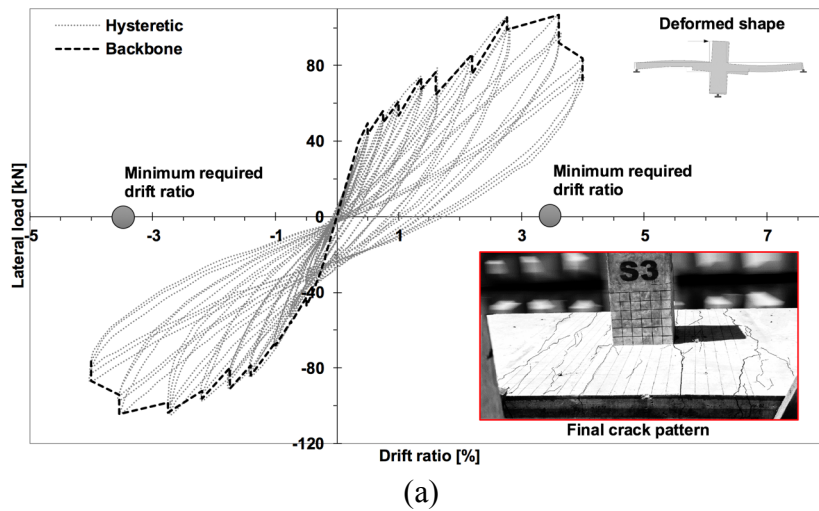


**Figure 4.3** Load-drift relationship of specimen S3: (a) hysteretic behaviour with additional photo of final crack pattern, (b) traditional hand-drawn crack pattern observed on the top and bottom surface of the slab.

In relation to crack progression during the course of testing, **Figure 4.3(b)** shows the crack evolution in the final sequence of the test located on the top-bottom surface of the slab and slab thickness. Differ to other previous specimens, the formation of flexural cracks in the final sequence of gravity load was evident (see **Figure 4.3(b)**). This then indicates that the effect of intermediate gravity shear ratio can genuinely induce the early cracking progression. It was interesting to note that the initial formation of flexural cracks at this point only occurred significantly at the cold interface between normal concrete and ECC, while the area at the critical section was not affected by any noticeable cracks. At the beginning of the cyclic lateral load, the newly-forming crack was not yet to occur. As the loading increased,

the additional flexural cracks started to appear on the top surface near to column face at 0.25% drift ratio which was also accompanied by the development of new small cracks formation underside of the plate. As the loading further increased, other cracks also took place on the slab face followed by the progression of localised cracks which was noticed to form inside the critical region as well as in the cold interface between concrete and ECC. These localised cracks were identified by the increase in length and width. It was interesting to note that, through the loading sequence, more discernible crack width was factually transpired along the interface of concrete and ECC rather than within the critical area. It was also shown that these localised crack bands apparently propagated toward the slab edge, both on the top and bottom side, and merged two crack profiles up and down thereby causing the vertical cracks to occur on the slab thickness. Although the dominant nonlinearity was caused by the prominently-localised cracks, it was also shown that prior to experiencing this situation, tight cracks width observed along the slab surface were proven, meaning that ECC material can evidently lessen the damage around the connection of the specimen throughout the post-yielding zone without suffering concrete spalling up to drift ratio of 4.0%.

For the purpose of discussion, the general comparisons on the behaviour of all specimens are discussed herein, concerning the response under combined

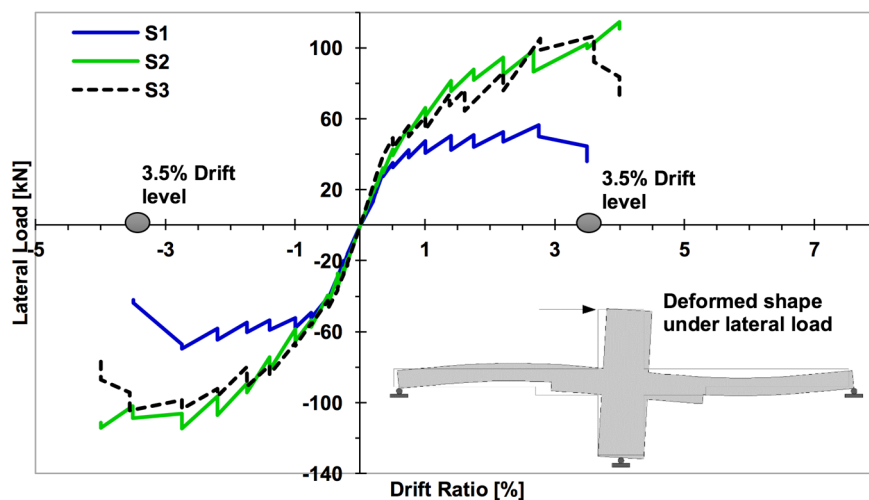


**Figure 4.4** Comparison of backbone (envelope) curves of all specimens in each cycle of the loading sequence.

gravity and cyclic lateral load. Presented in **Figure 4.4**, the comparison of backbone curves among the specimens clearly shows that specimen S2 has the greatest value in terms of lateral load capacity, while specimen S3 also exhibits in better lateral load capacity than specimen S1. Although having different performance, it is evident that all of these specimens still develop a discernible ductile plateau as indicated by the medium deflection prior to failure. This clearly signifies that slab flexural reinforcing bars must have been undergone the yielding response prior to concrete crushing thereby triggering the specimens to have sufficient nonlinear response. Through **Figure 4.4**, it is also seen that all specimens at least can achieve the minimum required drift ratio of 3.5% as specified in ACI to what is called as a standard of the earthquake-resistant structure. At this point, the response of the specimens is expected to behave in a ductile manner rather than a brittle behaviour under the earthquake loading – or even better, with the increase in strength. Considering all the above, it is also noticed that the influence of ECC as a replacement of conventional concrete apparently can lessen the damage level of the specimen as well as can maintain the steady and yet tight crack widths with a closely-spaced crack formation. However, at some point, it is important to realise that it might seem very tough to deal with intermediate gravity shear ratio since it was clearly shown in specimen S3 that the progression of numerous cracks was inevitable, therefore resulting in the tendency to undergo less stable response and notable pinching effect.

#### **4.2. Analytical Evaluation Based on Design Codes**

The analytical calculation in accordance with design provisions was undertaken to evaluate the shear stresses acting on the connection to each of the slab-column specimens. To determine these shear stresses, ACI Building Code is preferred as it presents decent information to find out whether the specimen exhibits the fail in punching or flexure. According to this code, the shear stresses are evaluated at the critical section around the slab-column joint with a distance of  $0.5d$  from the column face. Using this code, the shear stresses are calculated from the linear summation of direct shear stress  $V_u$  due to gravity load and a portion of the unbalanced moment  $M_u$  transferred as eccentric shear stress.

**Table 4.2** Analytical evaluation on the transfer mechanism of shear and moment flexure based on design specifications

Specimen (+ or -)	Unbalanced moment $M_u$ [kN.m]	Predicted direct shear force $V_g$ [kN]	Direct shear stress $v_g$ [Mpa]	Eccentric shear stress $\gamma_v M_u$ [kN.m]	Ultimate shear stress $v_u$ [Mpa]	Nominal shear stress of concrete $v_c$ [Mpa]	Nominal shear stress of fibre $v_f$ [Mpa]	Total nominal shear stress $v_n = v_c + v_f$ [Mpa]	Shear ratio $v_u/v_n$ [-]	Flexural portion of applied moment $\gamma_f M_u$ [kN.m]	moment capacity $c_2 + 3h$ $f_y$ $M_f$ [kN.m]	Moment ratio $c_2 + 3h$ $f_y$ $\gamma_f M_u/M_f$
(1)	(2)	(3)	(4)	(5)	(6)	(7)	(8)	(9)	(10)	(11)	(12)	(13)
S1+	98.9	54.6	0.37	0.84	1.21	2.29	0.00	2.29	0.53	59.4	37.35	1.59
S1-	-121.7	62.2	0.42	1.04	1.45	2.29	0.00	2.29	0.63	73.0	37.35	1.96
S2+	200.7	88.5	0.60	1.71	2.30	2.26	2.69	4.95	0.46	120.4	37.27	3.23
S2-	-200.0	88.3	0.59	1.70	2.30	2.26	2.69	4.95	0.46	120.0	37.27	3.22
S3+	186.7	131.5	0.89	1.59	2.47	2.39	2.77	5.16	0.48	112.0	37.57	2.98
S3-	-182.6	130.2	0.88	1.55	2.43	2.39	2.77	5.16	0.47	109.5	37.57	2.92

To provide more clear information regarding this matter, values and results for the peak lateral load, unbalanced moment, and shear stress around the critical perimeter for each specimen are summarised in **Table 4.2**. The first column in the relevant table contains the designation of the slab-column specimen. Each specimen has two rows: the first row lists the results for the peak lateral load in the positive direction, while the second row refers to the peak lateral load in the negative direction. The second column is the total unbalanced moment transferred between the slab and the column at peak lateral load. These values are calculated by multiplying the peak lateral load by the total height of the column (1750 mm). Column (3) lists the predicted direct shear force due to gravity load being carried by the specimen at the same time as the peak lateral load. These values are obtained by the mere numerical simulations using simple, yet applicable, structural software SAP2000 since the appropriate instrumentations were unavailable during the experimental test. In regard to the values from Column (3), the direct shear stress (Column (4)), uniformly distributed alongside the joint due to the constant gravity load, can be calculated by dividing the predicted shear force over the critical area of the connection ( $b_0 \times d$ ), where  $b_0$  is the critical perimeter of the slab-column connection, and  $d$  is the effective height of slab measured from the tensile (top) reinforcing bar to the compression surface (bottom) of the slab. The proportion of the unbalanced moment assumed to be transferred by eccentric shear stress is recapped in Column (5). This variable is utterly necessary to be considered as it can

govern the prominent shear transfer mechanism during the loading course if the specimen is suspected to undergo the punching shear failure.

In Column (6), the ultimate shear stress is the maximum shear stress acting on the critical perimeter due to the loading condition present during the application of the peak lateral load. Referring to **Equation (3.2)** in the previous chapter, these values are based on the linear shear stress distribution between Column (4) and Column (5). The nominal shear stress provided by concrete is listed in Column (7) where the value of each specimen is calculated using the formula from ACI Building Code as also mentioned in the previous chapter ( $v_c = 4\sqrt{f'_c}$ ). Since the slabs do not contain any shear reinforcement, the contribution of nominal shear stress due to stirrups is neglected; therefore, the nominal shear stress capacity of the specimen is ideally represented only by the concrete. However, this does not apply to the specimens that use distinct material properties such as ECC. Owing to this matter, the contribution of nominal shear stress due to fibres being cast all together with matrix material must be included along with the nominal shear stress provided by concrete (Column 8). Using the equation from JSCE specification, the nominal shear stress from fibres can be calculated (refer to **Equation 3.4**).

The ratio of the maximum shear stress induced by the loading condition at the peak lateral load to the nominal shear capacity of the connection is listed in Column (10). Generally, a value of more than 1.0 for the shear ratio indicates that the connection is more prone of the punching shear response where the formation of diagonal cracks appears over the surface of the slab, with the cracks extend in width and length. In Column (10), however, it is found that the ratio of shear stress in each of test specimens is not greater than 1.0, signifying the formation of diagonal shear crack is yet to occur during the similar loading condition.

Another scenario being associated with the slab-column connection is that it may also fail in flexure. Considering this fact, the ACI Building Code has specified the portion of the unbalanced moment carried by flexure,  $\gamma_f M_u$ , where  $\gamma_f = 1 - \gamma_v$ . These values have been calculated and are listed in Column (11) of **Table 4.2**. If this moment exceeds the flexural moment capacity  $M_f$  (Column (12)), then the specimen will fail in flexure. To find out in regard to this matter, Column (13) lists the moment ratio of the unbalanced moment being carried by the specimen in the

form of flexure to the nominal moment capacity of the slab within  $c + 3h$  where  $c$  is the column width, and  $h$  is the slab thickness. It is shown that the moment ratio of control specimen is greater than 1.0, owing to the fact that the failure is in flexure due to the majority of latter cracks being showed perpendicularly to the loading direction. When facing this circumstance, the specimen will fail first in flexure before punching shear dominate the damage. In addition to the control specimen, the moment ratio of specimen S2 and S3 is also beyond 1.0 but with much greater value. Given that these specimens indicate the majority of cracks are in the form of flexure with less punching shear cracks. This is also in correspondence with the formation of cracks occurred in the specimens S2 and S3 during the course of loading. Considering all the above statements that in general, when the slab-column specimen, designed to fail in flexure, is tested under cyclic lateral load, the initiation and formation of crack bands are in the form of flexure followed by the punching shear cracks after the specimen has achieved its full capacity.

#### **4.3. Connection Lateral Drift Capacity**

When considering the appropriate design of the flat slab structure, the limitation of lateral drift level must be taken into account in order to avoid the progressive punching failure. As demonstrated in the prior studies, the lateral drift capacity is dependent on the gravity shear ratio at the critical section; therefore, it is a necessity to provide such proper approximation when dealing with punching failure. Following this Pan and Moehle (1989) identified a limiting gravity shear ratio of 0.4 if the connection is desired to reach 1.5% drift level without punching shear failure. Hueste and Wight (1999) also formalised this relationship based on numerous test results from past research studies (**Figure 4.5**). For a gravity shear ratio less than 0.2, the connection is anticipated to exceed 4.0% lateral drift ratio without suffering punching shear failure. They also presumed that with gravity shear ratio of 0.4 and 1.0, the connection could sustain 1.5% and 0.5% lateral drift ratio respectively. When joining the points from these limitations using straight lines, the design drift limit proposed by Hueste and Wight results in the trilinear curve (see **Figure 4.5**). Concerning the use of conventional concrete in the reinforced flat slab structure, the trilinear curve proposed by Hueste and Wight

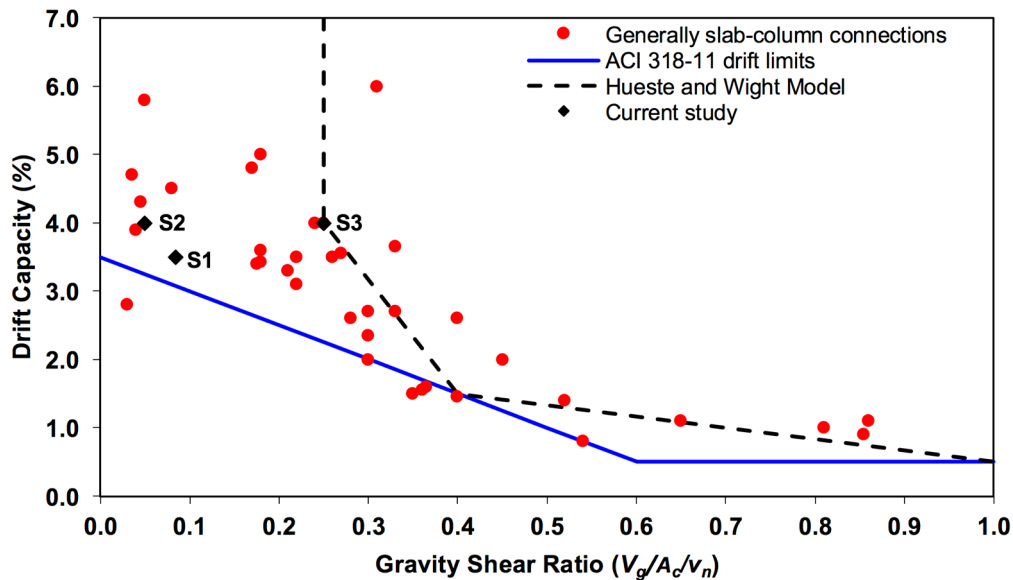


**Figure 4.5** Drift capacity versus gravity shear ratio of slab-column connections using drop panel with continued slab reinforcements.

gives a good approximation to the average results from the previous tests. This curve would also seem appropriate for the connections with continuity reinforcements to prevent the total slab collapse after punching shear dominates the failure mechanism. Besides this approximation, the ACI 318-14 also determines the drift limit of the flat slab structure needed to be considered to avoid the progressive collapse. The curve is in the form of the bilinear curve where the minimum required drift ratio is 3.5% and it is associated with zero gravity shear ratio. As the gravity shear ratio increases, the capacity of drift limit has a prone to decrease gradually up to the ratio of 0.6. After reaching this point, adding more gravity shear ratio has no effect on the reduction of lateral drift capacity by any means.

In correspondence to the peak lateral load from the test specimens, **Figure 4.5** also shows the plots of gravity shear ratio and lateral drift capacity, along with other test results from past research of reinforced concrete slab-column connections without the use of any shear reinforcement. Most of these test results were collected and compiled by Pan and Moehle (1989). Concerning the results of this present work, the specimen S1 somewhat suits the bilinear curve proposed by ACI thereby suggesting that the ACI design drift limit is impeccably accurate of predicting the

lateral drift capacity when using the conventional concrete. On the other hand, it is interesting to note that the ECC specimens exhibit higher lateral drift capacity and show a notable discrepancy with the proposed curves being plotted in the figure. It is clearly indicating that the compatibility of design drift limit by ACI 318 does not seem entirely fit with the results of ECC. It can be seen that more discernible gap occurs in specimen S3 where the design drift limit is highly underestimated the drift capacity obtained from ECC specimen.

#### **4.4. Evaluation of Acceptance Criteria**

As mentioned earlier in Chapter 2, the need to assess the integrity of structure to which members are imposed under earthquake loading is imperative where the structural behaviour must be in the inelastic response without having the sudden drop in strength capacity. In this regard, the evaluation of acceptance criteria for the earthquake-resistant structure is assessed throughout this section. The ACI Building Code 318 has specified the minimum requirement needed to be achieved for providing such better structure when appraising the structural toughness. Nevertheless, there are some contextual limitations specified in this design code as it cannot cover in detail for all the types of structure. Given that ACI Building Code 374.1-05 provides the more general requirement to deal with this matter when concerning the evaluation of performance criteria for the structural element. This assessment can be done through the research whether in experimental tests or analytical approaches. To provide greater detail regarding this matter, the criteria specified in the design codes are discussed in the following subsections to each of the slab-column specimens.

##### **4.4.1. Strength degradation**

The illustration in evaluating the feasibility with regard to the strength of each test specimen is presented in **Figure 4.6**, with a summary of the strength degradation for each of slab-column specimens listed in **Table 4.3**. It is shown that only specimen S1 suffers the degradation in strength towards the minimum drift ratio of 3.5% with value on the verge of load limit specified by ACI Code. Differ to control specimen, the specimen S2 does not even undergo such fettle, but the

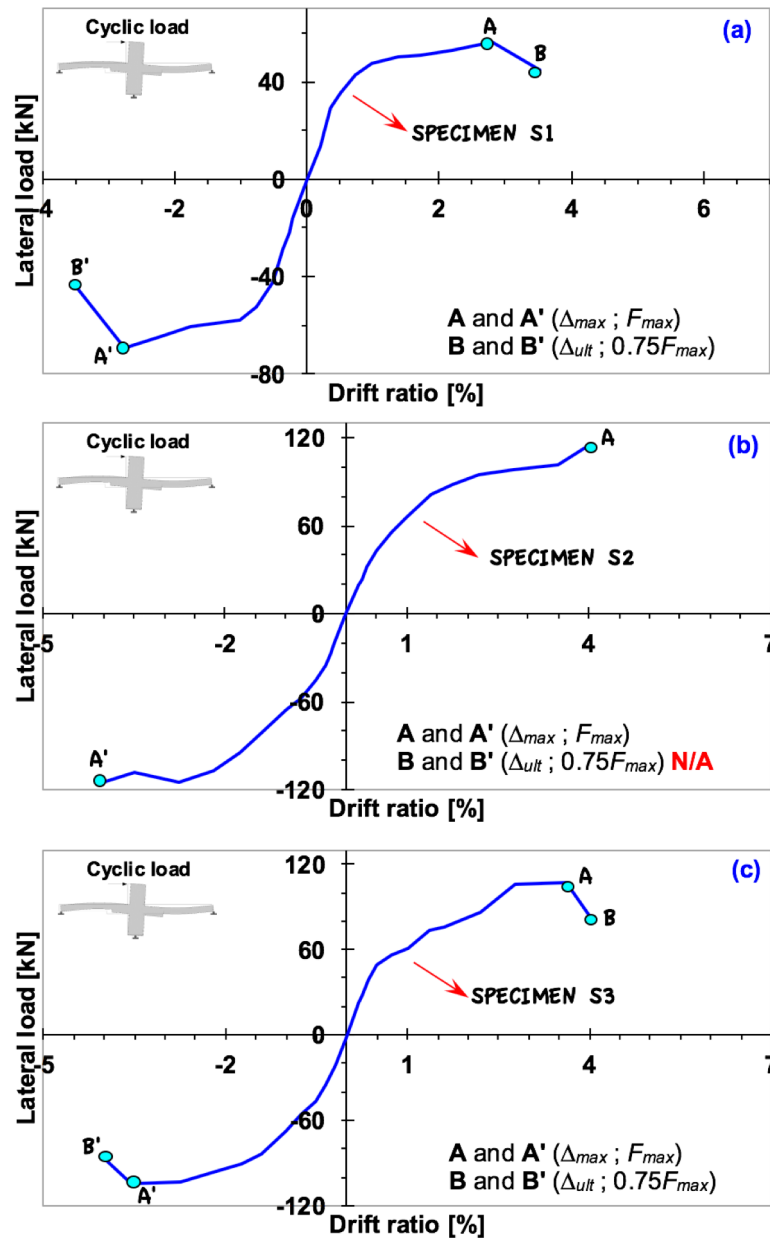


**Figure 4.6** Illustrated graph for defining the strength degradation for all specimens: (a) specimen S1, (b) specimen S2, (c) specimen S3.

lateral load still continues to increase along with the increment of drift ratio. For specimen S3, the strength degradation is apparent to occur when the lateral load has surpassed the 3.5% drift ratio. From what is encountered on this evaluation, it can be concluded that all test specimens have satisfied the requirement of having the sufficient strength as the value still in excess of  $0.75F_{max}$  particularly for control specimen.

**Table 4.3** Feasibility of strength degradation to each of test specimens

Specimen (+ or -)	Peak load, $F_{max}$ [kN]	Drift ratio at peak load, $\Delta_{max}$ [mm]	Ultimate load, $F_{ult}$ [kN]	Drift ratio at ultimate load, $\Delta_{ult}$ [mm]	Ratio of ultimate load and peak load $F_{ult} \geq 0.75F_{max}$
(1)	(2)	(3)	(4)	(5)	(6)
S1+	56.54	2.75	44.57	3.50	0.79
S1-	69.57	2.75	43.99	3.50	0.63
S2+	114.68	4.00	N/A	N/A	$> 0.75F_{max}$
S2-	114.30	4.00	N/A	N/A	$> 0.75F_{max}$
S3+	106.70	3.50	83.64	4.00	0.78
S3-	104.33	3.50	86.96	4.00	0.83

#### 4.4.2. Concept of strong column/weak beam

The concept of strong column/weak beam in the earthquake-resistant structure is mainly driven by the consideration to construct such proper structural system where the horizontal members, like beam or plate, must fail first before column. In order to let this concept work effectively, it is a necessity to attest that plastic hinge mechanism must occur in the slab rather than in the column. By plastic hinge, it means that the majority of cracking progression should be derived in the slab thereby allowing the slab to fail in advance of column member. In correspondence with this matter, ACI 374.1-05 has specified the minimum requirement need to be satisfied for ensuring that the structure has stronger column members. Given that the maximum lateral resistance  $F_{max}$  recorded in the test shall not have exceeded  $\lambda F_{exp}$ , where  $\lambda$  is the specified overstrength factor for the test column.

The evaluation of this criterion with respect to the test specimens in the present work is succinctly listed in **Table 4.4**. The first column denotes the labels to each of the slab-column specimens. Every specimen has two rows where each row is associated with the loading direction being applied to the specimen. The second column represents the nominal moment capacity for column  $M_{nc}$  obtained from PCACol. When performing the design analysis of column, the nominal moment capacity is normally calculated based on the equilibrium of axial forces and bending moments interaction in a balanced condition. However, as it takes quite

some time to proceed this method, the utilisation of the computational software is preferred to determine the value of nominal moment capacity. In Column (3) and (4), the probable moment strength  $M_{pr}$  occurred at the joint and column is listed respectively. The values are obtained using **Equation (4.1)** in accordance with ACI Building Code 318.

$$M_{pr} = 1.25 f_y A_s \left( d - \frac{a}{2} \right) \quad (4.1)$$

where  $M_{pr}$  is the probable moment strength,  $f_y$  is yield strength of reinforcing steel,  $A_s$  is area of reinforcing steel,  $d$  is slab effective height, and  $a$  is depth of equivalent rectangular stress block. The probable moment strength is calculated from conventional flexural theory considering the *as*-designed cross section using  $\phi=1.0$ , and assuming the reinforcement yield strength equals to or at least  $1.25f_y$ . In this present work, the probable moment strength is present to establish the slab-column joint strength as part of the capacity-design process. Since the design of this elements depends on the amount of flexural reinforcement, it is important to consider the proper use of reinforcing bars.

In Column (5), the overstrength factor of the column to each of test slab-column specimens is listed. The values are calculated by dividing the probable moment strength of column over the summation of the probable moment strength at joint. By summation, it means that the positive and negative probable moment strength are added altogether by neglecting the minus mark thereby resulting in the absolute value. When designing the column member, the value of overstrength factor shall not be less than 1.2 in order to govern the concept of strong column/weak beam thereby letting the horizontal member to fail in advance of the plastic hinge mechanism in the column. Column (6) and (7) present the respective results of the lateral resistance  $F_{exp}$  and peak lateral load  $F_{max}$  of the slab-column specimens observed from the experimental tests. The values of lateral resistance are obtained in correspondence with the yielding point to each of test specimens. In Column (8), the overstrength-lateral resistance of the slab-column specimens is also listed. To consider the response of strong column/weak beam in test specimens, it is important

**Table 4.4** Evaluation of strong column/weak beam to each of test specimens

Specimen (+ or -)	Nominal moment from PCACol, $M_{n,c}$ [kN-mm]	Probable moment at joint, $M_{pr,s}$ [kN-mm]	Probable moment at column, $M_{pr,c}$ [kN-mm]	Over strength factor, $\lambda$ [-]	Lateral resistance , $F_{exp}$ [kN]	Peak lateral load, $F_{max}$ [kN]	Over strength - lateral resistance, $\lambda F_{exp}$ [-]
(1)	(2)	(3)	(4)	(5)	(6)	(7)	(8)
S1+	73.38	57.27	28.64	2.56	29.50	56.54	75.59
S1-	73.38	57.27	28.64	2.56	36.70	69.57	94.04
S2+	73.38	58.15	29.08	2.52	55.60	114.6	140.32
S2-	73.38	58.15	29.08	2.52	59.50	114.3	150.16
S3+	73.38	58.32	29.16	2.52	47.20	106.7	118.78
S3-	73.38	58.32	29.16	2.52	45.30	104.3	113.99

to note that Column (7) should not be greater than Column (8). Given that from what is seen in **Table 4.4**, it is noticeably evident that all of the specimens meet the requirement. In relation to the visual observation during the course of testing, it was also found that indeed all three slab-column specimens did not exhibit prominent cracks formation on the column nearby slab face. It was spotted that there were only a number hairline cracks appeared, owing to the fact that column had not experienced the plastic hinge mechanism throughout the loading process.

#### 4.4.3. Initial stiffness

The test module is categorised as having an adequacy of initial stiffness if the lateral resistance is equal to or greater than nominal strength  $F_n$  before its drift ratio exceeds the value consistent with the allowable story drift limitation of the International Building Code. The allowable story drifts  $\Delta_a$  are specified in Table 1617.3 of IBC 2000. According to the relevant table, the allowable drift ratio for *risk category* I/II, III, and IV is 0.020, 0.015, and 0.010 respectively. The limiting initial drift ratio (LDR) consistent with  $\Delta_a$  is calculated by  $\Delta_a/\phi C_d h$ , where  $\phi$  is the strength reduction factor taken as 0.9. Since the flat slab structure is projected as special moment resisting frame and it is also associated with the dual system, the required displacement amplification factor  $C_d$  is taken as 5.5. Using the equation of

limiting initial drift ratio, the lateral resistance  $F_{LDR}$  or similar to  $F_{exp}$  for each *risk category* can be known.

**Table 4.5** presents the average value of two distinct loading directions being calculated to each of slab-column specimens. The first column lists the label of each specimen while the second column lists the designation of risk category being considered to each of test specimens. In Column (3), calculation of limiting initial drift ratio is also listed. Referring to the value of Column (3), the lateral resistance  $F_{IDL}$  can be known by plotting the value into the backbone curve to each of slab-column specimens. Column (4) presents the results of lateral resistance of each specimen. In Column (5), the nominal strength  $F_n$  is obtained by dividing nominal moment strength  $M_n$  over the total height of the column (1750 mm). This theory is derived from the simple equation for calculating the unbalanced moment using the lateral load from the experimental test (refer to the previous section).

Based on **Table 4.5**, it is clearly shown that all of the specimens only satisfy the minimum requirements of adequate initial stiffness in *risk category* I/II and III. In regard to ASCE specification, the proposed flat slab model has ideally achieved the acceptability to be constructed as special moment resisting frames for some types of building that represent a substantial hazard to human life in the event to failure such as education facilities (schools or universities) and apartments,

**Table 4.5** Ratio of lateral resistance and nominal strength for the evaluation of initial stiffness for all test specimens

Specimen	Seismic design category, <i>SDC</i> [-]	Limiting drift ratio, <i>LDR</i> [%]	Lateral resistance, $F_{LDR}$ [kN]	Nominal strength, $F_n$ [kN]	Ratio of $F_{LDR}$ over $F_n$ [-]
(1)	(2)	(3)	(4)	(5)	(6)
S1	I/II	0.4	29.01	21.34	1.36
	III	0.3	22.01	21.34	1.03
	IV	0.2	16.335	21.34	0.77
S2	I/II	0.4	34.80	21.30	1.63
	III	0.3	27.23	21.30	1.28
	IV	0.2	20.35	21.30	0.96
S3	I/II	0.4	35.48	21.47	1.65
	III	0.3	26.53	21.47	1.24
	IV	0.2	20.52	21.47	0.96

residential buildings, etc. However, as the specimens do not satisfy the adequate initial stiffness for *risk category IV*, it then implies that the proposed flat slab model according to the used geometry and reinforcement layouts is hence not suitable to be designated for essential facilities, including the emergency treatment facilities, the power-generating stations, and so on. It is worth mentioning that if the stiffness becomes too small around the initial response, the structure will be prone to large displacements for small lateral force changes following a major earthquake. To deal with this, there might be an alternative to increasing the initial stiffness of the proposed model. One such way can be done by increasing the thickness of the drop panel member or the slab element. However, further research must be carried out to understand the behavioural response of such prototype or model – considering the fact that increasing the thickness of slab member can provoke the tendency of structure to govern the dominant formation of punching shear cracks propagated alongside the critical perimeter around the connection, particularly when neglecting the use of any shear reinforcement.

#### **4.4.4. Stiffness degradation**

The profound consideration to determine the limitation of a structure having sufficient stiffness degradation in the earthquake-resistant structure is regarded important as the structure must possess the adequate residual stiffness when being subjected to high seismic loading (long period earthquake). At this point, it is anticipated that the structure still has the integrity to sustain gravity load though only by relying on the residual strength. In accordance with ACI Code, the evaluation of stiffness degradation in the test module is also associated with *secant stiffness*. The test module is considered to have the acceptable stiffness degradation if the ratio of the *secant stiffness* from a drift ratio of  $\pm 3.5\%$  over the initial drift ratio of  $\pm 0.35\%$  equals to or exceeds the value of 0.05. The stiffness at 3.5% drift ratio is calculated by referring to the illustration from **Figure 4.7** to each of slab-column specimens. In general term, the stiffness in the loading direction is depicted as a slope from point *A* to *A'*, while the stiffness in the reversed loading direction is portrayed as a slope from point *B* to *B'*. Point *C* and *D* respectively denotes the initial drift ratio of -0.35% and +0.35%. **Table 4.6** summarised the evaluation of

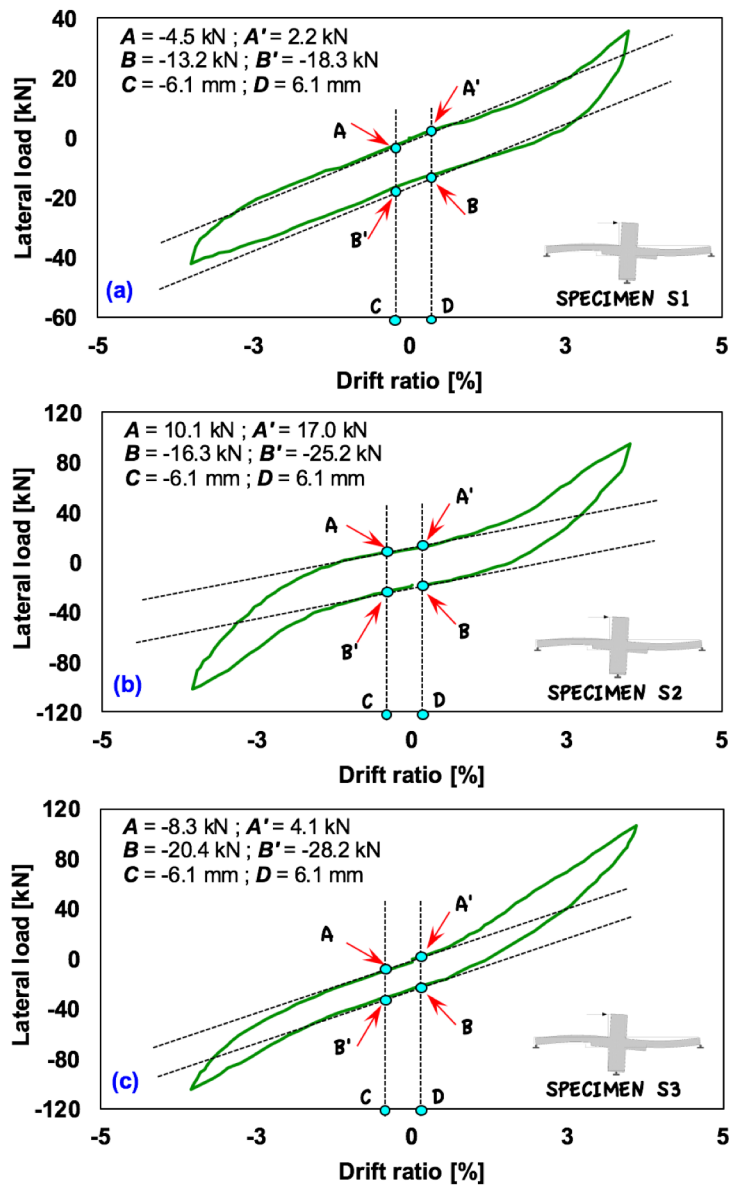


**Figure 4.7** Illustrated graph for describing the stiffness degradation for all specimens: (a) specimen S1, (b) specimen S2, (c) specimen S3.

stiffness degradation owned by each specimen both in positive and negative directions. From what is seen in **Table 4.6**, it is evident that all specimens have the adequacy of the stiffness degradation up to 3.5% drift ratio. It is then indicated that the utilisation of drop panel as the supplementary element can maintain the integrity of structure when being subjected to the cyclic lateral load. Not only does it provide the sufficient initial stiffness but also it alleviates the degradation of the lateral stiffness during the increase of lateral load.

**Table 4.6** Adequacy of stiffness degradation of all test specimens

Specimen (+ or -)	Initial drift [mm]	Initial load [kN]	Initial stiffness, $K_o$ [kN/mm]	Secant drift at 3.5% [mm]	Secant load at 3.5% [kN]	Secant stiffness at 3.5%, $K'$ [kN/mm]	Ratio of $K'$ over $K_o$ [-]
(1)	(2)	(3)	(4)	(5)	(6)	(7)	(8)
S1+	3.53	13.52	3.83	12.26	6.70	0.55	0.14
S1-	3.63	16.34	4.50	12.26	5.10	0.42	0.09
S2+	3.50	19.35	5.53	12.26	6.90	0.56	0.10
S2-	3.50	20.35	5.81	12.26	8.90	0.73	0.12
S3+	3.50	22.31	6.37	12.26	12.40	1.01	0.16
S3-	3.50	21.45	6.13	12.26	7.80	0.64	0.10

#### 4.4.5. Energy dissipation

The energy dissipation of the reinforced concrete members is one the fundamental structural capacities that determine their earthquake resistance. It is found that the failure mechanism of reinforced concrete structures is not only dependent on the loading path and the history of crack formation, but it is also affected by the presence of relatively low energy dissipation during the seismic event. If the structural member has low energy dissipation, there may be inadequate damping of the structure. In addition to that, oscillation may also continue for a considerable time after an earthquake, producing low-cycle fatigue effects, and lateral displacements may become excessive. Given that it is regarded important to determine the minimum requirement of tolerable energy dissipation in the structural members when being subjected to seismic demands. For reinforced concrete structures designed to accommodate damage without collapse due to the seismic event, the input energy is dissipated through the hysteretic response of structural elements. Considering all the above, the ACI Code 374.1-05 has specified the required relative energy dissipation ratio where the value should not be less than 1/8. This relative energy dissipation is defined as the ratio of *actual* to *ideal* energy dissipated by test module during reversed cyclic response between given drift ratio limits. The *actual* energy dissipation is expressed as the area in the hysteretic loop per load cycle and can be calculated by referring to the **Equation (4.2)**.

$$E = \sum_{i=1}^n \left( \frac{F_i + F_{i+1}}{2} \right) \times \Delta_x \quad (4.2)$$

where:

- $E_n$  = *actual* energy dissipation in  $n$  increment of drift ratio  
 $\Delta_x$  = deviation of two displacements,  $x_{i+1} - x_i$   
 $F_i$  = lateral load at the beginning of incremental displacement  
 $F_{i+1}$  = lateral load at the end of incremental displacement

Presented in **Figure 4.8** to each of slab-column specimens, the *ideal* energy dissipation is defined as the area of the circumscribing parallelograms ABCD and DEFA in the elastoplastic condition during the third cycle of 3.5% drift ratio. These parallelograms are formed according to the following process:

- (i) the slope lines AB and CD are parallel to OA1, representing the initial stiffness in the positive direction (line AB for loading and CD for unloading);
- (ii) the slope lines FA and DE are parallel to OA2, depicting the initial stiffness in the negative direction (line DE for reversed loading and FA for unloading);
- (iii) lines BC and EF describe the peak lateral load in the loading and reversed loading condition respectively.

The evaluation of relative energy dissipation ratio to all slab-column specimens is concisely summarised in **Table 4.7**. It is evident that each of test specimens is eligible as the structure of having tolerable energy dissipation. In terms of providing a direct comparison, specimen S1 and S2 ideally represent the behavioural response of concrete and ECC as they have identical gravity shear ratio being carried by the specimen. From what is seen in **Table 4.7**, it is evident that specimen S2 has higher energy dissipation than control specimen. This phenomenon has also been presented in the prior research with regard to the performance of ECC material as a replacement of concrete in structural members, for instance, the research conducted by Fukuyama *et al.* (2000); therefore, it is not surprising if the ECC specimen could achieve a large amount of energy dissipation when being subjected to cyclic lateral loading. In addition to the justification from the past research, it is worth mentioning that energy dissipation is a cumulative

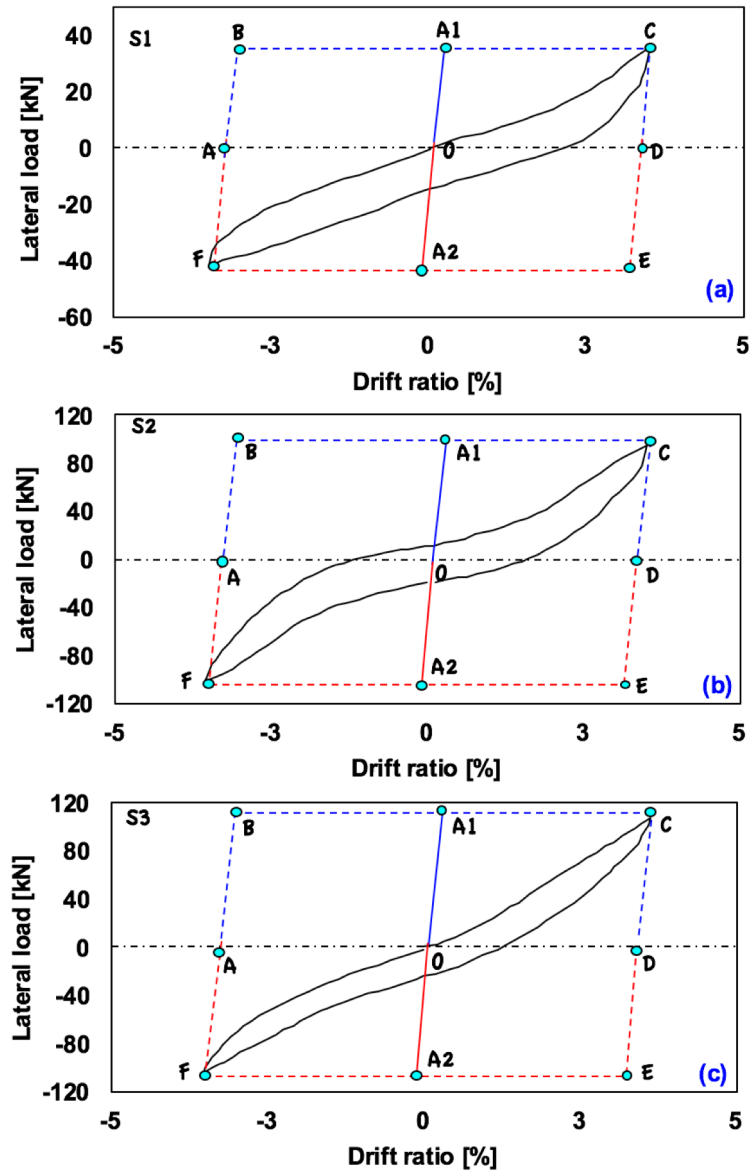


**Figure 4.8** Illustrated graph of the parallelogram of ideal energy dissipation for all specimens: (a) specimen S1, (b) specimen S2, (c) specimen S3.

function of the energy dissipated by concrete and reinforcing steel (longitudinal and stirrup). Thus, it does make sense if the influence of ECC has the important role in generating a large amount of energy dissipation due to its capability of exhibiting high tensile ductility. In spite of specimen S1 and S2, it is also interesting to note that although utilising ECC material, energy dissipation of specimen S3 is rather lower than control specimen. This phenomenon most likely arises due to the

**Table 4.7** Ratio of actual and ideal energy dissipation of all test specimens

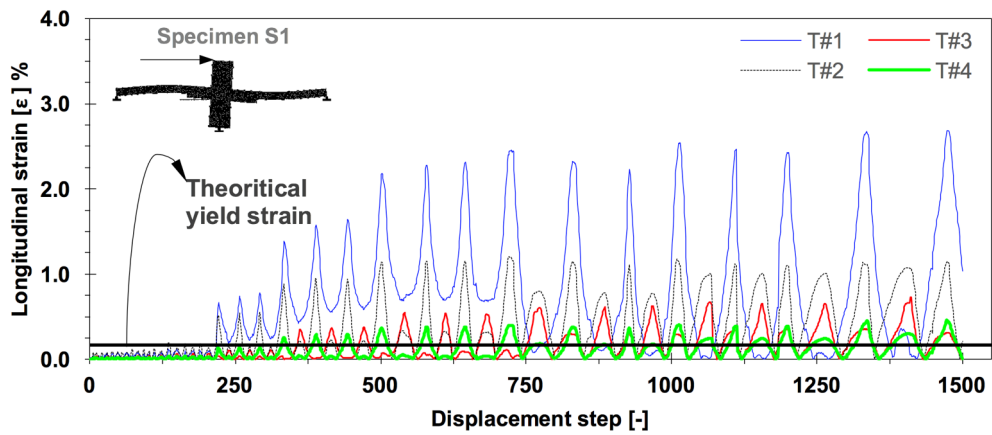
Specimen	Actual energy dissipation [·10 <sup>6</sup> N-mm]	Ideal energy dissipation [·10 <sup>6</sup> N-mm]			Ratio between actual and ideal energy dissipation [-]
		ABCD	DEFA	Total	
(1)	(2)	(3)	(4)	(5)	(6)
S1	1.37	3.74	4.45	8.18	0.17
S2	3.12	8.32	8.87	17.19	0.18
S3	3.37	11.64	11.16	22.79	0.15

presence of high gravity load being carried by specimen S3 compared to control specimen. As above-mentioned in the matter of intermediate gravity shear ratio, not only does it reduce the lateral load capacity, but it also generates less stable response thereby leading to more pinching effect in the hysteretic behaviour.

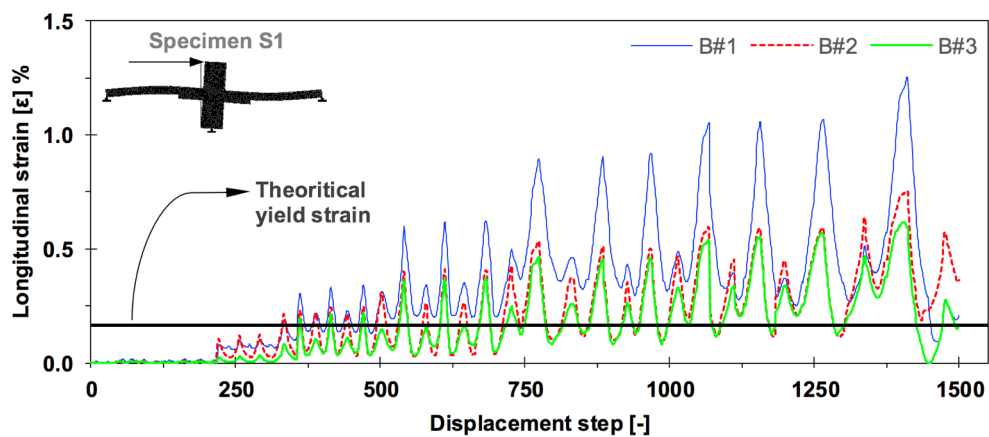
#### 4.5. Slab Flexural Reinforcement Strain Readings

The longitudinal strain of the reinforcement in the slab-column specimen was measured in the several distances of the plate to give an idea when and if the flexural bars have yielded. Typical foil strain gauge with the single element (FLA-2-11) was applied to all flexural bars since it is capable of recording the yield of reinforcement during the extension of gauge length which is also associated with the strain profile in reinforcement. The response of relevant strain gauge used in this experiment is presented in the figures and meticulously discoursed in accordance with the evolution of strain distribution during the displacement step. For the reason of delivering more insights when identifying the response of the gauges, each of slab-column specimens is distinctly presented in this section.

Prior to discussing the strain measured in the test specimens, it is worth mentioning that regardless the number of gauges being mounted on the slab adjacent to the two opposite sides of column face; however, only one side of the gauges is examined throughout this section for the purpose of discussion since both sides exhibit the identical response due to the lateral load being applied back and forth.



(a)



(b)

**Figure 4.9** Longitudinal strain profiles of specimen S1 measured in the slab reinforcing bars: (a) top reinforcing bars, (b) bottom reinforcing bars

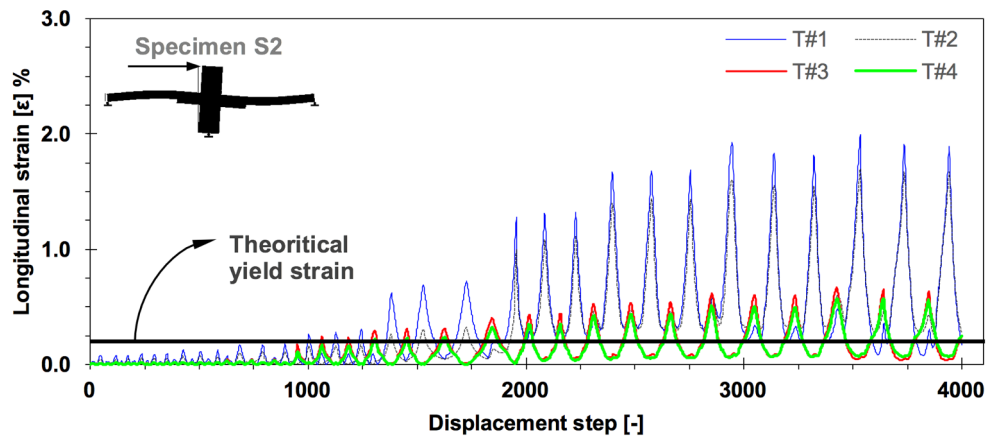
### Specimen S1

In this present work, the gauges labelled as T#1, T#2, T#3 and T#4 were applied to the several to flexural reinforcing bars in the slab such that they were located in the respective distance of 0, 120 mm, 240 mm, and 600 mm measured from the centre of the column (see **Figure 3.16(a)**). In addition to the top flexural bars, three gauges labelled as B#1, B#2, and B#3 were also mounted on the bottom reinforcing bars which they were placed separately in the distance of 60 mm, 300 mm, and 500 mm. To examine the response of the flexural bars during testing, the

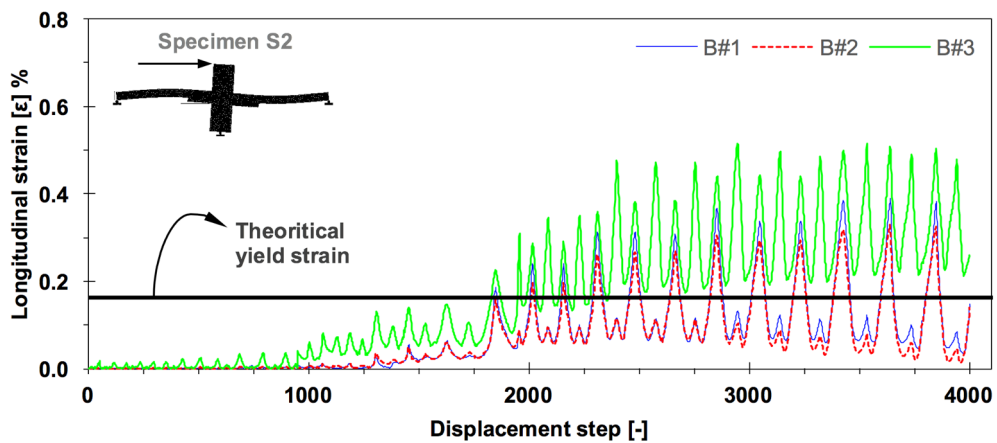
recorded strain profiles both in the top and bottom reinforcement are plotted in **Figure 4.9**. Analysing **Figure 4.9(a)**, it is evident that in the initial response of specimen S1, there are no signs of flexural yielding in any gauges. With the displacement step being increased, the onset of yielding is apparent in gauge T#1 by which is highlighted with a sudden jump in the strain profile around the displacement step 250 or in correspondence with 0.5% drift cycle. Similarly, the commencement of yielding in gauge T#2 is also apparent but with value rather smaller than T#1.

It is also spotted that the gauges T#3 and T#4 still remain in the elastic response at this stage. This clearly signifies that linearity response of the flexural bars begins to act around the joint area. This is also associated with the first formation of flexural cracks transpired at the peripheral line of the column face and slab. As the displacement increases around step 375, the large increase in strain profile of T#1 and T#2 is apparent indicating the noticeable crack opening during the post-cracking zone. It is at this stage where gauges T#3 and T#4 also gradually increase and somewhat have surpassed the theoretical yield strain level. Based on these readings, all of the flexural gauges have behaved in the nonlinear regime with the maximum strain of 2.65% recorded in the gauge T#1 at the final stage of loading while the values of other gauges are lower than T#1.

In addition to the top flexural reinforcing bars, the response of strain in the bottom reinforcement is also analysed. Presented in **Figure 4.9(b)**, it is evident that strain readings of B#1, B#2, and B#3 are relatively low during the initial response of the specimen. It is also spotted that when the top flexural bars showing the excess in yield strain level, the bottom reinforcements still remain elastic. This then implies that the significant increase of crack openings is mostly occurred at the top surface of the slab, while in the underside face, the specimen does not undergo such fettle. However, as the displacement being increased beyond step 375, all of the bottom gauges have slightly exceeded the theoretical strain yield thereby indicating that the response of bottom flexural bars is in the nonlinear regime. After reaching this point, the strain constantly increases towards the end of the step and results in the maximum strain of 1.23% occurred in the B#1.



(a)



(b)

**Figure 4.10** Longitudinal strain profiles of specimen S2 measured in the slab reinforcing bars: (a) top reinforcing bars, (b) bottom reinforcing bars

### Specimen S2

In specimen S2, the strain gauges placed on the top and bottom mat of the reinforcement were also distanced similar to control specimen. The strain profiles of these gauges are plotted in **Figure 4.10** showing the increment of the longitudinal strain both in the top and bottom reinforcement respectively. Presented in **Figure 4.10(a)**, during the early stage of loading, all top flexural reinforcements behave in the linear response due to the strain profiles have yet to exceed the theoretical yield strain level. It is also seen that beyond the distance of 120 mm from the centre of the column, the strain readings are relatively low indicating the insignificant

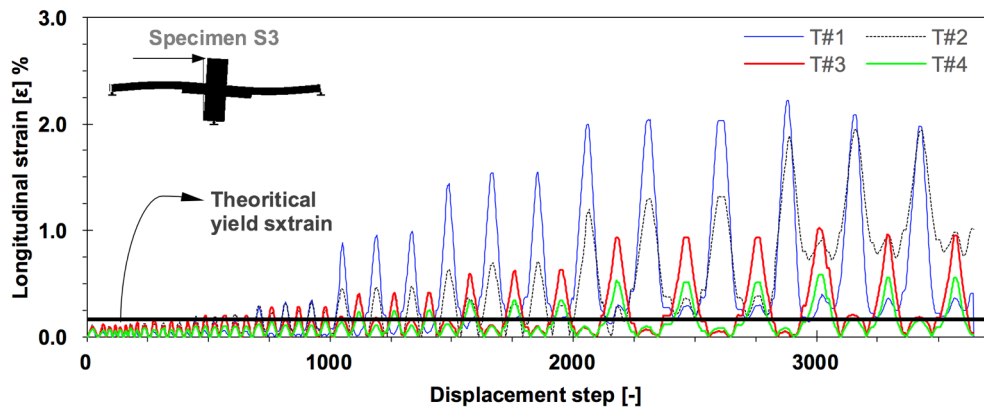
response of relevant flexural bars. As the displacement increases around the step 1250 (corresponding to 1.0% drift cycle), a large strain is apparent in gauge T#1 while T#2 and T#3 show a slight resemblance in terms of strain value. These three gauges have exceeded the theoretical yield level thereby signifying the commencement of flexural bars showing the nonlinear response. On the other hand, gauges T#4 still exhibits minor increase due to the strain value still under the yield level.

A second sudden jump is obvious on the gauge T#1 around the step 1500 followed by the similar condition to other three gauges. At this point, all of the gauges have indicated the nonlinear response. After reaching this point, each strain profile of top flexural bars constantly goes up with a maximum value 1.9%. In terms of providing the direct comparison to control specimen, it is clearly proven that the longitudinal strain value of specimen S2 is smaller than specimen S1. The underlying reason for this occurrence is driven by the micromechanical behaviour between fibre-matrix interaction within ECC thereby allowing the suppression of crack growth with the replacement of smaller cracks form. As a result, the strain readings of the reinforcing bar in ECC material are way smaller than in concrete.

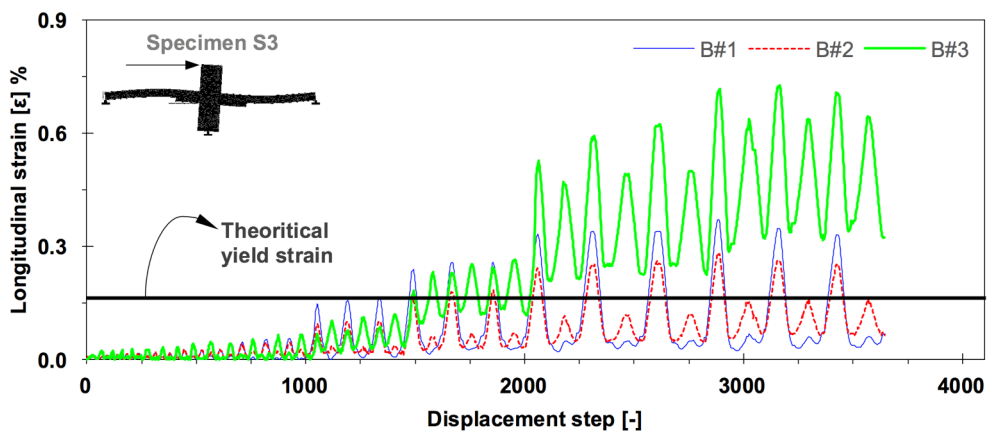
Apart from the response of top flexural bars, the development of strain profile in gauge B#1, B#2, and B#3 is relatively low, and they apparently remain constant under the linear elastic response before exceeding 1.0% drift cycle (see **Figure 4.10(b)**). It is worth mentioning that, at this point, the response of bottom reinforcement shows the delay with regard to the development of strain value due to top flexural bars has surpassed the yield level. With the displacement being increased ensuing the step 2000, the flexural yielding of all bottom reinforcement is apparent. It is of interest to note that the readings in gauge B#3 exhibits higher strain value than that of gauge B#1 and B#2. Needless to say that this condition is utterly associated with ECC material being used in the local thickening thereby allowing the suppression of crack growth.

### **Specimen S3**

The readings of gauges in specimen S3 is similar in many respect to specimen S2 but with higher strain value due to the application of intermediate gravity shear



(a)



(b)

**Figure 4.11** Longitudinal strain profiles of specimen S3 measured in the slab reinforcing bars: (a) top reinforcing bars, (b) bottom reinforcing bars

ratio where it is also associated with wider crack opening compared to specimen S2. Each response of the gauges in specimen S3 is plotted in **Figure 4.11**. During the commencement of displacement up to step 500, the response of the top flexural bars is linear elastic as the readings show the longitudinal strains still under the theoretical yield level (see **Figure 4.11(a)**). As the displacement slightly increases, the first sign of flexural yielding in the top reinforcing bars is apparent at step 750 indicating the strain readings from gauge T#1, T#2, and T#3 have somewhat exceeded the level of yield strain except for gauge T#4. In the displacement step 1000 (corresponding to drift ratio 0.75%), the notable jump in strain observed in gauge T#1 followed by the slight increase in strain value of T#2. This then indicates

that the gauges located close to the centre of the column or around critical section experience significant crack growth compared to those which are located outside the critical section. Throughout the loading course, it is seen that the recorded maximum strain in the top flexural bar is 2.2%. Following this, **Figure 4.11(b)** also shows the strain readings in bottom flexural bars. According to what is seen in the figure, the strain profiles of three bottom gauges are relatively low with the strains remain in linear elastic response in the displacement step ranging from 0 to 1750. It is also of interest to note that the bottom gauges show the delay in the development of strain compared to top gauges. In addition to that, it is also seen that the strain in gauge B#3 is way higher than gauge B#1 and B#2. The reason for this has been explained in the specimen S2 as it uses the same material constituents.

## CHAPTER 5

### FINITE ELEMENT ANALYSIS

This chapter presents the constitutive modelling of reinforced concrete and ECC slab-column connections using finite element software packages. Three distinct packages namely ABAQUS, SAP2000, and ZEUS-NL were used to facilitate direct comparisons of the experimental work in terms of overall results. In this chapter, each of software packages is presented in each section as work package, addressing the modelling techniques and the results. For the purpose of discussion, all figures are analysed toward the end of this chapter.

#### 5.1. Work Package 1 — ABAQUS

##### 5.1.1. Overview

Over the past few decades, the implementation of finite element software has gained popularity among practising engineers and researchers due to the capability of providing an efficient and valuable tool for analysis of complex structures. The use of finite element software does not only offer the substantial savings in the cost, time, and effort, but it also provides the comprehensive results, for example, the internal mechanisms of a structural model such as principal stress, plastic and logarithmic strain, and damage level. In certain finite element software, a feature of predicted crack pattern is also available. Considering its practical value,

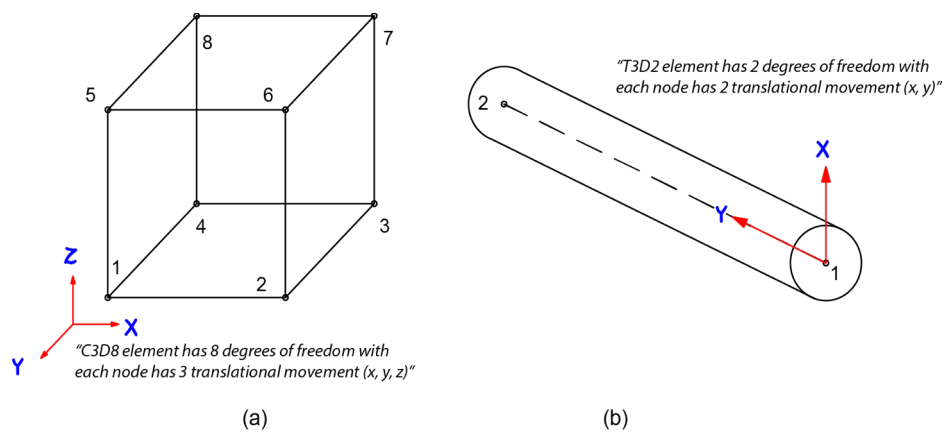


**Figure 5.1** Element types of FE model: (a) C3D8R linear brick element for concrete; (b) T3D2 truss element for reinforcement bars.

the nonlinear finite element analysis was then performed in this study. The results from numerical analysis were compared against the experimental data. A commercial software named ABAQUS was used as it provides wide-ranging nonlinear analysis for concrete and quasi-brittle material. In this study, the numerical model of slab-column connection was made in accordance with the actual geometry tested in the laboratory. Other parameters such as the properties of the material, the interaction of interface between elements, and the loading scenario were also defined based on what has been applied to the test specimen.

### **5.1.2. Element model**

Solid continuum C3D8R element was used for concrete and ECC as a form of the eight-nodal linear brick element. This element consists of three degrees of freedom in each node in the form of translational movement U1, U2, and U3 (see **Figure 5.1(a)**). C3D8R is also known as the isoperimetric element which is generally preferable to be used in modelling case as it offers faster convergence during the iteration process. In C3D8R element, the reduced integration (refer to the underlined letter), is preferred to be used for reducing the computation time in the nonlinear 3D analysis. As shown in **Figure 5.1(b)**, a two-node truss element (T3D2) with 3D wire was used to define the element of reinforcing steel in which this element was homogenised over the concrete. In T3D2, the two-node depicts two degrees of freedom consisting of compression and tension which the flexural moment is hence neglected. To account a perfect bond between solid concrete and reinforcement element, embedded constraint technique was adopted. In this case, the element of T3D2 was embedded inside the concrete thereby eliminating any transitional degree of freedom and slip of node as the reinforcing steel has merged with the concrete nodes.

### **5.1.3. Material properties**

In conventional concrete, the concrete damage plasticity (CDP) was chosen due to its characteristic to denote the strength and stiffness degradation of material in damage level of concrete. The CDP model is continuum, plasticity-based, damage model which is presumed that the main failure mechanisms consist of

tensile cracking and compressive crushing (Tambusay *et al.*, 2017). In general, the main concepts of continuum mechanics are effectuated to simulate the complex nonlinear behaviour of quasi-brittle material (*e.g.* concrete). In addition, the concepts of continuum mechanics are projected to provide a better prediction in relation to structural response for any type and level of loading. Not only from this perspective, but the concepts are also anticipated for assessing the nonlinear behaviour of the structural member(s) especially for high loads (*e.g.* earthquake and impact). With regard to the adequacy of adopting the concepts of continuum mechanics, CDP has also been assessed as one of the best models to represent the complex behaviour of concrete by implementing isotropic damaged elasticity in combination with isotropic compressive and tensile plasticity for accounting the inelastic behaviour.

As stated in ABAQUS manual book, the advantages of using CDP model are listed as follows:

- (i) It provides a general capability for modelling concrete and quasi-brittle materials in all types of structure (beams, truss, shells, solids, and so on).
- (ii) It uses concepts of isotropic damaged elasticity in combination with isotropic tensile and compressive plasticity to represent the inelastic behaviour of concrete.
- (iii) It consists of the combination of non-associated multi-hardening plasticity and scalar (isotropic) damage elasticity to describe the irreversible damage that occurs during the fracturing process.
- (iv) It allows user to control stiffness recovery effect during cyclic load reversals.
- (v) It can be used for plain concrete even though it is intended primarily for the analysis of reinforced concrete structures.
- (vi) It can be used with rebar to model the concrete reinforcement.
- (vii) It is suitable for monotonic, cyclic, and dynamic analysis, while in contrast smeared cracking concrete can only perform monotonic analysis, and brittle cracking concrete cannot be used for fibrous material.

In ABAQUS, parameters of concrete damage plasticity have been developed in a number of approaches. A wide range of studies has now been carried out to provide reliable equations regarding the purpose to generate a reasonable predicted

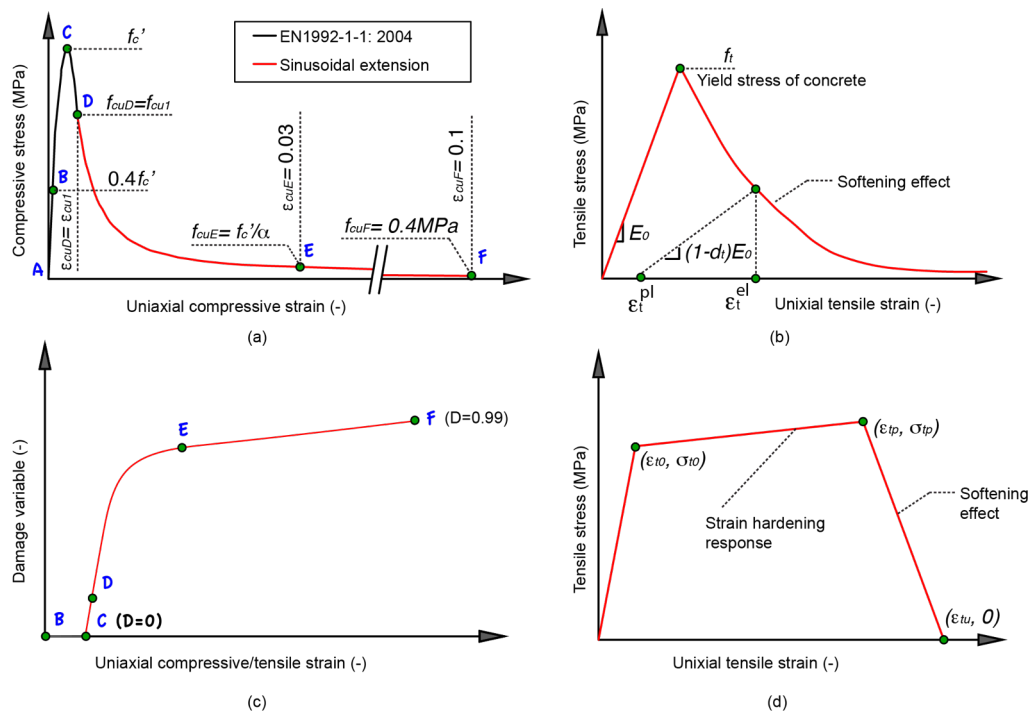


**Figure 5.2** Parameters of concrete damage plasticity model: (a) compressive response of concrete and ECC; (b) tensile response of concrete; (c) typical damage evolution of concrete and ECC; (d) tensile response of ECC.

results when compared against observed results from the experiment. Given that the need for examining material investigations, such as biaxial and triaxial tests, is not then necessary since the ready-made equations have now covered the results of such tests. In order to generate the graph of stress-strain relationship and damage criteria of concrete, the results from uniaxial compressive and tensile tests are well enough.

In this study, the linear equations in regard to CDP input were used according to what has been suggested in the manual book of ABAQUS. The important parameters in the linear region consist of concrete density, Young's modulus and Poisson's ratio of concrete. In the nonlinear region, input parameters of CDP model include compressive and tensile behaviour and plasticity. To generate the graph of stress and strain relationship, the developed equations proposed by Pavlovic *et al.* (2013) were adopted. The compressive stress  $\sigma_c$  is defined as a function of uniaxial strain  $\epsilon_c$  according to Eurocode EC2 (see **Equation (5.1)**).

$$\sigma_c = f_{cm} \frac{k\eta - \eta^2}{1 + (k-2)\eta}, \quad \eta \leq \varepsilon_{cu1}/\varepsilon_c \quad (5.1)$$

where  $k = 1.05 \varepsilon_{c1} E_{cm} / f_{cm}$ ,  $\eta = \varepsilon_c / \varepsilon_{c1}$  and nominal ultimate strain  $\varepsilon_{cu1} = 0.003$  are determined according to EC2. The uniaxial strain  $\varepsilon_{c1}$  at peak of compressive stress is derived from **Equation (5.2)** where it is taken based on the previous study conducted by Kmiecik and Kaminski (2011).

$$\varepsilon_{c1} = 0.0014 \left[ 2 - \exp(-0.024 f_{cm}) - \exp(-0.14 f_{cm}) \right] \quad (5.2)$$

It should be noted that the plasticity curve, unfortunately, can only be defined up to nominal ultimate strain  $\varepsilon_{cu1}$ . It is not a problem since in reinforced concrete analysis, the compressive strain of concrete is likely below  $\varepsilon_{cu1}$ . However, considering the fact when taking concrete compression behaviour only up to strain  $\varepsilon_{cu1}$ , it can lead to iteration issues and overestimation of concrete crushing strain in finite element modelling. For this reason, the extension curve for the uniaxial strain beyond the limit of the curve is needed. Pavlovic *et al.* (2013) proposed the extended curve by using sinusoidal expression between points D-E and the linear part between points E-F (see **Figure 5.2(a)**). Detail of equation can be seen in **Equations (5.3)**.

$$\sigma_c = \begin{cases} f_{cm} \left[ \frac{1}{\beta} - \frac{\sin(\mu^{\alpha_{iD}} \cdot \alpha_{iE} \pi / 2)}{\beta \cdot \sin(\alpha_{iE} \pi / 2)} + \frac{\mu}{\alpha} \right], & \varepsilon_{cuD} < \varepsilon_c \leq \varepsilon_{cuE} \\ \left[ f_{cuE} (\varepsilon_{cuF} - \varepsilon_c) + f_{cuF} (\varepsilon_c - \varepsilon_{cuE}) \right] / (\varepsilon_{cuF} - \varepsilon_{cuE}), & \varepsilon_c > \varepsilon_{cuE} \end{cases} \quad (5.3)$$

where the first equation corresponds with the sinusoidal part and the second equation relates to linear part. It was reported by Pavlovic *et al.* (2013) that using these equations, it was possible to undergo much faster in running process than any other methods yet result in a good agreement compared to experiment. For more details, variable of  $\mu = (\varepsilon_c - \varepsilon_{cuD}) / (\varepsilon_{cuE} - \varepsilon_{cuD})$  is a relative coordinate between point D to E, and  $\beta = f_{cm} / f_{cu1}$  with  $f_{cu1}$  associates to  $\varepsilon_{cu1}$ . Point D is defined as  $\varepsilon_{cuD} = \varepsilon_{cu1}$  and  $f_{cuD} = f_{cu1} = \sigma_c(\varepsilon_{cu1})$ . Point E is the end of the sinusoidal descending part at

strain  $\varepsilon_{cuE}$  that corresponds with the reduction of concrete strength of  $f_{cuE}$  by the factor  $\alpha = f_{cm}/f_{cuE}$ . Constant independent factors such as  $\alpha_{tD} = 0.5$  and  $\alpha_{tE} = 1.0$  are generally taken into account to govern tangents angles of the sinusoidal part at points D and E, resulting in the smooth stress-strain curve. In the linear section which equals to point E to F, strain  $\varepsilon_{cuE} = 0.04$  is used as the conservative value in regard to compression test of the concrete cube.

For the tensile behaviour of CDP model, since the tension stiffening may considerably affect the results of the analysis, the tensile stress-strain relationship of concrete (see **Figure 5.2(b)**) was proposed using the modified Wang and Hsu (2001) formula for the weakening function as uttered in **Equation (5.4)**.

$$\sigma_t = f_{ct} \left( \frac{\varepsilon_{cr}}{\varepsilon_t} \right)^n, \quad \varepsilon_t > \varepsilon_{cr} \quad (5.4)$$

where  $n$  represents the rate of weakening with value varies from 0.4 to 1.5.

As part of concrete damage plasticity model, plasticity parameters were also considered using default values as specified in ABAQUS. The parameters included the biaxial/uniaxial compressive strength ratio  $\sigma_{b0}/\sigma_{c0} = 1.16$ , flow potential eccentricity  $\varepsilon = 0.1$ , and deviatoric invariant ratio  $K = 0.667$ . Dilation angle  $\Psi$  of 31 degrees was iteratively calibrated to match the experimental results. Viscosity parameter  $\nu$  of 0.01 was found based on sensitivity analysis to satisfy the reasonable results with test specimen.

Damage states in tension and compression are characterised independently by two hardening variables: plastic strains in tension and compression. The evolution of the variables are simply derived by the following expressions,  $d_c = 1 - f_{cm}/\sigma_c$  and  $d_t = 1 - f_{ct}/\sigma_t$ , for compression and tension respectively. Damage constitutive model was adopted to present the stiffness degradation during the loading process. If damage constitutive model was not present, the structure behaved as plasticity model without any loss of stiffness and strength. **Figure 5.2(c)** shows the formation of damage behaviour of concrete both in compression and tension.

In addition to the input method for CDP model in normal concrete, the attention of how to address the material properties of ECC material is imperative. In essence, the response of ECC under compression does not significantly differ with conventional concrete, although the softening region may prone to be constant. Similarly, the tensile response of ECC beyond the softening region is identical with the conventional concrete. However, it should be noted that prior to softening, ECC delivers strain hardening response with increasing stress thereby producing higher ductility in tensile strain. Given that the equation proposed by Wang and Hsu (2001) cannot, therefore, be used. The tensile response of ECC is generally characterised by three distinct features including the linear elastic region, strain hardening region associated with multiple micro cracking phenomena, and tension softening (see **Figure 5.2(d)**). To account these three features in accordance with the actual behaviour of ECC, the uniaxial direct tensile test was then carried out for governing the stress-strain relationship of ECC under tension. The result of this test is presented in the previous chapter.

For reinforcing steel, the elasto-plastic material property was adopted using normal plasticity model. This model assumes that the yield surface of reinforcing steel remains in the same shape and it expands with increasing or decreasing stress. In most cases, the stresses tend to increase gradually during strain hardening region and prior to rupture. However, to provide a simplified technique for assigning the

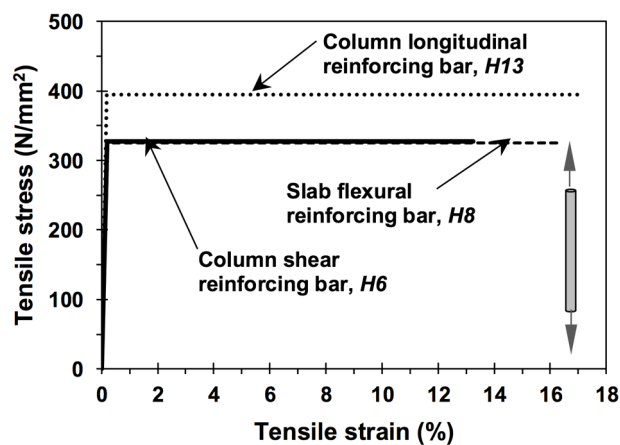


**Figure 5.3** Assumed average stress-strain relationship of reinforcements embedded in concrete.

parameter of steel, the uniaxial tensile stress-strain relationship embedded in concrete was assumed to be in the bilinear curve in which the response begins with the linear elastic curve, and upon the yielding point, the response is in the perfectly plastic region without experiencing an increase in stress by any means. The idealised tensile stress-strain responses of reinforcing steel in differing diameter are shown in **Figure 5.3**. It is important to note that the values of stress and strain plotted in **Figure 5.3** were not merely taken from the material tests, but they were further calculated by following these expressions [**Equation (5.5)** to **(5.7)**].

$$\sigma_{true} = \sigma_{nom} (1 + \varepsilon_{nom}) \quad (5.5)$$

$$\varepsilon_{true} = \ln(1 + \varepsilon_{nom}) \quad (5.6)$$

$$\varepsilon_{pl} = \varepsilon_{true} - \left( \frac{\sigma_{true}}{E_s} \right) \quad (5.7)$$

where  $\sigma_{true}$  is the true stress from reinforcing bar,  $\sigma_{nom}$  is the nominal stress of reinforcing bar,  $\varepsilon_{true}$  and  $\varepsilon_{nom}$  is the true strain and the nominal strain of reinforcing bar respectively, and  $\varepsilon_{pl}$  is the plastic strain of the reinforcing bar.

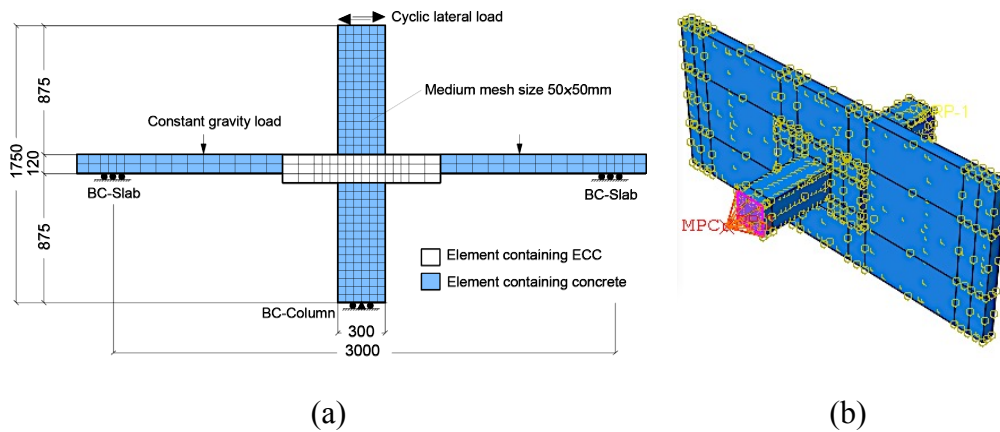


**Figure 5.4** (a) Finite element mesh and (b) boundary conditions of column and slab (unit in millimetre).

#### 5.1.4. Mesh and boundary conditions

A typical finite element mesh used to perform the analysis is shown in **Figure 5.4**. Boundary conditions of finite element model were assigned by arranging the input of degree of freedom on the nodes of concrete and in the location where supports were placed in the actual specimen. In order to model a pinned support on the column base, degrees of freedom U1, U2, and U3 were restrained using multipoint constrains (MPC) to avoid any translational movement during the course of loading (see **Figure 5.4 (b)**). On the other hand, UR1, UR2, and UR3 were not restrained to allow the rotational movement occurred on the specimen as how the pinned support should effectively work. Roller supports, similar to pin-ended support to the actual specimen, were then modelled by restraining U2, U3, UR1, UR2, and UR3, while U1 was left unchecked to permit the horizontal movement of the slab. In terms of the abbreviation, U and UR in respective order stand for translational and rotational movement while the number of 1, 2, and 3 refer to the direction of X, Y, and Z respectively.

#### 5.1.5. Loading scenario

In finite element simulation, the magnitude of gravity loading was given analogous to the experimental test in the form of uniform distributed load along the transversal span of the slab. The self-weight load was specified in density property in the part of material properties. The superimposed dead load and live load were

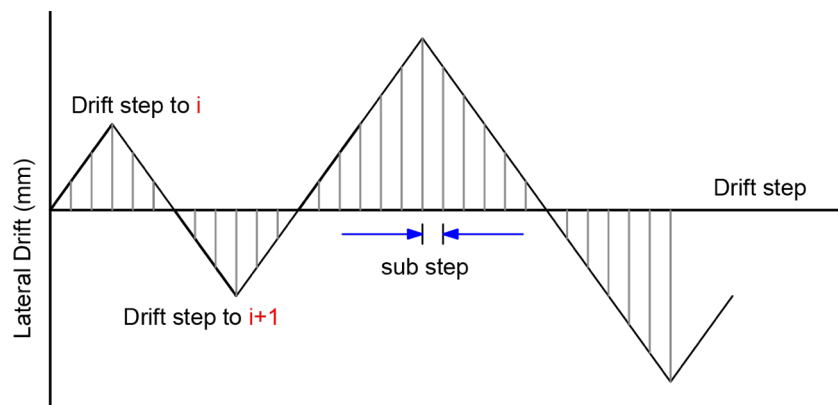


**Figure 5.5** Loading etiquette in numerical simulation using displacement control method.

previously summed up and then given on the surface of the slab using pressure load. In similar to the test specimen, the structural model was subjected to gravity load prior to cyclic loading. Upon this step, the cyclic lateral load was then applied at the top of the column in the form of displacement control, starting from the small magnitude of drift level and gradually increasing beyond the post-yielding regime. Differ to experimental test whereby an increment in drift level was given in three cycles, the cyclic lateral load in the finite element analysis was only given as one cycle to speed up the computation time. In addition, amplitude feature was used to govern load and load reversal (see **Figure 5.5**).

#### **5.1.6. The solution of nonlinear problems**

In ABAQUS package, the solutions are specified into two different iterative solvers. They are generally known as explicit and implicit analysis, also referred to as ABAQUS/Standard and ABAQUS/Explicit respectively. An explicit finite element solver does the incremental procedure at the end of each time step, the update of the system matrices is executed, and the new system of equations is solved without iteration. If the increments are small enough, accurate results will be computed; otherwise, the solution may diverge due to the fact that the equilibrium is not strictly enforced. In implicit solver, the approach is analogous to the one discussed for the explicit system with the difference that in each increment, the Newton-Raphson algorithm is applied to the equilibrium. Given that larger increments are possible and the accuracy is typically higher as in the explicit case. However, this solution normally takes heavy computational loads since the system matrices are also updated in the Newton-Raphson iterations. In most cases, the implicit solver is assessed to be more efficient for solving smooth nonlinear problems, whereas explicit is the clear choice for a wave propagation analysis. Nevertheless, static or quasi-static analysis can be performed well with either program.

##### ***A. Steps, increments, and iterations***

In ABAQUS, the load is assigned to the step module whether or not it consists of one or more steps. The step module generally provides an analysis procedure

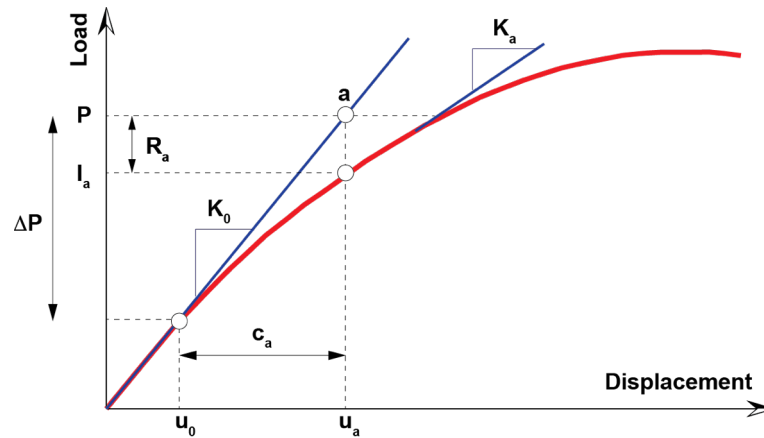


**Figure 5.6** First equilibrium iteration in an increment.

option such as static and dynamic, loading options, and output request options. Different loads, boundary conditions, analysis procedure options, or even output request options can be used in each step whereby they are interrelated to one and another. An increment is part of a step which is used to break the total load applied into smaller increments so that the nonlinear solution path can be followed. This increment is modifiable, meaning that users can define the size of the subsequent increments according to their consideration. However, it should be noted that a small number of increment is preferable as it governs the accuracy of the results. An iteration is an attempt at finding the equilibrium solution in certain increment when undertaking the analysis with the implicit method. If the model is not in equilibrium at the end of the iteration, the system tries another iteration until the system reaches the equilibrium solution. Given that the running may need many iterations to complete the analysis thereby making it time-consuming.

### ***B. Equilibrium iterations and convergence***

In general, the nonlinear response of a structural member is shown in **Figure 5.6** with particular representing the small increment,  $\Delta P$ , for equilibrium iterations. As can be seen from the figure, ABAQUS/Standard uses the initial stiffness of the structure,  $K_0$ , which is based on its configuration at  $u_0$ , and  $\Delta P$  to calculate a displacement correction,  $c_a$ , for the structure. Using  $c_a$ , the configuration of the structure is updated to  $u_a$ . ABAQUS/Standard forms a new stiffness  $K_a$ , for the

structure, based on its updated configuration  $u_a$ . The system also calculates  $I_a$  in the updated configuration. The difference between the total applied load,  $P$ , and  $I_a$  can now be calculated as expressed in **Equation (5.8)**.

$$R_a = P - I_a \quad (5.8)$$

where  $R_a$  is the force residual for iteration. If  $R_a$  is zero at every degree of freedom in the model, point  $a$  in **Figure 5.6** would lie on the load-deflection curve, and the structure would be in equilibrium. However, in the nonlinear problem, it is almost impossible to have force residual equal to zero, in particular for those models which have a complex response such as slab-column connection. Given that ABAQUS considers to put tolerance value and compares the force residual with that value. If  $R_a$  is less than the force residual tolerance, the system accepts the updated configuration of the structure as the equilibrium solution. It is of importance to know that by default, the tolerance value is set to 0.5% of an average force in the structure, averaged over time. Therefore, the system automatically calculates the tolerance value and time-averaged force spatially throughout the course of the simulation.

If  $R_a$  is less than the current tolerance value,  $P$  and  $I_a$  are in equilibrium, and  $u_a$  is a valid equilibrium configuration for the structure under the applied load. Nonetheless, ABAQUS/Standard accepts the solution as well as checks that the displacement correction,  $c_a$ , is small relative to the total incremental displacement,  $\Delta u_a = u_a - u_0$ . If  $c_a$  is greater than one percent of the incremental displacement, ABAQUS/Standard then performs another iteration. Both convergence checks must be satisfied before a solution is said to have *converged* for that load increment. The exception to this rule is the case of a *linear* increment, which is defined as any increment in which the largest force residual is less than  $10^{-8}$  times the time-averaged force. Any case that passes such stringent comparison of the largest force residual with the time-averaged force is considered linear and does not require further iteration. The solution is accepted without any check on the size of the displacement correction.

If the solution from an iteration is not converged, ABAQUS/Standard performs another iteration by trying to bring the internal and external forces into

balance. This second iteration uses the stiffness,  $K_a$ , calculated at the end of the previous iteration together with  $R_a$  for the purpose of determining another displacement correction,  $c_b$ , that brings the system closer to equilibrium (see point  $b$  in **Figure 5.7**). Given that ABAQUS/Standard calculates a new force residual,  $R_b$ , using the internal forces from the new configuration of the structure,  $u_b$ . Again, the largest force residual at any degree of freedom,  $R_b$ , is compared against the force residual tolerance, while the displacement correction for the second iteration,  $c_b$ , is compared to the increment of displacement,  $\Delta u_b = u_b - u_0$ . If the convergence condition yet is not satisfied, ABAQUS/Standard perform further iteration with repeating the same process as aforementioned.

### ***C. Automatic incrementation control***

ABAQUS/Standard automatically adjusts the size of the load increments so that it solves nonlinear problems easily and efficiently. However, it is of an essence to note that the first increment in each step of the simulation must be input using the reasonable size. If the first increment is not provided, ABAQUS/Standard will try to apply all of the loads defined in step in the first increment. In such situation, when performing the highly nonlinear problems, ABAQUS/Standard will have to reduce the increment size repeatedly, resulting in waste CPU time. The number of iterations needed to find a converged solution for a load increment will vary depending on the degree of nonlinearity in the system. By default, if the solution appears to diverge, ABAQUS/Standard aborts the increment and starts again with the increment size set to 25% of its previous value. An attempt is then made at finding a converged solution with this smaller load increment. If the increment still fails to converge, the system reduces the increment size again.

In ABAQUS/Standard, the maximum number of increments allowed during the step is available to be specified. Nevertheless, it should be noted that the system normally terminates the analysis with an error message if it needs more increments than this limit to complete the step. The default number of increments for a step is 100; if significant nonlinearity is present in the simulation, the analysis may require many more increment. There is no strict limitation for this as the greater value is preferable to avoid such error. In addition to the step increment, a step in the

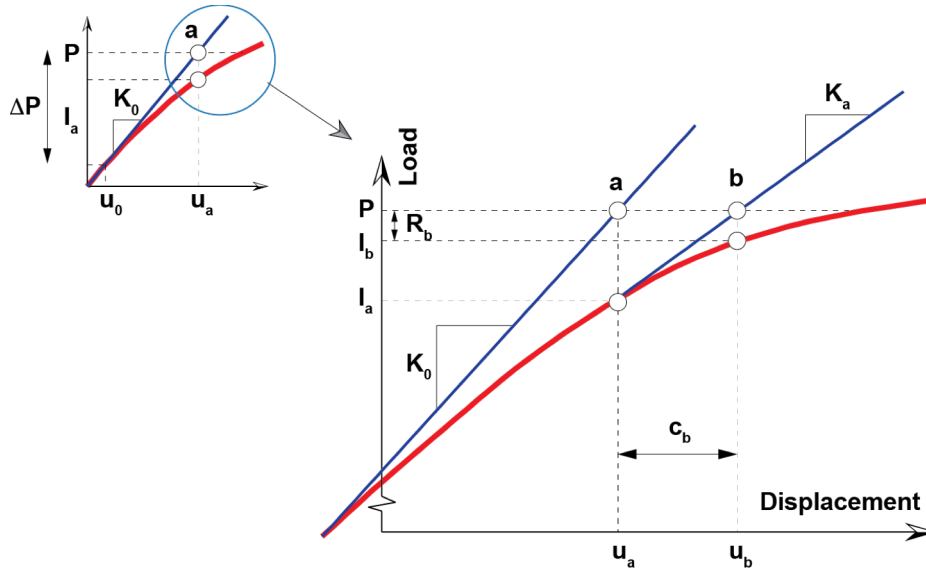


**Figure 5.7** Second equilibrium iteration in an increment.

nonlinear analysis also takes place over a finite period of time, although this time has no physical meaning unless inertial effects of the rate-dependant behaviour are present, particularly when performing the explicit analysis. In ABAQUS/Standard, the initial time increment,  $\Delta T_{initial}$ , and the total step time,  $T_{total}$ , must be specified. The ratio of the initial time increment to the step time is used to denote the proportion of load applied in the first increment thereby giving the initial load increment as expressed in **Equation (5.9)**.

$$\frac{\Delta T_{initial}}{T_{total}} \times \text{Load magnitude} \quad (5.9)$$

The choice of the initial time increment can be critical in certain nonlinear simulations, but for most analyses, an initial increment size that is 5% to 10% of the total step time is usually sufficient. In static simulations, the total step time is usually set to 1.0 for convenience, unless, for example, rate-dependent material effects or dashpots are included in the model. With a total step time of 1.0, the proportion of load applied is always equal to the current step time i.e. 50% of the total load is applied when the step time is 0.5.

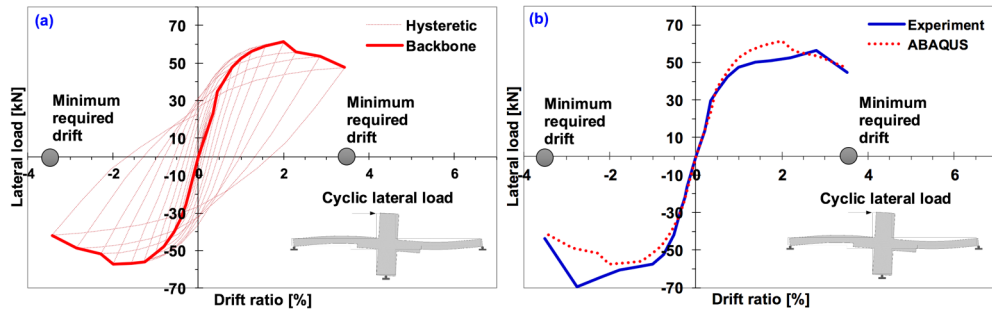


**Figure 5.8** Predicted load-drift relationship of specimen S1: (a) hysteretic loop and (b) backbone curves.

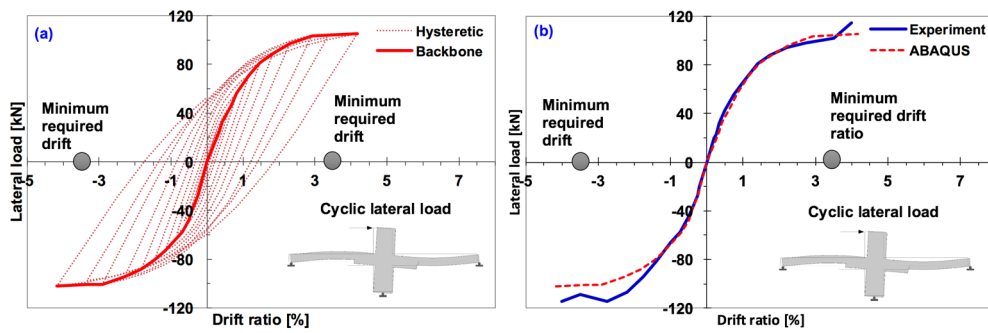


**Figure 5.9** Predicted load-drift relationship of specimen S2: (a) hysteretic loop and (b) backbone curves.

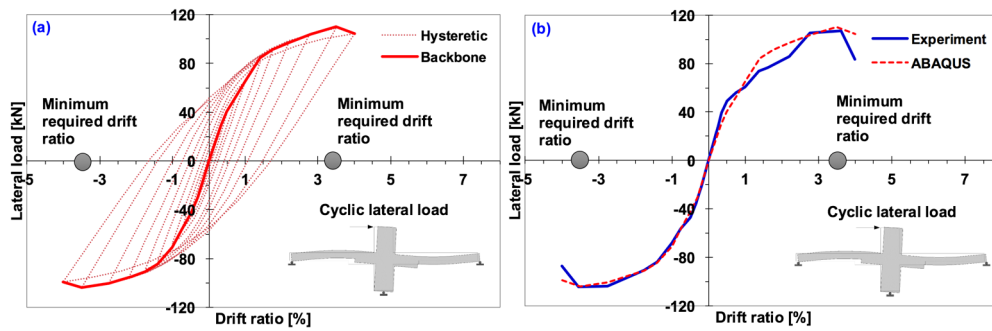


**Figure 5.10** Predicted load-drift relationship of specimen S3: (a) hysteretic loop and (b) backbone curves.

### 5.1.7. Results and discussion of ABAQUS

#### A. Load-drift relationship

The predicted load-drift hysteretic loops for the three specimens are presented in **Figure 5.8** toward **Figure 5.10** along with the maximum lateral load

sustained during each cycle is shown as part of a load-drift envelopes. These envelopes, often referred to as backbone curves, are plotted in the same figures with the purpose of facilitating direct comparison with the experimental results. Referring to figures of hysteretic loops (see section (a) in **Figure 5.8** to **Figure 5.10**), pinching effect cannot be perfectly modelled. This means that the internal mechanism causing the opening and closing of concrete cracks is not comprised in the constitutive modelling of ABAQUS thereby leading to significantly overestimate energy dissipation. The similar case has been reported by Wan *et al.* (2001) and Mousavi *et al.* (2014). In addition, the assumption of interaction between concrete and reinforcing steel to be perfectly bonded may also cause the insufficiency of ABAQUS to model the pinching effect of concrete as to what has been understood that pinching is caused by the lag of deformation due to opening and closing of cracks and bond losses of reinforcing steel to the concrete. Apart from this inadequacy, however, the predicted backbone curves of all structural models are in good agreement with the experimental results.

According to **Figure 5.8(b)** in predicted load-drift relationship of specimen S1, it is apparent that the initial response begins as linear elastic line, depicting an increase in load with the proportional increase in displacement. This continues until the load reaches 40 kN when the change in gradient curve is apparent thereby causing the specimen to deviate from linearity. Upon the post-yielding region, the load is not proportional to the deflection due to the significant degradation of lateral stiffness. The specimen eventually fails at a load 60 kN due to loss of strength.

With regard to the comparison of the observed and predicted backbone curves of specimen S1 presented in **Figure 5.8(b)**, it is evident that ABAQUS shows a reasonable agreement with the experimental results, in terms of overall response and stiffness in the linear elastic zone, although there is a slight discrepancy at approximately 15% of the curve trend in nonlinear region. This indication may be affected by damage state due to tensile cracking of concrete. In ABAQUS, the equation of concrete damage is relatively straightforward which also follows the general trend of tension softening rules. It is worth mentioning that when the principal strain is in excess of tensile capacity, the tensile strength carried by concrete is released thereby creating a major development of crack opening. This

crack opening may trigger the loss of strength earlier than that of observed specimen. Another case may also be driven by a phenomenon to what is called as *hourglass effect* acting on the linear brick elements. Since the concrete adopts the reduced integration elements, the integration points lie along the centre vertical place in an eight-node brick element; hence, as having hourglass effect, this element could wrap into a trapezoidal shape from a rectangular shape without the integration point experiencing any stress. In addition, hourglass effect is also associated with spurious deformation which leads to inaccurate results in the nonlinear region due to a significant deformation.

In specimen S2, a comparison of observed and predicted backbone curves is presented in **Figure 5.9(b)**. The behaviour of specimen S2 is similar, in many respect, to specimen S1. The only exception is that this specimen develops a higher load carrying capacity nearly two times higher than specimen S1 which the specimen S2 is yet to exhibit loss of strength up to drift ratio of 4%. It is also seen that the in the post-yielding, the load is exceeded 80 kN which is much higher than control specimen. In terms of backbone trend, the predicted backbone curve of specimen S2 also generates a close resemblance with the experimental results, with the difference roughly 12%. This indication can be regarded due to tensile strain hardening behaviour in ECC. In such condition, damage state is not yet taken place over ECC, meaning the tensile strength of ECC is not released and hence crack opening is assumed to be very subtle. A somewhat discrepancy may also be affected by hourglass effect.

Referring to the predicted backbone curve of specimen S3 in **Figure 5.10(b)**, it is shown that ABAQUS exhibits a reasonable agreement with the experimental results. The load carrying capacity is seen to be rather lower than specimen S2. The overall trend such as strength and stiffness prior to yielding of reinforcement is regarded identical due to a very small measure of discrepancy (up to 6%) in both curves. It is interesting to note that in negative loading, the predicted curve seems to be proportional to the observed backbone curve in terms of stiffness. On the contrary, the stiffness in the positive loading direction is somewhat lower.

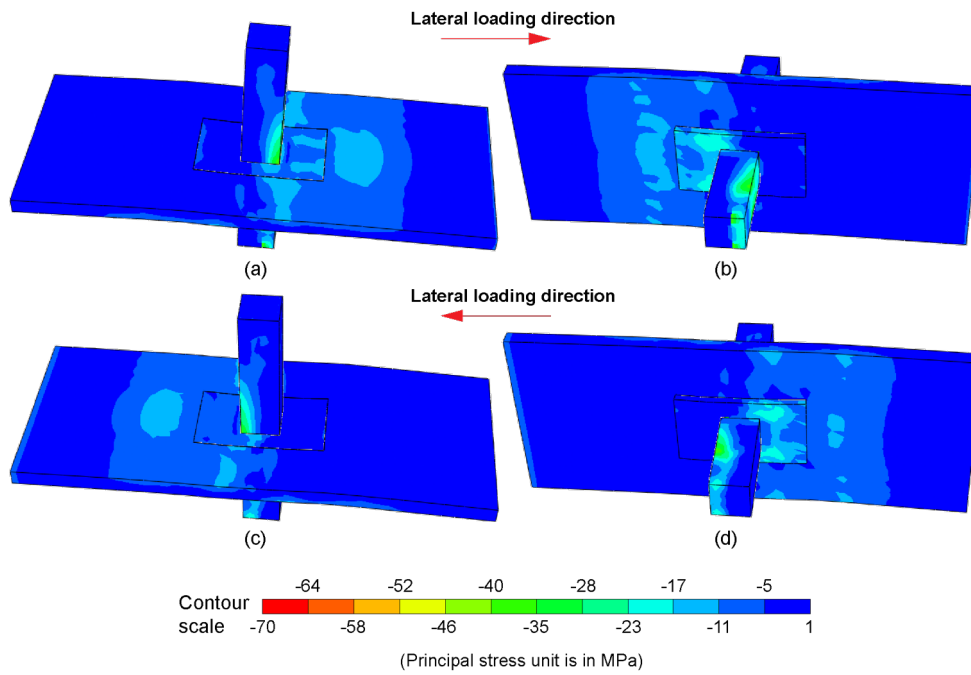


**Figure 5.11** Principal stress distribution of specimen S1: (a) stress at the slab top surface in the positive loading, (b) stress at the slab bottom surface in the positive loading, (c) stress at the slab top surface in the negative loading, and (d) stress at the slab bottom surface in the negative loading.

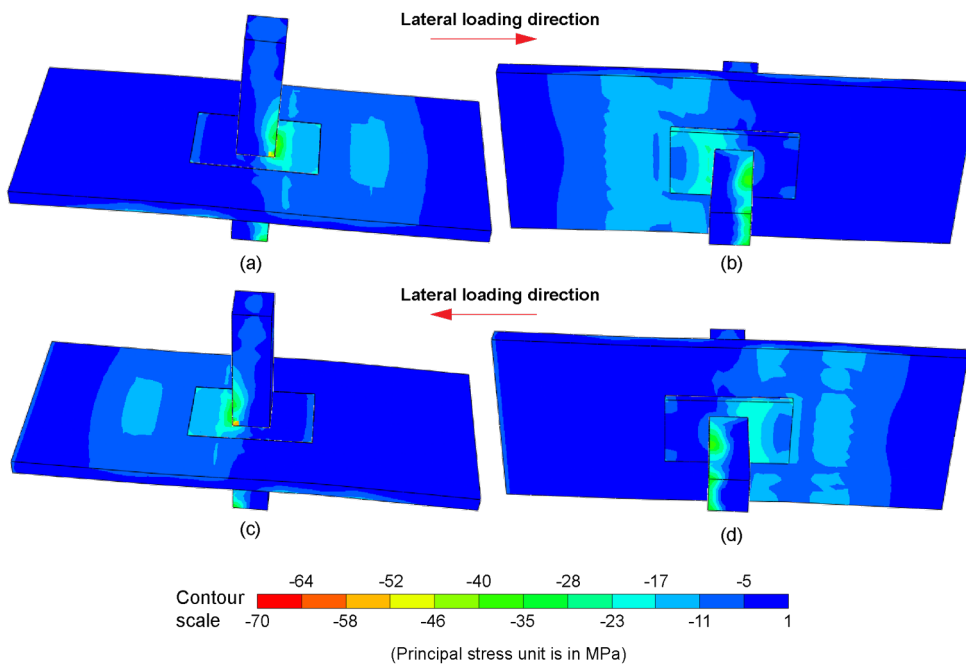


**Figure 5.12** Principal stress distribution of specimen S2: (a) stress at the slab top surface in the positive loading, (b) stress at the slab bottom surface in the positive loading, (c) stress at the slab top surface in the negative loading, and (d) stress at the slab bottom surface in the negative loading.

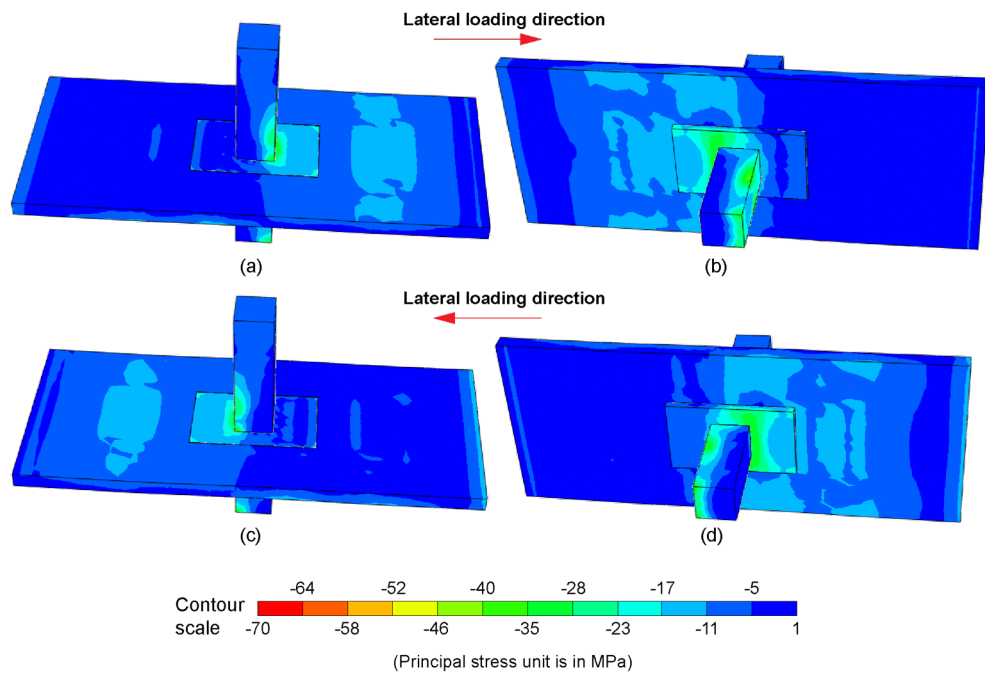


**Figure 5.13** Principal stress distribution of specimen S3: (a) stress at the slab top surface in the positive loading, (b) stress at the slab bottom surface in the positive loading, (c) stress at the slab top surface in the negative loading, and (d) stress at the slab bottom surface in the negative loading.

### ***B. Principal stress distribution of concrete***

To provide a better picture of the occurring internal mechanism in concrete and ECC, the distributions of principal stress obtained from the finite element analysis are presented in **Figure 5.11** toward **Figure 5.13**. In overall response, it is apparent that during the loading stage in the positive direction, the development of discernible stress is governed in East side over the top surface of the slab adjacent to the column face, joining the similar stress trend in West side in opposite face of the slab. With the load being reversed, the stress in East side devolves to the bottom face of the slab while in West side the stress turns over the top surface of the slab. It is interesting to note that the average magnitude of stresses in each of specimens is roughly not more than 35 MPa, owing to the fact that the load is still less than the maximum compressive stress of concrete. This then suggests that concrete does not undergo a *crushing* phenomenon.

In addition to the stress distribution, **Figure 5.14** shows the development of *diagonal compression strut* occurred at the joint (see the red box in each snapshot).

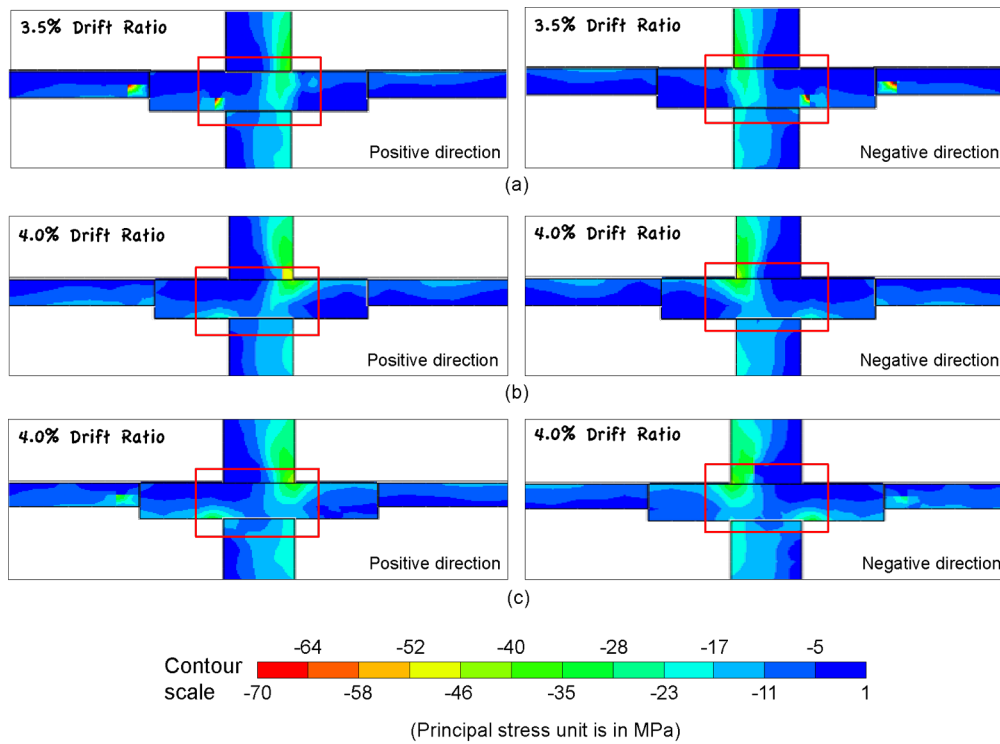


**Figure 5.14** Diagonal compression struts: (a) specimen S1, (b) specimen S2, and (c) specimen S3.

From the mechanics' point of view, the presence of diagonal compression struts sustains the compression forces transferred from the column and slab compression zones. It has been acknowledged as one of the significant factors which provide the shear resistance of concrete. If the stress in diagonal compression zone exceeds the allowable compressive stress, the crushing of concrete may be the case which is also accompanied by a significant action of shear transfer mechanism at the joint. Referring to **Figure 5.14**, it is found that the stress in diagonal compression strut is less than the allowable compressive stress, meaning that crushing of concrete is prevented. However, the indication of concrete crushing might still be the case if the loading level is increased due to the prominence of stress occurs at the joint.

### ***C. Length of plastic hinge***

In slab-column connection subjected to high loading rate, slab flexural bars located adjacent to the column face would relatively reach their yield stresses. In such situation, if the specimen is designed as under reinforced section, the concrete

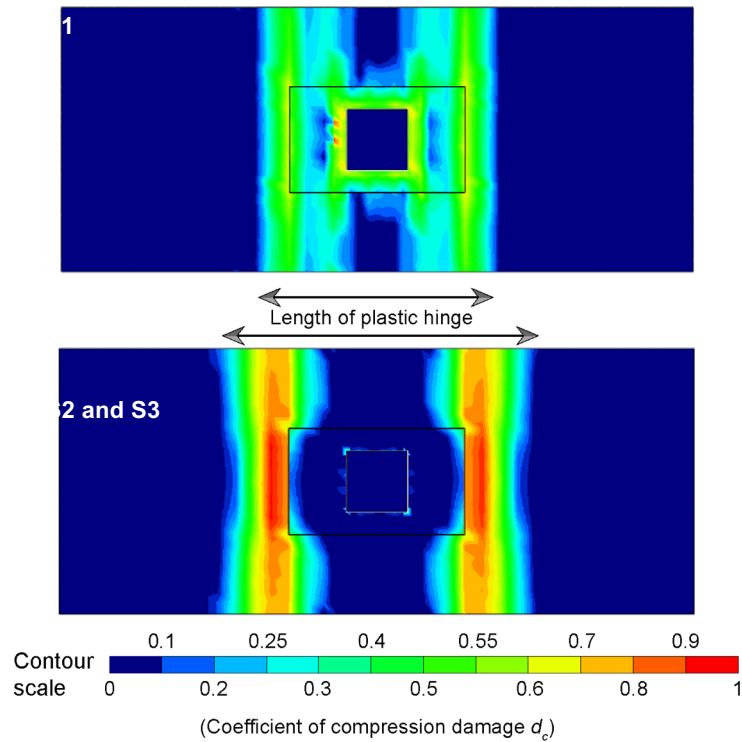


**Figure 5.15** Location of plastic hinge zone in the slab-column connection.

slab is assumed to be cracking thereby allowing the possibility of concrete *crushing* if the magnitude of concrete stress has exceeded the allowable compressive stress. The area surrounding this action is regarded as plastic hinge zone. In terms of the definition, a plastic hinge in structural engineering refers to the deformation of a part of a beam or slab wherever plastic deformation occurs. The hinge is defined as a structural member has no capability of resisting moment; therefore, a plastic hinge behaves as a standard hinge, permitting free rotation. In this study, plastic hinge zone at a drift ratio of 3.5% is concerned as part of the significant action in slab adjacent to column face which potentially causes concrete crushing. The numerical results shown in **Figure 5.15** indicates that ECC specimen is capable of governing wider plastic hinge length. It is also associated with the higher energy dissipation of ECC material.

#### ***D. Longitudinal strain plots***

To provide a bigger picture into the full behaviour of reinforced concrete slab-column connection, the longitudinal strain fields of specimen S1, otherwise referred

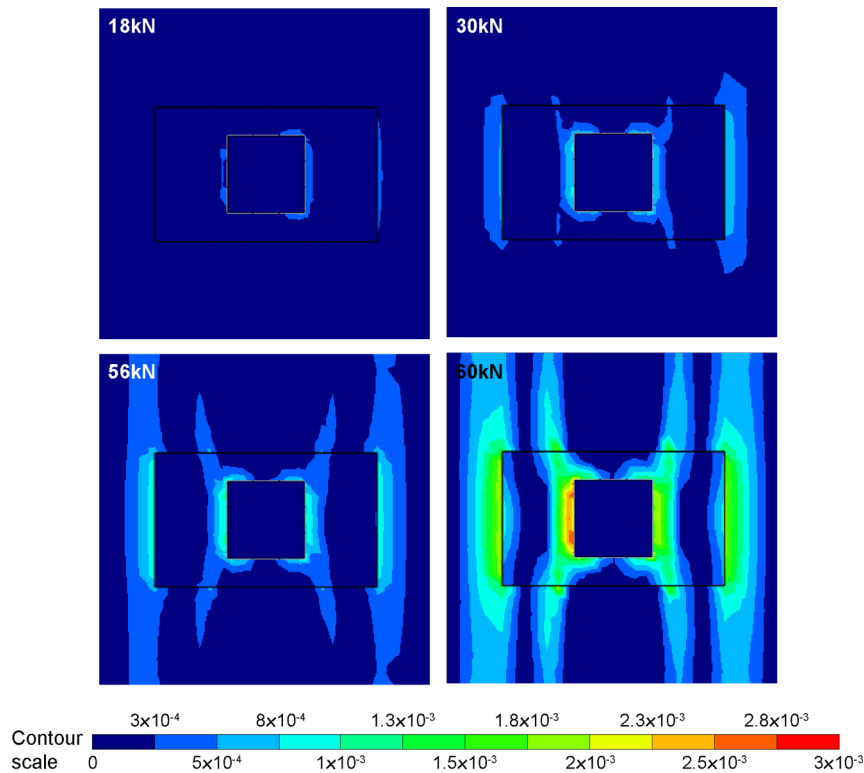


**Figure 5.16** Longitudinal strain plots of specimen S1.

to as a crack pattern, are presented in **Figure 5.16**, emphasising the onset of cracking ( $\sim 18\text{kN}$ ), the post-cracking response prior to yielding ( $30\text{kN}$ ), the post-yielding response before peak load ( $55\text{kN}$ ), and the peak point response ( $60\text{kN}$ ). As shown in the figure, it is evident that in the early phase of loading stage, there is only a minimal development of strain whereby this phase is associated with the onset of flexural crack. As the loading increases in a range of post-cracking region, the longitudinal strain fields begin to propagate increasing in length and width. The progression of strain profiles is apparent during the increase of load beyond the post-yielding zone. It is shown that the strain tip has extended over the slab edges. As the load further increases, the specimen reaches the peak load following a discernible increase in strain widths of slab around the column face (see the change in contour colour). According to what is seen in **Figure 5.16**, the predicted strain fields resemble the actual crack pattern of the observed test specimen (for illustration, see **Figure 4.1(b)**).

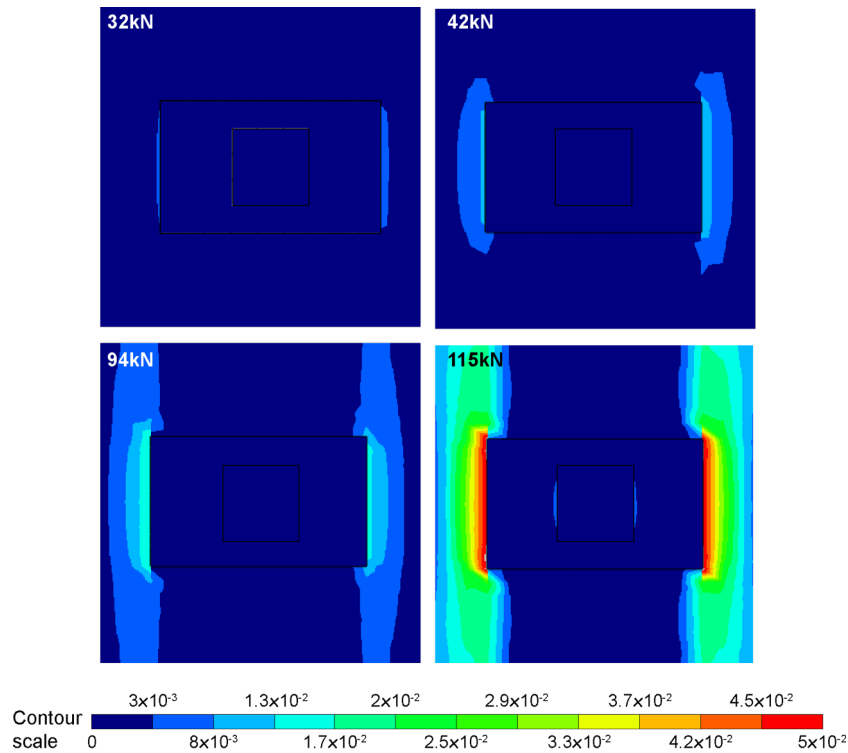


**Figure 5.17** Longitudinal strain plots of specimen S2.

For the purpose of discussion for ECC of specimen S2 and S3, only the strain plots of Specimen 2 are examined herein concerning their identical response under similar loading condition. As shown in **Figure 5.17**, a very weak development of longitudinal strain strips during the early phase of loading can be seen at the interface between ECC and conventional concrete, which would represent flexural cracking. It is interesting to note, that the first crack does not form in the critical section of slab-column connection, signifying that tensile ductility of ECC. As the loading progresses at a load of 42 kN, the increase in strain width is evident which is also followed by the subtle increase of strain in length. With the load being increased roughly 94 kN, the strain tip also extends on both sides of the slab. At this point, the development of strain in the connection is still not apparent, which is dissimilar with the crack pattern obtained from laboratory test. In peak point at a load of 115 kN, a noticeable change in contour colour is evident, implying the significant crack opening. Beyond this point, the increase in strain width is stopped whereby there is only the change in contour colour.

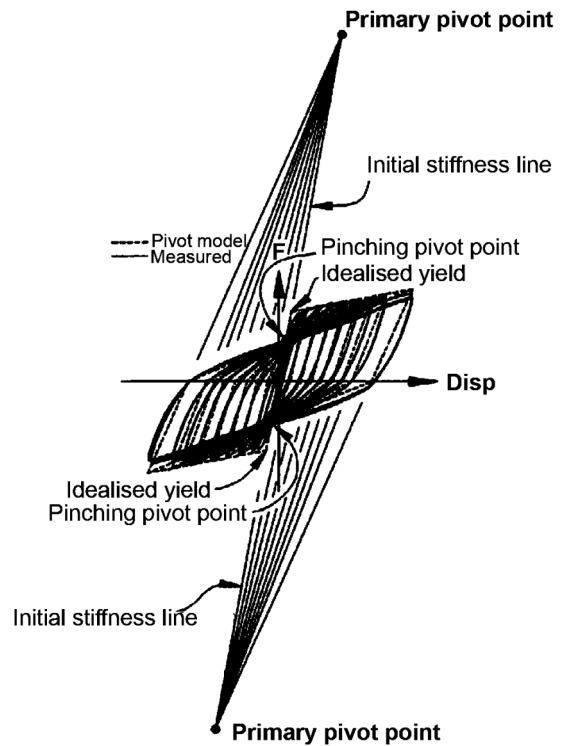


**Figure 5.18** Hysteretic characteristic of a typical reinforced member and the idealisation (Dowel *et al.* 1998).

## 5.2. Work Package 2 — SAP2000

### 5.2.1. Overview

Concrete is known to be a highly nonlinear material which is more prone to undergo severe hysteresis beyond yield. In such condition, the hysteretic behaviour becomes more complex due to the effect of reinforcing steel and the bonding between concrete and reinforcement under cyclic loading. To apprehend this phenomenon, a number of studies have been carried out many years ago to propose the appropriate model on predicting the hysteretic behaviour of reinforced concrete in structural members. In the past, elasto-plastic hysteretic rules that idealise the hysteretic loops in the bilinear format were frequently used. Such an idealisation, though reasonable for steel members, it was found to be over-simplified for reinforced concrete. Given that some other models provided more profound considerations to account other effects, such as stiffness degradation, pinching due

to opening and closing of cracks, and bond slip, even though the computational time was found to be more demanding.

One of the most popular hysteretic models for reinforced concrete members was proposed by Takeda *et al.* (1970) which is widely termed as the Takeda degrading stiffness model nowadays. This model has led to predict the constantly changing stiffness of reinforced concrete thereby leading to less energy dissipation than that of predicted model using elasto-plastic hysteretic rules. It was also shown that the model proposed by Takeda *et al.* (1970) was able to exhibit excellent comparison of the cyclic behaviour of reinforced concrete member(s) tested in the laboratory. Following this proposition, a few other hysteretic models have been developed by researchers many years after, as discussed by Gosh (1991). For instance, Dowel *et al.* (1998) proposed a so-called *pivot hysteretic model* for reinforced concrete member(s). The model was basically developed for circular columns with the purpose of serving the nonlinear analysis of bridge pier column. The pivot hysteretic model utilised the observations made from experimental

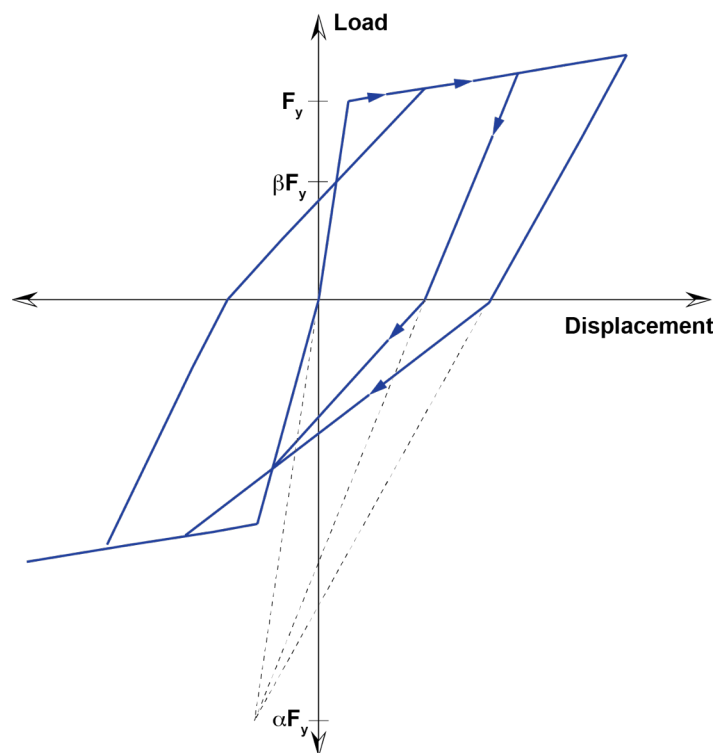


**Figure 5.19** Basic parameters for pivot hysteretic model (Dowel *et al.* 1998).

results which the unloading stiffness decreased as drift level increased. Upon load reversal, unlike elasto-plastic response, the load-drift path also crossed the idealised initial stiffness line before reaching the idealised yielding point. From further closer look from **Figure 5.18**, it is shown that the unloading response, back to zero force from any drift level, is generally guided toward a single point called primary pivot point. In addition, the load-drift paths are prone to cross the elastic loading line at roughly the same point, meaning that pinching pivot point is present (see **Figure 5.18**).

Apart from its use for circular columns, however, it has turned out the pivot hysteretic model can also be used for predicting the response of other members including beams and joints. With that being stated, therefore, this work extends the use of pivot hysteretic model, utilising SAP2000 to predict the hysteretic behaviour of slab-column connections. The model is then validated against previous test results. The assumption and formulations for modelling technique are also presented in the following sub-sections for clarity purposes.

### 5.2.2. Hysteretic rules

The pivot model is governed by a set of rules that depend on the properties of a reinforced concrete member and loading history. The two basic and most important parameters that define the pivot hysteretic model are  $\alpha$  parameter and  $\beta$  parameter. The parameter of  $\alpha$  is given to govern the pivot point for unloading curve from the load, while  $\beta$  is given for load and load reversal. In other words,  $\alpha$  and  $\beta$  are used to control the pinching. In the closer observation from **Figure 5.19**, pivot model is considered that whilst unloading, the load-drift path is directed towards a common point namely primary pivot point ( $\alpha F_y$ ). As has been previously mentioned, it is also noticed that the load-drift paths tend to cross the elastic loading line for both loading directions ( $\beta F_y$ ) which this is also associated with pinching effect. By assigning these parameters to nonlinear springs for joints or members, the hysteretic rules containing pinching profile can, therefore, be attained.

The work presented of using this method is relatively straightforward of which the monotonic or cyclic backbone load-displacement curve is obtained from the experimental study. It is of importance to note that, if the un-symmetrical behaviour

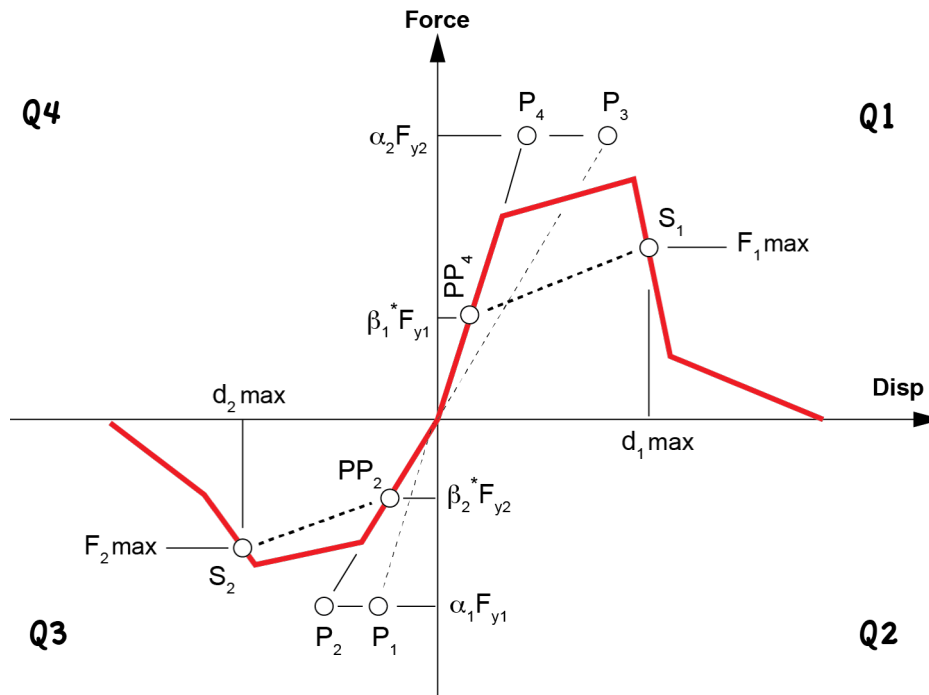


**Figure 5.20** Pivot point designations (Dowel *et al.* 1998).

occurs in both loading directions, the curve backbone curve of both loading directions must be present. Following this,  $\alpha$  and  $\beta$  are also given in both directions (see **Figure 5.20**). The parameters of  $\alpha_1, \beta_1$  and  $\alpha_2, \beta_2$  shown in **Figure 5.20** control the response in positive and negative loading direction respectively. The primary pivot point of  $P_1$  to  $P_4$  is also present to control the amount of softening expected with increasing drift while pinching pivot point of  $PP_2$  and  $PP_4$  is discretely used to fix the degree of pinching following a load reversal. Upon the response is in excess of yield deformation in either direction, the modified backbone curve, reflecting as upper bound for the following curve, is defined by lines joining point  $PP_4$  to  $S_1$ , while for lower bound in negative direction, the line is formed by point  $PP_2$  to  $S_2$  (for illustrative purpose, see **Figure 5.20**). While there seems to be quite comprehensive, however, in SAP2000 the parameters of  $\alpha$  and  $\beta$  are assigned by (only) inputting the corresponding value to the box provided along with  $\eta$  parameter to determine the amount of degradation of the elastic slopes after plastic deformation in which the value should be set in a range between 0 to 1.

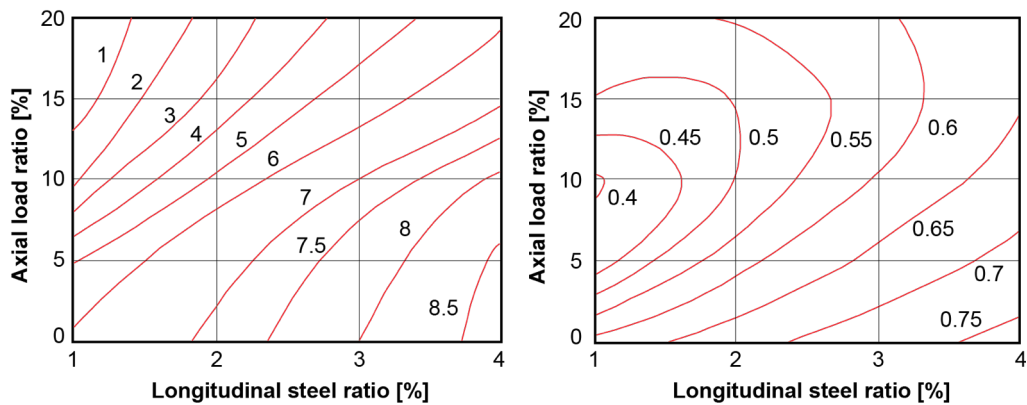


**Figure 5.21** Contours for (a)  $\alpha$  parameter and (b)  $\beta$  parameter suggested by Dowel *et al.* (1998).

### 5.2.3. Parameters controlling hysteretic response

In the original model proposed by Dowel *et al.* (1998), parameters of  $\alpha$  and  $\beta$  are determined by the contours shown in in **Figure 5.21(a)** and **(b)** respectively, depicting a function of axial load ratio and longitudinal reinforcement ratio. The contours were initially developed using the fibre element analysis of various circular reinforced concrete columns and were verified with experimental results. Based on **Figure 5.21(a)** and **(b)**, it is assumed that a higher value of  $\alpha$  somehow signifies more energy dissipation thereby increasing the value of  $\alpha$  should be followed by the increase in longitudinal steel ratio.

In addition to energy dissipation, it is of interest to note that the increase in axial load ratio also increases the brittleness of the member. Concerning the  $\beta$  parameter, the longitudinal reinforcement ratio also contributes towards confinement of concrete; therefore, the value of  $\beta$  should then be increased. In this work, these parameters assigned to simulate the pivot hysteretic model were  $\alpha_1 = \alpha_2 = 6$ ,  $\beta_1 = \beta_2 = 0.6$ , and  $\eta = 0$ .

### 5.2.4. Developed model of slab-column connection using SAP2000

In SAP2000, the modelling technique of slab-column connection is relatively straightforward. Material properties of the elements were simply determined by inputting the corresponding values without concerning the governed

stress-strain curves for each material. Cross-sections were also input based on the geometry of test specimen. In this work, the structural model was made using 2D analytical model, consisting of a number of frames (see **Figure 5.22**). The joint restraints were then assigned to the nodes of column support and slab edges using pinned, and roller supports respectively. In addition to supports, boundary conditions at the top of the column were also assigned to avoid any undesirable movement of loading course. The transitional and rotational boundary condition in any direction were fixed except for translation in the longitudinal direction (x-axis).

There are essentially two different techniques to govern the hysteretic rules for pivot model. In SAP2000 package, they are referred to as fibre hinge model and link model. Either technique exhibits similar results to a given problem. Fibre hinge is normally used when envelope curve for the structural model is not provided. A governing hysteretic response is achieved if a frame is assigned to a hinge property (viz, moment or shear). This is essential as it creates the internal mechanisms occur in a frame. In terms of computation time, however, fibre hinge model seems to be time demanding than link model. In the link model, a frame is simulated based on the given envelope curve. The link model is not hence associated with stand-alone model due to its dependency of previous information in regard to envelope curve obtained from experiment. Apart from its simplicity, however, the predicted

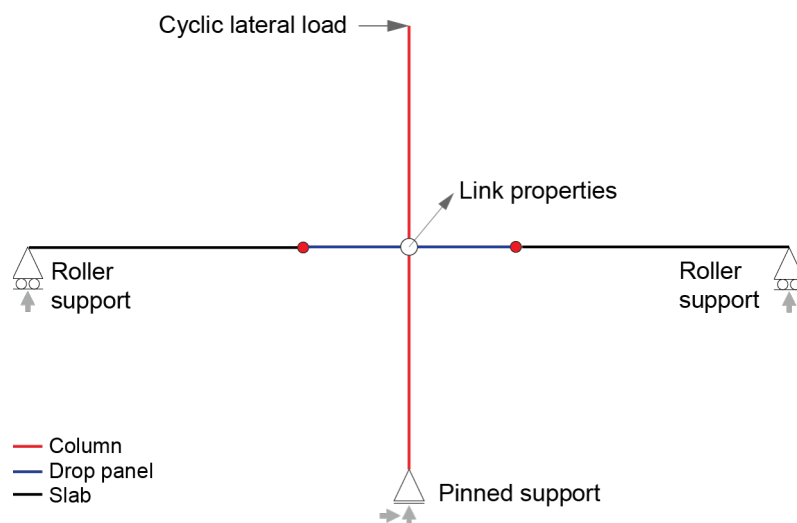


**Figure 5.22** Developed model of slab-column connection in SAP2000.

hysteretic response can be tailored to the experimental results thereby making it suitable for widespread use in simple numerical modelling.

In this study, the pivot model was created as a single joint using multilinear plastic featured in the link properties. This single joint was positioned at the centre of the connection. To account the directional properties of the link, the movement in transversal direction was fixed, while the nonlinear property of the link was assigned in the longitudinal direction, representing the same direction with the experimental test. As shown in **Figure 5.23**, the data from envelope curve, both in load and load reversal, were manually input in the nonlinear properties box along with pivot hysteretic parameters ( $\alpha$ ,  $\beta$  and  $\eta$ ). Upon the definition of the pivot parameters, a nonlinear time history type *direct integration* analysis was then performed whereby the structural model was subjected to the artificial earthquake ground motion in the longitudinal direction. It should be noted that direct integration analysis is extremely sensitive to time-step size in a way that is not true for modal analysis. Therefore, in order to attain smooth and reasonable results, a very small time increment and is imperative. In addition, when performing the direct integration analysis, these following paths must be considered:

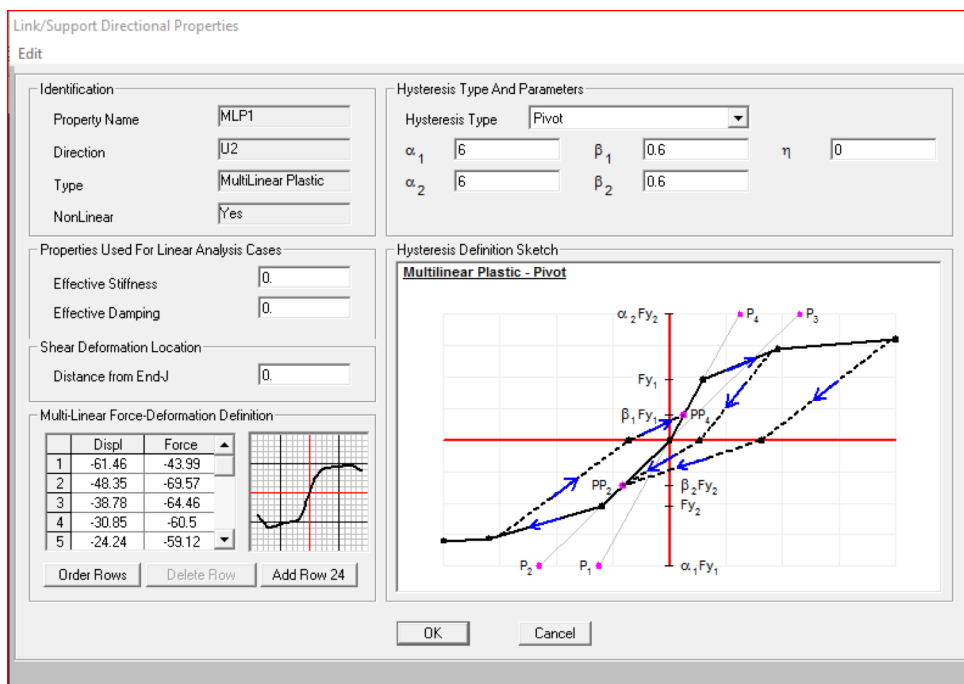
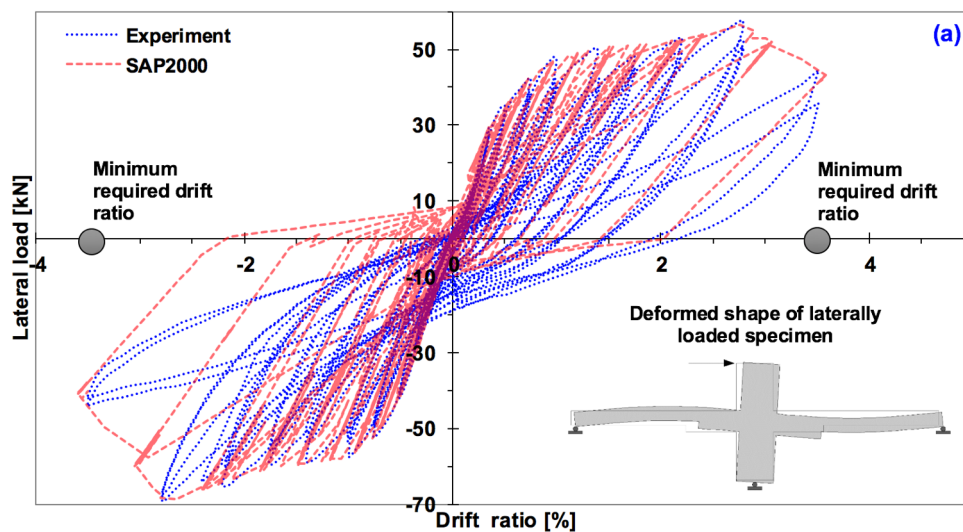


**Figure 5.23** Input parameters of pivot hysteretic model.

1. The load should be scaled up or down to achieve the monitored reversal lateral displacement as desired for each cycle;
2. The time function should consist of linear for positive and negative directions;
3. In each cycle sequence, the peak value from positive and negative directions must be found.

### 5.2.5. Results and discussion of SAP2000

The results from cyclic tests are compared against the SAP2000. A comparison of observed and predicted hysteretic responses is presented in **Figure 5.24**. It is shown that SAP2000 is capable of depicting the pinching effect of reinforced concrete structure. It is also apparent that the concrete and ECC constitutive models capture a reasonable accuracy in regard to hysteretic responses. A shortcoming of each model is generally driven by the complexity of iterative solution from nonlinear direct integration analysis. As can be seen from the figure, the hysteresis format obtained from SAP2000 is completely different with the experimental hysteretic. It is due to the influence of fluctuating values of ground motion, whereas in experimental testing, the applied load is set to be fully in order starting from the small displacement with steady increments up to specimen failure.



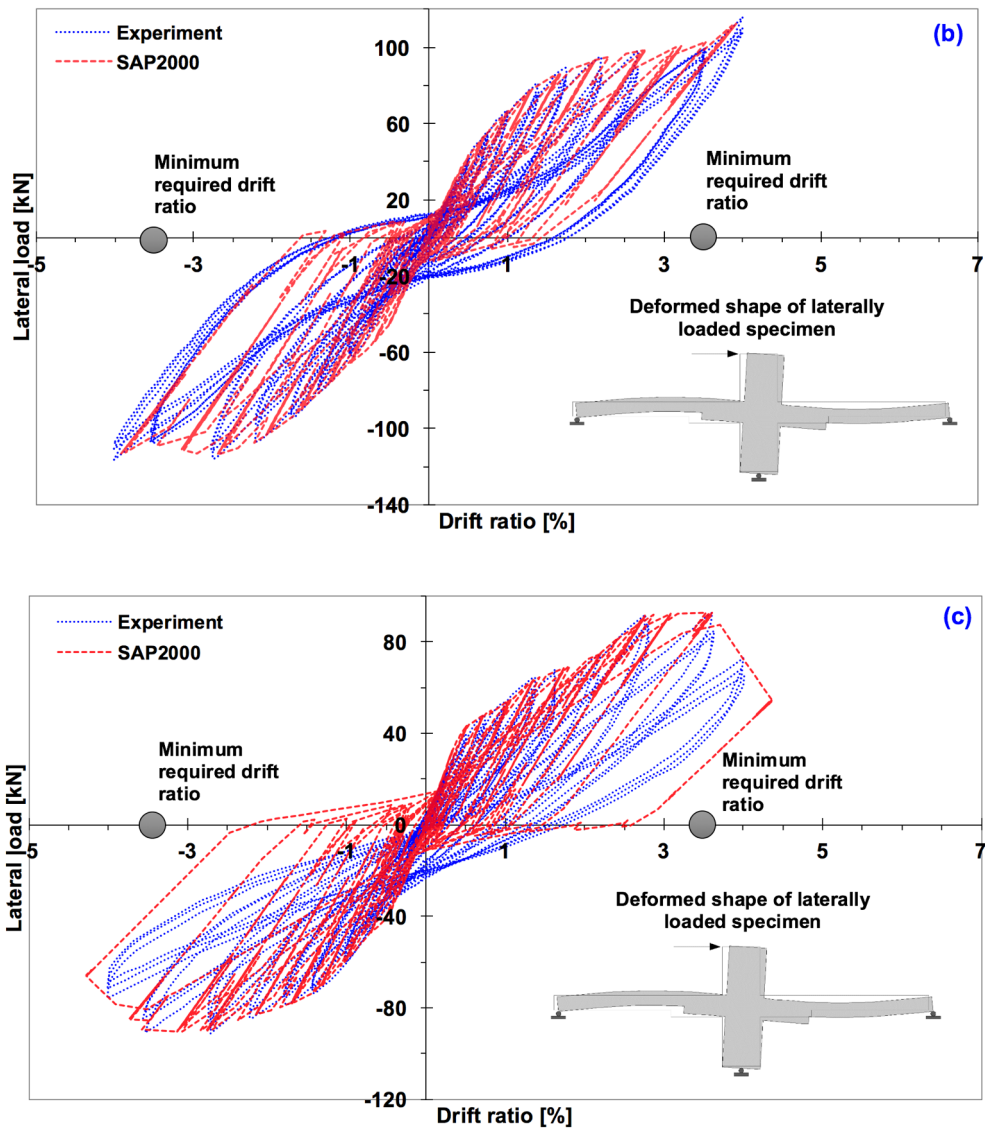


**Figure 5.24** Computed hysteretic loop from SAP2000 with the superimposed hysteretic loop from experiments: (a) specimen S1, (b) specimen S2, and (c) specimen S3.

Regarding the response of specimen individually, it can be seen from **Figure 5.24(a)** that the predicted hysteretic response of specimen S1 highlights a close resemblance compared with the experimental result. The various features from the hysteretic loop such as initial stiffness, stiffness degradation, and maximum strength are also well predicted with sufficient degree of accuracy. A somewhat discrepancy in terms of energy dissipation is however apparent whereby during the load reversal, the constitutive model tends to enlarge the area of the loop. According

to **Figure 5.24(b)**, the nonlinear hysteretic response of specimen S2 from SAP2000 is impeccably similar to the observed loop. It is also evident that the overall response such as stiffness and strength is found to be identical. More importantly, the pinching shape obtained from the numerical analysis is in good agreement with the experimental result. For specimen S3 (see **Figure 5.24(c)**), the hysteretic format is similar, in many respect, to specimen S1. It is observed that the constitutive model tends to overestimate the energy dissipation thereby leading to less pinching effect. Although there is a small measure of discrepancy in terms of energy dissipation and pinching effect, the results from SAP2000 are regarded capable of predicting the true response of test specimens.

### 5.3. Work Package 3 — ZEUS NL

#### 5.3.1. Overview

Zeus nonlinear, otherwise referred to as ZEUS-NL, is the analysis and simulation platform of the multi-hazard approach of engineering (MAE) centre. This platform is a state-of-the-art 3D static and dynamic analysis which is specifically developed for earthquake engineering application. ZEUS-NL is a freeware numerical tool which was first established by Arm S. Elnashai and his team at the University of Illinois in Urbana-Champaign. With regard to the application of this software, ZEUS-NL provides an easy and efficient way to run accurate nonlinear dynamic time-history, conventional and adaptive pushover, and

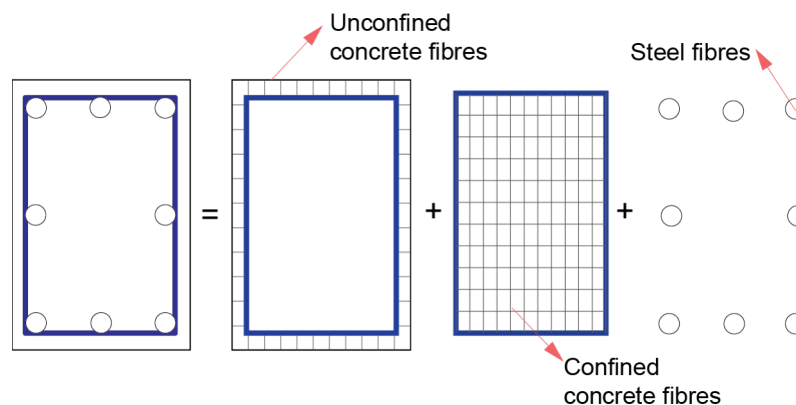


**Figure 5.25** Decomposition of a rectangular reinforced concrete section (Elnashai *et al.* 2000).

eigenvalue analysis. More importantly, it is not only used for reinforced concrete and steel structure, but it can also be used to model the fibre reinforced concrete, particularly ECC as it has a distinctive feature to determine the ECC material properties. Given that ZEUS-NL is considered to be the first software which is able to perform the structural analysis of fibrous material with practical use.

ZEUS-NL can be used to predict the large displacement behaviour of plane and space frames under static and dynamic loading, taking into account the influences of both geometric and material nonlinear behaviour. The applied loading can also be assigned to be in the form of force or displacement control thereby making it very convenient to compare the results from the experimental test with the same loading protocol. On top of that, unlike other similar analysis packages, the dynamic analysis in ZEUS-NL is made by simple steps, using fully visual approach. This means that the structural model is made by point-and-click process and let the programme run the analysis in details. **Figure 5.25** shows a decomposition of a rectangular reinforced concrete section of which the element is computed by assembling the responses of individual materials that consist of many monitoring points. Each of those materials is determined by the relation of stress and strain.

### 5.3.2. Material models

*Concrete* — The material of concrete in ZEUS-NL was modelled by the nonlinear concrete model according to the graph shown in **Figure 5.26(a)**. The graph essentially consists of four interrelated parameters, namely compressive strength  $f_c$ , tensile strength  $f_t$ , strain when the concrete has crushed  $\epsilon_{co}$ , and confinement factor (*if any*). This model was initially derived from the results of the research conducted by Mander *et al.* (1998), with the following rules of cyclic behaviour governed in the model were further improved by Martinez-Rueda and Elnashai (1997). It was done to enable the prediction of continuing cyclic degradation of strength and stiffness as well as to ensure better numerical constancy under large displacement analysis.

*Reinforcing steel* — Reinforcement was modelled with the bilinear elasto-plastic model with kinematic strain hardening in ZEUS-NL. The illustration of the

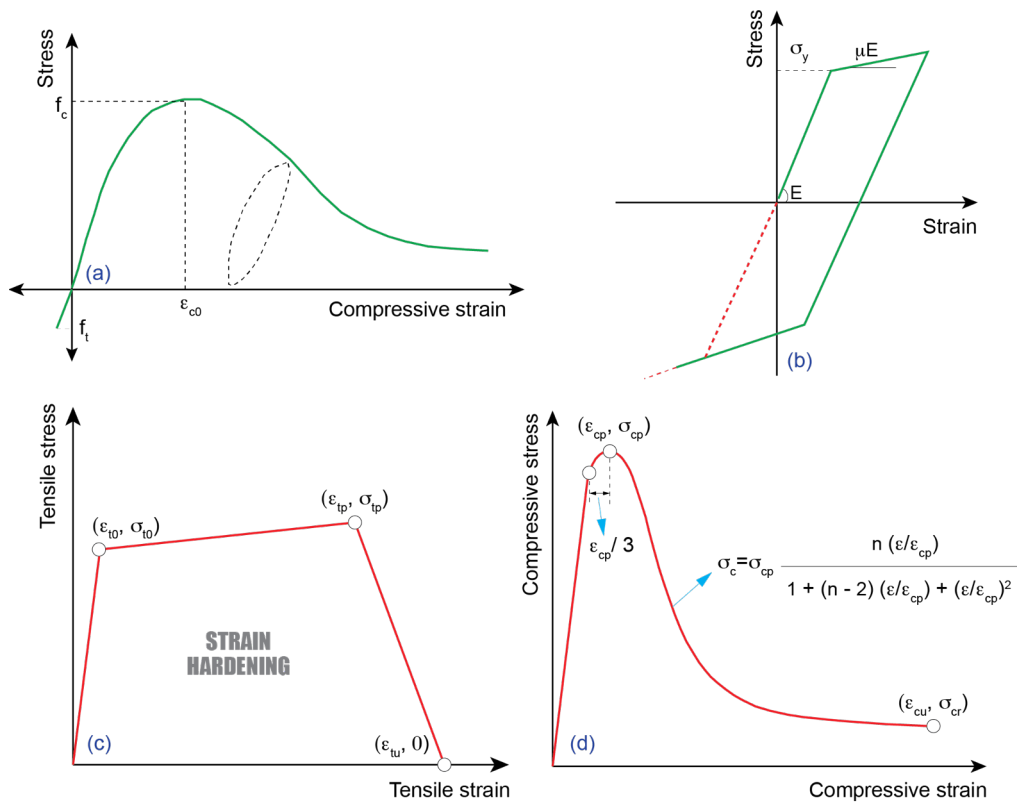


**Figure 5.26** Material models for ZEUS-NL analysis: (a) compressive response of concrete, (b) tensile response of steel, (c) tensile response for ECC, and (d) compressive response for ECC.

stress-strain relationship of the reinforcing steel is presented in **Figure 5.26(b)**. As can be seen from the figure, three parameters are required for the model, including elastic modulus of steel  $E_s$ , the yield strength of steel  $f_y$ , and the strain hardening parameter  $\mu$ . In this study, the values of modulus elasticity of steel, as well as the yield strength, were taken in accordance with the test results. It is important to note that strain hardening parameter turns out to play an important role as the reinforcing steel is the part which maintains the ductility of reinforced concrete or ECC members. The strain hardening parameter is considered to be a constant value of 0.01.

*Engineered cementitious composite (ECC)* — In ZEUS-NL, the tensile properties of ECC illustrated in **Figure 5.26(c)** were modelled in accordance with the monotonic tests by Kesner and Billington (2004). The results of the tests indicated that ECC tensile behaviour is generally characterised by three distinct

regions (for illustration, see three lines in **Figure 5.26(c)**). According to the figure, the material exhibits linear behaviour until it reaches the cracking strain  $\varepsilon_{t0}$ . With the formation of multiple cracking, the material stiffness is then significantly reduced; however, the material still undergoes a pseudo-strain hardening response with increasing stress  $\sigma_{tp}$  prior to strain softening effect. As the tensile strain goes beyond the peak stress, crack localisation in the material starts to form, causing the stress to soften in correspondence of increasing strain. Once the ultimate tensile strain  $\varepsilon_{tu}$  is exceeded, the material is hence unable to carry any tensile stress. For compressive properties in ZEUS-NL, the behaviour of ECC is found to be similar to that observed in conventional concrete, with the slight discrepancy in the pre-peak response whereby ECC is observed to be better represented by linear elastic relationship up to two-thirds of the strain corresponding to peak stress as shown in **Figure 5.26(d)**.

### 5.3.3. Element model

In this study, the cubic element was used to model the structural elements. The cubic element is an elasto-plastic 3D beam-column element used for detailed nonlinear modelling. Since the numerical integration of the governing equation is calculated by two *Gauss* points, the element forces of monitoring areas are computed by numerical integration at the two *Gauss* points. For example, 100

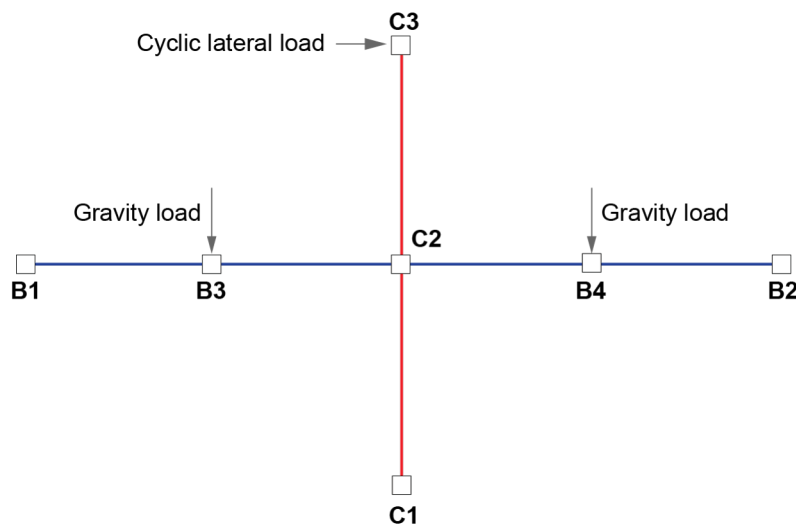


**Figure 5.27** 2D analytical model of slab-column connection in ZEUS-NL.

monitoring points may be used for a solid rectangular section without steel bar which is single-material section. However, 1000 or more monitoring points may be required when modelling the complicated section such as reinforced concrete T-section. In this present work, 20000 monitoring points were used to avoid any critical warning during the running process.

#### **5.3.4. Analytical model of slab-column connection using ZEUS-NL**

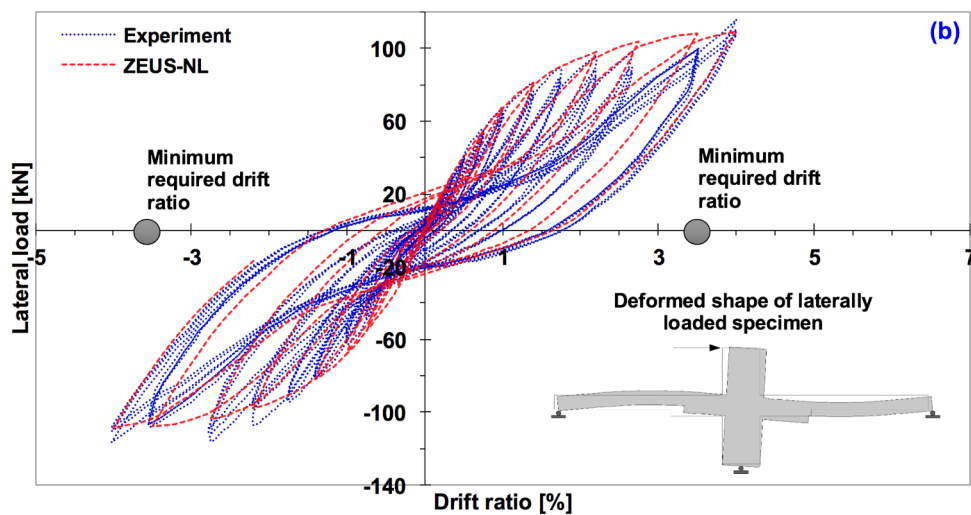
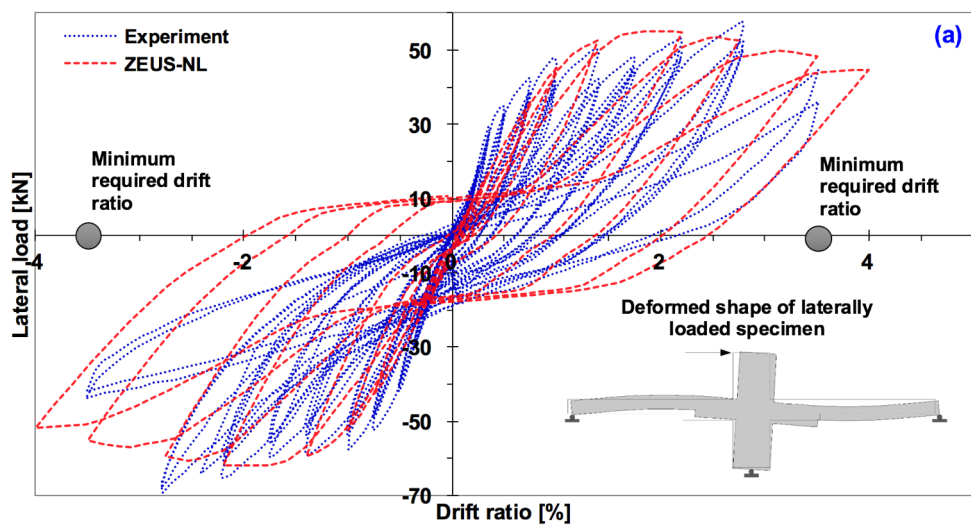
In ZEUS-NL, the slab-column connection was created using 2D analytical model (see **Figure 5.27**). Materials and section properties of slab-column connection were input by following the data from experimental tests. Initial loads for gravity loading were applied to the slab as two point loads placed at the centre of each side of the slab (see nodes B3 and B4). The value of gravity load for each specimen was in accordance with the gravity shear ratio in design. Upon these gravity loads, cyclic lateral load in the form of static time-history was then applied at the column tip (node C3) of the specimen. This was done using displacement control method. The structural model was restrained at column support (node C1) and slab edges (nodes B1 and B2) following the boundary conditions in the actual specimen (for precision, see boundary conditions set in ABAQUS).

#### **5.3.5. Results and discussion of ZEUS-NL**

A comparison of the observed and predicted load-drift responses of specimen S1 presented in **Figure 5.28(a)**. With regard to the numerical results from ZEUS-NL, it is apparent that the predicted response of specimen S1 shows a reasonable agreement with the experimental result, in terms of overall response. It is also evident that ZEUS-NL is capable of predicting the stiffness degradation along with pinching effect which is occurred due to the influence of opening and closing of cracks. It is interesting to note that the predicted response of specimen S1 tends to exhibit larger energy dissipation compared to the experimental result, even though the pinching is shown to be more prominent. In addition, the stiffness is also found to be rather lower, and the strength degradation is slightly constant.

Apart from the complex mechanics due to the interaction between randomly well-dispersed fibres and ECC matrix, the predicted response of ECC model in

specimen S2 shows a high degree of accuracy (see **Figure 5.28(b)**). It is apparent that the pinching shape in the hysteretic loop is perfectly modelled with only showing a small measure of divergence from the experimental result. Furthermore, from what is seen in **Figure 5.28(b)**, the predicted model does not show any degradation in strength, except for a slight discrepancy in terms of the increment of load carrying capacity which is still reasonably well. While there seems to be a close resemblance in overall behaviour, however, the results from the predicted response in specimen S3 highlights a notable irrelevance in regard to energy dissipation (see **Figure 5.28(c)**). During the initial response, the energy dissipation is observed to be realistically similar. This noticeable difference is seen in the high nonlinear region where the formation of major cracks has been taken place over the entire width of the slab.



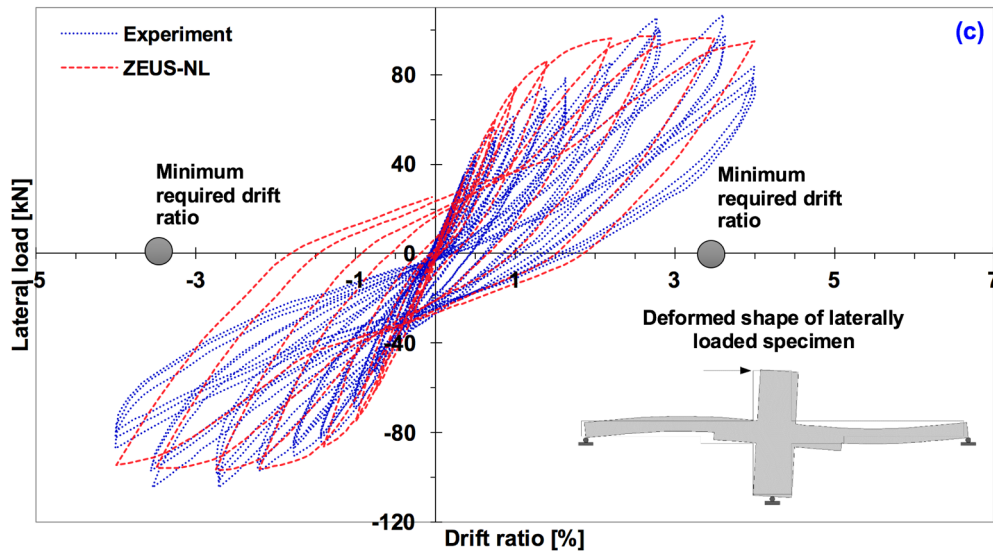


**Figure 5.28** Computed hysteretic loop from ZEUS-NL with the overlaid hysteretic loop from experiments: (a) specimen S1, (b) specimen S2, (c) and specimen S3.

When compared to the behaviour of specimen S3 during the initial course of testing, the slab surface around the interface between concrete and ECC was dominated by the flexural crack prior to cyclic loading. This then signifies the pinching behaviour of the specimen in the subsequent loading stages. On the other hand, in the scale of modelling, these cracks are neglected, and hence the response tends to overestimate the results from the experiment. Furthermore, on account of specimen S2 during testing, the flexural crack was not yet to occur in the phase of gravity loading. The development of crack widths was also controlled by fibre-matrix interaction. Due to small crack width, the pinching behaviour between experimental and numerical results hence shows a high degree of accuracy.

#### 5.4 Summary of Numerical Analyses

The comparisons of predicted response of slab-column connections obtained from the nonlinear finite element analysis are presented in **Figure 5.29**. It is shown that the numerical simulations have run based on the appropriate technique thereby displaying only a small measure of discrepancy when being compared to one another. It is apparent from the figure that the difference of lateral load capacity

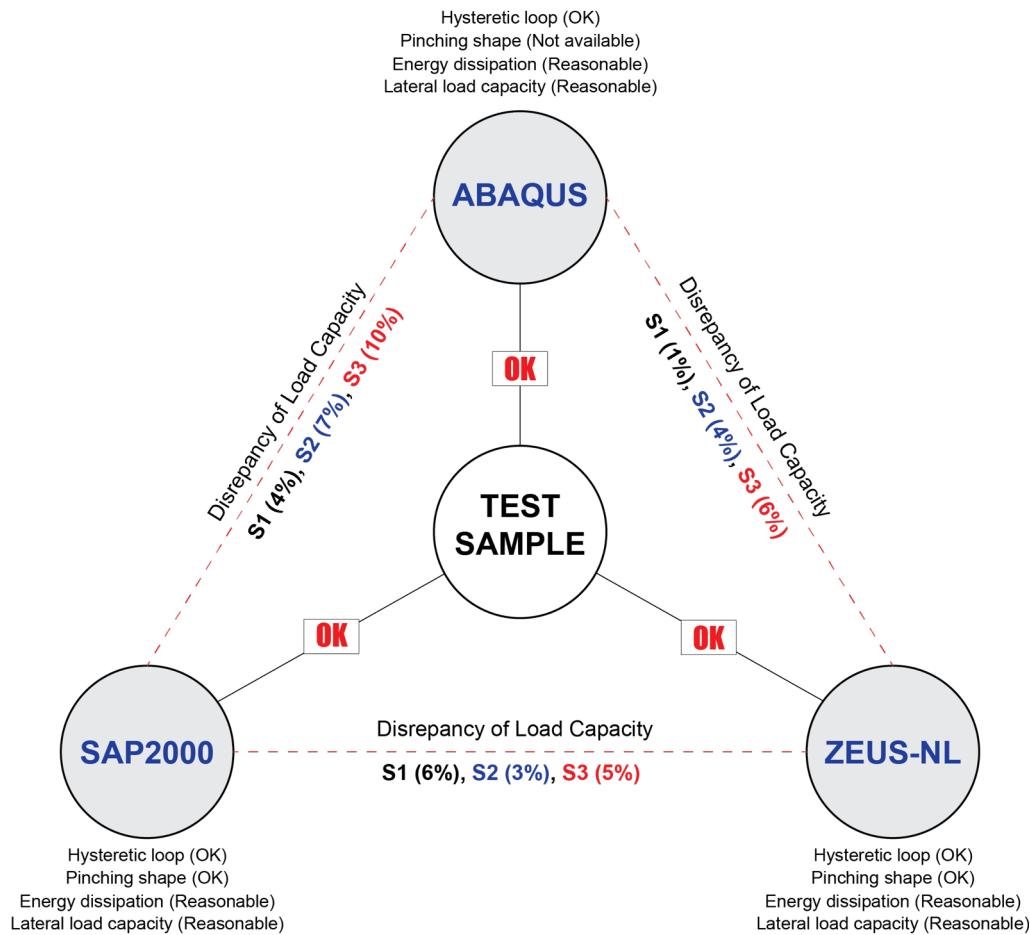


**Figure 5.29** Schematic comparisons among finite element packages.

between each of two software packages is not greater than 10%, meaning the response has shown a close resemblance. In addition to the lateral load capacity, other output parameters such as hysteretic loop, pinching shape and energy dissipation are shown to be reasonably well when being compared to each of work packages.

### 5.3. Further Analysis of Prototype Slab-Column Connections

Further analysis of the prototype of slab-column connections referring to the actual geometry has been undertaken to facilitate direct comparison from the half-scale specimen. This is to ensure whether or not the scaling technique is appropriate to be applied on a scale of the laboratory-based experiment. To provide improved insights into the full behaviour of prototype slab-column connections, a nonlinear

**Table 5.1** Summary of scale factors for reinforced concrete *true model* (Harris and Sabnis (1999)).

(1)	Quantity (2)	Dimension (3)	True Model (4)	Scale Factor of Half-Scale Test Specimen (5)
Material-Related Property	Concrete stress, $\sigma_c$	$FL^{-2}$	$S_\sigma$	1
	Concrete strain, $\varepsilon_c$	—	1	1
	Modulus of concrete, $E_c$	$FL^{-2}$	$S_\sigma$	1
	Poisson's ratio, $\nu_c$	—	1	1
	Specific weight, $\gamma_c$	$FL^{-3}$	$S_\sigma/S_i$	0.5
	Reinforcing stress, $\sigma_s$	$FL^{-2}$	$S_\sigma$	1
	Reinforcing strain, $\varepsilon_s$	—	1	1
	Modulus of concrete, $E_s$	$FL^{-2}$	$S_\sigma$	1
	Bond stress, $u$	$FL^{-2}$	$S_\sigma$	—
Geometry	Linear dimension, $l$	$L$	$S_i$	2
	Displacement, $\Delta$	$L$	$S_i$	2
	Angular displacement, $\beta$	—	1	—
	Area, $A$	$L^2$	$S_i^2$	4
Loading	Concentrated load, $Q$	$F$	$S_\sigma S_i^2$	4
	Force, $P$	$F$	$S_\sigma S_i^2$	4
	Line load, $w$	$FL^{-1}$	$S_\sigma S_i$	2
	Pressure, $q$	$FL^{-2}$	$S_\sigma$	1
	Moment, $M$	$FL$	$S_\sigma S_i^3$	8

**Table 5.2** Ratio of maximum load capacity of prototype over half-scale model of slab-column connections.

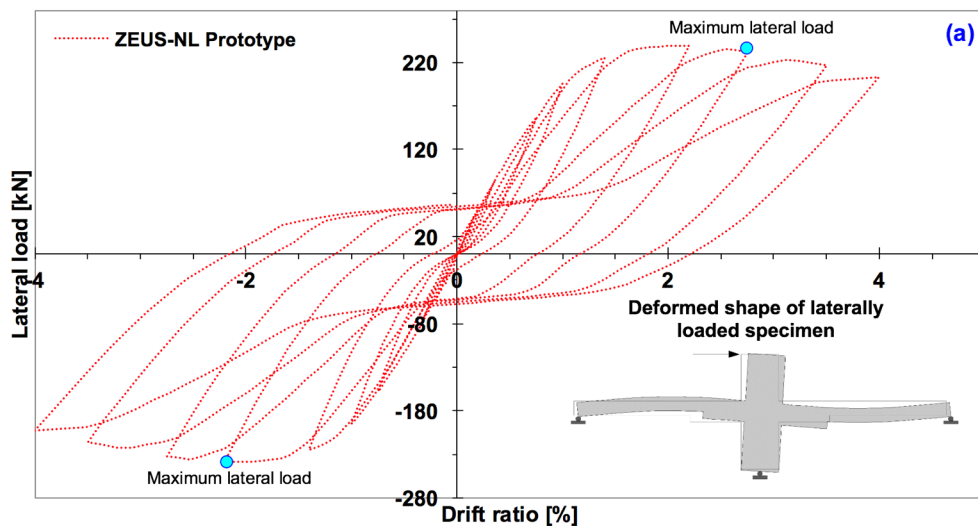
Specimen (+ or -)	Maximum load capacity of half-scale model [kN]	Maximum load capacity of prototype [kN]	Ratio of maximum load capacity between prototype and half-scale model [-]
(1)	(2)	(3)	(4)
S1+	58.3	238.7	4.09
S1-	58.5	238.6	4.07
S2+	109.1	492.4	4.51
S2-	108.6	491.5	4.53
S3+	97.2	388.7	3.99
S3-	96.7	386.3	3.99

finite element analysis has been performed using ZEUS-NL due to its capability of resulting in better pinching effect as well as high degree of accuracy in terms of hysteretic behaviour. In addition, ZEUS-NL is also preferably used as it provides an accessible and intuitive graphical user interface with simple point-and-click process thereby making it a number one choice over the other two packages.

Referring to the principles of scaling technique as lucidly explained by Harris and Sabnis (1999), the relationship of the scale and prototype model of reinforced concrete structure is generally expressed in **Equation (5.10)**.

$$P = S_i \times M \quad (5.10)$$

where  $P$  is a scale on prototype structure,  $M$  is a scale on model structure, and  $S_i$  is a scaling factor. This equation is substantially projected toward the use of scaling technique in a reinforced concrete model. Apart from this straightforward equation, however, it is of importance to note that it is not easy to model the complete inelastic behaviour of a reinforced concrete model, including the proper failure mode and capacity. It is due to the highly inelastic nature of concrete under both tensile and compressive stress states which are being a substantial problem. In addition, another major difficulty is in the reinforcing phase of this two-component material by which the strength properties and surface roughness characteristic (bond capacity) must be given a profound attention if successful models are to be realised.



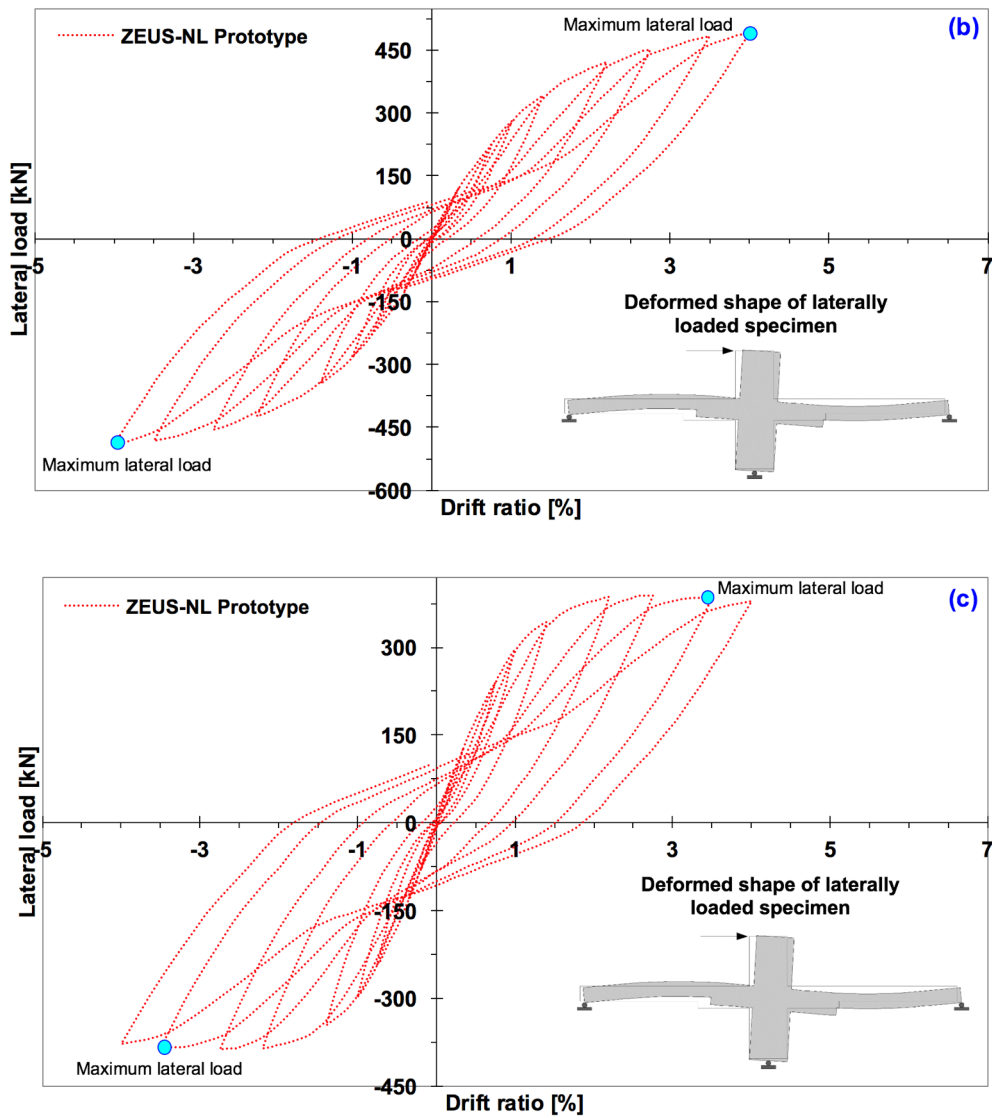


**Figure 5.30** Computed hysteretic loop of prototype slab-column specimens: (a) specimen S1, (b) specimen S2, (c) and specimen S3.

As a matter of fact, the failure criteria for model concrete subjected to multiaxial stresses should be identical with that of the prototype concrete as the lack of a well-defined failure criterion normally leads one to relax the requirement as outlined below:

- (i) Stress–strain curves must be geometrically similar to model and prototype concrete for both uniaxial compression and tension.

- (ii) The strain of the model and prototype concrete must be equal to at failure under uniaxial compression and tension ( $S_\epsilon = 1$ ).
- (iii) The stress of the model and prototype concrete must be equal to at failure under uniaxial compression and tension ( $S_\sigma = 1$ ).

For more detailed, the requirements concerning the similitude between model and prototype are summarised in **Table 5.1** (Column (4)) as *true model*.

With regard to the numerical analysis of prototype structures of slab-column connections, geometry and loading of the half-scale model were multiplied according to what is presented in **Table 5.1** (Column (5)), whereas the material properties of concrete, ECC, and reinforcing steel were left unedited as they follow the rules of similitude requirements. The results from nonlinear analysis of the prototype structure to each of test specimens are shown in **Figure 5.30**, with the summary of the ratio of maximum lateral load between model and prototype listed in **Table 5.2**. From what is seen in **Figure 5.30**, it is evident that the hysteretic loops have formed the resemblance to those which are resulted in half-scale models. It is also shown that the ratio of maximum lateral load capacity between prototype and half-scale model is 4.0, meaning the value is in good agreement with the scale factor specified in **Table 5.1** for loading.

## CHAPTER 6

### CONCLUSIONS AND RECOMMENDATIONS

#### 6.1. Conclusions

Experimental investigations into the full behaviour of slab-column connection under combined gravity and cyclic lateral load are presented. Emphasis has been made on studying the improvement of reinforced slab-column connection using the engineered cementitious composite (R/ECC) as a replacement on the use of ordinary concrete as well as the drop panel as a supplementary member at the connection. This work aims to provide direct evidence whether or not ECC is capable of displaying better hysteretic response when being subjected to high loading conditions. In addition to hysteretic responses, the work presented has been directed towards the analytical study based on the evaluation of acceptance criteria stated in ACI specification as a requirement for earthquake proof and resistant structure. The results of nonlinear numerical analysis have also been included for comparative purposes. Based on the experimental and analytical work presented, the following conclusion can be drawn:

1. The results from load-drift relationship in the form of hysteretic responses confirm that R/ECC specimen with low gravity shear ratio occupies higher lateral load capacity with the value approximately twice higher than that of RC specimen using the similar gravity shear ratio. It is also shown that upon the minimum phase of required drift ratio of 3.5%, there is no sign of strength degradation of R/ECC specimen even up to 4.0% drift ratio. In addition, R/ECC specimen subjected to intermediate gravity shear ratio resembles the similar response, in many respect, to the R/ECC specimen which utilises the low gravity shear ratio. The only exception is that the strength degradation occurs at a drift level of 4.0%. The lower-than-observed load capacity is seemingly affected by the significant development of flexural cracks on the slab thereby leading to less stable response.
2. The experimental work presented suggests that the development and propagation of cracks during the course of loading are regarded as flexural cracks, implying the reinforcing bars on slab have been yielded prior to failure

of the specimen. Analytical calculation of internal mechanisms of slab-column connection in accordance with ACI specification also confirms that the average shear ratio is less than 1.0, whereas the flexural moment ratio is greater than 1.0, owing to the fact that the failure is in flexure prior to punching. In other words, the reinforcing bars would achieve their flexural capacity before punching shear dominates the failure mechanism.

3. The results from the plot of drift capacity versus gravity shear ratio confirm that RC specimen is in good agreement with the results from prior tests using the typical slab-column connection with drop panel attached to the connection as a supplementary member. It is also shown that ACI drift limit in the form of bilinear curve tends to underestimate the behavioural response of slab-column connection. In addition to the control specimen, the drift capacity of R/ECC specimens are reasonably well with prior studies. However, it is interesting to note that despite the intermediate gravity shear ratio applied to the R/ECC specimen, the drift capacity is assessed to have been showing good response as the results from the past research. It is shown that in the gravity shear ratio of 0.25, R/ECC specimen occupies high lateral drift capacity.

4. The results relating to the evaluation of acceptance criteria based on ACI code are pin down as follows:

*a) Strength degradation*

In regard to the strength, RC specimen undergoes the degradation in strength towards the minimum required drift ratio of 3.5 with the value on the verge of load limit stated in ACI specification. On the contrary, low-gravity R/ECC specimen exhibits steady response with the lateral load not suffering from a degradation up to 4% drift level. Another case is encountered in high-gravity R/ECC specimen whereby the degradation in strength occurs at a drift ratio of 4%, with the less critical loss of lateral strength compared to RC specimen.

*b) Concept of strong/column weak beam*

The analytical results show that all specimens meet the requirement as the structure having sufficient strong in column thereby allowing the slab to

fail first before column. In accordance with the visual observation in the laboratory tests, it is found that there is only a weak development of cracks in column face nearby slab surface. This then signifies that plastic hinge mechanisms firstly develop in the slab prior to the column.

*c) Initial stiffness*

Based on the analytical results presented, all specimens have met the requirement of having an adequacy of initial stiffness in seismic design category I/II and III, meaning that flat slab can be designed as special moment resisting frame in these categories. However, none of the specimens satisfies the initial stiffness in seismic design category IV. This means that the proposed flat slab model cannot, therefore, be designed for essential buildings such as emergency treatment facilities and power-generating stations.

*d) Stiffness degradation*

In terms of stiffness degradation, the analytical evaluation confirms that all specimens have the adequacy of stiffness degradation up to 3.5% drift ratio. This then indicates that the use of drop panel as the supplementary member can hence maintain the integrity of structure when being subjected to the cyclic lateral load.

*e) Energy dissipation*

The evaluation of relative energy dissipation ratio suggests that all specimens have met the requirement, with low-gravity R/ECC specimen showing highest energy dissipation and high-gravity R/ECC specimen displaying lowest energy dissipation due to prominent effect of pinching.

5. The results from strain gauge readings imply that all reinforcing bars are in excess of their theoretical yield strain in which the strain in each reinforcing bar extends along with increasing load. It is of importance to mention that in the R/ECC specimen the strain adjacent to the joint shows the delay as the strain is still carried by the ECC.
6. The load-drift relationships obtained from nonlinear finite element analysis is shown to compare reasonably well with those obtained from experimental

work. The results have been regarded comparable as the results from nonlinear finite element analysis only show slight discrepancies.

7. Referring to the principal stress distribution at the final sequence of loading stage, it is apparent that the magnitude of stress is less than the compressive stress thereby preventing the specimen to undergo concrete crushing phenomenon. It is also shown that the distribution of stress highlighted in numerical results resembles the actual condition of the test specimen in which the concentration of stress would generally develop on the top surface of the slab across the negative moment section at the face of the column and on the bottom of the slab on the opposite face. In addition, the numerical results show that diagonal compression strut forms within the joint with the value of stress less than the compressive strength, giving the idea that damage in the joint area is yet to occur. This is also associated with experimental results whereby there is no sign of compression crushing.
8. With regard to the numerical results, the use of ECC material tends to extend the plastic hinge zone in which this is also corresponding with higher energy dissipation. It is also shown in the longitudinal strain plots obtained from nonlinear finite element analysis, the surface of strain appears as smooth strips of high strain. The longitudinal strain plots are in the similar trend with actual the crack patterns obtained from the experimental work.

## **6.2. Recommendations for Future Research**

The work presented within this study poses limitations as does with any research from prior work. However, many interesting avenues of research have been opened up as a direct result of the work described in this thesis. Given that for any further testing of a similar nature to be carried out, the following suggestions could be adopted:

1. The width of the slab should be designed wider to govern the behaviour of two-way slab thereby allowing the complex mechanics of slab due to unbalanced moments acting in two directions.

2. The axial load should be applied to the column as a means of representing the actual weight of the upper structure. The magnitude of axial load should be assigned not less than 10 percent of the nominal capacity of the column.
3. A constant gravity load simulated using prestressing strands is presumed to be convenient over other methods. Nevertheless, it is a necessity to provide sufficient instrumentation as it can be used to accurately monitor the magnitude of gravity load being applied to the specimen, as well as the loss of load due to prestressing strand relaxation.
4. The design should consider the use of thicker slab with the employment of low reinforcement ratio to upgrade the initial stiffness.
5. The slab-column connection is recommended to be tested under biaxial-lateral displacement in accordance with ACI 374.2R-13 in order to monitor the transfer of unbalanced moments, as the form of shear forces and flexural moments, in two all sides of the column.
6. The slab-column connection should be cast by extending the ECC member in order to avoid prominent cracks transpired along the substantial part of the high moment and shear forces. However, profound consideration must be taken into account as adding the volume of the matrix will increase the number of fibres used in the specimen. This condition is not preferably permitted since ECC is relatively expensive for extensive use. In addition, it would be very difficult to achieve the dispersion fibre within the matrix if the material is case in a massive batch.
7. In a level of finite element simulation, the interaction between concrete and reinforcing steel should be modelled using actual bond rather than the perfect bond. This is to ensure that bond losses of reinforcing steel can occur when being subjected to high loading conditions.

*This page intentionally left blank*

## REFERENCES

- ABAQUS, "Abaqus analysis user's manual version 6.14," *Dassault system*, 2014.
- ACI-ASCE Committee 352, "Recommendations for design of slab-column connections in monolithic reinforced concrete structures (ACI 352.1r-89)," *American Concrete Institute*, 2004.
- ACI Committee 374, "Acceptance criteria for moment frames based on structural testing and commentary (ACI 374.1-05)," *American Concrete Institute*, 2005.
- ACI Committee 374, "Guide for testing reinforced concrete structural elements under slowly applied simulated seismic loads (ACI 374.2R-13)," *American Concrete Institute*, 2005.
- ACI-ASCE Committee 421, "Guide to shear reinforcement for slabs (ACI 421.1R-08)," *American Concrete Institute*, 2008.
- ACI Committee 318, "Building code requirements for structural concrete (ACI 318-14) and commentary," *American Concrete Institute*, 2014.
- ASCE Committee, "Handbook for the seismic evaluation of buildings (FEMA 310)," *American Society of Civil Engineers*, 1998.
- ASCE Committee, "Prestandard and commentary for the seismic rehabilitation of buildings (FEMA 356)," *American Society of Civil Engineers*, 2000.
- ASCE Committee, "Minimum design loads for buildings and other structures (ASCE/SEI 7-10)," Structural Engineering Institute, American Society of Civil Engineers, Reston, Virginia, 2010.
- ASTM C618-15, "Standard specification for coal fly ash and raw or calcined natural pozzolan for use in concrete," *ASTM International*, West Conshohocken, PA, 2015, [www.astm.org](http://www.astm.org)
- ASTM C109 / C109M-16a, "Standard test method for compressive strength of hydraulic cement mortars (using 2-in. or [50-mm] cube specimens)," *ASTM International*, West Conshohocken, PA, 2016, [www.astm.org](http://www.astm.org)
- ASTM A370-05, "Standard test methods and definitions for mechanical testing of steel products," *ASTM International*, West Conshohocken, PA, 2005, [www.astm.org](http://www.astm.org)
- Baba, N., and Nishimura, Y., "Seismic behavior of RC column-beam moment frames," *The 12<sup>th</sup> World Conferences on Earthquake Engineering (WCEE)*, 2000.

- Bhide, S. B., and Collins, M. P., "Influence of axial tension on the shear capacity of reinforced concrete members," *ACI Structural Journal*, vol. 86, no. 5, pp. 570-581, 1989.
- Bompa D.V., "Behaviour of column—flat slab connections," *Doctorate Thesis Abstract*, Faculty of Civil Engineering, Technical University of CLUJ, Napoca, 2011.
- Broms, C.E., "Ductility of flat plates: comparison of shear reinforcement system," *ACI Structural Journal*, vol. 104, no. 6, pp. 703-711, 2007.
- Collins, M. P., Vecchio, F. J., Selby, R. G., and Gupta, P. R., "The failure of an offshore platform," *ACI Concrete International*, vol. 19, no. 8, pp. 29-35, 1997.
- Collins, M. P., and Kuchma D. A., "How safe are our large, lightly reinforced concrete beams, slabs, and footings," *ACI Structural Journal*, vol. 96, no. 4, pp. 482-490, 1999.
- Choi, J.W., Kim, C.S., Song, J.G., and Lee, S.G., "Effective beam width coefficients for lateral stiffness in flat plate structures," *KCI Concrete Journal*, vol. 13, no. 2, pp. 49-57, 2001.
- Dovich, L. M., and Wight, J. K., "Effective slab width model for seismic analysis of flat slab frames," *ACI Structural Journal*, vol. 102, no. 6, pp. 868-875, 2005.
- Dowell, R. K., Seible, F., and Wilson, E. W., "Pivot hysteresis model for reinforced concrete members," *ACI Structural Journal*, vol. 95, no. 5, pp. 607-617, 1998.
- Elnashai, A.S., Pinho, R., and Antoniou, "INDYAS— A program for inelastic dynamic analysis of structures," *Research Report ESEE/00-2*, Engineering Seismology and Earthquake Engineering Section, Imperial College, London, 2000.
- Elnashai, A. S., Papanikolaou, V., and Lee, D. H., "ZEUS-NL user manual", *Tutorial Book*, University of Illinois at Urbana-Champaign / Mid-America Earthquake Center, 2002.
- El-Dardiry, E., Wahyuni, E., Ji, T., and Ellis, B. R., "Improving FE models of a long-span flat concrete floor using natural frequency measurements," *Computers and Structures*, vol. 80, pp. 2145-2156, 2002.
- EN 1992-1-1: "Design of concrete structure, part 1-1: general rules for building," *European Committee for Standardization*, Brussels, Belgium, 2004.

- Erberik, M.A., and Elnashai, A.S., “Fragility analysis of flat-slab structures,” *Engineering Structures*, vol. 26, pp. 937–948, 2004.
- Fischer, G., and Li, V. C., “Effect of matrix ductility on deformation behavior of steel reinforced ECC flexural members under reversed cyclic loading conditions,” *ACI Structural Journal*, vol. 99, no. 6, pp. 781–790, 2002a.
- Fischer, G., and Li, V. C., “Deformation behavior of fiber-reinforced polymer reinforced engineering cementitious composite (ECC) flexural members under reversed cyclic loading conditions,” *ACI Structural Journal*, vol. 100, no. 1, pp. 25–35, 2003a.
- Fischer, G., and Li, V. C., “Intrinsic response control of moment resisting frames utilizing advanced composite materials and structural elements,” *ACI Structural Journal*, vol. 100, no. 2, pp. 166–176, 2003b.
- Fukuyama, H., Sato, Y., Li, V.C., Matsuzaki, Y., and Mihashi, H., “Ductile engineered cementitious composite elements for seismic structural application,” *The 12<sup>th</sup> World Conferences on Earthquake Engineering (WCEE)*, 2000.
- Fukuyama, H., Matzuzaki, Y., Sato, Y., Iso, M., and Suwada, H., “Structural performance of engineered cementitious composite elements,” *Composite and Hybrid Structures*, 6<sup>th</sup> ASCCS Int’l Conference on Steel-Concrete Composite Structures, pp. 969–976, 2000.
- Fukuyama, H., Suwada, H., and Mukai, T., “Test on high-performance wall elements with HPRCC,” *Proceedings of Int’l RILEM Workshop HPRCC in Structural Applications*, Eds. Fischer, G., and Li, V. C., published by RILEM SARL, pp. 365–367, 2006.
- Genikomsou, A.S., and Polak, M.A., “Finite element analysis of a reinforced concrete slab-column connection using ABAQUS,” *Structural Congress ASCE*, pp. 813-823, 2014.
- Ghee, A. B., Priestley, M. J. N., and Paulay, T., “Seismic shear strength of circular reinforced concrete columns,” *ACI Structural Journal*, pp. 45–59, 1989.
- Ghosh, S. K., “Earthquake resistant concrete structures inelastic response and design,” ACI SP-127, *American Concrete Institute*, Detroit, 1991.
- Gunadi, R., Budiono, B., Imran, I., and Sofwan, A., “Studi eksperimental perilaku hubungan pelat-kolom terhadap kombinasi beban gravitasi dan lateral siklis,” *Jurnal Teoretis dan Terapan Bidang Rekayasa Sipil*, vol. 19, no.3, pp. 195–205, 2012.

- Gunadi, R., “Perilaku hubungan pelat-kolom bertulangan geser terhadap beban siklis lateral,” *Disertasi*, Fakultas Teknik Sipil dan Lingkungan, Institut Teknologi Bandung, Bandung, 2014.
- Harris, H. G., and Sabnis, G. M., “Structural modelling and experimental techniques second edition, *Textbook*, Florida, USA, 1999.
- Heger, F.J., “Public safety issues in collapse of L’ambiance Plaza,” *Journal of Performance of Constructed Facilities*, vol. 5, no. 2, pp. 92–112, 1991.
- Horikoshi, T., Ogawa, A., Saito, T., and Hoshiro, H., “Properties of polyvinyl alcohol fiber as reinforcing materials for cementitious composites,” *HPFRCC International Workshop*, Honolulu, US, pp. 1–8, 2005.
- Hueste, M.D., and Wight, J.K., “Nonlinear punching shear failure model for interior slab-column connections,” *Journal of Structural Engineering Division*, vol. 125, no. 9, pp. 998–1008, 1999.
- Hueste, M.B.D., Browning, J.A., Lapage, A., and Wallace, J.W., “Seismic design criteria for slab-column connections, *ACI Structural Journal*, vol. 104, no. 4, pp. 448–458, 2007.
- Jirsa, J.O., “Determination of critical shear, moment, and deformation interactions for RC slab-column connections,” *Doctoral Thesis*, Structural Engineering of the University of Texas, Austin, 2009.
- Kabele, P., and Kanakubo, T., “Experimental and numerical investigation of shear behavior of PVA-ECC in structural elements,” *Proceedings of Fifth International RILEM Workshop on High Performance Fiber Reinforced Cementitious Composite (HPFRCC)*, Eds. Reinhardt and Naaman, pp. 137–146, 2007.
- Kakuma, K., Marsumoto, T., Hayashikawa, T., and He, X., “An analytical study on the stress-strain relation of PVA-ECC under tensile fatigue,” *Fracture Mechanics of Concrete and Concrete Structures, High Performance, Fiber Reinforced Concrete, Special Loadings and Structural Applications*, ISBN 978-89-5708-182-2, Korea Concrete Institute, pp. 1683–1690, 2010.
- Kanda, T., Watanabe, S., and Li, V. C., “Application of pseudo strain hardening cementitious composites to shear resistant structural elements,” *Fracture Mechanics of Concrete Structures Proceedings FRAMCOS-3*, AEDIFICATIO Publishers, D-79104 Freiburg, Germany, pp. 1477–1490, 1998.
- Kang, T.H-K., Wallace, J.W., and Elwood, K.J., “Dynamic tests and modeling of RC and PT slab-column connections,” *Proceedings of the 8<sup>th</sup> U.S. National Conference on Earthquake Engineering*, San Francisco, California, USA, 2006.

- Kesner, K. E., and Billington, S. L., “Tension, compression and cyclic testing of engineered cementitious composite material,” *Technical Report MCEER-04-0002*, Multidisciplinary Center for Earthquake Engineering Research, 2004.
- Kesner, K. E., and Billington, S. L., “Investigation of infill panels made from engineered cementitious composites for seismic strengthening and retrofit,” *Journal of Structural Engineering*, vol. 131, no. 11, pp. 1712–1720, 2005.
- King, S., and Dellate, N.J., “Collapse of 2000 commonwealth avenue—punching shear case study,” *Journal of Performance of Constructed Facilities*, vol. 18, no. 1, pp. 54–61, 2004.
- Kim, Y. Y., Fischer, G., and Li, V. C., “Performance of bridge deck link slabs designed with ductile ECC,” *ACI Structural Journal*, vol. 101, no. 6, pp. 792–801, 2004.
- Kinnunen, S., and Nylander, H., “Punching of concrete slabs without shear reinforcement,” *Transactions of the Royal Institute of Technology*, Stockholm, Sweden, no. 158, 1960.
- Kmiecik, P. and Kaminski, M., “Modeling of reinforced concrete structures and composite structures with concrete strength degradation taken into consideration,” *Archives of Civil and Mechanical Engineering*, vol. XI, no. 3, 2011.
- Leung, C. K. Y., Cheung, A. K. F., and Zhang, X., “Partial use of pseudo-ductile cementitious composites in concrete components to resist concentrated stress,” *Key Engineering Materials*, vol. 312, pp. 319–324, 2006.
- Li, V.C., and Wu, H-C., “Conditions for pseudo strain-hardening in fiber reinforced brittle matrix composites,” *Applied Mechanics*, vol. 45, no. 8, pp. 390–398, 1992.
- Li, V.C., and Kanda, T., “Engineered cementitious composites for structural applications,” *ASCE J. Materials in Civil Engineering*, vol. 10, no. 2, pp. 66–69, 1998.
- Li, V.C. “Reflections on the research and development of engineered cementitious composites (ECC),” *Proceedings*, DFRCC-2002, Takayama, Japan, pp. 1–22, 2002.
- Li, V.C., “Bendable composites ductile concrete for structures,” *Structure Magazine*, pp. 45–48, July 2006.
- Li, V.C., “Engineered cementitious composites (ECC) – material, structural, and durability performance,” *Concrete Construction Engineering Handbook*, Chapter 24, 2007.

- Li, M., Luu, K., and Wu, C., “Seismic performance of reinforced engineered cementitious composite shear walls,” *Earthquakes and Structures*, vol. 7, no. 5, pp. 691–704, 2014.
- Li, V. C., and Wang, S., “Failure mode and structural ductility of GFRP reinforced engineered cementitious composite beams,” *ACI Materials Journal*, vol. 99, no. 1, pp. 11–21, 2002.
- Maekawa, K., and An, X., “Shear failure and ductility of RC columns after yielding of main reinforcement,” *Engineering Fracture Mechanics*, vol. 65, no. 2, pp. 335–368, 2000.
- Mander, J. B., Priestley, M. J., and Park, R., “Theoretical stress-strain model for confined concrete,” *Journal of Structural Engineering*, vol. 114, no. 8, pp. 1804–1826, 1988.
- Martínez-Rueda, J. E., and Elnashai, A. S., “Confined concrete model under cyclic load,” *Materials and Structures*, vol. 30, no. 3, pp. 139–147, 1997.
- McHarg, P.J., Cook, W.D., Mitchell, D., and Yoon, Y-S., “Benefits of concentrated slab reinforcement and steel fibers on performance of slab-column connections,” *ACI Structural Journal*, vol. 97, no. 2, pp. 225–235, 2000.
- Megally, S. and Ghali, A., “Punching shear design of earthquake-resistance slab-column connections,” *ACI Structural Journal*, vol. 97, no. 5, pp. 720–730, 2000.
- Mousavi, S. A., Zahrai, S. M., and Bahrami-Rad, A., “Quasi-static cyclic tests on super-lightweight EPS concrete shear walls,” *Engineering Structures*, vol. 65, pp. 62–75, 2014.
- Muttoni, A., “Punching shear strength of reinforced concrete slabs without transverse reinforcement,” *ACI Structural Journal*, vol. 105, no. 4, pp. 440–450, 2008.
- Nawy, E.G., “Reinforced concrete—a fundamental approach 2<sup>th</sup> edition,” New Jersey, Prentice Hall, 1998.
- Nur, O.F., “Analisa pengaruh penambahan tulangan tekan terhadap daktilitas kurvatur balok beton bertulang,” *Jurnal Rekayasa Sipil*, vol. 5, no. 1, pp. 23–34, 2009.
- Pan, A., and Moehle, J.P., “Lateral displacement ductility of reinforced concrete flat plates,” *ACI Structural Journal*, vol. 86, no. 3, pp. 250–258, 1989.
- Pan, A., and Moehle, J.P., “An experimental study of slab-column connection,” *ACI Structural Journal*, vol. 89, no. 6, pp. 626–637, 1992.

- Parra-Montesinos, G., and Wight, J. K., “Seismic response of exterior RC column-to steel beam connections,” *Journal of Structural Engineering*, vol. 126, no. 10, pp. 1113–1121, 2000.
- Prawatwong, U., Tandian, C.H., and Warnitchai, P., “Seismic performance of post-tensioned interior slab-column connections with and without drop panel,” *The 14<sup>th</sup> World Conferences on Earthquake Engineering (WCEE)*, 2008.
- Paulay, T. and Priestley, M.J.N., “Seismic design of reinforced concrete and masonry buildings,” *Text Book*, A Wiley Interscience Publication, John Wiley & Sons Inc., New York, 1992.
- Pavlovic, M., Markovic, Z., Veljkovic, M., and Budevac, D., “Bolted shear connectors vs. headed studs behaviour in push-out tests,” *Journal of Constructional Steel Research*, vol. 88, pp. 134–149, 2013.
- Qian, K., and Li, B., “Experimental study of drop-panel effects on response of reinforced concrete flat slabs after loss of corner column,” *ACI Structural Journal*, vol. 110, no. 2, pp. 319–330, 2013.
- Qian, S., and Li, V. C., “Influence of concrete material ductility on the shear response of stud connection,” *ACI Materials Journal*, vol. 103, no. 1, pp. 60–66, 2006.
- Qian, S., and Li, V. C., “Simplified inverse method for determining the tensile strain capacity of strain hardening cementitious composites,” *Journal of Advanced Concrete Technology*, vol. 5, no. 2, pp. 235–246, 2007.
- Rashid, M.A., and Mansur, M.A., “Reinforced high-strength concrete beams in flexure,” *ACI Structural Journal*, vol. 102, no. 5, pp. 462–471, 2005.
- Robertson, I.N., and Durrani, A.J., “Gravity load effect on seismic behavior of interior slab-column connection,” *ACI Structural Journal*, vol. 89, no. 1, pp. 37–45, 1992.
- Robertson, I.N., Kawai, T., Lee, J., and Enomoto, B., “Cyclic testing of slab-column connection with shear reinforcement,” *ACI Structural Journal*, vol. 99, no. 5, pp. 605–613, 2002.
- Roth, M.J., “Flexural and tensile properties of thin, very high-strength, fiber-reinforced concrete panels,” *Final Report of Geotechnical and Structures Laboratory*, 2008.
- Sahmaran, M., and Li, V.C., “Durability of mechanically loaded engineered cementitious composites under highly alkaline environments,” *Cement and Concrete Composite Journal*, vol. 30, no. 2, pp. 72–81, 2008.

- Sathawane, A.A., and Deotale, R.S., “Analysis and design of flat slab and grid slab and their cost comparison,” *International Journal of Advanced Technology in Civil Engineering*, ISSN: 223 –5721, vol. 1, no. 2, pp. 122–126, 2012.
- Shaaban, A.M., and Gesund, H., “Punching shear strength of steel fiber-reinforced concrete flat plates,” *ACI Structural Journal*, vol. 91, no. 1, pp. 406–414, 1994.
- Shah, A. A., Dietz, J., Tue, N.V., and Koenig, G., “Experimental investigation of column-slab joints,” *ACI Structural Journal*, vol. 102, no.5, pp. 103–113, 2005.
- Sherwood, E. G., Lubell, A. S., Bentz, E, C., & Collins, M. P., “One-way shear strength of thick slab and wide beams,” *ACI Structural Journal*, vol. 103, no. 6, pp. 794–802, 2006.
- Shimizu, K., Kanakubo, T., Kanda, T., and Nagai, S., In *Proceedings Int’l RILEM Workshop HPRCC in structural Applications*, Eds. Fischer, G., and Li, V. C., published by RILEM SARL, pp. 443–451, 2006.
- SNI Committee, “Tata cara perencanaan ketahanan gempa untuk struktur bangunan dan non gedung (SNI 1726:2012),” *Badan Standardisasi Nasional Indonesia*, Jakarta, 2012.
- SNI Committee, “Tata cara perhitungan struktur beton untuk bangunan gedung (SNI 2847:2013),” *Badan Standardisasi Nasional Indonesia*, Jakarta, 2013.
- Soe, K.T., Zhang, Y.X., and Zhang, L.C., “Impact resistance of hybrid-fiber engineered cementitious composite panels,” *Composite Structure*, vol. 104, pp. 320–330, 2013.
- Sotoud, S., and Aboutaha, R.S., “Performance of RC bridge columns subjected to lateral loading,” *Proceeding of Istanbul Bridge Conference*, 2014.
- Suryanto, B., Nagai, K., and Maekawa, K., “Modeling and analysis of shear-critical ECC members with anisotropic stress and strain fields,” *Journal of Advanced Concrete Technology*, vol. 8, pp. 239–258, 2010.
- Suryanto, B., Maekawa, K., and Nagai, K., “Time-dependent deformations of PVA-ECC under sustained loads: correlation with plasticity and damage,” *Technical paper*, vol. 34, no. 1, pp. 280–285, 2012
- Swamy, R.N., and Ali, S.A.R., “Punching shear behavior of reinforced slab-column connections with steel fiber concrete,” *ACI Journal*, vol. 79, no. 5, pp. 392–406, 1982.

- Takeda, T., Sozen, M. A., and Nielsen, N. N., "Reinforced concrete response to simulated earthquakes," *Journal of Structural Engineering Divisions*, vol. 96, no. 12, pp. 2257–2273, 1970.
- Tambusay, A., Suprobo, P., Faimun, & Amiruddin, A. A., "Finite element modelling of a reinforced concrete slab-column connection under cyclic lateral load," *International Journal of Applied Engineering Research* ISSN 0973–4562, vol. 12, no. 9, pp. 1987–1993, 2017.
- Tambusay, A., Suprobo, P., Faimun, & Amiruddin, A. A., "Finite element analysis on the behaviour of slab-column connections using PVA-ECC material," *Jurnal Teknologi (Science and Engineering)*, vol. 79, no. 5, pp. 23–32, 2017.
- Tavio and Hemawan, L., "Studi lebar efektif pelat pada struktur flate plate akibat beban gempa," *Dinamika TEKNIK SIPIL*, Akreditasi BAN DIKTI No. 110/DIKTI/Kep/2009, 2009
- Tegos, J.A., and Tsonos, A.G., "Punching strength decay of slab-column connections under seismic loading," Eleventh World Conference on Earthquake Engineering, ISBN: 0 08 042822 3, 1996.
- Terzic, V., Mackie, K., & Stojadinovic, B., "Experimental evaluation of the residual axial load capacity of circular bridge columns," *The 14<sup>th</sup> World Conference on Earthquake Engineering (WCEE)*, 2008.
- Tian, Y., Jirsa, J.O., Bayrak, O., Widanto, and Argudo, J.F., "Behavior of slab-column connections of existing flat-plate structures," *ACI Structural Journal*, vol. 105, no. 5, pp. 561–569, 2008.
- Walter, R., Li, V. C., and Stang, H., "Comparison of FRC and ECC in a composite bridge deck," *Proceedings of 5<sup>th</sup> PhD Symposium in Civil Engineering*, Delft, Netherlands, pp. 477–484, 2004.
- Wan, S., Loh, C. H., and Peng, S. Y., "Experimental and theoretical study on softening and pinching effects of bridge column," *Soil Dynamic and Earthquake Engineering*, vol. 21, pp. 75–81, 2001.
- Wang, T., and Hsu, T.T.C., "Nonlinear finite element analysis of concrete structures using new constitutive models," *Computers and Structures*, vol. 79, Iss. 32, pp. 2781–2791, 2001.

*This page intentionally left blank*

## APPENDIX A: PRELIMINARY DESIGN OF SPECIMEN S1

### A.1. Material Properties

Concrete strength, $f_c'$	=	45 MPa
Yield strength of slab reinforcing bar, $f_{yp}$	=	325 MPa
Yield strength of column longitudinal bar, $f_{yc}$	=	395 MPa
Yield strength of stirrup, $f_{ys}$	=	327 MPa

### A.2. Specimen Dimension

According to **Figure 3.2**, the following details of dimensions of S1 are:

Slab length, $L_s$	=	3000 mm
Slab width, $B_s$	=	1500 mm
Slab height, $h_s$	=	120 mm
Slab effective depth, $d_s$	=	100 mm
Drop panel length, $L_d$	=	1000 mm
Drop panel width, $B_d$	=	600 mm
Drop panel height, $h_d$	=	180 mm
Drop panel effective depth, $d_d$	=	160 mm
Column height, $H$	=	1750 mm
Column cross-section, $c_1 = c_2 = c$	=	300 mm
Column effective depth, $d_c$	=	275 mm
Critical region at slab, $c_s = d_s + c$	=	400 mm
Critical region at drop panel, $c_d = d_d + L_d$	=	1160 mm
Length of column strip, $B_s/2$	=	750 mm
Length of slab effective width, $c + 3h$	=	660 mm

### A.3. Approximation of Column Reinforcement

According to **Figure 3.3(c)**, the following details of column reinforcement are:

Number of reinforcing bars, $n_c$	=	12 Nos
Diameter of longitudinal bar, $D_c$	=	13 mm

Diameter of web reinforcement, $D_s$	= 6 mm
Stirrup spacing, $s$	= 50 mm
Concrete cover, $d'$	= 20 mm
Area of 1 longitudinal bar, $A_s = \frac{1}{4} \times \pi \times D_c^2$	= 132.7 mm <sup>2</sup>
Area of 12 longitudinal bars, $n_c A_s$	= 1592.8 mm <sup>2</sup>
Cross-sectional area of stirrup, $A_s = 2 \times \frac{1}{4} \times \pi \times D_s^2$	= 56.5 mm <sup>2</sup>

#### A.4. Approximation of Slab Reinforcement

According to **Figure 3.3(a)** and **Figure 3.3(b)**, the following details of slab reinforcement are:

Number of top reinforcing bars, $n_t$	= 19 Nos
Number of bottom reinforcing bars, $n_b$	= 10 Nos
Diameter of slab rebar, $D_p$	= 8 mm
Concrete cover, $d'$	= 15 mm
Area of 1 longitudinal bar, $A_s = \frac{1}{4} \times \pi \times D_p^2$	= 50.3 mm <sup>2</sup>

#### A.5. Gravity Shear Ratio

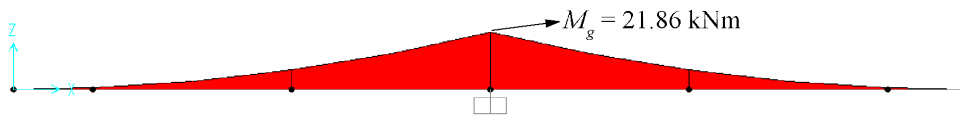


**Figure A1.** Moment diagram of specimen S1 due to gravity load

With regard to moment due to gravity loading as shown in **Figure A1**, self-weight of the specimen as loading input is calculated based on specific gravity of concrete multiplied by total width and height of slab and drop panel. Superimposed dead load is given afterwards as a modifiable variable to determine the magnitude of gravity shear ratio being applied to the specimen. Details of gravity loads are summarised below:

$$\begin{aligned} \text{Self-weight, } Q_{sw} &= 4.32 \text{ kN/m} \\ \text{Superimposed dead load as two-point loading, } P_{sdl} &= 40 \text{ kN} \end{aligned}$$

To obtain shear forces acting along the shear span, simulation through the use of structural analysis package namely SAP2000 is performed. Presented in **Figure A2(a)**, the value of shear force alongside the span is already known. Due to the presence of local thickening at the connection, the critical region of test specimen consists of two locations i.e. critical region nearby column face ( $c + d_d$ ) and critical region nearby drop panel face ( $L_d + d_s$ ) (for visual information see **Figure A2(b)**). It is also should be noted, as the geometry of slab is in the form of one-way slab, area of critical region is not calculated by multiplying perimeter ( $b_o$ ) with slab or drop panel effective depth, instead perimeter is replaced with lines ( $b_o'$ ) taking into account two lines perpendicular to loading direction. Details of calculations with regard to gravity shear ratio are presented below:

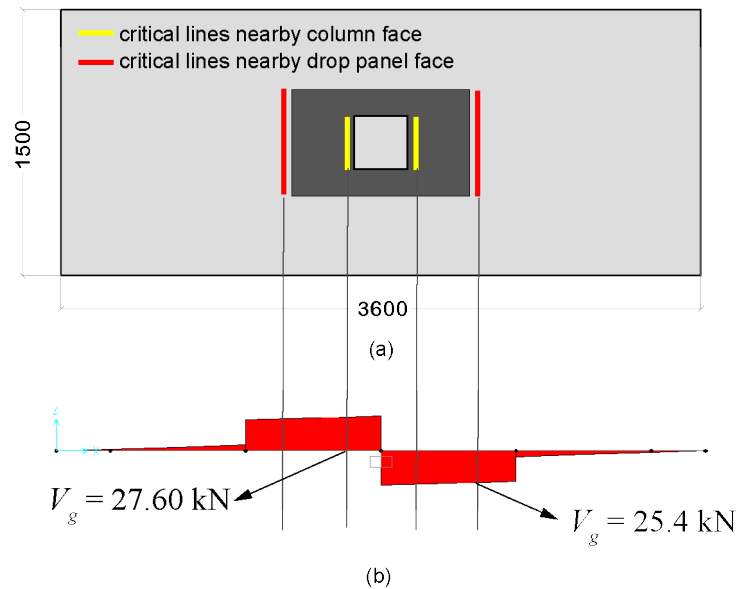


**Figure A2.** (a) plan and (b) Shear diagram of specimen S1 due to gravity load

$$\begin{aligned} \text{Direct shear force located at } (c + d_d), V_g &= 27.6 \text{ kN} \\ \text{Drop panel effective depth, } d_d &= 160 \text{ mm} \\ \text{Critical lines, } b_o' = 2 \times (c + d_d) &= 920 \text{ mm} \end{aligned}$$

$$\text{Nominal shear stress, } v_n = v_c = \frac{1}{3} \sqrt{f'_c} = 2.24 \text{ MPa}$$

$$\text{Gravity shear ratio, } \frac{V_g / (b'_o \times d_d)}{v_n} = 0.08$$

$$\text{Direct shear force located at } (L_d + d_s), V_g = 25.4 \text{ kN}$$

$$\text{Slab effective depth, } d_s = 100 \text{ mm}$$

$$\text{Critical lines, } b'_o = 2 \times (L_d + d_s) = 2200 \text{ mm}$$

$$\text{Nominal shear stress, } v_n = v_c = \frac{1}{3} \sqrt{f'_c} = 2.24 \text{ MPa}$$

$$\text{Gravity shear ratio, } \frac{V_g (b'_o \times d_s)}{v_n} = 0.05$$

According to calculation, it is found that gravity shear ratio nearby column face shows a higher value than gravity shear ratio near to drop panel face. Therefore, the value of gravity shear ratio of 0.08 should be taken into account.

#### A.6. Internal Forces due to Lateral Load

$$\text{Allowable drift ratio, } \Delta_a = 0.01$$

$$\text{Strength reduction factor, } \phi = 0.9$$

$$\text{Displacement amplification factor, } C_d = 5.5$$

$$\text{Limiting drift ratio, } LDR = \frac{\Delta_a}{\phi C_d} = 0.2\%$$

$$\text{Lateral load obtained from backbone curve, } L_x = 16.34 \text{ kN}$$

$$\text{Unbalanced moment, } M_u = L_x \times H = 28.6 \text{ kNm}$$

$$\text{Fraction of unbalanced moment in flexure, } \gamma_f = 0.6$$

#### A.7. Inspection of Slab Reinforcement within Total Width ( $B_s$ )

$$\text{Slab total width, } B_s = 1500 \text{ mm}$$

$$\text{Number of top reinforcing bars, } n_t = 19 \text{ Nos}$$

$$\text{Diameter of slab reinforcing bar, } D_p = 8 \text{ mm}$$

$$\text{Area of 19 reinforcing bars, } n_t A_s = 955.04 \text{ mm}^2$$

Depth of equivalent rectangular stress block,

$$a = \frac{A_s \times f_y}{0.85 \times f'_c \times B_s} = 6.38 \text{ mm}$$

$$\text{Nominal moment, } M_n = A_s \times f_y \times \left( d - \frac{a}{2} \right) = 37.93 \text{ kNm}$$

$$\text{Moment obtained from SAP2000, } M_{load} = M_g = 21.86 \text{ kNm}$$

$$\text{Ratio of } M_n/M_{load} = 1.74$$

#### A.8. Inspection of Slab Reinforcement within Column Strip ( $B_s/2$ )

$$\text{Slab total width, } B_s/2 = 750 \text{ mm}$$

$$\text{Number of top reinforcing bars, } n_t = 15 \text{ Nos}$$

$$\text{Diameter of slab reinforcing bar, } D_p = 8 \text{ mm}$$

$$\text{Area of 15 reinforcing bars, } n_t A_s = 753.98 \text{ mm}^2$$

Depth of equivalent rectangular stress block,

$$a = \frac{A_s \times f_y}{0.85 \times f'_c \times B_s / 2} = 10.07 \text{ mm}$$

$$\text{Nominal moment, } M_n = A_s \times f_y \times \left( d - \frac{a}{2} \right) = 29.38 \text{ kNm}$$

Ultimate moment obtained from SAP2000,

$$M_{load} = \frac{M_g + M_u}{2} = 25.23 \text{ kNm}$$

$$\text{Ratio of } M_n/M_{load} = 1.16$$

#### A.9. Inspection of Slab Reinforcement Within Slab Effective Width ( $c + 3h$ )

$$\text{Slab total width, } c + 3h = 660 \text{ mm}$$

$$\text{Number of top reinforcing bars, } n_t = 13 \text{ Nos}$$

$$\text{Diameter of slab reinforcing bar, } D_p = 8 \text{ mm}$$

$$\text{Area of 13 reinforcing bars, } n_t A_s = 653.45 \text{ mm}^2$$

Depth of equivalent rectangular stress block,

$$a = \frac{A_s \times f_y}{0.85 \times f'_c \times B_s / 2} = 9.91 \text{ mm}$$

$$\text{Nominal moment, } M_n = A_s \times f_y \times \left( d - \frac{a}{2} \right) = 32.12 \text{ kNm}$$

Ultimate moment obtained from SAP2000,

$$M_{load} = \gamma_f \left( \frac{M_u}{2} \right) + \frac{c + 3h}{B_s} \times M_g = 18.20 \text{ kNm}$$

$$\text{Ratio of } M_n/M_{load} = 1.76$$

**Note:** The ratio of  $M_n/M_{load}$  with the value in excess 1.0 indicates that during the course of loading, the slab reinforcing bars have not been yielded.

## APPENDIX B: PRELIMINARY DESIGN OF SPECIMEN S2

### B.1. Material Properties

Strength of concrete and ECC, $f_c'$	= 45 MPa
Yield strength of slab reinforcing bar, $f_{yp}$	= 325 MPa
Yield strength of column longitudinal bar, $f_{yc}$	= 395 MPa
Yield strength of stirrup, $f_{ys}$	= 327 MPa

### B.2. Specimen Dimension

According to **Figure 3.2**, the following details of dimensions of S2 are:

Slab length, $L_s$	= 3000 mm
Slab width, $B_s$	= 1500 mm
Slab height, $h_s$	= 120 mm
Slab effective depth, $d_s$	= 100 mm
Drop panel length, $L_d$	= 1000 mm
Drop panel width, $B_d$	= 600 mm
Drop panel height, $h_d$	= 180 mm
Drop panel effective depth, $d_d$	= 160 mm
Column height, $H$	= 1750 mm
Column cross-section, $c_1 = c_2 = c$	= 300 mm
Column effective depth, $d_c$	= 275 mm
Critical region at slab, $c_s = d_s + c$	= 400 mm
Critical region at drop panel, $c_d = d_d + L_d$	= 1160 mm
Length of column strip, $B_s/2$	= 750 mm
Length of slab effective width, $c + 3h$	= 660 mm

### B.3. Approximation of Column Reinforcement

According to **Figure 3.3(c)**, the following details of column reinforcement are:

Number of reinforcing bars, $n_c$	= 12 Nos
Diameter of longitudinal bar, $D_c$	= 13 mm

Diameter of web reinforcement, $D_s$	= 6 mm
Stirrup spacing, $s$	= 50 mm
Concrete cover, $d'$	= 20 mm
Area of 1 longitudinal bar, $A_s = \frac{1}{4} \times \pi \times D_c^2$	= 132.7 mm <sup>2</sup>
Area of 12 longitudinal bars, $n_c A_s$	= 1592.8 mm <sup>2</sup>
Cross-sectional area of stirrup, $A_s = 2 \times \frac{1}{4} \times \pi \times D_s^2$	= 56.5 mm <sup>2</sup>

#### B.4. Approximation of Slab Reinforcement

According to **Figure 3.3(a)** and **Figure 3.3(b)**, the following details of slab reinforcement are:

Number of top reinforcing bars, $n_t$	= 19 Nos
Number of bottom reinforcing bars, $n_b$	= 10 Nos
Diameter of slab rebar, $D_p$	= 8 mm
Concrete cover, $d'$	= 15 mm
Area of 1 longitudinal bar, $A_s = \frac{1}{4} \times \pi \times D_p^2$	= 50.3 mm <sup>2</sup>

#### B.5. Gravity Shear Ratio

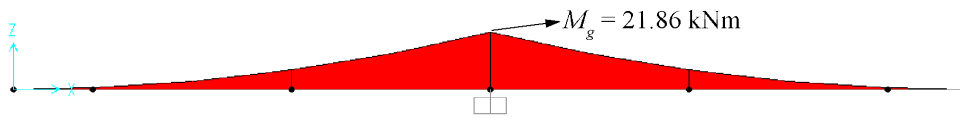


**Figure B1.** Moment diagram of specimen S2 due to gravity load

With regard to moment due to gravity loading as shown in **Figure B1**, self-weight of the specimen as loading input is calculated based on specific gravity of concrete multiplied by total width and height of slab and drop panel. Superimposed dead load is given afterwards as a modifiable variable to determine the magnitude of gravity shear ratio being applied to the specimen. Details of gravity loads are summarised below:

$$\begin{aligned} \text{Self-weight, } Q_{sw} &= 4.32 \text{ kN/m} \\ \text{Superimposed dead load as two-point loading, } P_{sdl} &= 40 \text{ kN} \end{aligned}$$

To obtain shear forces acting along the shear span, simulation through the use of structural analysis package namely SAP2000 is performed. Presented in **Figure B2(a)**, the value of shear force alongside the span is already known. Due to the presence of local thickening at the connection, the critical region of test specimen consists of two locations i.e. critical region nearby column face ( $c + d_d$ ) and critical region nearby drop panel face ( $L_d + d_s$ ) (for visual information see **Figure B2(b)**). It is also should be noted, as the geometry of slab is in the form of one-way slab, area of critical region is not calculated by multiplying perimeter ( $b_o$ ) with slab or drop panel effective depth, instead perimeter is replaced with lines ( $b_o'$ ) taking into account two lines perpendicular to loading direction. Details of calculations with regard to gravity shear ratio are presented below:

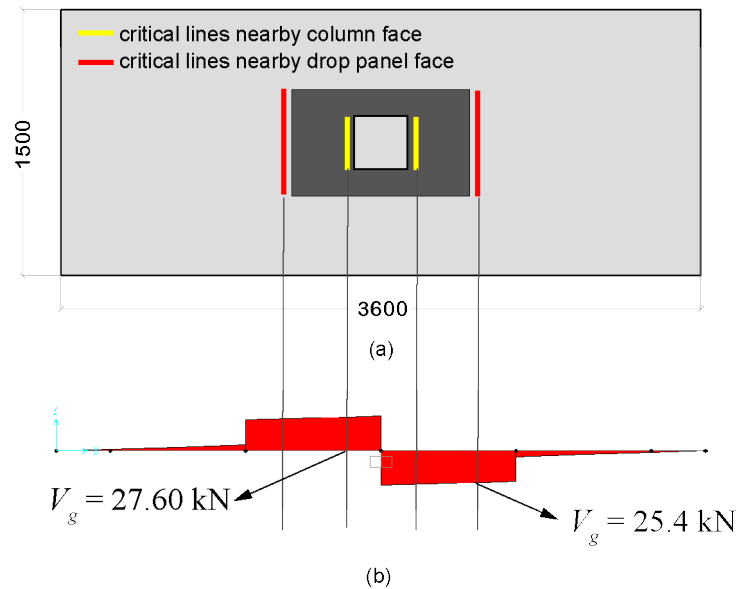


**Figure B2.** (a) plan and (b) Shear diagram of specimen S2 due to gravity load

$$\begin{aligned} \text{Direct shear force located at } (c + d_d), V_g &= 27.6 \text{ kN} \\ \text{Drop panel effective depth, } d_d &= 160 \text{ mm} \\ \text{Critical lines, } b_o' = 2 \times (c + d_d) &= 920 \text{ mm} \end{aligned}$$

$$\text{Nominal shear stress, } v_n = v_c + v_f = \frac{1}{3} \sqrt{f'_c} + \left( \frac{f_t}{\gamma_b} \right) = 4.55 \text{ MPa}$$

$$\text{Gravity shear ratio, } \frac{V_g / (b'_o \times d_d)}{v_n} = 0.04$$

$$\text{Direct shear force located at } (L_d + d_s), V_g = 25.4 \text{ kN}$$

$$\text{Slab effective depth, } d_s = 100 \text{ mm}$$

$$\text{Critical lines, } b'_o = 2 \times (L_d + d_s) = 2200 \text{ mm}$$

$$\text{Nominal shear stress, } v_n = v_c = \frac{1}{3} \sqrt{f'_c} = 2.24 \text{ MPa}$$

$$\text{Gravity shear ratio, } \frac{V_g (b'_o \times d_s)}{v_n} = 0.05$$

According to calculation, it is found that gravity shear ratio nearby drop panel face shows a higher value than gravity shear ratio near to column face. Therefore, the value of gravity shear ratio of 0.05 should be taken into account.

#### B.6. Internal Forces due to Lateral Load

$$\text{Allowable drift ratio, } \Delta_a = 0.01$$

$$\text{Strength reduction factor, } \phi = 0.9$$

$$\text{Displacement amplification factor, } C_d = 5.5$$

$$\text{Limiting drift ratio, } LDR = \frac{\Delta_a}{\phi C_d} = 0.2\%$$

$$\text{Lateral load obtained from backbone curve, } L_x = 20.35 \text{ kN}$$

$$\text{Unbalanced moment, } M_u = L_x \times H = 35.6 \text{ kNm}$$

$$\text{Fraction of unbalanced moment in flexure, } \gamma_f = 0.6$$

#### B.7. Inspection of Slab Reinforcement within Total Width ( $B_s$ )

$$\text{Slab total width, } B_s = 1500 \text{ mm}$$

$$\text{Number of top reinforcing bars, } n_t = 19 \text{ Nos}$$

$$\text{Diameter of slab reinforcing bar, } D_p = 8 \text{ mm}$$

$$\text{Area of 19 reinforcing bars, } n_t A_s = 955.04 \text{ mm}^2$$

Depth of equivalent rectangular stress block,

$$a = \frac{A_s \times f_y}{0.85 \times f'_c \times B_s} = 6.38 \text{ mm}$$

$$\text{Nominal moment, } M_n = A_s \times f_y \times \left( d - \frac{a}{2} \right) = 37.93 \text{ kNm}$$

$$\text{Moment obtained from SAP2000, } M_{load} = M_g = 21.86 \text{ kNm}$$

$$\text{Ratio of } M_n/M_{load} = 1.73$$

### **B.8. Inspection of Slab Reinforcement within Column Strip ( $B_s/2$ )**

$$\text{Slab total width, } B_s/2 = 750 \text{ mm}$$

$$\text{Number of top reinforcing bars, } n_t = 15 \text{ Nos}$$

$$\text{Diameter of slab reinforcing bar, } D_p = 8 \text{ mm}$$

$$\text{Area of 15 reinforcing bars, } n_t A_s = 753.98 \text{ mm}^2$$

Depth of equivalent rectangular stress block,

$$a = \frac{A_s \times f_y}{0.85 \times f'_c \times B_s / 2} = 10.07 \text{ mm}$$

$$\text{Nominal moment, } M_n = A_s \times f_y \times \left( d - \frac{a}{2} \right) = 29.38 \text{ kNm}$$

Ultimate moment obtained from SAP2000,

$$M_{load} = \frac{M_g + M_u}{2} = 28.73 \text{ kNm}$$

$$\text{Ratio of } M_n/M_{load} = 1.02$$

### **B.9. Inspection of Slab Reinforcement Within Slab Effective Width ( $c + 3h$ )**

$$\text{Slab total width, } c + 3h = 660 \text{ mm}$$

$$\text{Number of top reinforcing bars, } n_t = 13 \text{ Nos}$$

$$\text{Diameter of slab reinforcing bar, } D_p = 8 \text{ mm}$$

$$\text{Area of 13 reinforcing bars, } n_t A_s = 653.45 \text{ mm}^2$$

Depth of equivalent rectangular stress block,

$$a = \frac{A_s \times f_y}{0.85 \times f'_c \times B_s / 2} = 9.91 \text{ mm}$$

$$\text{Nominal moment, } M_n = A_s \times f_y \times \left( d - \frac{a}{2} \right) = 32.12 \text{ kNm}$$

Ultimate moment obtained from SAP2000,

$$M_{load} = \gamma_f \left( \frac{M_u}{2} \right) + \frac{c + 3h}{B_s} \times M_g = 20.3 \text{ kNm}$$

$$\text{Ratio of } M_n/M_{load} = 1.58$$

**Note:** The ratio of  $M_n/M_{load}$  with the value in excess 1.0 indicates that during the course of loading, the slab reinforcing bars have not been yielded.

## APPENDIX C: PRELIMINARY DESIGN OF SPECIMEN S3

### C.1. Material Properties

Strength of concrete and ECC, $f_c'$	= 45 MPa
Yield strength of slab reinforcing bar, $f_{yp}$	= 325 MPa
Yield strength of column longitudinal bar, $f_{yc}$	= 395 MPa
Yield strength of stirrup, $f_{ys}$	= 327 MPa

### C.2. Specimen Dimension

According to **Figure 3.2**, the following details of dimensions of S3 are:

Slab length, $L_s$	= 3000 mm
Slab width, $B_s$	= 1500 mm
Slab height, $h_s$	= 120 mm
Slab effective depth, $d_s$	= 100 mm
Drop panel length, $L_d$	= 1000 mm
Drop panel width, $B_d$	= 600 mm
Drop panel height, $h_d$	= 180 mm
Drop panel effective depth, $d_d$	= 160 mm
Column height, $H$	= 1750 mm
Column cross-section, $c_1 = c_2 = c$	= 300 mm
Column effective depth, $d_c$	= 275 mm
Critical region at slab, $c_s = d_s + c$	= 400 mm
Critical region at drop panel, $c_d = d_d + L_d$	= 1160 mm
Length of column strip, $B_s/2$	= 750 mm
Length of slab effective width, $c + 3h$	= 660 mm

### C.3. Approximation of Column Reinforcement

According to **Figure 3.3(c)**, the following details of column reinforcement are:

Number of reinforcing bars, $n_c$	= 12 Nos
Diameter of longitudinal bar, $D_c$	= 13 mm

Diameter of web reinforcement, $D_s$	= 6 mm
Stirrup spacing, $s$	= 50 mm
Concrete cover, $d'$	= 20 mm
Area of 1 longitudinal bar, $A_s = \frac{1}{4} \times \pi \times D_c^2$	= 132.7 mm <sup>2</sup>
Area of 12 longitudinal bars, $n_c A_s$	= 1592.8 mm <sup>2</sup>
Cross-sectional area of stirrup, $A_s = 2 \times \frac{1}{4} \times \pi \times D_s^2$	= 56.5 mm <sup>2</sup>

#### C.4. Approximation of Slab Reinforcement

According to **Figure 3.3(a)** and **Figure 3.3(b)**, the following details of slab reinforcement are:

Number of top reinforcing bars, $n_t$	= 19 Nos
Number of bottom reinforcing bars, $n_b$	= 10 Nos
Diameter of slab rebar, $D_p$	= 8 mm
Concrete cover, $d'$	= 15 mm
Area of 1 longitudinal bar, $A_s = \frac{1}{4} \times \pi \times D_p^2$	= 50.3 mm <sup>2</sup>

#### C.5. Gravity Shear Ratio

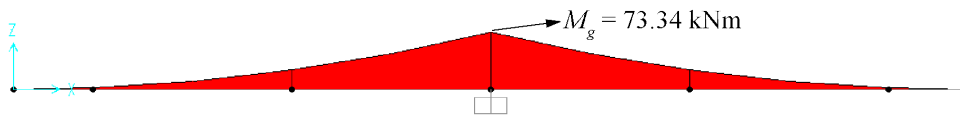


**Figure C1.** Moment diagram of specimen S3 due to gravity load

With regard to moment due to gravity loading as shown in **Figure C1**, self-weight of the specimen as loading input is calculated based on specific gravity of concrete multiplied by total width and height of slab and drop panel. Superimposed dead load is given afterwards as a modifiable variable to determine the magnitude of gravity shear ratio being applied to the specimen. Details of gravity loads are summarised below:

$$\begin{aligned} \text{Self-weight, } Q_{sw} &= 4.32 \text{ kN/m} \\ \text{Superimposed dead load as two-point loading, } P_{sdl} &= 240 \text{ kN} \end{aligned}$$

To obtain shear forces acting along the shear span, simulation through the use of structural analysis package namely SAP2000 is performed. Presented in **Figure C2(a)**, the value of shear force alongside the span is already known. Due to the presence of local thickening at the connection, the critical region of test specimen consists of two locations i.e. critical region nearby column face ( $c + d_d$ ) and critical region nearby drop panel face ( $L_d + d_s$ ) (for visual information see **Figure C2(b)**). It is also should be noted, as the geometry of slab is in the form of one-way slab, area of critical region is not calculated by multiplying perimeter ( $b_o$ ) with slab or drop panel effective depth, instead perimeter is replaced with lines ( $b_o'$ ) taking into account two lines perpendicular to loading direction. Details of calculations with regard to gravity shear ratio are presented below:

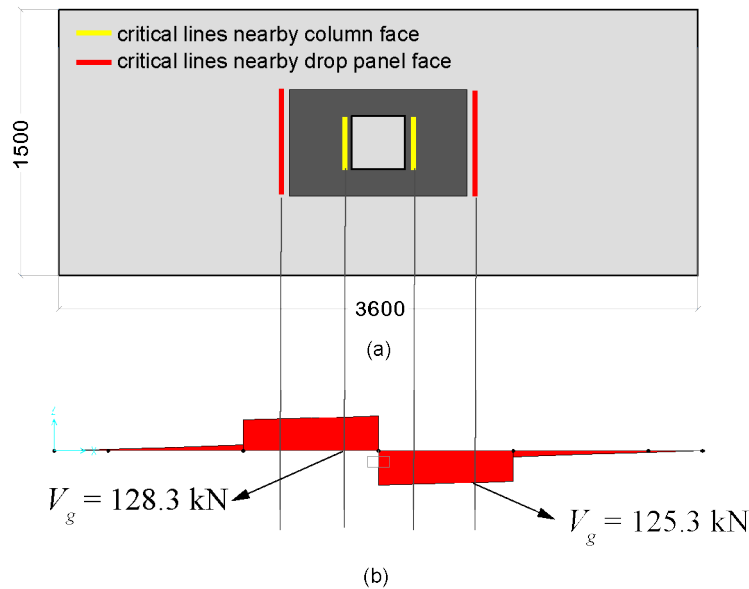


**Figure C2.** (a) plan and (b) Shear diagram of specimen S3 due to gravity load

$$\begin{aligned} \text{Direct shear force located at } (c + d_d), V_g &= 128.3 \text{ kN} \\ \text{Drop panel effective depth, } d_d &= 160 \text{ mm} \\ \text{Critical lines, } b_o' = 2 \times (c + d_d) &= 920 \text{ mm} \end{aligned}$$

$$\text{Nominal shear stress, } v_n = v_c + v_f = \frac{1}{3} \sqrt{f'_c} + \left( \frac{f_t}{\gamma_b} \right) = 4.55 \text{ MPa}$$

$$\text{Gravity shear ratio, } \frac{V_g / (b'_o \times d_d)}{v_n} = 0.19$$

$$\text{Direct shear force located at } (L_d + d_s), V_g = 125.3 \text{ kN}$$

$$\text{Slab effective depth, } d_s = 100 \text{ mm}$$

$$\text{Critical lines, } b'_o = 2 \times (L_d + d_s) = 2200 \text{ mm}$$

$$\text{Nominal shear stress, } v_n = v_c = \frac{1}{3} \sqrt{f'_c} = 2.24 \text{ MPa}$$

$$\text{Gravity shear ratio, } \frac{V_g (b'_o \times d_s)}{v_n} = 0.25$$

According to calculation, it is found that gravity shear ratio nearby drop panel face shows a higher value than gravity shear ratio near to column face. Therefore, the value of gravity shear ratio of 0.25 should be taken into account.

### C.6. Internal Forces due to Lateral Load

$$\text{Allowable drift ratio, } \Delta_a = 0.01$$

$$\text{Strength reduction factor, } \phi = 0.9$$

$$\text{Displacement amplification factor, } C_d = 5.5$$

$$\text{Limiting drift ratio, } LDR = \frac{\Delta_a}{\phi C_d} = 0.2\%$$

$$\text{Lateral load obtained from backbone curve, } L_x = 20.52 \text{ kN}$$

$$\text{Unbalanced moment, } M_u = L_x \times H = 35.9 \text{ kNm}$$

$$\text{Fraction of unbalanced moment in flexure, } \gamma_f = 0.6$$

### C.7. Inspection of Slab Reinforcement within Total Width ( $B_s$ )

$$\text{Slab total width, } B_s = 1500 \text{ mm}$$

$$\text{Number of top reinforcing bars, } n_t = 19 \text{ Nos}$$

$$\text{Diameter of slab reinforcing bar, } D_p = 8 \text{ mm}$$

$$\text{Area of 19 reinforcing bars, } n_t A_s = 955.04 \text{ mm}^2$$

Depth of equivalent rectangular stress block,

$$a = \frac{A_s \times f_y}{0.85 \times f'_c \times B_s} = 6.38 \text{ mm}$$

$$\text{Nominal moment, } M_n = A_s \times f_y \times \left( d - \frac{a}{2} \right) = 37.93 \text{ kNm}$$

$$\text{Moment obtained from SAP2000, } M_{load} = M_g = 73.34 \text{ kNm}$$

$$\text{Ratio of } M_n/M_{load} = \mathbf{0.52}$$

### C.8. Inspection of Slab Reinforcement within Column Strip ( $B_s/2$ )

$$\text{Slab total width, } B_s/2 = 750 \text{ mm}$$

$$\text{Number of top reinforcing bars, } n_t = 15 \text{ Nos}$$

$$\text{Diameter of slab reinforcing bar, } D_p = 8 \text{ mm}$$

$$\text{Area of 15 reinforcing bars, } n_t A_s = 753.98 \text{ mm}^2$$

Depth of equivalent rectangular stress block,

$$a = \frac{A_s \times f_y}{0.85 \times f'_c \times B_s / 2} = 10.07 \text{ mm}$$

$$\text{Nominal moment, } M_n = A_s \times f_y \times \left( d - \frac{a}{2} \right) = 29.38 \text{ kNm}$$

Ultimate moment obtained from SAP2000,

$$M_{load} = \frac{M_g + M_u}{2} = 54.62 \text{ kNm}$$

$$\text{Ratio of } M_n/M_{load} = \mathbf{0.54}$$

### C.9. Inspection of Slab Reinforcement Within Slab Effective Width ( $c + 3h$ )

$$\text{Slab total width, } c + 3h = 660 \text{ mm}$$

$$\text{Number of top reinforcing bars, } n_t = 13 \text{ Nos}$$

$$\text{Diameter of slab reinforcing bar, } D_p = 8 \text{ mm}$$

$$\text{Area of 13 reinforcing bars, } n_t A_s = 653.45 \text{ mm}^2$$

Depth of equivalent rectangular stress block,

$$a = \frac{A_s \times f_y}{0.85 \times f'_c \times B_s / 2} = 9.91 \text{ mm}$$

$$\text{Nominal moment, } M_n = A_s \times f_y \times \left( d - \frac{a}{2} \right) = 32.12 \text{ kNm}$$

Ultimate moment obtained from SAP2000,

$$M_{load} = \gamma_f \left( \frac{M_u}{2} \right) + \frac{c + 3h}{B_s} \times M_g = 43.04 \text{ kNm}$$

$$\text{Ratio of } M_n/M_{load} = \mathbf{0.75}$$

**Note:** The ratio of  $M_n/M_{load}$  with the value not greater than 1.0 indicates that during the course of loading, the slab reinforcing bars have yielded.

## BIOGRAPHY

1. Name : Asdam Tambusay
2. Place, Date of Birth : Kendari, 18 August 1990
3. Gender : Male
4. E-mail : asdam.tambusay13@mhs.ce.its.ac.id
5. Mobile Phone : +62 812 2181 2041
6. Home Address : Jalan Asempayung 1 No. 3  
Gebang Putih, Sukolilo, 60117  
Surabaya, East Java, Indonesia
7. Field of Study : Structural Engineering

## EDUCATIONAL QUALIFICATIONS:

Academic Level : **DOCTOR OF PHILOSOPHY**  
Institution : Sepuluh Nopember Institute of Technology  
Field of Study : Structural Engineering  
Graduation Period : 2017  
Research Topic : Cyclic Behaviour of Slab-Column Connections  
using the Engineered Cementitious Composite

Academic Level : **BACHELOR OF ENGINEERING**  
Institution : Hasanuddin University  
Field of Study : Civil Engineering  
Graduation Period : 2012  
Research Topic : A Review Design of Upper-structural Building  
of Patria Artha University

## ACADEMIC ACTIVITY:

Internship : **VISITING SCHOLAR PROGRAMME**  
Institution : Heriot-Watt University  
Edinburgh, Scotland, United Kingdom  
Intake Period : 2016/2017  
Research Project : Investigating the Influence of Pre-Existing  
Cracks on the Shear Behaviour of Reinforced  
Concrete and Engineered Cementitious  
Composite (ECC) Beams  
Host-Supervisor : Benny Suryanto, BEng MEng PhD FHEA

### **RESEARCH INTEREST:**

- Testing of Reinforced Concrete Members;
- Utilisation of cement-based material with particular focusing on the use of engineered cementitious composite;
- Modelling of Reinforced Concrete using the advanced finite element software;
- Shear and flexural behaviour of reinforced concrete structure;
- Crack mapping of reinforced concrete member using the digital image correlation.

### **INTERNATIONAL JOURNAL PUBLICATIONS:**

1. **TAMBUSAY A, SUPROBO P, FAIMUN, AMIRUDDIN AA** (2017) “Finite element analysis on the behaviour of slab-column connections using PVA-ECC material,” *Jurnal Teknologi (Science and Engineering)*, Vol. 79, No. 5, pp. 23–32.
2. **TAMBUSAY A, SUPROBO P, FAIMUN, AMIRUDDIN AA** (2017) “Finite element modelling of a reinforced concrete slab-column connection under cyclic lateral load,” *International Journal of Applied Engineering Research*, ISSN 0973–4562, Vol. 12, No. 9, pp. 1987–1993.
3. **FAIMUN, TAMBUSAY A, SUPROBO P** (2017) “The influence of gravity shear ratio on the behaviour of Slab-Column Connections with Shear Reinforcement,” *International Journal of Applied Engineering Research* (accepted for publication).
4. **SURYANTO B, TAMBUSAY A, SUPROBO P** (2017) “Influence of Shear Reinforcement Spacing on the Strength and Ductility of Reinforced Concrete Beams,” *Civil Engineering Dimension* (accepted for publication).
5. **SURYANTO B, TAMBUSAY A, SUPROBO P** (2017) “Crack mapping on a reinforced concrete beam using digital image correlation,” *Proceedings of the Institution of Civil Engineers – Structures and Buildings* (second round review).
6. **TAMBUSAY A, SUPROBO P, FAIMUN, AMIRUDDIN AA** (2016) “Finite element prediction on the post-punching behaviour of slab-column connections,” *Applied Mechanics and Materials*, ISSN: 1662-482, Vol. 851, pp. 714–719.

### **CONFERENCE PROCEEDINGS:**

1. **TAMBUSAY A, SURYANTO B, SUPROBO P** (2017) “Visualization of shear cracks in a reinforced concrete beam using the digital image correlation,” *Proceedings of the RCCE-ICCER*, August 2017, Surabaya, Indonesia.

2. **TAMBUSAY A**, SUPROBO P, FAIMUN, AMIRUDDIN AA (2016) “Analyses behaviour of slab-column connections using ECC material based on finite element approach,” Proceedings of the EASEC 14, January 2016, Ho Chi Minh City, Vietnam.
3. **TAMBUSAY A**, SUPROBO P, FAIMUN, AMIRUDDIN AA (2015) “Studi numerik perilaku hubungan pelat-kolom pada struktur flat slab menggunakan beton mutu tinggi,” Prosiding KNPTS 2015, November 2015, Bandung, Indonesia.
4. **TAMBUSAY A**, SUPROBO P, FAIMUN, AMIRUDDIN AA (2015) “Experimental study of engineered cementitious composite material for structural application,” Proceedings of the 2<sup>nd</sup> MICCE 2015, August 2015, Makassar, Indonesia.
5. **TAMBUSAY A**, SUPROBO P, FAIMUN (2014) “Studi eksperimental perilaku hubungan pelat-kolom menggunakan drop panel dengan serat PVA-ECC terhadap beban siklik lateral,” Prosiding KNPTS 2014, November 2014, Bandung, Indonesia.

#### **FUNDED RESEARCH PROJECTS:**

1. SUPROBO P, FAIMUN, AMIRUDDIN AA, **TAMBUSAY A** (2014) “Studi peningkatan perilaku hubungan pelat-kolom menggunakan drop panel dengan material PVA-ECC terhadap beban siklik lateral,” Hibah Penelitian Program PMDSU, Kementrian Riset, Teknologi, dan Pendidikan Tinggi Republik Indonesia.

#### **AWARDS AND ACHIEVEMENTS:**

1. In recognition for **BEST PAPER** on the 3<sup>rd</sup> International Conference on Advanced Materials, Structures, and Mechanical Engineering (ICAMSME), May 2016, Incheon, South Korea.
2. In recognition for **BEST PAPER** on the National Conference of Postgraduate Civil Engineering (KNPTS-15), November 2015, Bandung Institute of Technology, Bandung, Indonesia.
3. In recognition for **BEST PRESENTER** on the 2<sup>nd</sup> Makassar International Conference on Civil Engineering (MICCE 2015), Hasanuddin University, Makassar, Indonesia.
4. In recognition for **BEST PAPER** on the National Conference of Postgraduate Civil Engineering (KNPTS-14), November 2014, Bandung Institute of Technology, Bandung, Indonesia.

*This page intentionally left blank*